

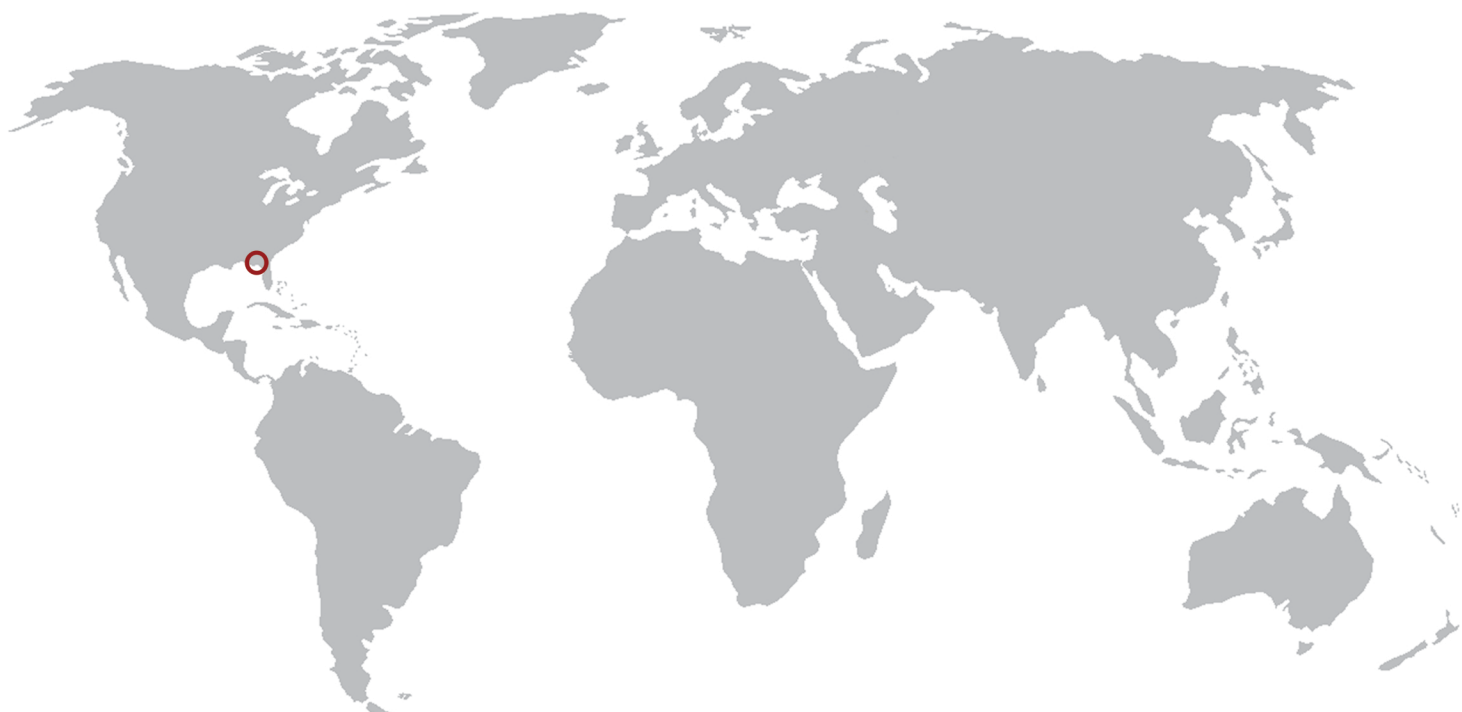
P R O C E E D I N G S

MMM 2008
Fourth
International Conference

MULTISCALE MATERIALS MODELING

OCTOBER 27-31, 2008 • TALLAHASSEE, FLORIDA, USA

*Tackling Materials Complexities
via Computational Science*



Hosted by the Department of Scientific Computing and Florida State University

DEPARTMENT OF
Scientific
COMPUTING



Proceedings of

MMM 2008
*Fourth
International Conference*
MULTISCALE MATERIALS MODELING
OCTOBER 27-31, 2008 • TALLAHASSEE, FLORIDA, USA

Anter El-Azab
Editor

**Organized and Hosted by
The Department of Scientific Computing and
Florida State University**

DEPARTMENT OF
Scientific
COMPUTING



Papers published in this volume constitute the proceedings of the Fourth International Conference on Multiscale Materials Modeling (MMM-2008). Papers were selected by the program committee for oral or poster presentation. They are published as submitted, in the interest of timely dissemination.

ISBN 978-0-615-24781-6

Copyright © 2008
Department of Scientific Computing
Florida State University
400 Dirac Science Library
P.O. Box 3064120
Tallahassee, FL 32306-4120

All rights reserved. No part of this publication may be translated, reproduced, stored in a retrieval system, or transmitted in any form or by any means, electronic, mechanical, photocopying, recording or otherwise, without the written permission of the publisher.

Printed in the United States of America

Forward

The field of multiscale modeling of materials promotes the development of predictive materials research tools that can be used to understand the structure and properties of materials at all scales and help us process materials with novel properties. By its very nature, this field transcends the boundaries between materials science, mechanics, and physics and chemistry of materials. The increasing interest in this field by mathematicians and computational scientists is creating opportunities for solving computational problems in the field with unprecedented levels of rigor and accuracy. Because it is a part of the wider field of materials science, multiscale materials research is intimately linked with experiments and, together, these methodologies serve the dual role of enhancing our fundamental understanding of materials and enabling materials design for improved performance.

The increasing role of multiscale modeling in materials research motivated the materials science community to start the Multiscale Materials Modeling (MMM) Conference series in 2002, with the goal of promoting new concepts in the field and fostering technical exchange within the community. Three successful conferences in this series have been already held:

- The First International Conference on Multiscale Materials Modeling (MMM-2002) at Queen Mary University of London, UK, June 17-20, 2002,
- Second International Conference on Multiscale Materials Modeling (MMM-2004) at the University of California in Los Angeles, USA, October 11-15, 2004, and
- Third International Conference on Multiscale Materials Modeling (MMM-2006) at the University of Freiburg, Germany, September 18-22, 2006.

The Fourth International Conference on Multiscale Materials Modeling (MMM-2008) held at Florida State University comes at a time when the wider computational science field is shaping up and the synergy between the materials modeling community and computational scientists and mathematicians is becoming significant. The overarching theme of the MMM-2008 conference is thus chosen to be “*Tackling Materials Complexities via Computational Science*,” a theme that highlights the connection between multiscale materials modeling and the wider computational science field and also reflects the level of maturity that the field of multiscale materials research has come to. The conference covers topics ranging from basic multiscale modeling principles all the way to computational materials design. Nine symposia have been organized, which span the following topical areas:

- Mathematical basis for multiscale modeling of materials
- Statistical frameworks for multiscale materials modeling
- Mechanics of materials across time and length scales
- Multiscale modeling of microstructure evolution in materials
- Defects in materials
- Computational materials design based on multiscale and multi-level modeling principles

- Multiscale modeling of radiation effects in materials and materials response under extreme conditions
- Multiscale modeling of bio and soft matter systems

The first five topical areas are intended to cover the theoretical and computational basis for multiscale modeling of materials. The sixth topical area is intended to demonstrate the technological importance and industrial potential of multiscale materials modeling techniques, and to stimulate academia-laboratory-industrial interactions. The last two topical areas highly overlap with the earlier ones, yet they bring to the conference distinct materials phenomena and modeling problems and approaches with unique multiscale modeling aspects.

This conference would not have been possible without the help of many individuals both at Florida State University and around the world. Of those, I would like to thank the organizing team of MMM-2006, especially Professor Peter Gumbsch, for sharing their experience and much organizational material with us. I also thank all members of the International Advisory Board for their support and insight during the early organizational phase of the conference, and the members of the International Organizing Committee for the hard work in pulling the conference symposia together and for putting up with the many organization-related requests. Thanks are due to Professor Max Gunzburger, Chairman of the Department of Scientific Computing (formerly School of Computational Science) and to Florida State University for making available financial, logistical and administrative support without which the MMM-2008 would not have been possible. The following local organizing team members have devoted significant effort and time to MMM-2008 organization: Bill Burgess, Anne Johnson, Michele Locke, Jim Wilgenbusch, Christopher Cprek and Michael McDonald. Thanks are also due to my students Srujan Rokkam, Steve Henke, Jie Deng, Santosh Dubey, Mamdouh Mohamed and Jennifer Murray for helping with various organizational tasks. Special thanks are due to Bill Burgess and Srujan Rokkam for their hard work on the preparation of the proceedings volume and conference program.

I would like to thank the MMM-2008 sponsors: Lawrence Livermore National Laboratory (Dr. Tomas Diaz de la Rubia), Oak Ridge National Laboratory (Dr. Steve Zinkle) and Army Research Office (Drs. Bruce LaMattina and A.M. Rajendran) for the generous financial support, and thank TMS (Dr. Todd Osman) for the sponsorship of MMM-2008 and for advertising the conference through the TMS website and other TMS forums.

I would also like to thank all plenary speakers and panelists for accepting our invitation to give plenary lectures and/or serve on the conference panels. Lastly, I would like to thank the session chairs for managing the conference sessions.

Anter El-Azab
Conference Chair

International Advisory Board

Dr. Tomas Diaz de la Rubia	LLNL, USA
Prof. Peter Gumbsch	Fraunhofer Institute IWM, Freiburg, Germany
Dr. A.M. Rajendran	ARO, USA
Dr. Steve Zinkle	ORNL, USA
Prof. Anter El-Azab	FSU, USA
Prof. Michael Zaiser	Edinburgh, UK
Prof. Xiao Guo	Queens, London, UK
Prof. Shuichi Iwata	University of Tokyo, Japan
Prof. Jan Kratochvil	CTU, Prague, Czech Republic
Prof. Nasr Ghoniem (Chair)	UCLA, USA
Dr. Ladislav Kubin	ONERA-LEM, France
Prof. Shaker Meguid	Toronto, Canada
Prof. Alan Needleman	Brown, USA
Prof. Michael Ortiz	Caltech, USA
Prof. David Pettifor	Oxford, UK
Prof. Robert Phillips	Caltech, USA
Prof. Dierk Raabe	Max Planck Institute, Duesseldorf, Germany
Prof. Yoji Shibutani	Osaka University, Japan
Prof. Subra Suresh	MIT, Massachusetts USA
Prof. Yoshihiro Tomita	Kobe University, Japan
Prof. Erik Van der Giessen	University of Groningen, The Netherlands
Dr. Dieter Wolf	INL, USA
Prof. Sidney Yip	MIT, USA
Prof. David Bacon	Liverpool, UK
Dr. Michael Baskes	LANL, USA
Prof. Esteban Busso	Ecole des Mines, France
Prof. Timothy Cale	RPI, New York, USA
Dr. Moe Khaleel	PNNL, USA
Prof. David Srolovitz	Yeshiva, USA
Prof. Emily Carter	Priceton University, USA
Dr. Dennis Dimiduk	AFRL, USA
Prof. Rich Le Sar	Iowa State University, USA

International Organizing Committee

Weinan E	Princeton University, USA
Max Gunzburger	Florida State University, USA
Mitchell Luskin	University of Minnesota, USA
Rich Lehoucq	Sandia National Laboratories, USA
A.M. Rajendran	U.S. Army Research Office, USA
Stefano Zapperi	University of Rome, Italy
M.-Carmen Miguel	University of Barcelona, Spain
Mikko Alava	Helsinki University of Technology, Finland
Istevan Groma	Eötvös University, Hungary
Tom Arsenlis	Lawrence Livermore National Laboratory, USA
Peter Chung	Army Research Laboratory, USA

Marc Geers	Eindhoven University of Technology, The Netherlands
Yoji Shibutani	Osaka University, Japan
Dieter Wolf	Idaho National Laboratory, USA
Jeff Simmons	Air Force Research Laboratory, USA
Simon Phillpot	University of Florida, USA
Anter El-Azab (Chair)	Florida State University, USA
Daniel Weygand	University of Karlsruhe (TH), Germany
Zi-Kui Liu	Pennsylvania State University, USA
Hamid Garmestani	Georgia Institute of Technology, USA
Moe Khaleel	Pacific Northwest National Laboratory, USA
Mei Li	Ford Motor Company, USA
Fie Gao	Pacific Northwest National Laboratory, USA
Roger Stoller	Oak Ridge National Laboratory, USA
Pascal Bellon	University of Illinois, Urbana-Champaign, USA
Syo Matsumura	Kyushu University, Japan
Jeffery G. Saven	University of Pennsylvania, USA
Wei Yang	Florida State University, USA
T.P. Straatsma	Pacific Northwest National Laboratory, USA
L.P. Kubin	CNRS-ONERA, France
S.J. Zinkle	Oak Ridge National Laboratory, USA
Jaafar El-Awady	University of California, Los Angeles, USA
Shahram Sharafat	University of California, Los Angeles, USA
Hanchen Huang	Rensselaer Polytechnic Institute, USA
Yury N. Osetskiy	Oak Ridge National Laboratory, USA
Ron O. Scattergood	North Carolina State University, USA
Anna M. Serra	Universitat Politècnica de Catalunya, Spain

Local Organizing Committee (Florida State University, USA)

Prof. Anter El-Azab (Chair)
 Prof. Max Gunzburger (Co-Chair)
 Anne Johnson (Public relations and marketing)
 Bill Burgers (Graphics and publications)
 Srujan Rokkam (Proceedings and printing)
 Michael McDonald (Webmaster)
 Michele Locke (Finances)

Sponsors

Special thanks to the following sponsors:

- The Army Research Office
- Lawrence Livermore National Laboratory
- Oak Ridge National Laboratory

for their generous financial support, and to

- The Minerals, Metals & Materials Society (TMS)

for the sponsoring and advertising the conference through the TMS website.

Contents

Symposium 3

Development of sequential multi-scale analysis for nano structured materials	155
M. Cho, S. Yang, J. Choi Session M-B	
Polycrystal Plasticity Analysis of Bimodal Structures Considering the Three-Stage Characteristics of the Resolved Shear Stress vs. Strain Curves of Individual Grains	161
Y. Nakasone Session M-B	
Mesoscopic modelling and size effect for the mechanics of multi-walled carbon nanotubes	162
M. Arroyo, I. Arias Session M-B	
Investigation the stability of SWCNT-polymer composites in the presence of CNT geometrical defects using multiscale modeling	163
A. Montazeri, R. Naghdabadi Session M-B	
On the Multi-Scale Computation of Defect Driving Forces	167
S. Ricker, J. Mergheim, P. Steinmann Session M-C	
Numerical Material Testing for Strength Evaluation of Polycrystalline Metals	168
K. Terada, I. Watanabe Session M-C	
Modeling size effect dependence on mechanical behaviour using a Cosserat crystal plasticity framework	174
A. Gaubert, S. Forest Session M-C	
Combined Effects of Crystallographic and Grain Size Heterogeneities on Plasticity of Polycrystalline IF Steels	178
N. Nicaise, S. Berbenni, F. Wagner, M. Berveiller, X. Lemoine Session M-C	
Onset of Plasticity Under Nanoindentation: Influence of the Interatomic Potential	182
G. Ziegenhain, A. Hartmaier, H. M. Urbassek Session M-D	

Effect of Surface Structure on Strength of Si Thin Film	186
Y. Umeno Session M-D	
Dislocation-guided Dynamics of Surface Defects on a Multilayered Si-Ge Heterostructure	187
B. Yang Session M-D	
Dislocation Dynamics for Engineering Applications	188
V. V. Bulatov Session T-B	
Dilute Discrete Dislocation Dynamics	189
M.P. Ariza, M. Ortiz Session T-B	
Size and Bauschinger Effects in Micro-bending: A 3D Discrete Dislocation Dynamics Study	190
C. Motz, D. Weygand, P. Gumbsch Session T-B	
An analysis of the size effect in void growth in single crystals using discrete dislocation dynamics	191
J. Segurado, J. Llorca, I. Romero Session T-B	
Mesoscale Modelling of Dislocation Pile-up Based on Discrete Interactions	195
R.H.J. Peerlings, Y. Kasyanyuk, A. Roy, M.G.D. Geers Session T-B	
The role of the edge effects in the strain localization evolution in polycrystals on the mesolevel	199
G. Lasko, Y. Y. Deryugin, S. Schmauder Session T-C	
An Effective Interaction Potential Model of Stress- and Temperature-induced Martensitic Transformations in Perfect Bi-atomic Crystals	203
R. Elliott, N. Triantafyllidis, J. Shaw Session T-C	

Influence of the elastic anisotropy on the initial yielding of polycrystals	204
R. Brenner, R. A. Lebensohn, O. Castelnau Session T-C	
Micromechanical Modeling of Materials containing Intra-crystalline Particles	208
N. Bonfoh, P. Lipinski Session T-C	
Selfconsistent Modelling of the Mechanical Response of Viscoplastic Polycrystals Deforming by Glide and Climb	209
R. A. Lebensohn, C. N. Tomé, C. S. Hartley, O. Castelnau, S. A. Maloy Session T-C	
Large-Scale Simulation of Oscillating Metal-Nanorod: Application of the Hybrid Molecular-Dynamics/Coarse-Grained-Particle Approach	210
R. Kobayashi, T. Nakamura, S. Ogata Session W-B	
Atomistic/continuum models for multiscale heat conduction	214
K. Jolley, S. P.A. Gill Session W-B	
Hot Quasicontinuum calculations of nanovoids evolution under volumetric expansion	218
C. Arévalo, Y. Kulkarni, M.P. Ariza, M. Ortiz, J. Knap, J. Marian Session W-B	
Coupling Atomistic and Continuum Descriptions: Continuity of Energy Flux and Correlation	219
D. Nicholson, S. Namilae, P. K.V.V. Nukala, Y.N.Osteskiy, C.Y.Gao, D.J. Keffer Session W-B	
Reformulation of Continuum Mechanics to Include Multiple Length/Time Scales	220
Y. Chen, L. Xiong Session W-B	
A Comparative Study of Multiscale Modeling of Generalized Finite Elements and Molecular Dynamics	221
P. W. Chung, M. F. Macri Session W-B	

Reduced Models Obtained by Nonlocal Quasi-continuum-like Approaches	222
M. Anitescu, A. El-Azab, P. Zapol, D. Negrut Session W-B	
Mapping Mesoscale Heterogeneity in the Deformation of Single Crystal Copper	223
J. Morris, K. Magid, N. Tamura, J. Florando, D. Lassila, M. leBlanc Session W-C	
Continuum Modeling of Plastic Deformation in Polycrystalline Thin Films	224
S. Puri, A. Acharya Session W-C	
Role of Intra-granular Plastic Slip Heterogeneities on Lattice Rotations: comparisons between experimental measurements and a new micromechanical modeling	225
C. Perrin, T. Richeton, S. Berbenni, M. Berveiller, H. Vehoff Session W-C	
Higher Order Conditions at Grain Boundaries: Finite Element Simulations of Polycrystal Behavior	230
N. Cordero, E. Busso, S. Forest Session W-C	
Microstructural Aspects of Ductile Rupture in Solids	231
T.W. Wright, K.T. Ramesh Session Th-B	
Determination of Burgers Vectors from Atomistic Data	232
J. Hua, A. Hartmaier, M. Duchaineau Session Th-B	
Modelling the Growth of Hydrogen-Induced Platelets in Silicon with the “Learn On The Fly” Multiscale Molecular Dynamics Technique	233
G. Moras, L. C. Ciacchi, C. Elsässer, A. De Vita Session Th-B	
Heterogeneous Dislocation Nucleation in Defective Metal Surfaces During Nanoindentation	234
O. R. de la Fuente Session Th-B	

New Computational Technique for Evaluating Deformation of Nanocrystalline Metal using Phase Field Crystal Method T. Hirouchi, T. Takaki, Y. Tomita Session Th-B	235
Modeling the interphase layer between CNT and matrix in Nanocomposites using nonlinear large deformation hierarchical multiscale J. Ghanbari, R. Naghdabadi Session Th-B	239
Grain Size Effects in the Wedge Indentation of Polycrystals: a Discrete Dislocation Analysis A. Widjaja, A. Needleman, E. Van der Giessen Session Th-C	243
Multi-scale plasticity modeling: from atoms to continuum crystal plasticity W. Curtin Session Th-C	244
Applications of Adaptive Sampling in Multi-scale Simulations N. R. Barton, J. V. Bernier, J. Knap Session Th-C	245
Modeling Hydrogen Embrittlement in Metals: Coupling Quantum Mechanical, Empirical Potential and Kinetic Monte Carlo Approaches A. Ramasubramaniam, M. Itakura, M. Ortiz, E. A. Carter Session Th-C	246
Stress analysis during the interaction between dislocations and a main crack: Case of a bi-material M. Chabaat, H. Hamli Ben Zahar Session Th-D	247
Damage Evolution in Foams K. E. Aifantis, A. A. Konstantinidis, M. Zaiser Session Th-D	253
Adaptive Embedding of the Electronic-Density-Functional-Theory in the Classical Molecular Dynamics: Application to Nano-Indentation S. Ogata, Y. Abe, R. Kobayashi Session Th-D	257

Python Based Combined Continuum-atomic Modeling for Single Crystal Nickel	258
I. Tirtom, T. Shoji Session Th-D	
Investigating the Time Dependency of the Viscoelastic Bulk Modulus using Gnomix PVT Apparatus	262
M. K. Saraswat Session T-D	
Size Effect of Finite Deformable Nanopillar by Focused-ion-beam Chemical Vapor Deposition	263
H. Tanaka, Y. Shibutani Session T-D	
Reaction Pathway Analysis of Dislocation-Interface Interactions in Cu-Ni Multilayered Systems	267
S. Hara, T. Take, S. Izumi, S. Sakai Session T-D	
Elasto-Viscoplastic Micromechanical Modelling of the Transient Creep of Ice	271
O. Castelnaud, P. Duval, M. Montagnat, R. Brenner Session T-D	
Synthesis for Ceramic Oxides	272
X. Xie., H. Zhou., J. Zhu, J. Guo, S. Yan Session T-D	
Evaluation of influence of size of inclusion on the Effective Material Property of Particle reinforced Composites	276
A. Agrawal, R. Saha Session T-D	
Generalized self consistent polycrystalline model applied to Heterogeneous materials exhibiting log normal grain size distribution	277
Q. H. Bui, S. Ramtani, G. F. Dirras Session T-D	
Two Step Homogenization of Thermal Conductivities for Macroscopically Orthotropic C/C Composites	281
Jan Vorel, Michal Sejnoha Session T-D	

Failure of Granular Materials under Impact – Multiscale Simulations and High-Speed Experiments	285
M. O. Steinhauser Session T-D	
Multiscale Model of Nanoindentation Test in Cu and Ni	286
M. Černý, J. Pokluda, J. Horníková, P. Šandera Session T-D	
Hardening by completely and partially absorbed $\frac{1}{2}\langle 111 \rangle$ and $\langle 100 \rangle$ dislocation loops reacting with dislocations in α-Fe.	287
D. Terentyev, D.J. Bacon, P. Grammatikopoulos, Y.N. Osetsky Session T-D	
α-α' phase separation in Fe-Cr alloys and its impact on mechanical properties: An atomistic study	293
G. Bonny, D. Terentyev, L. Malerba Session T-D	
Dislocation Core Fields and Elasticity Theory: The Screw Dislocation in Iron	297
E. Clouet, L. Ventelon, F. Willaime Session T-D	
On micromechanical models of nonlocal media	298
X. Yuan Session T-D	
Analysis of Transformation Plasticity Using a Finite Element Model Coupled with a Phase Field Method	299
Y.-G. Cho, J.-Y. Kim, P.-R. Cha, J. K. Lee, H. N. Han Session T-D	
Al atomistic dislocation simulations using a tight-binding method	300
C. Gan, S.-S. Quek Session T-D	
Numerical Analysis of Ceramics under Impulsive Loads at Grain Scale	301
S. Knell, M. Sauer, K. Thoma Session T-D	
Virtual Processing of Dual Phase Steels – A Microstructure Based Simulation Approach	302
A. Butz, T. Rist, B. Springub, F. Roters, S. Schultz, Session T-D	

On a Finite Strain Micromorphic Plasticity Model for Bound Particulate Materials	306
R. Regueiro Session T-D	
Microyield Behaviour of Metallic Multilayers	307
M. Verdier Session T-D	
Numerical investigations of compact tension fracture specimens	308
P. Mueller, P. Spätig Session T-D	
An Energy Approach to Determine the Martensite Morphology in Nano-Structured NiTi Alloys	309
T. Antretter, W. Pranger, T. Waitz, F.D. Fischer Session T-D	
Towards identification of microstructure-property correlations in a titanium alloy using image-based modeling	310
M. A. S. Qidwai, A. C. Lewis, A. B. Geltmacher Session T-D	
Numerical and analytical homogenisation approach for modeling mechanical behaviour of heterogeneous geomaterials	314
D. P. Do, N. Belayachi, D. Hoxha, A. Giraud Session T-D	
An Adaptive Coarse-Graining Scheme for the Simulation of Elastomer Networks	318
M. Davies, A. Lew Session T-D	
Dislocation Quasi-Statics: Implicit Time Integration for Dislocation Dynamics Simulations	319
T. Arsenlis, V. Bulatov, G. Hommes, M. Rhee, M. Tang Session T-D	
Orientation Dependence of Friction in PTFE	320
P. R. Barry, P. Y. Chiu, S. S. Perry, W. G. Sawyer, S. R. Phillpot, S. B. Sinnott Session T-D	
Multiscale Analysis of Cell-Gold Adhesion	321
J. Fan, M. Chinappi Session T-D	

Stress relaxation and dynamic strain aging of Zr-Sn-Nb alloy	322
J. Tan, C. Li, C. Sun, S. Ying Session T-D	
Development of Statistically Equivalent Representative Volume Elements for Multi-scale Modeling of Composite Materials	323
T. Vaughan, C. McCarthy Session T-D	
Micromechanical modeling of the anisotropy of elastic biological composites - Theory and fundamental concepts	327
J. Rahmoun, J. Halgrin, F. Chaari, E. Markiewicz, P. Drazetic Session T-D	
Dusty Plasma - Multy Scale	331
V. Fortov, O. Petrov, O. Vaulina Session T-D	
Atomistic Simulations of Tribology at Sliding MoS Surfaces	332
T. Liang, W. G. Sawyer, S. S. Perry, S. R. Phillpot, S. B. Sinnott Session T-D	
Modelling Damage of the Crystalline Phase in Semicrystalline Polyethylene	333
J. A. Alvarado-Contreras, M. A. Polak, A. Penlidis Session T-D	
Composite piezoelectric structures used for energy harvesting	337
K. Cook-Chennault Session T-D	
On the micromechanical deformation of particle filled polypropylene compounds	338
M. Jerabek, Z. Major Session T-D	

Symposium 3

Multiscale mechanics

Development of sequential multi-scale analysis for nano structured materials

Maenghyo Cho¹, Seunghwa Yang¹, Jinbok Choi¹

**¹School of Mechanical and Aerospace Engineering, Seoul National University,
San 56-1, Shillim-Dong, Kwanak-Ku, Seoul, 151-744, South Korea
(E-mail: mhcho@snu.ac.kr)**

ABSTRACT

In this study, sequential multi-scale bridging method to characterize the size effect of nanoparticle on the mechanical properties of nanoparticle/polymer composites is developed and verified through a molecular dynamics(MD) simulation and continuum micro mechanics. In order to obtain the size effect of nanoparticle in detail, two sets of nanocomposites having dilute and non-dilute concentration of nanoparticles are considered in MD simulations. In total, five different unit cells with different particle size and same volume fractions were prepared in each case. Spherical silica nanoparticle and amorphous polyimide were chosen as reinforcement particulate fiber and matrix respectively and Parrinello-Rahman fluctuation method was used to obtain mechanical properties of each systems. In accordance with the volume fraction of each sets, two different multi scale bridging methods are developed incorporating the effective interface as a characteristic phase to describe the particle size effects. Postulating that the Young's modulus and shear modulus of the interface as functions of particle radius, monotonous decaying functions to represent shear modulus and Young's modulus were obtained from the least square approximation. In order to validate present scale bridging method, overall elastic modulus of nanocomposites are obtained using finite element analysis. As a result, enhanced reinforcing effect was observed in smaller particle reinforced cases and the present bridging method accurately follows MD simulation results. Also, elastic modulus obtained from the finite element analysis showed reliability and applicability of the present method for the design of the nanocomposites with continuum-based analysis.

1. Introduction

Due to the recent advance of nano-scale manufacturing technology, various types of nano-structured materials are developed and studied for their practical applications[1]. Among those nano materials, polymer-based nanocomposites with nanoparticles attract many researchers for their unusual properties and multi-functionalities[2]. It is generally known that the characteristics of the nano-sized particles are originated from the increased ratio of interface area to the volume of spherical particles and many researches are accompanied to verify and consider the size effect of particles. Regarding the effect of particle size on the mechanical properties, both positive and negative effects have been reported till now[3-4] and it still remains as an ongoing argument.

In this study, mechanical properties of the silica nanoparticle reinforced polymeric composites are characterized and the size effect of the nanoparticle is studied through a molecular dynamics(MD) simulation, micromechanics of dilute and non-dilute composites and

finite element method(FEM). The effective interface was adopted as a characteristic phase between the nanoparticle and matrix polymer and the way how to define the elastic modulus and volume fractions of the interface are elucidated in detail.

2. Molecular dynamics simulation

In MD simulations, commercial molecular simulation program MATERIAL STUDIO 4.0 was used and *ab-initio* COMPASS force field[5] which is optimized to condensed phase materials is chosen to describe inter- and intra-molecular interactions. The COMPASS forcefield is composed of three parties, valence, cross-terms and non-bond interactions and totally 12 terms are incorporated.

Table 1 Unit cell compositions of nanocomposites

(a) Dilute concentration					(b) Non-dilute concentration				
System	Particle radius(Å)	No. of chains	Cell length(Å)	Vol. fraction	System	Particle radius(Å)	No. of chains	Cell length(Å)	Vol. fraction
NPC3	5.6	3	29.07	0.03	NDPC4	9.97	4	32.64	0.12
NPC4	6.16	4	31.99	0.03	NDPC5	10.74	5	35.16	0.12
NPC6	7.05	6	36.62	0.03	NDPC6	11.41	6	37.36	0.12
NPC10	8.36	10	43.42	0.03	NDPC7	12.01	7	39.32	0.12
NPC12	8.89	12	46.14	0.03	NDPC8	12.56	8	41.04	0.12

In order to obtain particle size effect on the mechanical properties of nanocomposites, two kinds of molecular structures categorized as dilute concentration (low volume fraction) and non-dilute concentration (high volume fraction) are prepared. In each sets, five unit-cells having different particle radius with same volume fraction were constructed. The radius of selected nanoparticle(SiO_2 , silica) ranges from 5.6Å to 8.89Å in dilute nanocomposites and from 9.07Å

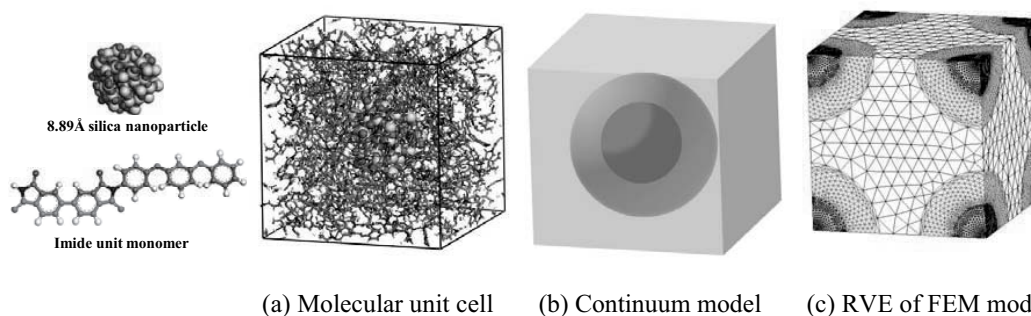


Figure.1 : Unit cell structures of nanocomposites and equivalent continuum models

to 12.01Å in non-dilute nanocomposites. Polyimide was chosen as amorphous matrix. Each polyimide molecular chain is composed of 12 repeated unit monomers and the number of chains in each sample sets is determined from the same volume fraction condition (in this study, 0.03 for dilute composites and 0.12 for non dilute composites). Details of the composition of the

particle, matrix and initial geometrical information of each cell are arranged in Tab 1 and atomistic structures of the constituents and unit cells are illustrated in Fig. 1.

After constructing the initial structures, the cells are minimized to their lowest potential energy state using Conjugate gradient method. After minimization, all the simulation cells are equilibrated at 300K and 1bar. In the equilibrated stage, totally 900ps(pico second) of isothermal and isobaric ensemble simulation(NPT) is applied via Andersen and Berendsen methods to control the external temperature and atmospheric pressure respectively. Elastic constants of the unit cells are obtained using Parrinello-Rahman fluctuation method. In order to ensure computational accuracy, all the molecular dynamics data were obtained from average over three and five different production runs in dilute and non-dilute cases respectively.

Table 2 Elastic modulus of the nanocomposites obtained from MD simulations

System	E(Gpa)	G(Gpa)	System	E(Gpa)	G(Gpa)
NPC3	3.81±0.43	1.37±0.16	NDPC4	4.66±0.10	1.74±0.04
NPC4	3.39±0.16	1.26±0.08	NDPC5	4.20±0.53	1.54±0.20
NPC6	3.12±0.26	1.14±0.13	NDPC6	3.99±0.26	1.45±0.11
NPC10	2.89±0.24	1.04±0.08	NDPC7	3.81±0.22	1.38±0.09
NPC12	2.76±0.28	1.00±0.09	NDPC8	3.60±0.34	1.30±0.14

Resultant Young's modulus and shear modulus of dilute nanocomposites and non-dilute nanocomposites are arranged with standard deviations in Tab 2. As shown in Tab 2, both Young's and shear modulus of the nanocomposites decrease as the particle radius increases. Based on the results obtained from MD simulations, elastic modulus of the interface can be estimated and the details of interface characterization will be described in next part.

3. Scale bridging method

3.1 Dilute effective interface model

As was shown in previous MD simulation results, elastic modulus of nanocomposites can be affected by the size of their reinforcing particles. In case of dilute concentration, Mori-Tanaka method has been widely used to estimate the effective elastic modulus of composites. But as this model only considers volume fraction and stiffness matrix of particle and matrix, this method is not suitable for nanocomposites. So, modified three-phase model consists of particle, matrix and effective interface between particle and matrix was considered as below

$$\mathbf{C} = \mathbf{C}_m + \left[(f_p + f_i)(\mathbf{C}_i - \mathbf{C}_m)\mathbf{A}_{pi} + f_p(\mathbf{C}_p - \mathbf{C}_i)\mathbf{A}_p \right] \left[f_m \mathbf{I} + (f_p + f_i)\mathbf{A}_{pi} \right]^{-1} \quad (1)$$

where, \mathbf{C} and f with subscript are the stiffness matrix and volume fraction of each phase and the subscript p, i, m corresponds to the particle, interface and matrix. \mathbf{A}_{pi} and \mathbf{A}_p are strain concentration tensors of particle and effective particle(particle with interface)[6]. In order to define the elastic modulus of effective interface, Eqn(1~2) were rearranged with respect to the stiffness matrix of the interface \mathbf{C}_i .

$$\begin{aligned} & \left[f_p \mathbf{C}_p \mathbf{A}_p - f_m (\mathbf{C} - \mathbf{C}_m) - f_p \mathbf{C} \mathbf{A}_p \right] \mathbf{S} (\mathbf{C}_m)^{-1} + f_i \mathbf{I} \Big\} \mathbf{C}_i \\ & = f_i \mathbf{C} + \left[f_p \mathbf{C}_p \mathbf{A}_p - f_m (\mathbf{C} - \mathbf{C}_m) - f_p \mathbf{C} \mathbf{A}_p \right] (\mathbf{S} - \mathbf{I}) \end{aligned} \quad (2)$$

Then, after defining the volume fraction of the effective interface, stiffness matrix of effective interface can be implicitly obtained from Eqn(2).

3.2 Non-dilute effective interface model

In case of highly concentrated composites, both particle-particle and particle-matrix interaction dominates the overall elastic behavior of composites. So, multi-inclusion model[7] was adopted for non-dilute nanocomposites unit cells and effective elastic modulus of nanocomposites can be give as

$$\mathbf{C} = \mathbf{C}_{\text{inf}} \left[\mathbf{I} + (\mathbf{S} - \mathbf{I}) \left(\sum_{r=1}^N f_r \mathbf{\Phi}_r \right) \right] \left[\mathbf{I} + \mathbf{S} \left(\sum_{r=1}^N f_r \mathbf{\Phi}_r \right) \right]^{-1} \quad (3)$$

where \mathbf{C}_{inf} is the stiffness matrix of the infinite medium surrounding the concentric layers of composites, \mathbf{C}_r and f are the stiffness matrix and volume fraction of r^{th} constituent, and $\mathbf{\Phi}_r$ is given as

$$\mathbf{\Phi}_r = \left[(\mathbf{C}_{\text{inf}} - \mathbf{C}_r)^{-1} \mathbf{C}_{\text{inf}} - \mathbf{S} \right]^{-1} \quad (4)$$

where \mathbf{S} is the Eshelby's tensor of the isotropic spherical inclusion.

In case of thick-coated particle which is a special case of FGM, all the elastic moduli of coated layer are identical (but resultant stress distributions in each coated layer are not identical), only 3 constituent ($r = p, i, m$ corresponds to particle, coating and matrix) are defined and manipulation of Eqn(3) with respect to the stiffness matrix of effective interface becomes easier. Eqn (3~4) were rearranged with respect to the interface stiffness matrix \mathbf{C}_i in order to calculate the interface stiffness matrix

$$\mathbf{C}_i = \mathbf{C} \left[\mathbf{I} - \left\{ f_i \left(\mathbf{I} + (\mathbf{S} - \mathbf{I}) (f_p \mathbf{\Phi}_p + f_m \mathbf{\Phi}_m) \right) - \mathbf{C} \mathbf{C}_{\text{inf}}^{-1} \left(\mathbf{I} + \mathbf{S} (f_p \mathbf{\Phi}_p + f_m \mathbf{\Phi}_m) \right) \right\}^{-1} + \mathbf{S} \right]^{-1} \quad (5)$$

Generally, in the application of Eqn(3) to the effective stiffness matrix of composites, \mathbf{C}_{inf} is set equal to the stiffness matrix of the composites \mathbf{C} [7], and as a result, the solution of the Eqn(3) is numerically obtained(This is similar to the Self Consistent method). On the other hands, in bridging process using Eqn(5), effective stiffness matrix of the nannocomposites is already given and \mathbf{C}_i was obtained from the assumption that the stiffness matrix of the infinite medium \mathbf{C}_{inf} was set equal to the stiffness matrix of the nanocomposites obtained from MD simulation.

3.3 Determination of the volume fraction of the interface

Prior to the calculation of the stiffness matrix of the effective interface using Eqn(3) and Eqn(5), volume fraction of the effective interface should be determined and it was estimated from the variation of the radial density distribution of the matrix polymer. Details of the estimation is shown in Ref[6] and resultant values are obtained as 7Å and 6.3 Å in dilute and non-dilute case respectively with the outer diameter of the adsorption layer as 4Å. In bridging process, the thickness of the interface can vary and both thick and soft or thin and stiffer phase are possible but the combination of the thickness and stiffness of the interface does not affect the estimation of the overall elastic modulus. The detailed description will be reported elsewhere.

4. Results and discussions

In order to correlate the elastic modulus of the effective interface with particle radius, both Young's and shear modulus of the effective interface were obtained from the stiffness matrix and fitted into the linear function of particle radius in logarithmic scale. Elastic modulus of the effective interface of the nanocomposites obtained from Eqn(2) and Eqn(5) are listed in Tab 3.

Table 3 Elastic modulus of the effective interface

(a) Dilute composites with dilute model						(b) Non-dilute composites with non-dilute model					
System	NPC3	NPC4	NPC6	NPC10	NPC12	System	NPC4	NPC5	NPC6	NPC7	NPC8
E(Gpa)	9.78	6.87	6.09	5.13	3.79	E(Gpa)	5.13	4.17	3.76	3.36	2.85
G(Gpa)	3.38	2.93	2.34	1.79	1.44	G(Gpa)	1.93	1.51	1.33	1.17	0.99

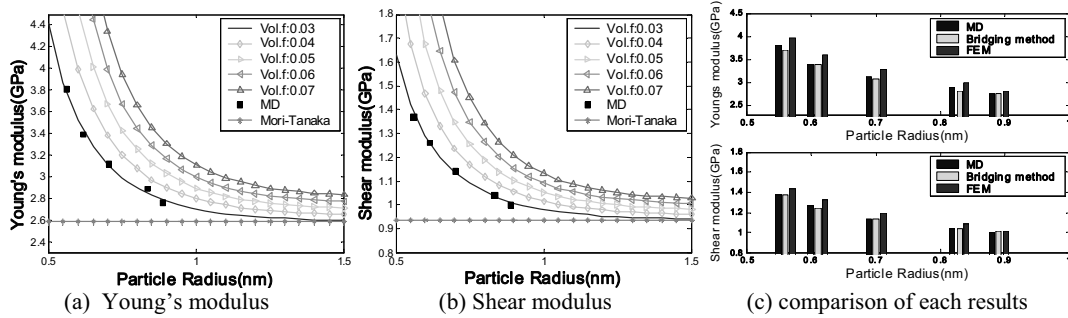


Figure 2. Elastic modulus of the dilute nanocomposites obtained from dilute multi-scale analysis and FEM analysis

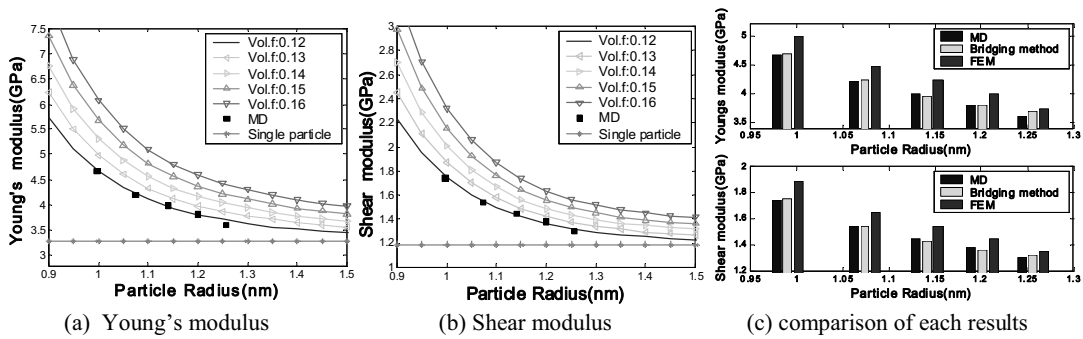


Figure 3 Elastic modulus of the Non-dilute nanocomposites obtained from Non-dilute multi-scale analysis and FEM analysis

As the particle radius increases, both modulus decrease and these variations describe the particle size-dependent elastic modulus variation of the nanocomposites. From the discrete values shown in Tab 3, Young's and shear modulus of the effective interface were fitted into the linear

function of the particle radius and under the assumption that the interface is isotropic, stiffness matrix of the effective interface can be reconstructed from both modulus as a function of the particle radius, as $C_I = C_I(r_p)$.

Elastic modulus obtained from the present bridging methods are obtained and compared in Fig. 2 and 3 with respect to the dilute and non-dilute compositions. As shown in each figures, the present bridging model accurately describes the particle size effect. In order to verify the present bridging method, elastic moduli of the nanocomposites are obtained from finite element analysis. In FEM verification, elastic moduli obtained from the bridging methods are used as input parameter of material properties and elastic modulus are obtained from the stress-strain relation under the pre-defined small uniaxial stress. As can be seen in Fig.2(c) and 3(c), elastic modulus obtained from MD, bridging method and FEM agree very well without any significant error.

5. Conclusion

In this study, efficient multi-scale analysis was developed and verified through MD simulations, scale bridging method based on the micromechanics and FEM. Overall elastic modulus showed enhanced reinforcing effect at smaller particle radius cases and the present bridging technique with the effective interface modeling showed accurate description of the particle size effect and applicability in FEM. Present multi-scale bridging method is expected to be a conventional analysis tool as a intermediate step for the linkage of the atomistic structures and macroscopic properties in the design of the nanocomposites.

Acknowledgements

This work was supported by the Korea Science and Engineering Foundation (KOSEF) through the National Research Lab. Program funded by the Ministry of Science and Technology (No. ROA-2007-000-20109-0).

References

- [1] Edelman. A. S., and Cammarta. R. C., *Nanomaterials : Synthesis, properties and applications*, Bristol: Institute of Physics Publishing, (2006).
- [2] Chen. G. H., Wu. D. J., Weng. W. G., and Yan. W. L., " Preparation of polymer/graphite conducting nanocomposites by intercalation polymerization," *J. Appl. Polym. Scie*, **82**, 2506, (2001).
- [3] J. Cho, M. S. Josh, and C. T. Sun, "Effect of inclusion size on mechanical properties of polymeric composites with micro and nanoparticles," *Compos. Sci. Technol*, **66**, 1941, (2006).
- [4] L. Jiang, Y. C. Lam, K. C. Tam, T. H. Chua, G. W. Sim, and L. S. Ang, "Strengthening acrylonitrile-nutadiene-styrene(ABS) with nano-sized and micron-sized calcium carbonate," *Polymer*, **46**, 243, (2005).
- [5] Accelrys Inc, San Diego, www.Accelrys.com.
- [6] S. Yang, M. Cho, "Scale bridging method to characterize mechanical properties of nanoparticle/polymer nanocomposites," *Appl.Phys.Lett*, **93**(4), 043111(2008).
- [7] Hori. M, and Nemat-Nasser. S, "Double inclusion model and overall moduli of multi-phase composite," *Mech. Mat'l*, **14**, 189, (1993).

Polycrystal Plasticity Analysis of Bimodal Structures Considering the Three-Stage Characteristics of the Resolved Shear Stress vs. Strain Curves of Individual Grains

Yuji Nakasone

**Dept. of Mechanical Eng., Tokyo University of Science
(E-mail: nakasone@rs.kagu.tus.ac.jp)**

ABSTRACT

In recent years, much attention has been paid to materials having bimodal structures consisting of nanostructured grains and submicron grains. It is known that a material having a bimodal structure has a high strength without large decrease of ductility.

The present paper describes the FEM code the present author has developed based on the theory of the polycrystal plasticity with dislocation distributions taken into account. The code also takes into account the three-stage stress-strain curves of individual grains. In order to simulate the deformation behavior of materials having bimodal structures, it is necessary for the code to simulate the mesoscopic deformation behavior with the size effect of the initial yield strength, or the 0.2% proof strength. The present code can simulate the size effect of 0.2% proof strength by modifying the Bailey-Hirsch relation. By using the modified relation, the size effect of the initial plastic yield is successfully reproduced.

Simulations of tensile deformation behavior in aluminum and copper alloys having bimodal structures are made by the developed code. Aluminum has higher stacking fault energy than copper and thus the alloys show different hardening behavior. The paper discusses the effects of the third stage of the shear stress vs. shear strain curves of the individual grains on the macroscopic nominal stress vs. strain curves of the polycrystalline alloys, or aggregates of the grains, having bimodal structures.

Mesoscopic modelling and size effect for the mechanics of multi-walled carbon nanotubes

Marino Arroyo, Irene Arias

Universitat Politecnica de Catalunya, Spain
(E-mails: marino.arroyo@upc.edu, irene.arias@upc.edu)

ABSTRACT

We propose to model thick multiwalled carbon nanotubes (MCNTS) as beams with non-convex curvature energy. Such models develop stressed phase mixtures composed of smoothly bent sections and rippled sections [1]. This model is motivated by experimental observations and large-scale atomistic-based simulations[2,3,4]. The model is analyzed, validated against large-scale simulations, and exercised in examples of interest. It is shown that modelling MWCNTs as linear elastic beams can result in poor approximations that overestimate the elastic restoring force considerably, particularly for thick tubes. In contrast, the proposed model produces very accurate predictions both of the restoring force and of the phase pattern. We characterize through large-scale simulations the nonlinear elastic response of MWNCNTs in torsion and bending [5]. We identify a unified law consisting of two distinct power-law regimes in the energy-deformation relation. This law encapsulates the complex nonlinear mechanics of rippling and is described in terms of elastic constants, a critical length-scale and an anharmonic energy-deformation exponent. The mechanical response of MWCNTs is found to be strongly size-dependent, in that the critical strain beyond which they behave nonlinearly scales as the inverse of their diameter. These predictions agree with available experimental observations.

- [1] M. Arroyo and I. Arias, “Rippling and a phase-transforming mesoscopic model for multiwalled carbon nanotubes”, *Journal of the Mechanics and Physics of Solids*, in press (2007).
- [2] Marino Arroyo and Ted Belytschko, “An atomistic-based finite deformation membrane for single layer crystalline films”, *Journal of the Mechanics and Physics of Solids* 50:1941-1977 (2002).
- [3] Marino Arroyo and Ted Belytschko, “Nonlinear mechanical response and rippling of thick multi-walled carbon nanotubes”, *Physical Review Letters*, 91:215505 (2003).
- [4] Marino Arroyo and Ted Belytschko, “Finite element analysis of the nonlinear mechanics of carbon nanotubes”, *International Journal for Numerical Methods in Engineering*, 59:419-456 (2004)
- [5] Arias and M. Arroyo, “Size-dependent nonlinear elastic scaling of multiwalled carbon nanotubes”, *Physical Review Letters*, in press (2008).

Investigation the stability of SWCNT-polymer composites in the presence of CNT geometrical defects using multiscale modeling

A. Montazeri¹, R. Naghdabadi^{1,2}

¹Institute for Nano Science and Technology, Sharif University of Technology, Tehran, Iran.
(E-mail: a_montazeri@mehr.sharif.edu)

²Mechanical Engineering Department, Sharif University of Technology, Tehran, Iran.
(E-mail: naghdabd@sharif.edu)

ABSTRACT

CNT-reinforced polymer composites have attracted attention due to their exceptional high strength. The high strength can be affected by the presence of defects in the nanotubes used as reinforcements in the practical nanocomposites. In this paper, a Molecular Structural Mechanics / Finite Element (MSM/FE) multiscale modeling is used to study the effect of carbon nanotube geometrical defects on the stability of SWCNT-polymer composites. Here, two types of representative volume elements (RVEs) for these nanocomposites are considered with perfect and defected CNT. These RVEs have the same dimensions. The nanotube is modeled at the atomistic scale using molecular structural mechanics whereas the polymer matrix deformation is analyzed by the finite element method. For modeling the polymer matrix, a three-dimensional eight-noded element is employed. The nanotube and polymer matrix are assumed to be bonded by van der Waals interactions based on the Lennard-Jones potential. In order to study the stability of the nanocomposites, the buckling strain is calculated for perfect and defected carbon nanotubes in the polymer nanocomposites. The results reveal that the presence of defects causes a decrease in axial buckling strain in comparison with perfect SWCNT-polymer composites.

1. Introduction

The discovery of carbon nanotubes has opened the door to enhance the mechanical properties of polymer composites by adding CNTs to the matrix materials. It has been theoretically and experimentally confirmed that carbon nanotubes possess exceptional high stiffness and strength [1]. These properties as well as their high aspect ratio and low density suggest that carbon nanotubes can be considered as ideal reinforcements for nanocomposites. In order to achieve the outstanding mechanical properties of CNTs, there are many problems to be considered. One of the most important issues is the presence of defects in the carbon nanotubes. We refer to defects in a broad sense of the word to reflect deviation of the material from the regular atomic scale structure. Thus, in the case of CNTs, defect is defined as a distortion of the perfect nanotube, which is a cylindrical graphene sheet, composed only of hexagons, except at each end [2].

The possible CNT defects can be classified into four main groups: incomplete bonding defects (vacancies, dislocations, etc), topological defects (introduction of ring sizes other than hexagons), rehybridization defects (ability of carbon atom to hybridize between sp^2 and sp^3), and heterogeneous defects (doping with other elements than carbon). It has been found that there is a decrease in stiffness of nanotubes in the presence of defects. The local elastic moduli are found to reduce to 60 % that of the defect-free nanotube [3]. Among the various types of defects in CNTs, vacancies have received much more attention than others. Vacancies result from missing

carbon atoms in the CNT walls that can happen when CNTs are subjected to irradiation. The carbon atoms might be knocked out by either high-energy electrons or ions.

The objective of this work is to examine the effect of CNT geometrical defects on the buckling onset strain of CNT-reinforced polymer composites using a MSM/FE multiscale modeling approach. In this method, the nanotube is modeled at the atomistic scale by the molecular structural mechanics method. The matrix deformation is analyzed at the macroscopic scale by the continuum finite element method. The nanotube and polymer matrix are assumed to be bonded by van der Waals interactions at the interface. This model is used to study the effect of CNT vacancy defects on the stability of CNT/polymer composites. To this end, the buckling onset strain is calculated for perfect and defected carbon nanotubes in the polymer nanocomposites. The results reveal that the presence of defects causes a decrease in the axial buckling strain in comparison with perfect SWCNT-polymer composites.

2. Modeling

From the traditional theoretical frame for evaluating the macroscopic mechanical properties of composites, a possible approach is to build up a representative volume element (RVE) constituted by a cubic body of matrix with an embedded nanotube [4]. In a similar manner, the stability behavior of CNT/polymer composites in the presence of CNT vacancy defects is predicted in this paper using MSM/FE multiscale modeling.

To construct this RVE, first, molecular structural mechanics is implemented to model the carbon nanotube in atomic scale. In this method, a SWCNT is viewed as a space frame, where the covalent bonds are represented as connecting beams and the carbon atoms as joint nodes. The element used for the covalent bonds is a uniaxial element with tension, compression, torsion, and bending capabilities and has six degrees of freedom at each node; three translations in x, y, and z directions and three rotations about x, y, and z axes. This element is defined by cross sectional area, moment of inertia, and material properties based on the energy equivalence between local potential energies in computational chemistry and elemental strain energies in structural mechanics. To this end, the force field constants of the covalent bonds are used as follows [4]:

$$\frac{EA}{L} = K_r, \quad \frac{EI}{L} = K_\theta, \quad \frac{GJ}{L} = K_\phi \quad (1)$$

where the force field constants K_r , K_θ , and K_ϕ represent stretching, bending and torsional stiffness of the covalent bonds, respectively. Also, E and G denote moduli of elasticity and shear of the element, respectively. Moreover, A is the cross sectional area, I the moment of inertia, J the polar moment, and L the length of the beam. The length of the element is assumed to be equal to the covalent distance of the carbon atoms (0.142 nm). Specific parameters of the element with a circular cross section could be obtained from Eqn (1) as:

$$d = 4 \sqrt{\frac{K_\theta}{K_r}}, \quad E = \frac{K_r^2 L}{4\pi K_\theta}, \quad G = \frac{K_r^2 K_\phi L}{8\pi K_\theta^2} \quad (2)$$

where d is the cross-sectional diameter of the element. Here, the force field constants obtained experimentally in the context of computational chemistry by Cornell et al. in 1995 are used.

These values are; $K_r = 6.52e2 nN nm^{-1}$, $K_\theta = 8.76e-1 nN nm rad^{-2}$, and $K_\phi = 2.78e-1 nN nm rad^{-2}$. In order to analyze the outer polymer matrix, continuum-based finite element formulation is implemented. Here, an isoparametric cubic element is used for modeling the matrix. The element is defined by 8 nodes having three translational degrees of freedom per node. The nanotube and polymer matrix are assumed to be bonded by van der Waals interactions based on Lennard-Jones potential at the interface. For modeling these forces, spring elements are implemented in this work. The spring element used here is defined by two nodes and a spring constant. It is a uniaxial tension-compression element with three translational degrees of freedom at each node. The spring stiffness of this element is determined by the second derivative of the LJ potential, as follows:

$$V_{LJ} = 4\varepsilon \left[\left(\frac{\sigma}{r} \right)^{12} - \left(\frac{\sigma}{r} \right)^6 \right], \quad k = \frac{d^2 V_{LJ}(r)}{dr^2} = \frac{624\varepsilon\sigma^{12}}{r^{14}} - \frac{168\varepsilon\sigma^6}{r^8} \quad (3)$$

where r is the interatomic distance, and ε and σ are the Lennard-Jones parameters. For carbon-carbon van der Waals interactions, these parameters are $\varepsilon = 0.0556 kcal/mol$ and $\sigma = 3.4 \text{ \AA}$ [4]. For computational modeling, a cylindrical unit cell, as shown in Fig. 1, is chosen as representative volume element (RVE). Geometrical characteristics of the RVE are as follows:

Armchair nanotube (5, 5): Radius = 0.34 nm, Length = 34.36 nm

Polymer matrix: Length = 34.36 nm, Inner radius = $R_{CNT} + h_{vdw} = 0.34 + 0.18 = 0.52$ nm

where h_{vdw} is the van der Waals separation distance between the CNT and polymer matrix.

Cross sectional dimension = 4.11 nm (carbon nanotube volume fraction equals to 5%)

In order to study the effect of vacancy defects on the stability of the nanocomposite, after constructing the RVE, we impose the geometrical defects. This is done by removing the proper nodes and elements from the model in accordance with removed atoms and bonds that might be knocked out by either high-energy electrons or ions in the synthesis process. In this study, we consider single, double and triple vacancies in the nanotube structure, as shown in Fig. 2.

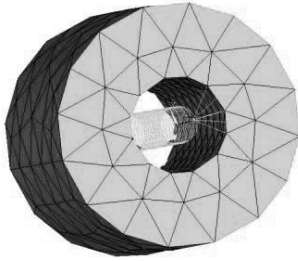


Figure 1. Schematic of computational model for CNT/Polymer composite

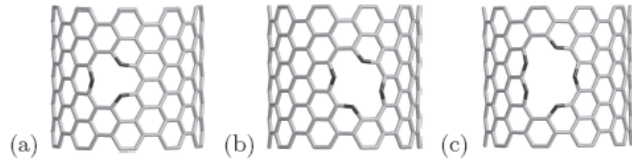


Figure 2. Atomic networks of SWCNTs with a) single, b) double c) triple vacancies [3]

3. Results and discussions

Using the molecular structural mechanics approach and the finite element method, the computational modeling of continuous CNT-reinforced polymeric matrix composites has been carried out in this paper. The main objective is to investigate the effect of CNT geometrical defects on the stability of these nanocomposites. To this end, the strain resulted in buckling is determined for perfect and defected carbon nanotube polymer composites. For this purpose, considering nonlinear analysis, we assume large deformations to occur during compression. One end of the nanocomposite is fixed and the other end is axially compressed in 100 steps. To

understand when buckling occurs, the axial force versus imposed displacement is plotted for one of the nodes subjected to the axial loading. After buckling, this force drops drastically. In order to study the effect of carbon nanotube vacancy defects, the buckling onset strain is determined for CNT-polymer composites with different geometrical defects such as single, double and triple vacancies. The results depicted in Tab 1 show that increasing the vacancies in CNTs, causes a noticeable decrease in the buckling onset strain of nanocomposites. Also, it is found that by increasing the axial load, the second mode of buckling can be achieved in the CNTs as shown in Fig. 3. The numbers in parenthesis give the percentage of reduction in the onset buckling strain of the defected nanocomposite in comparison with perfect one.

Table 1. Reduction in the axial buckling strain of CNT/polymer composites due to different types of vacancy defects

Type of Vacancy	Perfect CNT	Single Vacancy	Double Vacancy	Triple Vacancy
Onset buckling strain (%) - First mode	2.15%	0.41% (81)	0.41% (81)	0.35% (83.7)
Onset buckling strain (%) - Second mode	2.15%	1.11% (48.4)	1.09% (49.3)	1.05% (51.2)

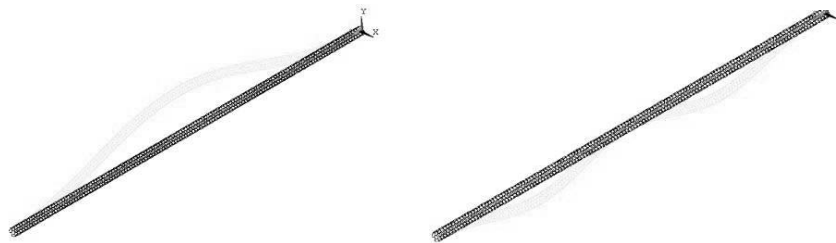


Figure 3. First & Second mode of buckled CNT

4. Conclusions

In this paper, a MSM/FE multiscale modeling of carbon nanotube/polymer composites under compression was implemented to study the role of carbon nanotube geometrical defects on the stability of these nanocomposites. The simulations revealed the strong effect of CNT defects on this behavior. It was shown that by considering the defects in the structure of carbon nanotubes which is a common problem in the synthesis process of these nanostructures, the buckling onset strain of embedded carbon nanotube decreases drastically.

References

- [1] O. Breuer, U. Sundararaj, "Big returns from small fibers: A review of polymer/carbon nanotube composites", *Polymer composites*, 25, 630 (2004).
- [2] C. Shet, N. Chandra, S. Namilaie, "Defect Annihilations in Carbon Nanotubes under Thermo-Mechanical Loading", *Journal of Materials Science*, 40, 27 (2005).
- [3] M. Sammalkorpi et al, "Mechanical Properties of Carbon Nanotubes with Vacancies and related Defects", *Physical Review B*, 1 (2004).
- [4] C. Li, T.W. Chou, "Multiscale Modeling of Compressive Behavior of Carbon Nanotube/Polymer Composites", *Composites Science and Technology*, 66, 2409 (2006)

On the Multi-Scale Computation of Defect Driving Forces

Sarah Ricker¹, Julia Mergheim¹, Paul Steinmann²

¹Chair of Applied Mechanics, University of Kaiserslautern, Gottlieb-Daimler-Strasse,
P.O.Box 3049, 67653 Kaiserslautern, Germany
(sricker@rhrk.uni-kl.de, mergheim@rhrk.uni-kl.de)

²Institute of Applied Mechanics, University of Erlangen-Nuremberg, Egerlandstr. 5, 91058
Erlangen, Germany (steinmann@ltm.uni-erlangen.de)

ABSTRACT

In many engineering applications materials which possess an underlying (heterogeneous) micro-structure play an important role. The simulation of such classes of materials, like e.g. fibre-reinforced composites, often demands the determination of the macroscopic material behavior in each material point based on the analysis of the underlying micro-setting, rather than a-priori assumed constitutive (overall) assumptions. Therefore, in our finite-element framework we obtain the required macroscopic stresses and the tangent operator within a computational homogenization scheme -see e.g. [1] and [2]- by solving a boundary value problem for an associated representative volume element (RVE) on the micro-level. The scope of the current work is the extension of the classical computational homogenization scheme to the homogenization of material forces. In contrast to classical spatial forces in the sense of Newton which are linked to the variation of spatial positions of physical particles with respect to the ambient space, the material forces in the sense of Eshelby are linked to the variations of material positions of physical particles with respect to the ambient material. This material description exhibits a wide range of applications in the field of defect mechanics. It can be shown that the material force at a crack tip corresponds to the J-integral –introduced by Rice [3]- which allows to decide whether a crack propagates or not. In this context the main goal of the extended homogenization scheme is to investigate the influence of different micro-structures onto the macroscopic material forces. Based on the pointed out analogy between the material force at a crack tip and the J-integral, this particular homogenization scheme is applied to study the impact of different heterogeneous micro-structures onto the macroscopic defect driving forces.

- [1] V. Kouznetsova, W.A.M. Brekelmans and F.P.T. Baaijens, “An Approach to Micro-Macro Modeling of Heterogeneous Materials”, *Computational Mechanics*, 27, 37 (2001).
- [2] C. Miehe, “Computational Micro-to-Macro Transitions for Discretized Micro-Structures of Heterogeneous Materials at Finite Strains based on the Minimization of Averaged Incremental Energy”, *Computer Methods in Applied Mechanics and Engineering*, 192, 559 (2003).
- [3] J.R. Rice “A Path Independent Integral and the Approximate Analysis of Strain Concentration by Notches and Cracks”, *Journal of Applied Mechanics*, 35, 379 (1968).

Numerical Material Testing for Strength Evaluation of Polycrystalline Metals

Kenjiro Terada¹, Ikumu Watanabe²

Department of Civil Engineering, Tohoku University, Aza-Aoba 6-6-06, Aramaki, Aoba-ku, Sendai 980-8579, Japan

(¹tei@civil.tohoku.ac.jp; ² ikumu@nde. civil.tohoku.ac.jp)

ABSTRACT

A method of numerical material testing is developed for evaluating the macroscopic yield strength of steel products after cold working process. The method is realized by the micro-macro decoupled analyses based on the crystal plasticity homogenization method. A unit cell for micro-scale analyses, which is composed of several grains, is regarded as a numerical specimen in this method. After validating the method of decoupled nonlinear homogenization, we devise a stepwise procedure for evaluating the yield strength of steel pipes subjected to cold-working. First, we perform a numerical simulation of a Pilger mill rolling process for a steel pipe. Second, the obtained macroscopic deformation history is applied to the unit cell to obtain the numerical specimens after the forming process. Then, numerical material tests are conducted on the specimens to characterize the anisotropy in macroscopic yield strengths and their results are compared with the experimental data.

1. Introduction

Most of steel members formed by cold working often reveal anisotropy in strength of polycrystalline metals. Some anisotropic material behaviors are caused by residual stresses and texture development inside the material. The understanding and prediction of such anisotropic strength is critical especially in designing and forming some types of steel members such as oil well tubular, which is most probably under severe usage environment. It is, however, difficult to predict the post-forming strength of metals that have experienced various plastic deformations and resulting residual stresses during cold working.

In this paper, we propose a method of numerical material testing for evaluating the macroscopic yield strength of polycrystalline metals after cold-working processes. The method is based on the micro-macro decoupled computational strategy along with crystal plasticity model [2, 3] for crystalline aggregates, which was originally introduced as an alternative to the micro-macro coupled or simultaneous analysis method for nonlinear homogenization of a variety of heterogeneous media with periodic microstructures, i.e., unit cells [1]. After validating the method of decoupled nonlinear homogenization, we devise a stepwise procedure for evaluating the post-forming yield strength of steel products. Then, by taking a cold-Pilger mill rolling process of a steel pipe as an example, we demonstrate the promise and potential of the proposed method with reference to the actual experimental data.

1. Method of Numerical Material Testing

1.1 Governing equation for representative volume elements

The governing equations for our numerical material testing on the reference configuration Y_0 of a representative volume element (RVE) are given as follows: $\tilde{\mathbf{N}}_Y \times \mathbf{P}(\mathbf{Y}) = \mathbf{0}$ and $\mathbf{F} = \tilde{\mathbf{N}}_Y (\mathbf{w}(\mathbf{Y}) + \mathbf{Y}) = \mathbf{H} + \mathbf{I} = \tilde{\mathbf{H}} + \hat{\mathbf{H}} + \mathbf{I}$ along with the constitutive equations in crystal plasticity [2] that relates \mathbf{F} to \mathbf{P} . Here, \mathbf{Y} is the position vector in Y_0 , $\mathbf{P}(\mathbf{Y})$ is the microscopic nominal stress, \mathbf{F} is the microscopic deformation gradient and $\mathbf{H} = \tilde{\mathbf{H}} + \hat{\mathbf{H}}$ is the microscopic displacement gradient, where $\tilde{\mathbf{H}}$ and $\hat{\mathbf{H}}$ are respectively the uniform and periodic parts [4]. We employ the periodic boundary conditions for microscopic displacement fields such that $\mathbf{w}(\mathbf{Y}_A) - \mathbf{w}(\mathbf{Y}_B) = \tilde{\mathbf{H}} \times (\mathbf{Y}_A - \mathbf{Y}_B)$, where and subscripts A and B indicate evaluation points on mutually opposite boundary surfaces of the RVE, and $\tilde{\mathbf{H}}$ is constant with respect to \mathbf{Y} . Also, the corresponding macroscopic nominal stress is defined as $\tilde{\mathbf{P}} = (1/|Y_0|) \int_{Y_0} \mathbf{P}(\mathbf{Y}) dY$ where $|Y_0|$ is the volume of the RVE in the initial configuration.

We employ the rate-dependent crystal plasticity constitutive model as in [3] for the material behavior of grains. The slip rate $\dot{g}^{(a)}$ of α -th slip system is given by $\dot{g}^{(a)} = \dot{g}_0 (t^{(a)}/g^{(a)}) / |t^{(a)}/g^{(a)}|^{n_s}$, where \dot{g}_0 the reference strain rate, $t^{(a)}$ is the resolved shear stress and n_s is the material rate sensitivity parameter. Here, $g^{(a)}$ is a function of the sum $g = \int_{t_0}^t \dot{g}^{(a)} dt$ so that its rate is evaluated as $\dot{g}^{(a)} = \sum_{b=1}^{n_{\text{slip}}} h_{ab} \dot{g}^{(b)}$. In this expression, h_{ab} is the hardening modulus such that $h_{ab} = qH(g) + (1-q)H(g)d_{ab}$ with $H(g) = H_0 \sinh^2 |g/(t_s - t_0)|$, where H_0 is the initial hardening modulus, t_s the saturated strength and $t_0 = g^{(a)}(0)$ is the critical resolved shear stress. The St. Venant model $\mathbf{S} = \mathbb{C} : \mathbf{E}$ is assumed for elastic response of crystal grains, where \mathbf{S} is the 2nd Piola-Kirchhoff stress, \mathbf{E} is the Green-Lagrange strain tensor and \mathbb{C} is the elasticity tensor whose independent components are C_{11} , C_{12} and C_{44} .

1.2 Numerical material testing with two-scale metal forming analysis

The first step of the proposed strength evaluation method is to generate a numerical specimen composed of several crystal grains, each of whose inelastic behavior is characterized by a crystal plasticity model described above, and to identify the microscale material parameters by calibration experiments on actual specimens. At the same time, we carry out a macroscopic metal forming simulation of the cold working process of a steel product by employing a classical plasticity model. Here, the macroscopic material parameters have to be determined by the calibration experiments independently of the microscopic counterparts.

In the second step, the macroscopic deformation history obtained by the metal forming simulation is imposed on the numerical specimen prepared in the first step to reproduce the microscopic state after cold-working. The third step is the simulation of the process of cutting out the numerical specimen from the macroscopic product to have the microscopic state equivalent to actual specimens cut out and shaped for strength tests. Finally, numerical material tests are conducted on the prepared numerical specimens to characterize the anisotropy in macroscopic post-forming yield strengths.

2. Numerical example

2.1 Polycrystalline aggregate model and identification of grain's material parameters

The material we selected is a SUS304 stainless steel whose crystal structure is known as FCC. The unit cell employed in this numerical example is a polycrystalline aggregate, which has 54 crystal grains, and the orientations of grains are assumed to be randomly distributed. Using the finite element (FE) model shown in Fig. 1(a), we carry out the numerical material test in order to identify the material parameters for the crystal plasticity model employed in this paper. The identified material parameters are as follows: $C_{11}=127509$, $C_{12}=111346$, $C_{44}=85305$, $h_0=220.0$, $\tau_s=330.0$ and $\tau_0=93.0$. The resulting calibration plot is shown in Fig. 1(b). Here, we assume $q=1.4$ as in [2] without identification.

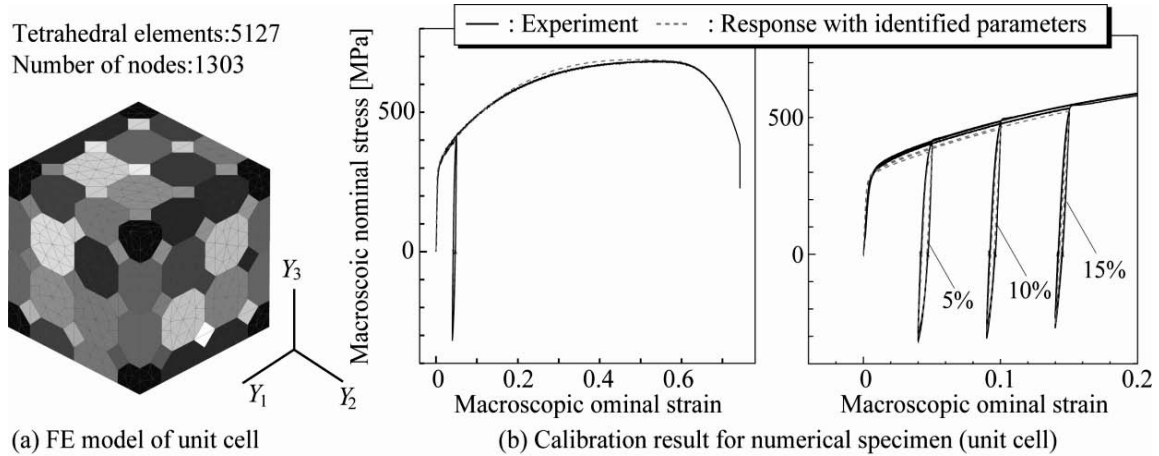


Figure 1. Unit cell model and identification of material parameters for crystal grains.

2.2 Macroscopic metal forming analysis

A Pilger mill rolling process of a steel pipe made of polycrystalline metal is simulated to evaluate the macroscopic mechanical behaviour subjected to cold-forming. This forming process is performed to reduce the diameter and the radial thickness of the pipe by drawing it by 10 mm and then rotating by 63 degree as illustrated in Figs. 2(a) and (b), the latter of which depicts the trajectory of a macroscopic material point of the pipe. The rolling process is conditioned so that the initial outer diameter 69.0 mm of the pipe becomes 60.5 mm, whereas the radial thickness 11.5 mm is reduced 10.0 mm; see Fig. 2(c). In this study, we employ the Rrandtl-Reuss flow theory with isotropic-kinematic (combined) hardening for the elastic-plastic behaviour of macroscopic material point.

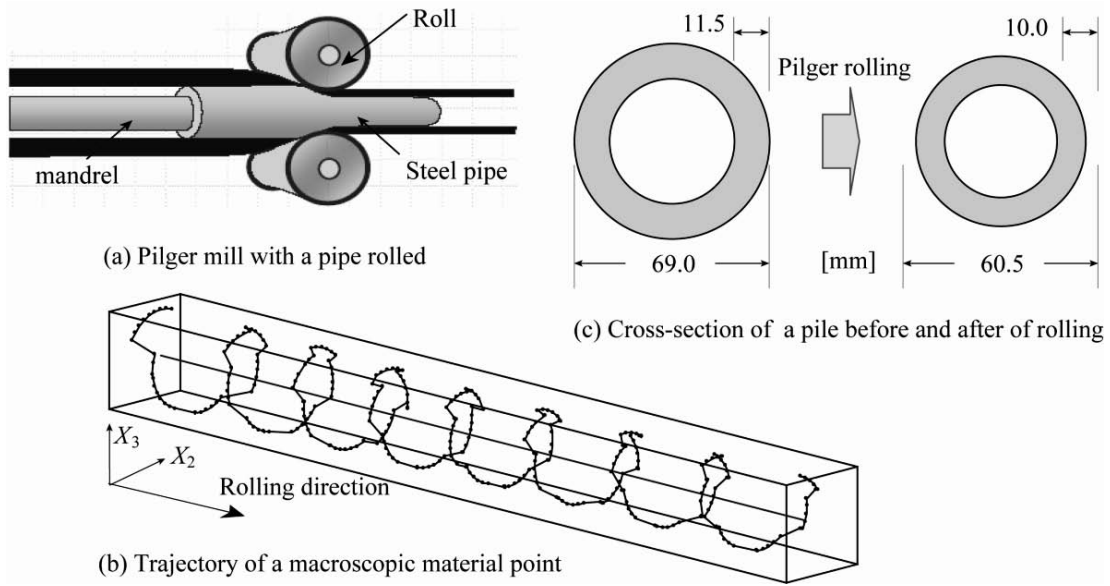


Figure 2. Cold Pilger mill rolling process of a steel pipe.

2.3 Microscopic metal forming analysis

After the macroscopic analysis of the Pilger mill rolling of the steel pipe, we proceed to the microscopic forming analysis on the unit cell model prepared above. This is called the localization analysis in the context of the homogenization method. For the analysis of the unit cell, we first select a representative macroscopic material point relevant for the macroscopic strength evaluation and then impose to it the deformation history, i.e., the set of time-series data of the macroscopic deformation gradient $\tilde{\mathbf{F}} = \tilde{\mathbf{H}} - \mathbf{I}$, which has been obtained in the macroscopic simulation. The volume average of the resulting microscopic stress, namely the macroscopic stress evaluated by the microscopic analysis, is presented in Fig. 3, with which the result obtained in the macroscopic analysis is put down. As can be seen from this figure, the histories of both macroscopic stresses are completely different, though the deformation histories are the same. It is, however, expected that the result of the localization analysis for the unit cell is more reliable than that evaluated with the classical plasticity model, since the macroscopic stress evaluated from the microscopic one contains more information about the mechanism of the macroscopic material behaviour.

2.4 Preparation of a numerical specimen for macroscopic strength evaluation

In order to investigate the anisotropy in the macroscopic yield strength of the metal after the forming, we need to perform numerical material tests on the unit cell that has experienced the cold-working performed in macro-scale. Also, for validating the method based on the micro-

macro decoupled analysis, the estimated post-forming strengths must be compared with those obtained by the actual experiment. However, the actual material test was carried out on the specimens cut out from the steel pipe after the forming, while the unit cell after the microscopic forming analysis above is assumed to be embedded in the macroscopic pipe. Therefore, for the purpose of comparison, we have to carry out an additional microscopic analysis by simulating the cutting out the numerical specimen, which is assumed to be the unit cell with the macroscopic stress being released. Preparing the boundary conditions corresponding of the unit cell to the actual cutting out process of the specimen, we perform the microscopic analysis to have a macroscopically stress-free numerical specimen; see Fig. 4.

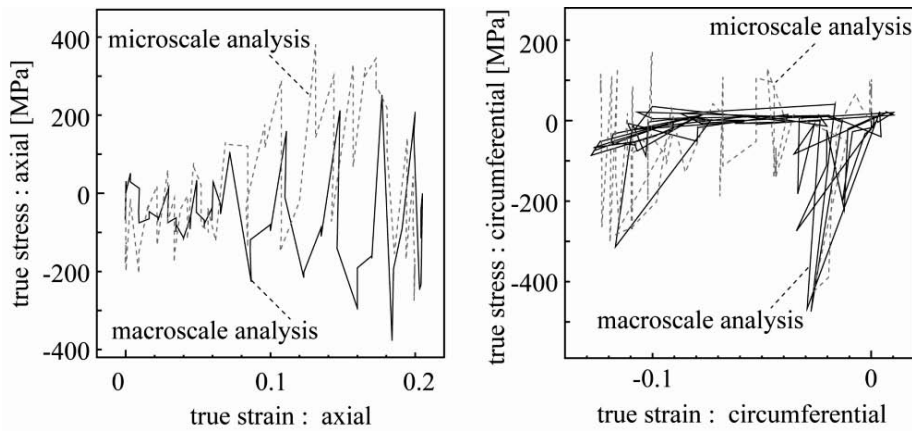


Figure 3. Macroscopic stress responses obtained from micro- and macroscopic analyses.

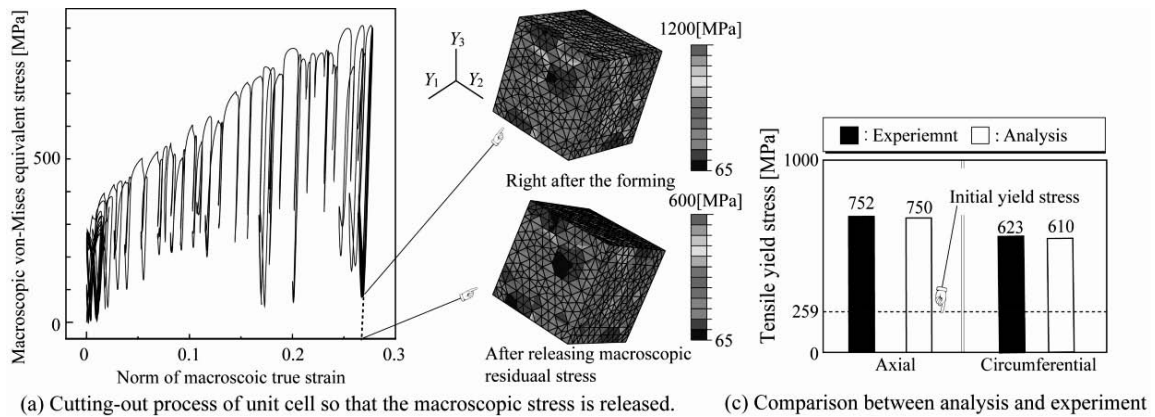


Figure 4. Numerical specimen and macroscopic strength evaluation

2.5 Macroscopic strength evaluation

Using the numerical specimen whose macroscopic stress has been released (see Fig. 4), we conduct a series of numerical material testing to characterize the anisotropy in the macroscopic

post-forming yield strength. Figure 5 shows the comparison between the experimental and analytical results. As can be seen from this figure, the proposed method provides reliable values of macroscopic yield strengths in different directions in comparison with the experimental ones.

The anisotropy observed in the experimental result and evaluated in the numerical material test has been caused by the micro-scale plastic deformation of the polycrystalline aggregate. In addition to the macroscopic strength evaluation, it might be possible to examine the effects of the microscopic residual stresses/plastic strains and the texture development on the anisotropy in the macroscopic strength.

3. Conclusion

A method of evaluating the macroscopic yield strength of polycrystalline metals after cold-working has been developed within the framework of nonlinear homogenization. Taking a cold-Pilger mill rolling process as an example problem, we carried out the micro-macro decoupled analysis, in which the conventional crystal plasticity model is employed for the material behavior of each grain of a polycrystalline aggregate. The macroscopic deformation history is given to the aggregate and the cutting-out process is simulated to have a numerical specimen of the material after the rolling process. The macroscopic post-forming yield strength obtained by the micro-macro decoupled analysis agrees well with the experimental one. It is therefore concluded that the proposed method can be applied for estimating the anisotropy of the yield strength of actual steel products subjected to various types of cold-working.

Acknowledgements

The authors would like to acknowledge the contribution of Dr. M. Akiyama at Kyoto Institute of Technology, and Dr. K. Kuroda and Mr. S. Kimura at Sumitomo Metal Industries Ltd. in providing the data of the macroscopic analysis and the experiments.

References

- [1] K. Terada and N. Kikuchi, "Nonlinear homogenization method for practical applications", in *Computational Methods in Micromechanics*, edited by S. Ghosh, M. and Ostoja-Starzewski, , (AMSE AMD, 1995), Vol. 212, 1-16.
- [2] R. J. Asaro, "Crystal plasticity", *Journal of Applied Mechanics*, **50**, 921 (1983)
- [3] D. Peirce, R.J. Asaro, and A. Needleman, "Material rate dependence and localized deformation in crystalline solids", *Acta Metall*, **31**, 1951 (1983).
- [4] K. Terada, I. Saiki, K. Matsui, Y. Yamakawa, "Two-scale kinematics and linearization for simultaneous two-scale analysis of periodic heterogeneous solids at finite strain", *Computer Methods for Applied Mechanics and Engineering*, **192**, 3531, (2003).

Modeling size effect dependence on mechanical behaviour using a Cosserat crystal plasticity framework

Anais Gaubert¹, Samuel Forest²

¹ ONERA DMSM/CEMN, 29 av. de la Division Leclerc, 92320 Chatillon, France

² MINES ParisTech, Centre des matériaux, CNRS UMR 7633, BP 87 91003 Evry Cedex,
France

anais.gaubert@onera.fr, samuel.forest@ensmp.fr

ABSTRACT

Ni-base superalloys size-dependent mechanical behaviour is investigated using the Cosserat crystal plasticity framework, more precisely using the back-stress related to the divergence of the couple stress tensor model formulated by [2]. A two-phase laminate under single glide is studied analytically to determine the role of each material parameter on the size effect predicted by the model.

1 Introduction

Nickel-base superalloys are widely used in aero-engine industries, owing their good mechanical properties at high temperatures. They inherit these properties from their characteristic microstructure consisting of cuboidal γ' precipitates surrounded by thin channels of γ matrix. Plastic slip mainly occurs in the matrix. The presence of the precipitates constrains dislocations to bow according to the Orowan bypass mechanism. This leads to a size-dependent mechanical behaviour for the two-phase material. In one hand, classical crystal plasticity fails to describe this kind of phenomenon because no length scale is included in the Cauchy continuum. In the other hand, simulations of discrete dislocations dynamics, which can reproduce the observed size effects are computationally very intensive. It is why a great number of generalized-continuum approaches have been proposed recently (see for instance [6, 5, 1]). The Cosserat continuum is one of these possibilities. It has already been employed to study size effects in single-crystals and polycrystalline materials [3]. Following [2], we wish to develop a more intrinsic formulation for the Cosserat single crystal plasticity and evaluating its ability to describe γ/γ' mechanical behaviour. We start to briefly recall the Cosserat continuum and the Cosserat crystal plasticity framework focusing on the consequences of the Schmid law with a non-symmetric stress tensor. Then, the model is employed to solve analytically the case of a two-phase laminate under glide loading.

2 Cosserat crystal plasticity

2.1 Cosserat continuum

The model is described here in the small perturbation framework. For more details on the Cosserat continuum, refer to [3]. In the theory, 3 degrees of freedom, represented by the rotation

pseudo-vector $\underline{\phi}$, are added to the classical displacement ones. The deformation measures of the Cosserat theory are the relative deformation tensor $\underline{\mathfrak{e}}$ and the torsion-curvature tensor $\underline{\kappa}$:

$$\underline{\mathfrak{e}} = \underline{\mathbf{u}} \otimes \underline{\nabla} + \underline{\underline{\epsilon}} \cdot \underline{\phi}, \quad \underline{\kappa} = \underline{\phi} \otimes \underline{\nabla} \quad (1)$$

The stress tensor $\underline{\sigma}$ and the couple stress tensor $\underline{\mathfrak{m}}$ are associated to $\underline{\mathfrak{e}}$ and $\underline{\kappa}$ respectively. They must satisfy the balance equations, which write in the static case :

$$\text{div } \underline{\sigma} = 0, \quad \text{div } \underline{\mathfrak{m}} + 2\underline{\underline{\underline{\sigma}}} = 0 \quad \text{where } \underline{\underline{\underline{\sigma}}} = -\frac{1}{2}\underline{\underline{\underline{\epsilon}}} : \underline{\sigma} \quad (2)$$

and boundary conditions which are not recalled here. It is important to note here that, in the general case, tensors are not symmetric in the Cosserat framework.

Considering an elastic transformation, a generalized Hooke law can be written. In the isotropic case, it reads :

$$\underline{\sigma} = \lambda(\text{tr} \underline{\underline{\underline{\mathfrak{e}}}}) \underline{\underline{\underline{\mathbf{1}}}} + 2\mu \underline{\underline{\underline{\mathfrak{e}}}}^{es} + 2\mu_c \underline{\underline{\underline{\mathfrak{e}}}}^{ea}, \quad \underline{\mathfrak{m}} = \alpha(\text{tr} \underline{\underline{\underline{\kappa}}}) \underline{\underline{\underline{\mathbf{1}}}} + 2\beta \underline{\underline{\underline{\kappa}}}^{es} + 2\gamma \underline{\underline{\underline{\kappa}}}^{ea} \quad (3)$$

λ and μ are the Lamé constants (unit MPa). μ_c is a coupling modulus that relates skew-symmetric parts of the relative deformation tensor and stress tensor. The additional Cosserat parameters α, β et γ (unit MPa.mm²) are intrinsic torsion and bending stiffnesses. For simplicity, we adopt $\beta = \gamma$.

2.2 Plasticity and Schmid law

The relative deformation can be splitted into elastic and plastic part : $\underline{\mathfrak{e}} = \underline{\mathfrak{e}}^e + \underline{\mathfrak{e}}^p$. We adopt a crystal plasticity formulation for $\underline{\mathfrak{e}}^p$. The Schmid criterion expresses that plastic slip is activated when the resolved shear stress on a given slip system reaches a critical value τ_c . Forest in [2] have recently pointed out that the skew-symmetric part of the Schmid law can be seen as a back stress related to the divergence of the couple stress tensor :

$$\tau^s = \underline{\sigma} : \underline{\underline{\underline{\mathbf{P}}}}^s = \underline{\underline{\underline{\sigma}}}^s : \underline{\underline{\underline{\mathbf{P}}}}^{ss} + \underline{\underline{\underline{\sigma}}}^a : \underline{\underline{\underline{\mathbf{P}}}}^{sa} = \tau_{sym}^s - x^s \quad \text{with } x^s = -\frac{1}{2}(\text{div} \underline{\mathfrak{m}}) \cdot (\underline{\mathbf{1}}^s \times \underline{\mathbf{n}}^s) \quad (4)$$

Denoting $\dot{\gamma}^s$ the increment of plastic slip and $\underline{\underline{\underline{\mathbf{P}}}}^s$ the orientation tensor for the slip system s , the kinematic of plastic flow reads :

$$\dot{\gamma}^s = \left\langle \frac{f^s}{k} \right\rangle^n \text{sign}(\tau^s) \quad \text{with } f^s = |\tau^s| - \tau_c^s = |\tau_{sym}^s - x^s| - \tau_c^s = 0 \quad (5)$$

3 Application to single slip in a two-phase laminate

The model is employed to study the case of a microstructure consisting of a periodic succession of hard elastic and soft elasto-plastic layers subjected to single glide perpendicular to the layer (see [4] for the microstructure). This case can be seen as an idealized γ/γ' microstructure. It has already been studied in the reference [4] and reexamined in [2]. Here we are looking for analytical expressions of the kinematic modulus and the macroscopic stress.

3.1 Analytical resolution

Calcul steps are not detailed here, but only the main results are shown. The analytical resolution leads to the following expression for the rotation in the elastic phase :

$$\phi_h^+ = a_h \cosh \left(\omega_h \left(x - \frac{s+h}{2} \right) \right) + d_h \text{ for } s/2 < x < (s+h)/2 \quad (6)$$

(7)

with $\omega_h^2 = \frac{2\mu_h\mu_{ch}}{\beta_h(\mu_h+\mu_{ch})}$ and a parabolic profile in the plastic phase : $\phi_s = a_s x^2 + d_s$.

Integration constants a_s , d_s , a_h and d_h are determined thanks to continuity and periodicity conditions. The resolution gives the following expression for the curvature of ϕ in the elasto-plastic phase :

$$a_s = \frac{-A}{\beta_s \left(Bl^2 + Cl \cotanh \left(\omega_h \frac{l(1-f_s)}{2} \right) + D \right)} \quad (8)$$

$$\begin{cases} A = \bar{\gamma} - \frac{\tau_c}{2\mu_h} \left(f_s + 2(1-f_s) + f_s \frac{\mu_h}{\mu_s} \right) \\ B = \frac{f_s^3}{6\beta_s} \\ C = \frac{f_s^2}{\beta_h \omega_h} \\ D = f_s \frac{\mu_s + \mu_{cs}}{\mu_s \mu_{cs}} - \frac{4f_s}{\mu_h} \left(1 + \frac{1-f_s}{f_s} \right) \end{cases}$$

We obtain a linear kinematic hardening owing that $x^s = -\beta_s a_s$.

3.2 Effect of the material parameters on the size effect

The macroscopic stress writes : $\Sigma = \langle \sigma_{xy} \rangle = \langle \sigma_{yx} \rangle = \tau_c - 4\beta_s a_s$. This expression show a size effect because a_s depends on the size of the microstructure l . Material coefficients for both phases are chosen as following. They have the same coefficients for classical elasticity $E=90000\text{MPa}$ and $\nu=0.3$. The β coefficient in the hard elastic phase is choosen very small, $\beta_h = 10^{-7}\text{MPa}\cdot\text{mm}^2$, whereas $\beta_s = 10^{-1}\text{MPa}\cdot\text{mm}^2$ because plasticity processes at the micron scale. Moreover, $\tau_c = 40\text{MPa}$ is a classical value for the resolved shear stress in the superalloys γ phase at high temperature.

Fig. 1 shows the effect of key parameters on the size effect predicted by the model. The left part of the figure shows that the β_s do not play any role when the condition $\beta_h \ll \beta_s$ is enforced. We can also note from the right part of the figure that the critical resolved shear stress play an important role on the size effect ($\Delta\sigma_{0.2}$ representing the difference in $\sigma_{0.2}$ between large microstructures and very small ones). For the material parameters set chosen here, we have potentially a 20MPa size effect which seems too law to describe γ/γ' behaviour.

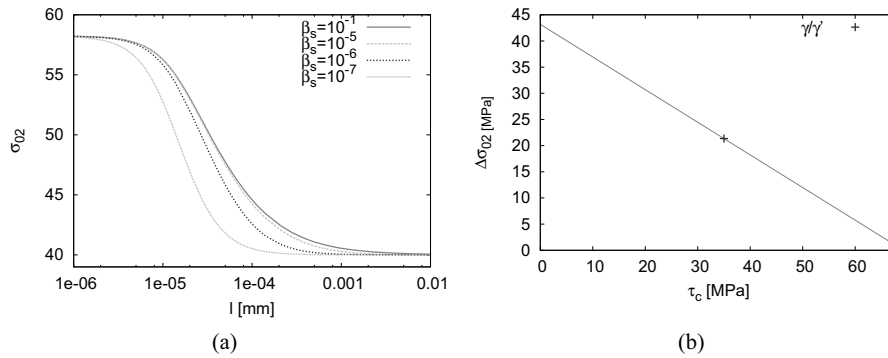


Figure 1: Effect of the (a) β_s coefficient and (b) critical resolved shear stress on the size effect

4 Conclusions

Analytical study of single glide in a two-phase laminate simulated with a Cosserat crystal plasticity model shows a macroscopic behaviour which includes a size dependent effect. However, this effect seems to be smaller than the one observed experimentally. Finite Elements simulations with the same model on the 12 octahedral slip systems of the γ phase tend to confirm this result. Further developpements of the Cosserat crystal plasticity framework are in progress to be able to reproduce the size effect existing in Ni-based superalloys.

References

- [1] L.P. Evers, W.A.M. Brekelmans, and M.G.D. Geers. "Non-local Crystal Plasticity Model with Intrinsic SSD and GND Effects". *Journal of the Mechanics and Physics of Solids*, 52:2379, (2004).
- [2] S. Forest. "Some Links between Cosserat, Strain Gradient Crystal Plasticity and the Statistical Theory of Dislocations". *Philosophical Magazine* (to be published), (2008).
- [3] S. Forest, F. Barbe, and G. Cailletaud. "Cosserat Modelling of Size Effects in the Mechanical Behaviour of Polycrystals and Multi-phase Materials". *International Journal of Solids and Structures*, 37:7105, (2000).
- [4] S. Forest and R. Sedláček. "plastic slip distribution in two phase laminate microstructures : dislocation-based versus generalized-continuum approaches". *Philosophical Magazine*, (83)(2):245, 2003.
- [5] M.E. Gurtin. "A Gradient Theory of Single-crystal Viscoplasticity that Accounts for the Geometrically Necessary Dislocations". *Journal of the Mechanics and Physics of Solids*, 50:5, (2002).
- [6] J.Y. Shu, N.A. Fleck, E. Van der Giessen, and A. Needleman. "Boundary Layers in Constrained Plastic Flow : Comparison of Nonlocal and Discret Dislocation Plasticity". *Journal of the Mechanics and Physics of Solids*, 49:1361, (2001).

Combined Effects of Crystallographic and Grain Size Heterogeneities on Plasticity of Polycrystalline IF Steels

Nicolas Nicaise¹, Stéphane Berbenni¹, Francis Wagner²,
Marcel Berveiller¹ and Xavier Lemoine³

¹LPMM, UMR CNRS 7554, ENSAM, 57078 Metz cedex 03, France

²LETAM, UMR CNRS 7078, University of Metz, Ile du Saulcy, 57012 Metz cedex, France

³Arcelor Mittal, Research Center, Maizières-les-Metz, France

(E-mail: nicolas.nicaise@metz.ensam.fr)

ABSTRACT

The overall behavior and the evolution of the local fields of IF steels, composed of grains with different sizes and crystallographic orientations, are simulated using an elastic-viscoplastic self-consistent approach. To have a good statistics on grain size distributions and texture, more than 16000 grains have been used. Computations and experimental measurements are performed on two different IF steels with different mean grain sizes, which allows us to investigate the different effects of grain size and texture. Numerical results display that the grain size effect is more important than the crystallographic texture effect on the yield stress, and, second, that grain size dispersion has an important influence on the mechanical properties and internal fields.

1. Introduction

The micro-macro transition theories were developed to model the plastic behavior of heterogeneous materials starting from the local behavior of their constituents mainly described by their crystallographic orientations. The interaction between grains is well described by Eshelby's inclusion approaches, which essentially assumed a uniform grain size distribution, i.e. without grain size heterogeneities. Some recent works [1] have studied the effect of grain size dispersion rather than crystallographic heterogeneities. The present study shows that grain size effect is more important than texture effect. In this approach, the two aspects of heterogeneity, i.e. crystallographic orientations distribution as well as grain size dispersion, are taking into account simultaneously. Experimental textures and grain size distributions, obtained by EBSD, will be used. The local behavior is supposed elastic-viscoplastic with a reference shear stress depending on the individual grain size. The fluctuations of mechanical fields related to grain size dispersion are compared to the ones due to crystallographic orientations.

2. Modeling

2.1 Local grain size dependent behavior

The single crystal behavior is supposed to be elastic-viscoplastic. For the sake of simplicity, small perturbations are assumed, so that the total strain rate splits into an elastic part and an inelastic (viscoplastic) part:

$$\dot{\boldsymbol{\varepsilon}} = \dot{\boldsymbol{\varepsilon}}^e + \dot{\boldsymbol{\varepsilon}}^{vp} = \dot{\boldsymbol{\varepsilon}}^e + \sum_s \mathbf{R}_{ij}^{(s)} \dot{\gamma}^{(s)} = \mathbf{s} : \dot{\boldsymbol{\sigma}} + \mathbf{m}(\boldsymbol{\sigma}, \underline{\mathbf{x}}) : \boldsymbol{\sigma}. \quad (1)$$

In Eqn.(1), the elastic compliances \mathbf{s} are supposed isotropic, and are defined by the shear modulus μ and the elastic Poisson's ratio ν . Furthermore, the secant viscoplastic compliances \mathbf{m} depending of the local stress field $\boldsymbol{\sigma}$ are obtained using Eqn.(1) and the plastic flow rule on each slip system. In Eqn.(1), $R_{ij}^{(s)}$ is the symmetric part of the Schmid orientation tensor of the slip system (s). Following Hutchinson [2], Molinari et al. [3], for each grain I, and on the slip system (s), the rate dependent flow rule is given by:

$$\dot{\gamma}^{(s)} = \dot{\gamma}_0 \cdot \left(\frac{|\tau^{(s)}|}{\tau_c^{(s)}(\rho, \gamma, D)} \right)^n \cdot \text{sign}(\tau^{(s)}). \quad (2)$$

The power n is a parameter corresponding to the inverse of the slip rate sensitivity of the material and $\dot{\gamma}_0$ is a reference slip rate. In Eqn.(2), $\tau^{(s)} = R_{ij}^{(s)} \sigma_{ij}$ is the resolved shear stress on slip system (s). For each slip system (s), the reference shear stress $\tau_c^{(s)}$ depends on the dislocation density $\rho^{(h)}$ and on the grain size D (equal to grain diameter for the here considered spherical grains) like:

$$\tau_c^{(s)} = \tau_{c0}^{(s)} + \frac{\kappa}{\sqrt{D}} + \alpha \cdot \mu \cdot b \cdot \sqrt{\sum_h a^{(sh)} \cdot \rho^{(h)}}. \quad (3)$$

where $\tau_{c0}^{(s)}$ is the initial critical shear stress, b is the magnitude of the Burgers vector, α (with $0 < \alpha < 1$) and κ are material parameters. In Eqn.(3), $a^{(sh)}$ is the cristallographic part of the hardening matrix determined in the case of b.c.c. metals like IF steels, as defined by Franciosi [4]. Following Essmann and Mughraby [5], Hoc et al. [6], the variation of dislocation density on slip system (s) is supposed to depend on the dislocation density on system (s) (due to annihilation of dislocation dipoles) but also on other slip systems (creation of new dislocations due to forest obstacles) and on the slip rate on the slip system (s):

$$\dot{\rho}^{(s)} = \frac{1}{b} \left(\frac{1}{D} + \frac{\sqrt{\sum_{i \neq s} \rho^{(i)}}}{K} - 2y_c \rho^{(s)} \right) \dot{\gamma}^{(s)}. \quad (4)$$

Through Eqn.(4), the mean free path of dislocations is limited by grain boundaries [6] so that it is initially on the order of the grain size D .

2.2 Transitions from the Micro- to the Macro- Scales

A self-consistent procedure using the ‘‘translated fields’’ technique was developed [7]. For an elastic-viscoplastic medium with homogeneous elastic moduli \mathbf{C} and heterogeneous viscoplastic compliances, the interaction law between local stress rates $\dot{\boldsymbol{\sigma}}$ and overall one $\dot{\boldsymbol{\Sigma}}$ reads:

$$\dot{\boldsymbol{\sigma}} = \dot{\boldsymbol{\Sigma}} + \mathbf{C} : (\mathbf{I} - \mathbf{S}^E) : (\mathbf{A}^{B^e} : \dot{\mathbf{E}}^{vp} - \dot{\boldsymbol{\epsilon}}^{vp}) \quad (5)$$

In Eqn.(5), \mathbf{S}^E is the elastic Eshelby tensor, $\dot{\mathbf{E}}^{vp} = \overline{\dot{\boldsymbol{\epsilon}}^{vp}}$, and, \mathbf{A}^{B^e} is the viscoplastic strain rate concentration tensor related to the homogenous viscoplastic moduli \mathbf{B}^e of the effective medium:

$$\mathbf{A}^{B^e} = \left(\mathbf{I} + \Gamma_l^{B^e} : \delta \mathbf{b}^e \right)^{-1}, \quad \delta \mathbf{b}^e = \mathbf{b} - \mathbf{B}^e. \quad (6)$$

In Eqn.(6), $\Gamma_l^{B^e}$ represents the local part of the modified Green tensor associated with \mathbf{B}^e .

3. Materials

Two different cold rolled and annealed IF steels are investigated. Their initial microstructures are determined by large EBSD measurements on the same window size (~16000 and 20000 grains), to have a good statistics in terms of grain size distributions and crystallographic orientation distribution function. The finest grain sized IF steel have a mean diameter of 8.75 μm for a relative grain size dispersion $\Delta D/D_{\text{mean}}$ of 4.56 where $\Delta D = D_{\text{max}} - D_{\text{min}}$ is the absolute range of grain size. The largest grain sized IF steel have a mean diameter of 12.96 μm and a relative dispersion $\Delta D/D_{\text{mean}}$ of 3.67. Their respective grain size distributions are reported on Fig. 1.



Figure 1. Grain size distribution for finest (right) and largest (left) grain sized IF steel.

Different crystallographic textures obtained with these steels will be tested to compare both mean grain size and grain size dispersion effects associated to plastic anisotropy owing to the different present crystallographic components (mainly γ and α fibers).

4. Results

Tensile tests at a prescribed strain rate of $|\dot{\mathbf{E}}| = 8 \times 10^{-3} \text{ s}^{-1}$ are performed. They are also simulated using the micro-macro scale transition model until a macroscopic strain of 10%. Macroscopic (both experimental and simulated) are presented as well as the simulated evolution of the internal structure (local fields) during the tensile tests.

The tensile stress/strain responses are reported on Fig. 2 for the two different IF steels. Materials parameters have been identified on the tensile test of the largest grain sized IF steel with its actual grain size dispersion. The global effect of grain size dispersion is on the order of the mean grain size effect (Fig. 2).

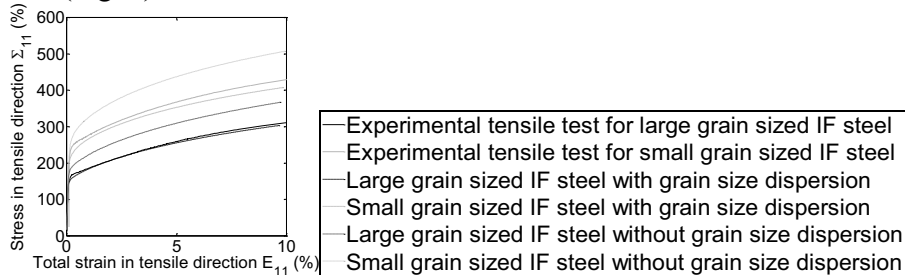


Figure 2. Experimental tensile responses for both steels and simulations with and without grain size distributions.

Local plastic strains and local stress components (in the tensile direction) are reported on Fig. 3 for the largest grain sized IF steel at 2.5% and 10% of total strain. This figure shows two different cases, the first one is the real case, with grain size heterogeneity, the second one has no grain size heterogeneity (i.e. all the grains have the same diameter equal to the mean diameter). It is demonstrated that important fluctuations of internal fields are observed in both cases. But, due to grain to grain accommodation (see Eqn.(5)), the strain fluctuations are bigger (conversely the stress fluctuations are a bit lower) when grain size dispersion is accounted for.

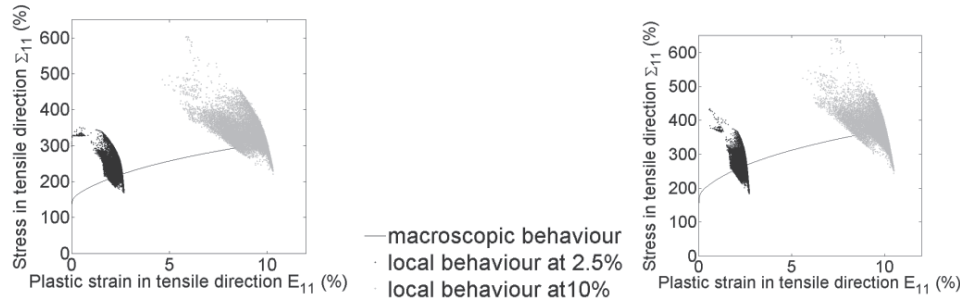


Figure 3. Local stress component in the tensile direction for the largest grain sized IF steel, with (left) and without (right) grain size dispersion.

5. Conclusion

Assuming grain size dependence on the critical shear stress and on the mean free path of dislocations, it is found that not only the mean grain size and/or texture play a role but also grain size dispersion has an impact on the overall behavior and on the evolution of the internal structure.

6. Acknowledgements

The authors thank the “Agence Nationale de la Recherche” (ANR) for financial support.

7. References

- [1] S. Berbenni, V. Favier and M. Berveiller, “Impact of the grain size distribution on the yield stress of heterogeneous materials”, *International Journal of Plasticity*, **23**, 114 (2007)
- [2] J.W. Hutchinson, “Bounds and self-consistent estimates for creep of polycrystalline materials”, *Proceedings of the Royal Society A*, **348**, 101 (1976)
- [3] A. Molinari, G.R. Canova and S. Ahzi, “A self-consistent approach of the large deformation polycrystal viscoplasticity”, *Acta Metallurgica*, **35**, 2983 (1987)
- [4] P. Franciosi, “The concepts of latent hardening and strain hardening in metallic single crystals”, *Acta Metallurgica*, **33**, 1601 (1985)
- [5] U. Essmann and H. Mughrabi, “Annihilation of dislocations during tensile tests and cyclic deformation and limit of dislocations densities”, *Philosophical Magazine A*, **40**, 731 (1979)
- [6] T. Hoc, C. Rey, J. Raphanel, “Experimental and numerical analysis of localization during sequential tests for IF-Ti steel”, *Acta Materialia*, **49**, 1835 (2001)
- [7] S. Berbenni, V. Favier, X. Lemoine and M. Berveiller, “Micromechanical modeling of the elastic-viscoplastic behaviour of steels having different microstructures”, *Materials Science and Engineering A*, **372**, 128 (2004)

Onset of Plasticity Under Nanoindentation: Influence of the Interatomic Potential

Gerolf Ziegenhain¹, Alexander Hartmaier², Herbert M. Urbassek¹

¹**Fachbereich Physik, Universität Kaiserslautern, Erwin-Schrödinger-Straße, D-67663 Kaiserslautern, Germany (E-mail: mail.gerolf@ziegenhain.com)**

²**Interdisciplinary Center for Advanced Materials Simulation (ICAMS), Ruhr-University Bochum, Stiepeler Str. 129 (UHW), 44780 Bochum, Germany**

ABSTRACT

In the last years the power of computers has become large enough to solve Newton's equations of motion numerically for a large number of particles. This enables us to simulate the plastic behavior of materials on the atomistic scale. Using the molecular dynamics method we specifically investigate the onset of plasticity under nanoindentation. In order to understand the atomistic plasticity and ductility of metals we address the question which microscopic properties are of importance for modeling plastic behavior. The microscopic properties - such as the cohesive energy, the elastic moduli, and the energy of point, line and planar defects - are determined through the interatomic potentials. Focusing on fcc materials, we investigate various pair and many-body potentials with respect to plasticity. It turns out that the dislocation nucleation under the indenter does not depend on the unstable stacking fault energy, which however governs the behavior of fully developed plasticity. Embryonic plasticity is dominated by crystal structure alone; it is well described even by simple pair potentials.

1. Introduction

On the atomistic scale materials are characterized in terms of cohesive energy, elastic moduli, and generalized stacking fault energy. These properties are modeled by potentials on the atomistic scale. It is known that pair potentials are suitable for modeling isotropic amorphous systems near the equilibrium. For crystals the missing crystalline anisotropy leads to qualitatively wrong results in the elastic regime. Can this potential class be used for plasticity? This is particularly of interest, because the Cauchy pressure is zero and, therefore, the two shear modes are not disjoint for pair potentials. What additional information is included in the many-body contributions contained in the embedding function? Is modeling plasticity using pair potentials meaningful? If so, what information can be drawn out of this?

2. Molecular Dynamics Approach to Nanoindentation

Using the velocity Verlet algorithm we solve Newton's equations of motion. We indent a relaxed fcc crystal (111,100,110) of 25nm side length by using a 8nm indenter with a constrained velocity $v=10\text{m/s}$. Neglecting adhesion we model the indenter by using a purely repulsive

potential [1]. Our Lennard-Jones (LJ) potential is fitted to the lattice constant of copper (3.615 Å) and the bulk modulus (134.4GPa). The Morse potential is additionally fitted to the cohesive energy (3.54eV) and the many-body potential is an EAM potential [2]. The generalized stacking fault energy is obtained using conjugate-gradient energy relaxation.

2. Results

In the elastic regime the hertzian theory holds in first order approximation. The load curves in Fig. 1 increase monotonically until the yield point. Although only two elastic constants are covered by the pair potentials the deviation in the elastic stiffness is only about 10%. For the other orientations the deviation is similar. We note that the hertzian model itself assumes an isotropic material and therefore leads to different reduced elastic moduli than analytical calculations [3].

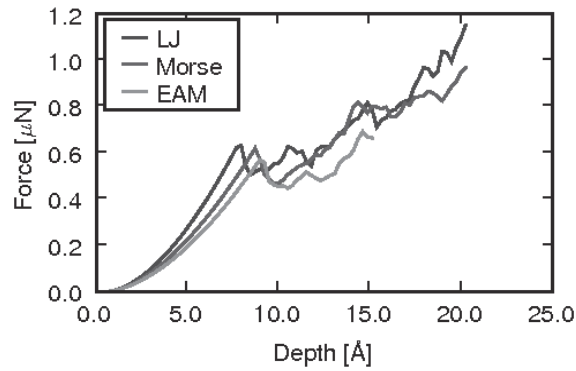


Figure 1. Force-depth curve for (111) Cu.

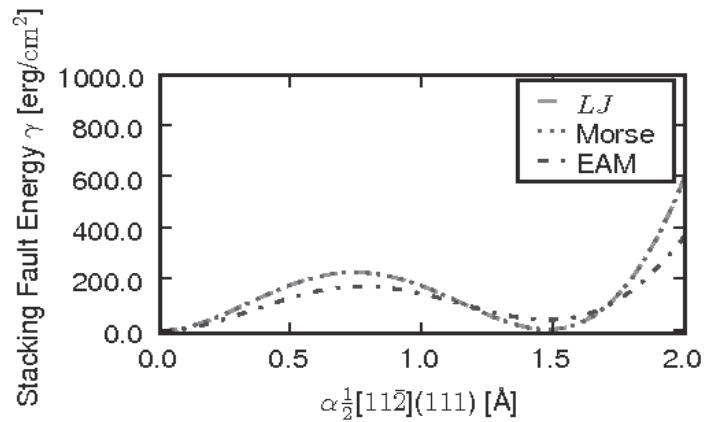


Figure 2. Generalized stacking fault energy for the LJ, Morse and EAM potential.

Plasticity is characterized through ductility. Similar to [4] we measure the ductility by the difference of unstable and stable stacking fault energy. In fig. 2 the generalized stacking fault energy for our potentials is shown. As expected, pair potentials underestimate the stable stacking

fault energy. The stable ground state (fcc / hcp) is not unique and we expect bigger stacking faults for pair potentials.

Surprisingly, the early defect generation is nearly independent of the potential type. It does not depend on the stable stacking fault energy. The unstable stacking fault energy, however, influences the primary onset of plasticity [5]. The fully developed plasticity depends on the stable stacking fault energy: The size of the stacking faults is much bigger for the (therefore brittle) LJ potential. Comparing Morse and EAM potential the Morse potential leads to a similar size of defect structures; nevertheless, the total number of defects is bigger for the former one. This is visualized in figure 4 in term of the stacking fault concentration.

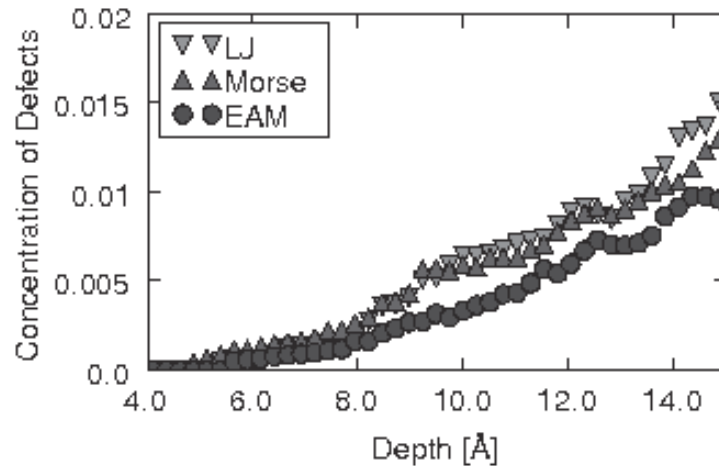


Figure 4. Stacking fault concentration normalized to total number of particles in the simulation.

5. Summary

Elastic behavior is quantitatively reproduced within approximately 10%. As the onset of plasticity is described even better; we conclude that it is dominated by the crystalline structure.

Acknowledgments

The authors acknowledge financial support by the Deutsche Forschungsgemeinschaft via the Graduiertenkolleg 814.

References

- [1] G. Ziegenhain, A. Hartmaier and H. M. Urbassek, “Pair vs many-body potentials: influence on elastic and plastic behavior in nanoindentation”, in preparation (2008)

- [2] Y. Mishin, M. Mehl, D. Papaconstantopoulos, A. Voter, and J. Kress: “Structural stability and lattice defects in copper: Ab initio, tight-binding, and embedded-atom calculations”, *Physical Review B*, **63**, 224106 (2001).
- [3] G. Ziegenhain, A. Hartmaier and H. M. Urbassek, “Influence of crystal anisotropy on the onset of plasticity in nanoindentation - a molecular dynamics study”, in preparation (2008)
- [4] J. Rice: “Dislocation Nucleation from a Crack Tip: An Analysis Based on the Peierls Concept”, *Journal of Mechanical Physics Letters*, **40**, 239 (1992).
- [5] G. Ziegenhain and H. M. Urbassek, “Effect of material stiffness on hardness: a computational study based on model potentials”, in preparation (2008).

Effect of Surface Structure on Strength of Si Thin Film

Yoshitaka Umeno

**Institute of industrial Science, The University of Tokyo,
4-6-1 Komaba Meguro-ku, Tokyo 153-8505, Japan,
(E-mail: umeno@iis.u-tokyo.ac.jp)**

ABSTRACT

The strength of materials is highly sensitive to their structure. Atomic structure of a surface can significantly affect the strength and fracture mechanism of thin films. In this study, tensile simulations of silicon nanofilms by means of classical molecular dynamics (MD) and ab initio density functional theory (DFT) calculations are performed to investigate the effect of surface structure on the tensile strength. Ab initio DFT calculations of Si films with (100) surfaces reveal that the surface does not reduce much the strength owing to its flat structure. Ab initio and empirical tensile simulations of films with surfaces with various Miller indices demonstrate how the variety of surface structure influences the mechanical properties. Surfaces with relatively high Miller indices can decrease the tensile strength owing to surface step structures. It is found that subtle difference in the dimer structure around the step can significantly affect the tensile strength. The effect of the surface and step structure, e.g. termination by hydrogen and rebonded/non-rebonded step-edge, is also examined by extensive ab initio DFT calculations. Moreover, how the various step structures affect the deformation and fracture mechanism is examined with the instability mode analysis which is to solve the eigenvalue problem of the dynamical matrix of the atomic structure.

- [1] Y. Umeno, A. Kushima, T. Kitamura, P. Gumbsch, and J. Li, “Ab initio study of the surface properties and ideal strength of (100) silicon thin films”, *Physical Review B*, **72**, 165431 (2005).

Dislocation-guided Dynamics of Surface Defects on a Multilayered Si-Ge Heterostructure

Bo Yang

**Department of Mechanical and Aerospace Engineering, Florida Tech., Melbourne, FL
(E-mail: boyang@fit.edu)**

ABSTRACT

We present a hierarchical multiscale modeling analysis of the dynamics of surface adatoms above a dislocation network in a multilayered Si-Ge heterostructure. The analysis is carried out in two steps. First, a Green's function-based multiscale modeling technique is applied to solve for the core structure and subsequently to derive the formation energy (i.e., enthalpy) and dipole tensor of a single Ge adatom on a bare Si(001) surface. The formation energy of their complexes (a few adatoms close to each other) is also examined. The Green's function method is efficient because the materials heterogeneities and extensive nano-features (i.e., dimers) are taken care of in the reference Green's function and the defects can then be locally handled. Second, the configurational force is employed to dictate the driving force on individual adatom migration and with that, the dynamics of a relatively large system of adatoms can be simulated. The configurational force acting on an individual adatom is due to the elastic interaction with the buried dislocation network and with other adatoms. The formation energy obtained above is used as the energy barrier in part to determine the defect migration speed and to determine when two nearby adatoms would coalesce or nearby adatom and vacancy would recombine. The model is applicable to adatom densities from dilute to moderate. We show that the adatom migration pattern is significantly influenced by the presence of the buried dislocation network. They tend to gather first above the junctions of the dislocation network and then above the individual dislocations. These results agree well with the experimental observations.

Dislocation Dynamics for Engineering Applications

Vasily V. Bulatov

**L-367, P.O. Box 808, Lawrence Livermore National laboratory,
Livermore, CA 94551, U.S.A.
(E-mail: bulatov1@llnl.gov)**

ABSTRACT

Dislocation Dynamics (DD) method is a link connecting dislocation motion on the atomistic scale directly to the length and time scales relevant for material performance in various engineering applications. Over the last 15-20 years this connection has been established in principle but the DD method is yet to deliver on its promise as a tool for engineering calculations. There are two primary difficulties standing in the way: (1) our insufficient understanding of atomistic mechanisms of dislocation behavior and (2) a very large computational cost of DD simulations on the engineering scales. Starting from 2000, *ParaDiS* project at LLNL has focused both on fidelity and computability of Dislocation Dynamics. In this presentation, we will describe how we use atomistic simulations to parameterize DD models in order to make *ParaDiS* simulations more accurate. We will also discuss the algorithms that enable us to run DD simulations efficiently on some of the world largest computational platforms. By enhancing the accuracy and computational efficiency of the DD method, *ParaDiS* team improves the quality of DD simulations, gains deeper physical insights into collective effects in dislocation motion and uses DD simulations for extracting constitutive models for large scale engineering calculations. At present, the *ParaDiS* code is employed by several research groups in Europe and the US who use the code as a development platform for further work on the DD methodology. To facilitate this development work, we created a *ParaDiS* user/developer community and made the source code freely available to others at <http://paradis.stanford.edu>.

Dilute Discrete Dislocation Dynamics

M.P. Ariza¹ and M. Ortiz²

¹Escuela Superior de Ingenieros, University of Seville, Camino de los descubrimientos s/n, 41092, Seville, Spain (E-mail: mpariza@us.es)

²Division of Engineering and Applied Science, California Institute of Technology, Pasadena, CA 91125, USA (E-mail: ortiz@aero.caltech.edu)

ABSTRACT

We present a study of 3D dislocation dynamics in BCC crystals based on discrete crystal elasticity. Ideas are borrowed from discrete differential calculus and algebraic geometry to construct a mechanics of discrete lattices. The notion of lattice complexes provides a convenient means of manipulating forms and fields defined over the crystal. Atomic interactions are accounted for via linearized embedded atom potentials thus allowing for the application of efficient fast Fourier transforms. Dislocations are treated within the theory as energy minimizing structures that lead to locally lattice-invariant but globally incompatible eigendeformations. The discrete nature of the theory automatically eliminates the need for core cutoffs. The quantization of slip to integer multiples of the Burgers vector along each slip system leads to a large integer optimization problem. We suggest a new method for solving this NP—hard optimization problem in the limit of dilute distributions of dislocations and also demonstrate the efficacy of our approach in simulating relatively large systems with fully atomistic resolution. Simulations with our model are shown to naturally produce strain-hardening, irreversibility and hysteresis, mediated by dislocation interactions.

This work was partially supported by the Ministerio de Educación y Ciencia of Spain (DPI2006-05045). The financial support is gratefully acknowledged.

Size and Bauschinger Effects in Micro-bending: A 3D Discrete Dislocation Dynamics Study

Christian Motz^{1,2}, Daniel Weygand², Peter Gumbsch^{2,3}

¹**Erich Schmid Institute, Austrian Academy of Sciences, A-8700 Leoben, Austria
(E-mail: motz@unileoben.ac.at)**

²**IZBS, University of Karlsruhe (TH), 76131 Karlsruhe, Germany
(E-mail: daniel.weygand@izbs.uni-karlsruhe.de)**

³**Fraunhofer Institute for mechanics of materials IWM, Germany
(E-mail: ilm@iwm.fhg.de)**

ABSTRACT

Size effects in plasticity are known a quite long time (e.g. N. J. Petch et al. 1953) and have become more attractive in recent time due to the ongoing miniaturization of components and systems in many modern technologies (e.g. MEMS). Thus, the understanding of the origin of these size effects and the related mechanisms are essential for a successful design at small length scales. In complex systems, mechanical loading usually induces stress and strain gradients, which may influence the mechanical properties and give rise to size effects. Therefore, in this work the influence of stress and strain gradients on the mechanical properties is studied in the micro-meter regime by means of 3D discrete dislocation dynamics simulations. The investigations are performed on micron-sized bending beams. Beam thicknesses are varied between 0.5 and 3.0 μm for a fixed thickness to length ratio of 1:3. Two different boundary conditions are used: (i) one end of the beam was fixed and on the other end displacement is prescribed normal to the beam axis to mimic cantilever like bending, and (ii) a "pure" bending case where on both ends bending moments are applied. All other surfaces are traction free. The initial dislocation density is taken to be constant in all samples. A strong size effect is found in the bending resistance with a size-scaling exponent of $n=-1$. Thin beams (high gradients) showed a higher bending resistance compared to the thick beams (low gradients). The resulting dislocation structure features dislocation pile-ups at the neutral plane of the bending beams, which cause a back stress on the operating dislocation sources and thereby is responsible for the strong size effect. These pile-ups are analyzed by statistical methods and the resulting pile-up stresses are incorporated in a simple analytical model to explain the observed size effect. Furthermore, the back stress is analyzed by unloading the deformed beams, where a strong Bauschinger effect is observed. A good agreement between the model and experiments is found.

An analysis of the size effect in void growth in single crystals using discrete dislocation dynamics

J. Segurado¹ J. Llorca¹, and I. Romero²

¹ **IMDEA-materials & Department of Material Science, Polytechnic University of Madrid.
E. T. S. de Ingenieros de Caminos, 28040 Madrid, Spain.**

² **Department of Structural Mechanics. Polytechnic University of Madrid.
E. T. S. de Ingenieros Industriales, 28006 Madrid, Spain.**

ABSTRACT

Ductile failure of metals is normally controlled by the nucleation, growth and coalescence of voids, whose size is of the order of microns. Void growth is caused by the plastic flow around the void and there is compelling experimental evidence that size effects appear in metals when the dimensions of the specimen are in the range of μm [1]. In this paper, void growth in single crystals is analyzed within the framework of 2D discrete dislocations dynamics developed by Needleman and Van der Giessen [2], which has been extended to account for the effect of dislocations leaving the crystal through a free surface in the case of non-convex domains [3]. The simulations analyze the growth of a cylindrical void in a square single crystal of a FCC material. Voids with diameters in the range 0.1 to 0.5 μm are studied and the void growth rate as well as the resistance to plastic flow of the voided crystal are obtained for different loading conditions.

1. Introduction

The overall ductility in metals is mainly controlled by the void growth rate from the nucleation stage up to the coalescence of neighbor voids into a crack. Beginning with the pioneer of work of Rice and Tracey [4] which computed the shape change during deformation of a spherical void embedded in an infinite matrix of a rigid-plastic non-hardening material, many models and numerical simulations have been carried out to account for the effect of different factors on void growth (strain hardening of the matrix, stress triaxiality, etc).

Most of these analyses were carried out in the framework of classical continuum plasticity, and fail to predict any intrinsic effect of the void size on the growth rate. On the contrary, there is experimental evidence of the size effect on the resistance to plastic flow when the characteristic dimension of the problem (i.e. void diameter) is in the range of a few microns [1]

Among the different simulation techniques that exist to account for the size effect in the growth of a void in metallic materials, discrete dislocation dynamics (DDD) arises as an ideal tool to perform "virtual tests" of a crystal with a hole in order to simulate the size effect. This is the strategy that has been followed in this study.

2. Numerical strategy

The numerical simulation of the growth of a cylindrical void within a single crystal is carried out within the framework of DDD developed by Van der Giessen and Needleman [2]. This strategy

was extended by the authors to non-convex domains through the use of finite elements with embedded discontinuities [3].

The model considers an elastic, isotropic crystal with plane strain conditions containing slip systems made up by families of parallel slip planes with different orientations. Straight edge dislocations are represented by linear singularities perpendicular to the crystal plane with Burgers vector \mathbf{b} . Dislocation dipoles can be nucleated at discrete points randomly distributed on the slip planes. Nucleation occurs when the resolved shear stress at the source τ exceeds a critical value τ_{nuc} during a period of time t_{nuc} .

Once generated, dislocations slip in their respective glide planes, and the speed v of a dislocation i is given by a drag relation (1)

$$v_i = B \tau / b \quad (1)$$

where τ stands for the resolved shear stress on the glide plane at the position of dislocation and B is the drag coefficient. Obstacles to dislocation motion can be considered and annihilation of opposite sign dislocations is also taken into account. Finally, the effect of a dislocation exiting the crystal is simulated by introducing a displacement jump of $b/2$ along the slip plane using the embedded discontinuity technology developed in [3].

The resolved shear stress at the position of the i th dislocation can be obtained by projecting the stress at the location of the dislocation, given by the superposition of two fields (2)

$$\boldsymbol{\sigma} = \sum_j \tilde{\boldsymbol{\sigma}}_j + \bar{\boldsymbol{\sigma}} \quad (2)$$

the first one stands for the sum of the stresses due to the rest of dislocations ($\tilde{\boldsymbol{\sigma}}_j$) and it is computed analytically from the expressions of the stress fields on an infinite continuum and the second, $\bar{\boldsymbol{\sigma}}$, includes the effect of the image forces induced by the crystal boundaries on the dislocations. This second term is computed by solving a linear elastic boundary problem using the finite element method with the appropriate boundary conditions and includes also the effect of the displacement jumps across the slip segments of the dislocations that have exited the crystal [3].

3. Results

The model described is applied to simulate the mechanical response of square single crystals of variable dimensions $L \times L$ with a circular void at the center occupying 10% of the area (Fig. 1(a)). The crystal was made up of a linear elastic and isotropic solid, with elastic modulus $E = 70$ GPa and Poisson's ratio $\nu = 0.33$ and contains two slip systems oriented at angles $\pm 35.25^\circ$ with respect to the main loading axis x_2 . This orientation corresponds to a planar model of a FCC crystal. The distance between the slip planes of each system was $100b$. The modulus of the Burgers vector was 0.25 nm and the drag coefficient $B = 10^{-4}$ Pa s. The critical resolved shear stress for nucleation was assigned randomly to the sources following a Gaussian distribution with an average value of 50 MPa, a standard deviation of 15 MPa, and a nucleation time of 0.01 μs . These magnitudes are similar to those used previously in several investigations [5].

3.1 Effect of the triaxiality

The aim of this section is to check the ability of the DD model to predict the influence of the triaxiality on the growth rate. For simplicity, it is assumed that dislocations can only abandon the crystal through the void surface (but not through the lateral surfaces of the crystal) and no obstacles are included along the slip planes. The crystal dimensions were given by $L=2.5 \mu\text{m}$ and three loading cases (with increasing triaxiality) were applied: uniaxial traction, uniaxial deformation and biaxial deformation. The source density was fixed to $150 \mu\text{m}^{-2}$ and the result for each loading case was obtained by averaging the results obtained with three different source arrangements. The crystal unit cell model used for the simulations together with the curves showing the evolution of the void size as a function of the deformation along x_2 for the three loading cases are plotted on Fig. 1.

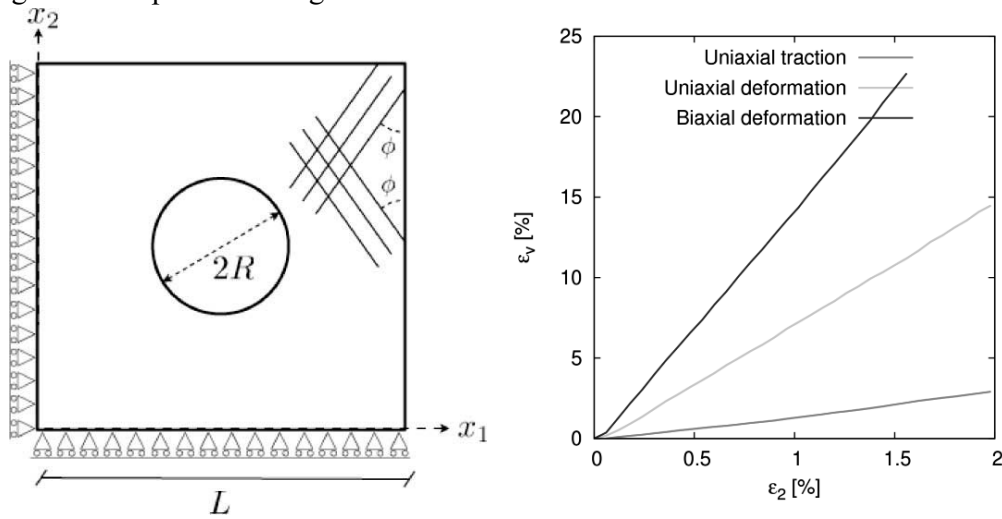


Figure 1. (a) Unit cell of the voided single crystal. (b) Evolution the void size as a function of the applied strain in direction x_2 for three different load cases

The results obtained with the DD simulations capture the dependence of the void growth rate (slope of curves in Fig. 1(b)) with the triaxiality and qualitatively reproduce the results of Rice and Tracey for spherical voids [4]: the void growth rate depends exponentially with the hydrostatic stress.

3.1 Effect of the crystal size.

In order to study the size effect in the growth of the voids, simulations of uniaxial traction in the x_2 direction were carried out using the same square unit cell (Fig. 1(a)) but changing the cell size from $L=0.5 \mu\text{m}$ to $L=2.5 \mu\text{m}$. Contrary to classical plasticity models, the DD simulations were able to predict the different response of crystals with different size without including any ad-hoc parameter. The predicted stress-strain curves and the evolution of the void size as a function of the stress in direction x_2 are plotted on Fig. 2 for the different crystal sizes.

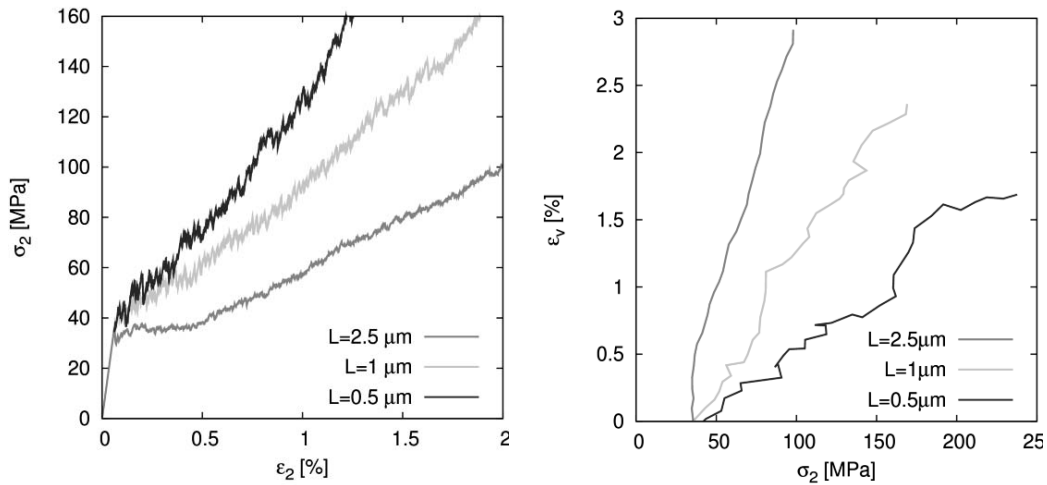


Figure 2. (a) Stress-strain curves. (b) Evolution of the void size as a function of the stress

The classical size effect of the type “the smaller the stronger” is reproduced and both the yield stress and the hardening increase when crystal size is reduced (Fig. 2(a)). The effect of the void size in its void growth rate is shown in Fig. 2(b): it is found that bigger holes grow faster than the smaller ones.

4. Conclusions

The DDD model developed in [3] arises as a powerful tool to predict the size effect in the growth of voids inside a metal. The model reproduces the effect of the triaxiality in the growth rate: the higher the triaxiality the faster the void grows. The DDD simulations also capture the size effect in the growth: larger voids grow faster.

References

- [1] Uchic MD, Dimiduk DM, Florando JN, Nix WD “Sample Dimensions Influence Strength and Crystal Plasticity”. *Science* **305**, 986-989 (2004)
- [2] E. van der Giessen and A. Needleman. “Discrete dislocation plasticity: a simple planar model” *Model Simulat Mater Sci Eng* **3**, 689–735 (1995)
- [3] I. Romero, J. Segurado and J. Llorca. “Dislocation dynamics in non-convex domains using finite elements with embedded discontinuities”, *Model Simulat Mater Sci Eng*, **16**, 035008 (2008)
- [4] J.R. Rice, and D.M. Tracey, “On the ductile enlargement of voids in triaxial stress fields”, *JMPS*, **17**, 201–217 (1969)
- [5] J. Segurado, I. Romero and J. Llorca “Computational Issues in the Simulation of Two-dimensional Discrete Dislocation Dynamics”. *Model Simulat Mater Sci Eng*, **15**, S361-S375 (2007)

Mesoscale Modelling of Dislocation Pile-up Based on Discrete Interactions

R.H.J. Peerlings, Y. Kasyanyuk, A. Roy, M.G.D. Geers

Department of Mechanical Engineering, Eindhoven University of Technology
PO Box 513, 5600 MB Eindhoven, The Netherlands
R.H.J.Peerlings@tue.nl

ABSTRACT

Conventional crystal plasticity formulations fail to correctly predict dislocation pile-ups against e.g. hard particles because they cannot capture the effect of short-range dislocation interactions. We illustrate this limitation by studying an idealised pile-up of infinite edge dislocation walls. In the limit where all discreteness is averaged out, as is done in crystal plasticity, the pile-up collapses into a continuous tilt wall and its finite width is lost. As a consequence, size effects such as the Hall-Petch effect can no longer be captured. Based on an analysis of the short-range interactions in the same idealised pile-up, we derive a back-stress which can be used to repair the conventional theory so that it predicts pile-ups of a finite width.

1. Introduction

Conventional crystal plasticity theories fail to correctly predict the pile-up of dislocations against e.g. hard particles in a plastically deforming matrix. Instead of a gradually increasing slip gradient (and therefore dislocation density) towards the particle, they predict a jump in slip (i.e. a continuous array of super-dislocations) at the particle–matrix interface. As a consequence, the interaction of the stress fields within the particle and matrix is incorrectly described and size effects, such as the Hall–Petch effect, cannot be captured. A number of higher-order crystal plasticity theories have been proposed in recent years which repair this shortcoming, e.g. [1–3]. Most of these theories are phenomenological and the relationship between the higher-order terms introduced and the underlying dislocation interactions is not always very clear.

In this contribution we aim to pinpoint the precise reasons for the limitations of the classical theory by studying an idealised pile-up configuration of infinite edge dislocation walls. A rigorous analysis, in which the dislocations are treated as discrete entities, serves as a reference. A transition towards a (crystalline) continuum is then made in a number of steps by subsequent averaging along and perpendicular to the slip direction. It is shown that the latter, i.e. averaging out the internal structure of an individual wall, eliminates the short-range dislocation interactions which govern the pile-up response. Based on the idealised configuration considered, a back-stress term is derived which, when inserted in the conventional theory, allows it to predict finite-size pile-ups and which turns out to be virtually identical to that proposed by Groma et al. [2] based on statistical arguments.

2. Discrete analysis

The discrete dislocation configuration on which our analysis is based is shown in Fig 1. It consists of a series of dislocation walls in an infinite linear elastic medium. A single slip system is assumed, with discrete slip planes perpendicular to the y coordinate at a constant spacing h . The dislocation lines are straight, infinitely long and perpendicular to the xy plane. They are organised in planar walls which are perpendicular to the x direction. The wall at $x = 0$ (indicated in red in Fig 1) is immobilised and the other walls pile-up against it under the influence of an externally applied shear stress σ . Here we limit ourselves to the case of edge dislocations with Burgers vector in the positive x direction; see Ref [4] for the screw dislocation case, as well as for details of the present analysis.

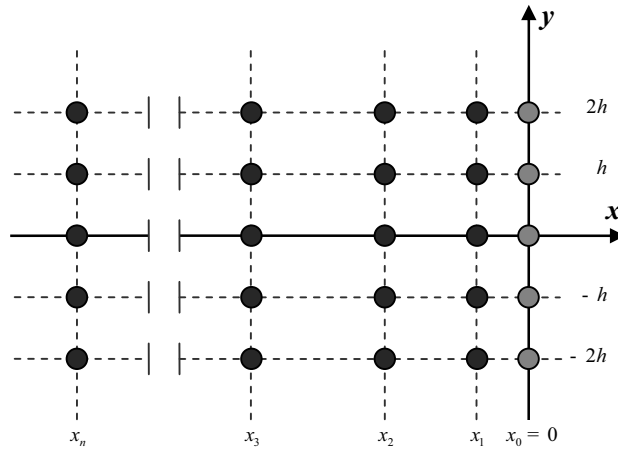


Figure 1. Discrete dislocation configuration considered.

The relevant stress component for dislocation motion is the shear stress σ_{xy} . As the dislocations sit on the individual slip planes, this stress component should be evaluated on such a plane. Given the periodicity of the configuration, we can freely choose $y = 0$. The shear stress acting on this slip plane due to a single dislocation wall at $x = x_j$ is given by

$$\tau(x, x_j) = \frac{G}{2(1-\nu)} \frac{b}{h} \frac{\bar{x}}{\sinh^2 \bar{x}}$$

where G , ν are the elastic constants, b is the length of the Burgers vector and $\bar{x} = \frac{\pi(x - x_j)}{h}$. This stress field decays rapidly (exponentially) with x and is of a short-range nature. The infinite walls considered here can indeed be shown not to generate a long-range stress field as they do not introduce a net incompatibility.

An equilibrium state is reached if for each of the n mobile walls in the pile-up the applied stress σ is balanced by the sum of the interaction stresses τ exerted by all other dislocation walls. This condition results in a set of n nonlinear equations in terms of the n unknowns x_i :

$$\sigma + \sum_{\substack{j=1 \\ j \neq i}}^n \tau(x_i, x_j) = 0 \quad (i = 1, \dots, n)$$

These equations have been solved numerically [4]. The numerical solution for $n = 50$ and an external stress of $\sigma = \frac{50Gb}{2h(1-\nu)}$ is shown in the diagram of Fig 2 by the circular markers. The vertical axis of the diagram shows the local dislocation wall density f , which is defined at each wall position x_i ($0 < i < n$) as $f(x_i) = 2/(x_{i-1} - x_{i+1})$. Both axes have been made dimensionless using the slip plane spacing h . The diagram clearly shows the typical pile-up response expected, with an increasing dislocation density (decreasing wall spacing) while approaching the barrier at $x = 0$.

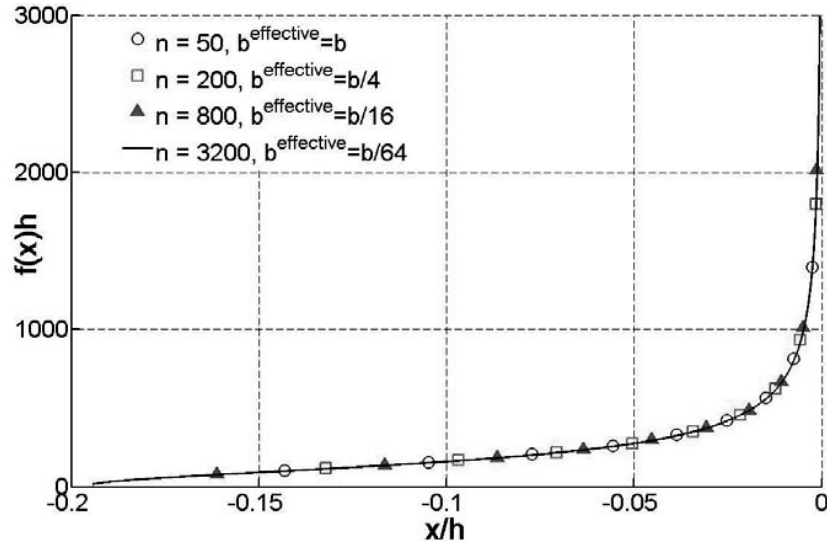


Figure 2. Discrete pile-up solution ($n = 50$) and distributions obtained as the discreteness of the walls is gradually removed.

3. Averaging towards crystal plasticity

We now examine the consequences of the transition from the above, fully discrete analysis to a continuum description in which the precise positions of the individual dislocations are no longer traced. First, the discreteness of the individual walls within the pile-up is gradually removed by increasing the number of walls while reducing the Burgers vector of the dislocations inversely proportionally. Results of this exercise are shown in Fig 2. They show that “smearing out” of the walls to – in the limit – a continuous distribution of walls leaves the shape of the pile-up essentially unchanged and is therefore allowed.

If however, instead of the (horizontal) discreteness of the walls, we attempt to average out the (vertical) internal discreteness of the walls, a different conclusion is reached. Continuous walls

are obtained by taking the limit $b \rightarrow 0$, $h \rightarrow 0$ while keeping constant the ratio $\frac{b}{h}$. In this limit, the interaction stress τ as defined above vanishes for all $\bar{x} \neq 0$. This implies that individual walls can no longer “sense” each other and the discrete balance equations can no longer be satisfied for finite wall spacings. As a consequence, the external stress σ drives all walls into the barrier at $x = 0$, thus creating a super-dislocation wall there. Removing the discreteness of the individual slip systems thus results in a non-physical response because it removes the short-range stress field associated with the wall.

Conventional crystal plasticity theories are fully continuous and thus combine both limits as discussed above. As a result of their failure to account for the short-range stresses associated with individual dislocations, they also predict a pile-up of vanishing width. This shortcoming can be partially repaired by introducing the effect of short-range interactions via a back-stress. Such a back-stress term can be derived for the discrete dislocation configuration of Fig 1 by considering for a given wall the resultant of the interaction stresses τ with its nearest neighbours. Expressing the wall distances in terms of the dislocation density ρ and second-order slip gradient $\frac{\partial^2 \gamma}{\partial x^2}$ and applying a first-order approximation then result in the following expression for the back-stress [5]:

$$\tau_b = \frac{Gb}{2\pi(1-\nu)} \frac{1}{\rho} \frac{\partial^2 \gamma}{\partial x^2}$$

Interestingly, this expression virtually coincides with that derived by Groma et al. [2] based on statistical arguments. Inserting it in a crystal plasticity formulation results in pile-ups of finite width, as in the discrete analysis [2,4,5]. Depending on the wall spacing and applied stress, however, the predicted pile-up distribution does not always match the discrete solution very well. This may be due to the assumption at short-range interactions take place only between nearest neighbours, whereas in the discrete case more remote walls also contribute significantly [5]. A further extension of the theory may be necessary to include this effect.

References

- [1] M.E. Gurtin. “A gradient theory of single-crystal viscoplasticity that accounts for geometrically necessary dislocations”, *J. Mech. Phys. Solids*, **50**, 5–32 (2002).
- [2] I. Groma, F.F. Csikor, and M. Zaiser, “Spatial correlations and higher-order gradient terms in a continuum description of dislocation dynamics”, *Acta Mat.*, **51**, 1271–1281 (2003).
- [3] L.P. Evers, W.A.M. Brekelmans, and M.G.D. Geers, “Non-local crystal plasticity model with intrinsic SSD and GND effects”, *J. Mech. Phys. Solids*, **52**, 2379–2401 (2004).
- [4] A. Roy, R.H.J. Peerlings, M.G.D. Geers, and Y. Kasyanyuk, “Continuum modelling of dislocation interactions: Why discreteness matters?”, *Mat. Sci. Eng. A*, **486**, 653–661 (2008).
- [5] Y. Kasyanyuk, R.H.J. Peerlings, and M.G.D. Geers. In preparation.

The role of the edge effects in the strain localization evolution in polycrystals on the mesolevel

G. Lasko^{1,2}, Ye. Ye. Deryugin¹ and S. Schmauder²

¹Institute of Strength Physics and Material Science, Siberian Branch of Russian Academy of Science ISPMS SB RAS);

² Institut für Materialprüfung, Werkstoffkunde und Festigkeitslehre (IMWF), Pfaffenwaldring 32, 70569, Germany

ABSTRACT

The results of modelling the process of plastic strain localization, accompanied by the intermittent flow (Portevin Le Chatelier effect) are presented. The phenomenon of self-organization of the band structures at the mesolevel have been simulated on the basis of Relaxation Element Method (REM). The developed REM model for the plastic deformation localization operates on the principles of cellular automata. The influence of edge effects on the spatio-temporal patterns of band evolution have been analysed.

1. Introduction

The classical cellular automata satisfy the condition of homogeneity of the system: no one automaton could differ from another in any peculiarities. However, in practice, the calculation field is limited by finite number of the cells. As a result an edge effects take place. In order to escape this the so called periodical boundary conditions are introduced.

On the other hand, when solving the problems of mechanics of deformed solid with application of analytical expressions of infinite plane, the technique of releasing of normal and tangential stresses is used, where there is no points of application of the external forces.

In order to check the reply of the modelled specimen to the different constraints imposed on the edge of the specimen, the simulation of the localization of plastic deformation in polycrystals have been performed for the polycrystals under the uniaxial tensile loading for three cases:

1. Without releasing of normal and tangential stress at the edges of the specimen
2. With application of periodic boundary conditions.
3. With accounting of normal and tangential stresses at the edges of the specimen..

2. Model

In the present work the model of the plastic strain localization of the polycrystal under uni-axial tensile loading is considered. The developed models on the basis of REM operate on the principle of cellular automata. The calculation field is divided into a number of cells, playing the role of grain in polycrystal. A single crystallite involved into plastic deformation becomes the relaxation element (RE) – the defect of mesoscopic scale with its own field of internal stresses. A decrease in the elastic energy in the cell, where plastic deformation took place, is accompanied by an stress increase beyond the cell. In such a manner, an element of structure is able to increase discretely the degree of plastic deformation and as stress concentrator effects the

stress state of the nearest neighbors. The state of all structural elements changes simultaneously in a definite time interval. The involvement of the structural elements into plastic deformation is realized by the Mises-Tresca – criterion, when the shear stress achieves its critical value τ_{cr} . It was assumed, that the plastic deformation of crystallites occurs on the scheme of pure shear. The distribution of shear stress in direction of 45° with respect to tensile axis [10] for a separate RE (the crystallite, undergone plastic deformation), is characterized by an expression:

$$\tau(x,y) = \Delta\sigma \left\{ \begin{array}{l} \frac{(\beta+1)a^2}{(\beta+3)r^2} \left[\frac{3(\beta+3)a^2}{(\beta+5)r^2} - 2 \right] \left[1 - 8(1-y^2/r^2)y^2/r_2 \right], \text{ if } r^2 \geq a^2, \\ -1 + \left(\frac{r}{a} \right)^{\beta+1} \left\{ \frac{\beta^2-1}{2(\beta+3)(\beta+5)} \left[1 - 8(1-y^2/r^2)y^2/r_2 \right] + 1 \right\}, \text{ if } r^2 \leq a^2 \end{array} \right\}. \quad (2.1)$$

Here r - is the distance from the center of RE to the point with the coordinates (x, y) , a - is the radius of RE, $\Delta\sigma$ defines the value of stress relaxation of the pure shear inside the RE, γ^p and β - define the value of the gradients of plastic deformation. The higher β , the higher are the gradients. Shown in Fig. 1 are the distributions of the inhomogeneous stress fields of shear stress $\tau(a)$ and shear strain $\gamma^p(b)$ at $\beta=6$.

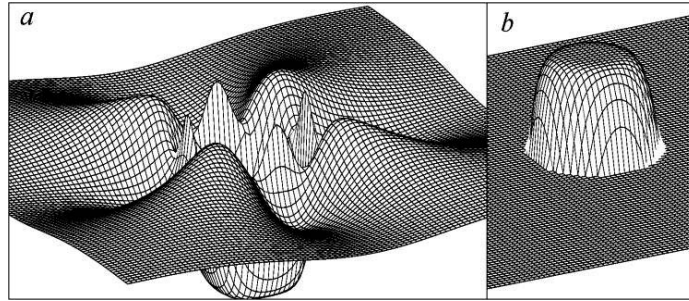


Fig. 1. Distributions of stress $\sigma(a)$ and shear strain $\gamma^p(b)$: $\beta=6$.

The calculation field is represented in the form of a conglomerate of 10×50 points - centers of presumed crystallites. Each act of element involvement into plastic deformation matches a definite time interval which we defined from physical reasoning. A separate grain is assumed to be involved into plastic deformation in the time of order $dt = 5 \times 10^{-4}$ s.

During this time a level of external stress in the value takes place

$$d\sigma = \frac{M(v_0 E b dt - 3\pi a^2 \Delta\sigma)}{(SE + Ml_0)b}. \quad (2.2)$$

Here M - is the rigidity of the testing machine v_0 - is the velocity of the clamps of the testing machine in its unloaded state, a - is the radius of the crystallite, S , l_0 and b - are the cross-section, length and the width of the working part of the specimen correspondingly. The parameter $\Delta\sigma$

include in itself the mechanisms of plastic deformation, i.e. the ability of the material to plastic formchanging. The stress drop was taken to be equal to $\Delta\sigma = 2(\tau_{max} - \tau_0)$, where τ_0 - is the stress of plastic flow. The σ - ε diagrams have been constructed by sum of the $d\sigma$ - increments.

3. Results and conclusion

Shown in Fig. 2a is the result without accounting of the edge effect. Limitations of the calculation field result in the reflection of the band of localized shear from the edge of the

specimen. Further the rapid transfer of plastic deformation along the formed bands of localized shear takes place. Due to this mechanism, the increase in the width of the bands takes place. At the later stage of simulations, the volumes before the formed bands are involved into plastic deformation. All the calculation field is filled by relaxation elements. The partial fragmentation of the material (δ) takes place along some boundaries. After filling out of the whole space with relaxation elements the stage of high work-hardening comes.

Another structure of the bands of localized shear is obtained in the case of the application of the periodic boundary conditions (Fig. 2*b*). Artificial shift of the relaxation element from one edge to another at the beginning results to the formation of the parallel bands of localized shear. Then these bands extended and the mesobands of conjugate direction are formed between them. Finally, unordered structure is formed.

In the case of accounting for the edge effects following the technique, described in the previous paragraph, we obtain a rapid transfer of plastic deformation from one element into another on the mechanism of Lüders band (Fig. 2*c*). A macroscopic deformation for all three cases starts at the same stress and is accompanied by decreasing in stress (Fig. 3). After the whole volume is spanned by plastic deformation, the stage of sharp work-hardening is observed. In the intermediate interval the loading diagrams differ. In the case of not accounting of edge effects (curve 1) after the flow «tooth» the stage of weak work hardening comes. On average as the space is filling out with plastic deformation the flow stress increases. Account for the edge effect by releasing of the normal and tangential stresses at the edge of the specimen is not accompanied by essential work-hardening (Curve 3). Using of periodical boundary conditions results at the beginning to the weak work hardening. Transfer to the stage with high strong hardening occurs already before the whole volume will be embraced with plastic deformation (curve 2).

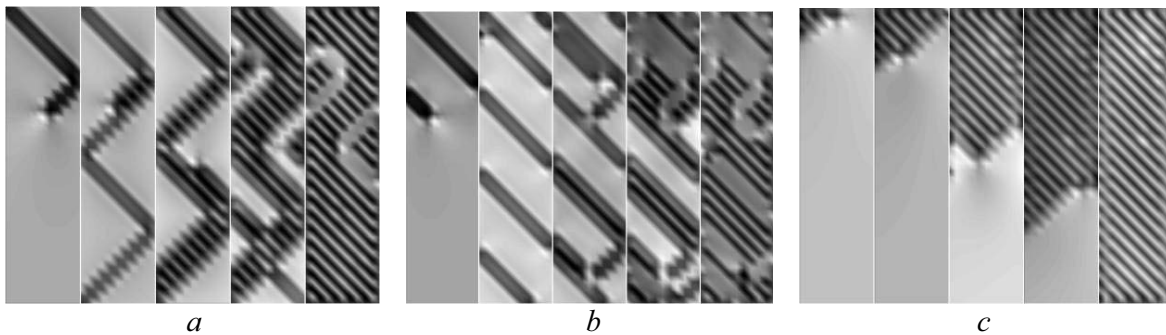


Fig. 2. Formation of the band structures without accounting of edge effects (*a*), with accounting of the periodic boundary conditions (*b*) and with accounting of the releasing of normal and tangential stresses at the edges of the specimen (*c*).

Comparisons with the real loading diagrams show, that the full coincidence is observed in the case of accounting of edge effects by releasing of normal and tangential stresses at the edges of the specimen. A sharp flow tooth and the flow plateau is observed at the initial stage of macroplastic deformation of many polycrystalline materials. The experience shows that the flow plateau is connected with the propagation of Lüders bands. The case of non-accounting of the edge effect qualitatively correctly reflects the behavior of polycrystalline materials, the surface of which from both sides is blocked by high-strength coatings. Than, really, plastic deformation

is developing on the mechanism of reflecting waves []. Accounting to the periodic boundary conditions they do not reflect any ordered mechanisms of the onset of macroplastic flow.

The analyse performed show that when simulating the effect of plastic strain localization the account for periodic boundary conditions doesn't result in the practically important results. In practice, when solving definite tasks the necessity arises to refuse from some of the properties of the classical models of cellular automata.

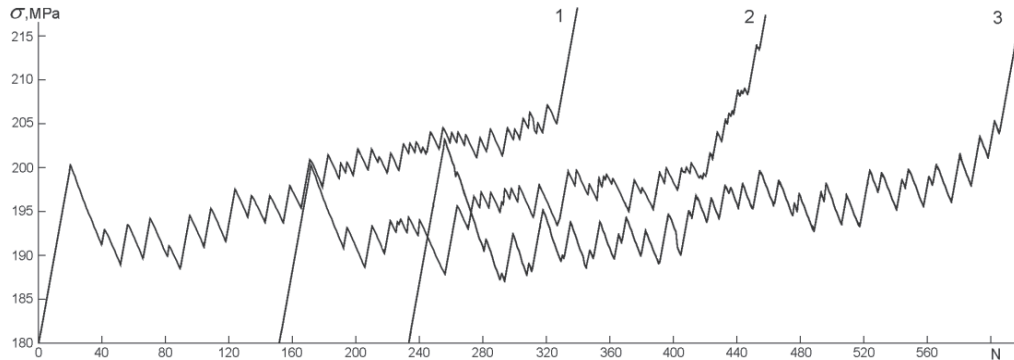


Fig. 3. Modelled diagrams of loading of the specimen without accounting of the edge effects (1), with accounting of periodical boundary conditions (2) with accounting of the releasing of the normal and tangential stresses at the edges of the specimen (3).

The analysis shown that not accounting of free edges of the specimen results to the reflection of the bands from the edge of the specimen. Accounting of periodical boundary conditions results to the band structures. Releasing of the normal and tangential stresses from the edge of the boundary results to the band propagations of Lüders type.

Acknowledgements

The authors are thankful for the financial support from German research Foundation (DFG) under project Schm 746/52-3 and № 07-08-00144-a.

References

1. Estrin Y, Kubin L.P. Spatial Coupling and Propagative Plastic Instabilities, *Continuum Models of Materials with Microstructure*, Chapter 2, Ed. H.-B. Mühlhaus (1995) John Wiley&Sons Ltd., 395-450.
2. Klose F.B., Ziegenbein A., Weidenmüller J., Neuhäuser H., Hähner P. Portevin-Le Chatelier effect in strain and stress controlled tensile tests // *Comput. Mat. Sci.* 26 (2003) 80-86.
3. Zhang Q., Jiang Z., Jiang H., Chen Z., Wu X. On the propagation and pulsation of Portevin-Le Chatelier deformation bands: An experimental study with digital speckle pattern metrology. *Int. J. Plasticity.* 21 (2005) 2150-2173.
4. Deryugin Ye.Ye., Lasko G.V., Schmauder S. Relaxation element method, *Computational Materials Science* 11 (3), (1998) 189-203.
5. Lasko G.V., Deryugin Ye.Ye., Schmauder, S. Simulation of the Evolution of Band Structures in Polycrystals on the Basis of Relaxation Element Method and Cellular Automata, *LNCS 4173* (2006), pp. 367-372.

An Effective Interaction Potential Model of Stress- and Temperature-induced Martensitic Transformations in Perfect Bi-atomic Crystals

Ryan Elliott¹, Nicolas Triantafyllidis², John Shaw²

¹University of Minnesota, Minnesota, USA (elliott@aem.umn.edu)

²University of Michigan, Michigan, USA (nick@umich.edu, jshaw@engin.umich.edu)

ABSTRACT

Solid-to-solid martensitic phase transformations are technologically important phenomena that result in unique macroscopic material properties such as the shape memory effect, ferromagnetism, and ferroelectric behavior. In shape memory alloys, such as CuAlNi and NiTi, the martensitic transformation can result from a change in temperature or the application of stress. In fact, *both* temperature-induced and stress-induced transformations are essential for the existence of shape memory behavior. An *Effective Interaction Potential* model for bi-atomic shape memory alloys, based on a set of temperature-dependent atomic pair-potentials, is presented. The equilibrium solutions of the governing nonlinear equations are found, as functions of temperature and applied stress, using symmetry arguments and *Branch-Following and Bifurcation* techniques. To check if a given equilibrium path is observable, its stability against perturbations of arbitrary (with respect to inter-atomic distance) wavelengths is investigated. This requires continuum-level energy calculations as well as a lattice-level phonon spectra analysis. Our work predicts the existence of a hysteretic two-step temperature-induced proper martensitic transformation from the high-temperature B2 cubic austenite phase, to an intermediate α IrV orthorhombic phase, to a final B19 orthorhombic martensite phase. Stress-induced transformation to the α IrV phase is predicted, at high temperatures, and characteristic properties such as tension-compression asymmetry are captured. Additionally, the transformation stress is found to increase with increasing temperature in agreement with experiment. The existence of both temperature- and stress-induced transformations indicates the possibility for shape memory behavior. Finally, the predicted transformation parameters show good correspondence with experimental values for the shape memory alloys CuAlNi and AuCd.

Influence of the elastic anisotropy on the initial yielding of polycrystals

R. Brenner¹, R. A. Lebensohn², O. Castelnau¹

¹Laboratoire des Propriétés Mécaniques et Thermodynamiques des Matériaux, Université Paris Nord, avenue Jean-Baptiste Clément, 93430 Villetaneuse, France,

²MST8 - MS G755, Los Alamos National Laboratory, Los Alamos, NM, 87545, USA

ABSTRACT

Based on the self-consistent estimate of the local stress field within an elastically anisotropic polycrystalline aggregate, an original definition of the initial yield surface of polycrystals is proposed. It makes use of the average and the standard deviation of the resolved shear stress on the different slip systems within a crystalline orientation. In the case of a copper polycrystal, our results show a strong influence of the stress heterogeneity with a decrease of the elastic limit estimate of about 20% compared to the customary estimates neglecting the intraphase field fluctuations. A good agreement with a full-field approach based on Fourier transforms is obtained.

1. Introduction

The experimental elastic limit of a polycrystalline metallic material is usually determined based on macroscopic stress-strain curves. A customary convention is to consider the macroscopic stress for an offset plastic strain of 0.2%. This definition gives necessarily an upper limit for the yield point of the polycrystal. On the other hand, the recent development of microdiffraction experiments allows to investigate the local plastic behaviour at the grain scale [1] and thus gives access to a local determination of the Yield Surface (YS) of a polycrystal. Such experimental results can be compared with predictions obtained with a micromechanical modelling which describes the heterogeneity of the mechanical fields resulting from the microstructural topology and the anisotropy of the elastoplastic constitutive behaviour. In the sequel, attention is focused on the role of the local elastic anisotropy since only *initial* yield surfaces will be considered. Our study addresses the modelling of the YS of a polycrystal based on the local stress field. With this aim in view, we consider two types of micromechanical approaches: a full-field modelling based on Fourier transform and a mean-field modelling using the self-consistent scheme. Local definitions of the initial YS in the mean-field context are proposed and the results are compared with the full-field method.

2. Stress field within elastically anisotropic polycrystals

We consider isotropic polycrystals (i.e equiaxed grains and no preferred crystalline orientations) with anisotropic local elastic stiffness $\mathbf{C}(\mathbf{x})$. It is assumed that this random elasticity tensor field is Statistically Homogeneous and Ergodic (SHE). To be able to predict the initial yielding within a Representative Volume Element (RVE) of such polycrystalline medium, it is necessary to describe the heterogeneity of the local stress field. This question is studied with different micromechanical approaches. In the sequel, all numerical applications have been performed with the elastic moduli of copper (cubic symmetry with an anisotropy ratio of about 2.8).

2.1 Full-field approach

The Fast-Fourier Transform (FFT) method has been proposed in [2] to determine the mechanical behaviour of a unit-cell representative of a heterogeneous material. It assumes periodic boundary conditions. This modelling makes use of a discrete spatial description of the microstructure and the local elastic behaviour. In the present case, the unit-cell adopted to represent an equiaxed polycrystalline microstructure is a 3D periodic Poisson-Voronoi tessellation (Fig. 1) made of 500 grains (i.e. Voronoi seeds) with a one-to-one correspondence between the set of grains and the set of crystalline orientations. To use the FFT method, the Voronoi tessellation is discretized into a regular grid consisting of $128 \times 128 \times 128$ voxels ($\sim 6,300,000$ degrees of freedom). Each grain thus comprises 4,200 voxels on average.

It is pointed out that the considered unit-cell is not a RVE of the polycrystal. To approximate the response of a RVE, a Monte-Carlo computation is performed by considering N different configurations of the unit-cell [3]. Different unit-cells are simulated by changing the Voronoi tessellation and keeping the same set of crystalline orientations. An estimate of the expectation of the stress and strain fields within a given crystalline orientation can thus be obtained. By using standard relations from the sampling theory, the relative error on the intracrystalline average fields can be obtained for a fixed number of configurations. In our case, 50 different unit-cells have been considered. With the local elastic behaviour of copper, a relative error lesser than 2% is obtained. Note that each unit-cell is subjected to a uniaxial tensile loading along the z axis.

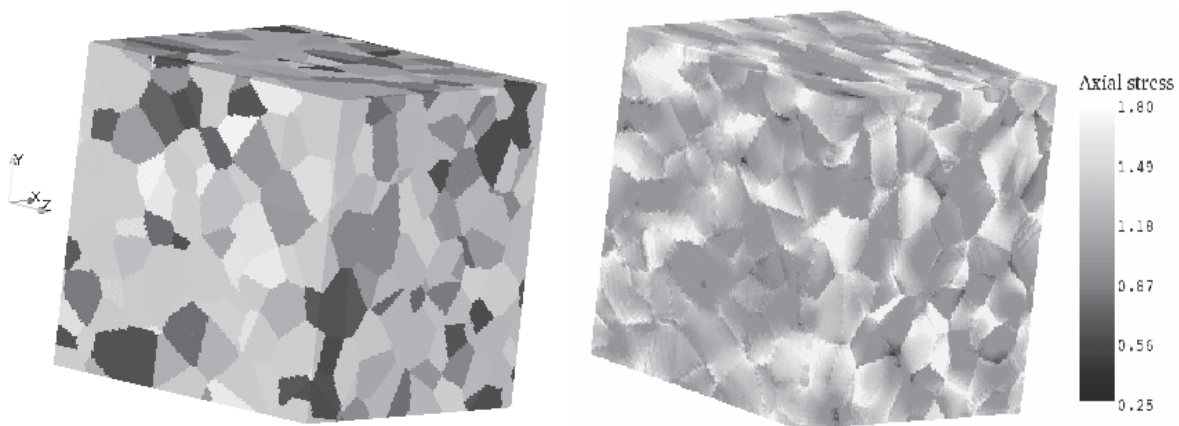


Figure 1. 3D periodic Poisson-Voronoi tessellation and field of the normalized axial stress s_{zz} for an uniaxial tensile test along the z axis.

For each configuration, a highly heterogeneous stress field is obtained. Indeed, the local axial stress component can reach almost twice the macroscopic value (Fig. 1.). Obviously, this stress fluctuation will give rise to an early plastic yielding within the polycrystal as compared to the isotropic elastic case.

Concerning the intracrystalline stress field, it is interesting to note that it does not follow a Gaussian distribution for each single configuration but it tends to become closer to it when it is averaged over the 50 different configurations (Fig. 2). This observation is consistent with previous results obtained on a RVE for a model 2D polycrystal with Voronoi microstructure [4].

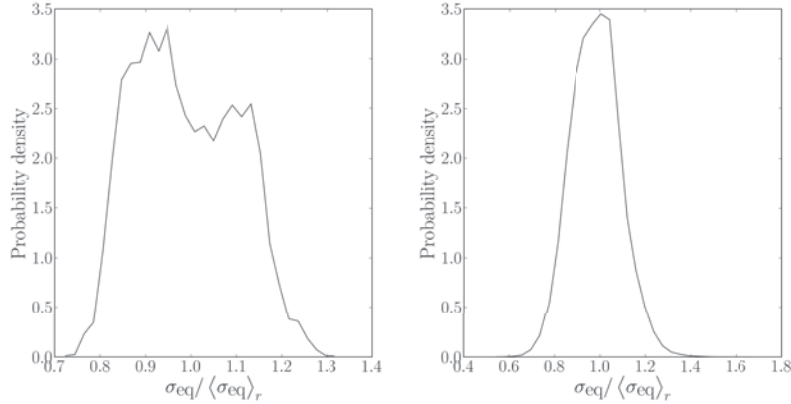


Figure 2. Probability densities of the normalized equivalent local stress for a given crystalline orientation. Left: single unit-cell configuration. Right: 50 unit-cell configurations.

2.2 Mean-field approach

The mechanical field fluctuations within a SHE polycrystalline aggregate can alternatively be quantified by using a mean-field approach making use of the elementary Eshelby's localisation relation. Such procedure rely on a statistical description of the microstructure via the n -points correlation functions. In this framework, it has been established that the self-consistent scheme (SC) is attained for “perfectly disordered” polycrystalline microstructures [5]. In the linear elasticity context, the mean-field approaches give an estimate of the first and second moments of the intraphase mechanical fields within the heterogeneous medium. For the considered polycrystalline microstructure, the average and the variance of the stress and strain fields for each crystalline orientation within a RVE can thus be obtained using the self-consistent scheme. In general, they have to be evaluated numerically. A good agreement between the FFT computation and the SC estimate has been previously reported for the intraphase first and second moments of the fields within polycrystalline microstructures [4,6]. In the present case, since the full-field approach shows that the fields follow a distribution close to gaussian, it is pointed out that the self-consistent scheme then leads to a particularly relevant estimate of the intraphase stress field distribution.

3. Yield surface estimate and stress heterogeneity

Based on the statistical description of the intraphase stress field available with the self-consistent scheme, it is proposed to define a *probability yield surface* related to the level of intraphase heterogeneity which is accounted for. By using the standard Schmid criterion, it is assumed that the yielding occurs in the polycrystal when some *reference* resolved shear stress (RRSS) reaches a critical value. In the context of self-consistent estimates, the RRSS usually corresponds to the maximal value of the average per crystalline orientation of the resolved shear stress on the different slip systems. Such definition leads to an upper bound for the initial YS. More realistic estimates can be obtained by using both *average* and *standard deviation* per crystalline orientation to define the RRSS. More precisely, it is proposed to define the RRSS as the upper value of a given confidence interval (CI) on the resolved shear stress distribution. SC estimates

of the YS for tensile-torsion tests are reported on Fig. 3. with different definitions: average, 68%, 95% and 99% confidence intervals.

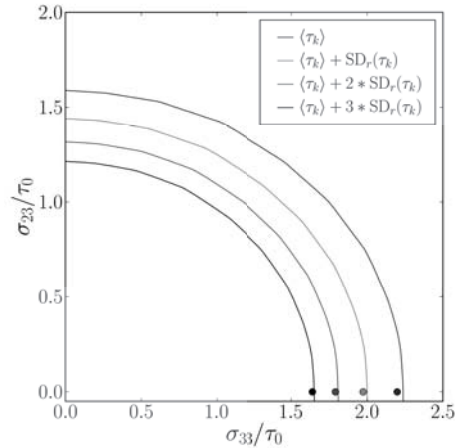


Figure 3. Prediction of the initial YS of an isotropic copper polycrystal using the SC scheme (lines) with different definitions of the RRSS. The points are FFT results for uniaxial tension.

- (i) A very good agreement is obtained between the FFT and the SC estimates for the initial tensile elastic limit. The discrepancy is consistent with the error of the ensemble averaging.
- (ii) In the particular case for which the local fields within the polycrystal follow a normal distribution, the mean-field approaches deliver an accurate description of this distribution.
- (iii) SC estimates of the YS is strongly influenced by the stress field heterogeneity which results from the local elastic anisotropy. If we adopt the 95% CI definition, the estimate of the elastic limit in uniaxial tension is decreased by $\sim 20\%$ compared to the customary average definition.

References

- [1] N. Tamura, A.A. MacDowell, R. Spolenak, B.C. Valek, J.C. Bravman, W.L. Brown, R.S. Celestre, H.A. Padmore, B.W. Batterman, J.R. Patel, “Scanning X-ray microdiffraction with submicrometer white beam for strain/stress and orientation mapping in thin films”, *J. Synch. Rad.*, **10**, 137-143 (2003).
- [2] H. Moulinec and P. Suquet, A fast numerical method for computing the linear and nonlinear mechanical properties of composites *C. R. Acad. Sci. Paris*, **318**, 1417-1423 (1994)
- [3] K. Sab, On the homogenization and the simulation of random materials *Eur. J. Mech. A/Solids*, **11**, 585-607 (1992)
- [4] O. Castelnau, R. Brenner, R. Lebensohn, The effect of strain heterogeneity on the work hardening of polycrystals predicted by mean-field approaches *Acta Mater.*, **54**, 2745-2756 (2006)
- [5] E. Kröner, Self-consistent scheme and graded disorder in polycrystal elasticity *J. Phys. F*, **8**, 2261-2267 (1978)
- [6] R. A. Lebensohn, Y. Liu, P. Ponte Castaneda, On the accuracy of the self-consistent approximation for polycrystals: comparison with full-field numerical simulations *Acta Mater.*, **52**, 5347-5361 (2004)

Micromechanical Modeling of Materials containing Intra-crystalline Particles

Napo Bonfoh, Paul Lipinski

**Laboratoire de Fiabilité Mécanique (LFM) - Ecole Nationale d'Ingénieurs de Metz
(ENIM), Ile du Saulcy, 57045 Metz, France. Metz
(bonfoh@enim.fr, lipinski@enim.fr)**

ABSTRACT

A two-level homogenization approach is developed for the micromechanical modeling of the elastoplastic behavior of polycrystals containing intracrystalline non-shearable particles. First, a micro-meso transition is employed to establish a constitutive relation for a single crystal containing particles. The behavior of an equivalent single crystal with particles is derived from the classical formulation of plasticity of the single crystal based on the Schmid's law and crystallographic gliding. Then, the transition to the macroscopic scale is performed with a self-consistent scheme to determine the elastoplastic behavior of the macro homogeneous material. The obtained global behavior is characterized by a mixed anisotropic and kinematic hardening related to an evolution of inter- and intra-granular material microstructure. Results have been analyzed in light of second and third order internal stresses developed during the plastic flow. Especially, yield surfaces have been determined for various preloadings and particle volume fractions.

Key words : B. Constitutive behavior, Crystal plasticity, Elastic-plastic material, Inhomogeneous material, Residual stress.

Selfconsistent Modelling of the Mechanical Response of Viscoplastic Polycrystals Deforming by Glide and Climb

Ricardo A. Lebensohn¹, Carlos N. Tomé¹, Craig S. Hartley², O. Castelnau³, Stuart A. Maloy¹

¹ **Materials Science and Technology Division, Los Alamos National Laboratory, MS G755, Los Alamos, NM, 87545, USA (lebenso@lanl.gov).**

² **El Arroyo Enterprises LLC, 231 Arroyo Sienna Dr., Sedona, AZ 86336, USA (cmshartley@msn.com).**

³ **Laboratoire des Propriétés Mécaniques et Thermodynamiques des Matériaux, Université Paris XIII, Av J.-B.Clement, 93430 Villetaneuse, France (oc@lpmtm.univ-paris13.fr).**

ABSTRACT

The viscoplastic selfconsistent (VPSC) code [1], originally conceived to predict the homogenized response of incompressible viscoplastic polycrystals deforming by dislocation glide, has been extended to incorporate climb of dislocations as an additional deformation mechanism at the single crystal level. Within this extension, the same dislocation modes that accommodate deformation by glide, are now also able to do so by climb. The constitutive relation for climb involves a geometric tensor (similar to the Schmid tensor for glide) defined in terms of the directions of the Burgers and dislocation density vector, which also depends on the ratio between the densities of edge and screw dislocations and has a non-vanishing spherical component [2]. The latter makes the local and homogenized response compressible, therefore requiring a major revamping of the originally incompressible VPSC code. The critical stresses and viscosity exponents associated with both glide and climb and the interactions between systems have to be determined for specific materials and deformation conditions. We present parametric studies to assess the relative contribution to deformation and the coupling between the glide and climb mechanisms predicted by the model.

[1] R.A. Lebensohn, and C.N. Tomé, " A selfconsistent approach for the simulation of plastic deformation and texture development of polycrystals: application to Zirconium alloys", *Acta Materialia*, **41**, 2611 (1993).

[2] C.S Hartley, "A method for linking thermally activated dislocation mechanisms of yielding with continuum plasticity theory", *Philosophical Magazine*, **83**, 3783 (2003).

Large-Scale Simulation of Oscillating Metal-Nanorod: Application of the Hybrid Molecular-Dynamics/Coarse-Grained-Particle Approach

Ryo Kobayashi,^{1,2} Takahide Nakamura,^{1,2} and Shuji Ogata^{1,2}

¹Department of Scientific and Engineering Simulation, Graduate School of Engineering,
Nagoya Institute of Technology, Gokiso-cho, Showa-ku, Nagoya, Aichi 466-8555, Japan

²CREST, Japan Science and Technology Agency,
4-1-8 Honcho, Kawaguchi, Saitama 332-0012, Japan

ABSTRACT

A new concurrent hybridization method, called the scale-coupling virtual-layers method, which couples two different coarsening scales, is proposed. The method is simple and computationally efficient compared to the former methods. In the method, we introduce the virtual particles for both fine-scale and coarse-scale sub-systems. The virtual particles couple the two sub-systems, and also offer proper boundary conditions to both sub-systems. Reasonable behavior of the wave propagation in both directions is demonstrated.

1. Introduction

We have developed the coarse-grained particle (CGP) method to apply it for concurrent hybrid simulation with the MD [1,2] or the fluid dynamics. In the CGP method virtual particles are distributed in the system, and each particle represents to a group of neighbouring atoms through the weighting function. Since the inter-particle interactions are calculated through the constrained statistical average of the atomic Hamiltonian, the CGP method gives high accuracies for the elastic property. However the CGP method in its original formulation has some drawbacks such as $O(N^3)$ computational cost (N is number of atoms) for calculating inter-particle interactions and the displacement representation of the potential energy with the fixed reference. We have improved these drawbacks to make the CGP method applicable to simulation of a variety of large-scale and macroscopically deformed structures [2].

Imagine that a fine-scale calculation method is applied to a certain region in a coarse-scale system; e.g., the MD embedded in the CGP system. We require that waves produced at the MD region should propagate across the boundary to the peripheral, CGP region. However, when two calculation methods with different length-scales meet each other, spurious wave-reflection usually occurs at the boundary relating to the difference of the minimum wavelengths. The bridging scale method [3] and the bridging domain method [4] have been proposed to couple different scales with suppressed spurious reflection. However both methods need a lot of extra computational cost: considering the time history or solving simultaneous equations to determine the Lagrange multipliers.

Motivated by these, in this paper, we propose a simple and efficient scale-coupling method to connect the MD and CGP methods and also to connect different coarse-graining scales in the CGP method.

2. A Novel Scale-Coupling Method

Figure 1 shows the particle configuration in a one-dimensional system to explain our scale-coupling virtual-layers method (SCVLM). The system is composed of two sub-systems: the fine-scale sub-system depicted at the top in Fig. 1 is to describe the fine-scale area Ω_f ; the coarse-scale sub-system at the bottom in Fig. 1, the coarse-scale area Ω_c . Each sub-system has the virtual particles located in the other area: that is, the ‘‘fine’’ virtual-particles in Ω_c (the open circles in Fig. 1) and the ‘‘coarse’’ virtual-particles in Ω_f (the open squares in Fig. 1). In the following, the uppercase and lowercase letters correspond to the coarse- and fine-scale systems, respectively. The displacements of the particles at one time-step after, depicted in Fig. 1, are obtained through the following three steps:

(i) Update $\{u_f\}$, $\{u_c^v\}$, and $\{U_c\}$ using the inter-particle interaction and the momenta at present in each scale.

(ii) In the coarse-scale sub-system, the displacements of the coarse virtual-particles in Ω_f are determined by coarse-graining those of the fine particles with a weighting matrix f :

$$U_{f,i}^v \leftarrow \sum_j f_{ji} u_{f,i} . \quad (1)$$

Note that no information about the momenta is necessary for the coarse virtual-particles.

(iii) In the fine-scale sub-system, the displacements and momenta of the fine virtual-particles in Ω_c are corrected by interpolating those of the coarse particles with an interpolation matrix N :

$$u_{c,i}^v \leftarrow u_{c,i}^v + \sum_j N_{ij}^+ (U_{c,j} - \sum_l f_{lj} u_{c,l}^v) \quad (2)$$

$$p_{c,i}^v / m \leftarrow \alpha p_{c,i}^v / m + \sum_j N_{ij}^+ (P_{c,j} / M - \alpha \sum_l f_{lj} p_{c,l}^v / m) \quad (3)$$

We define the weighting matrix as $f = (NN^+)^{-1} N$; therefore $fN^+ = 1$. Hence the average of $\{u_{c,i}^v\}$ holds the equality $\sum_j f_{ji} u_{c,i}^v = U_{c,j}$, while $u_{c,i}^v \neq \sum_j N_{ij}^+ U_{c,j}$ in general. It means that the fine virtual-particles may contain a short-wavelength wave, which cannot be described with the interpolation function, N . The scalar parameter α in Eqn. (3) changes gradually from 1 at the left-end of the virtual layers in the fine-scale, to 0 at the right-end of the virtual layers, as shown in Fig. 1. Therefore such a short-wavelength wave is suppressed fully ($\alpha = 0$) at the right-end of the virtual layers. We expect that no substantial reflection wave be produced.

We now explain how a wave propagates through the coarse-fine boundary, with the algorithm mentioned above. Firstly, consider the case in which a wave travels from the right (the coarse-scale) to the left (the fine-scale). The oscillation of $\{U_c\}$ in Ω_c is transferred to that of $\{u_c^v\}$ following Eqn. (2), ignoring any reaction to $\{U_c\}$. Then the wave travels in the fine-scale sub-

system to evolve $\{u_f\}$. The $\{u_f\}$ is transferred to $\{U_f^v\}$ following Eqn. (1). The $\{U_f^v\}$ offers the “non-reflecting” boundary condition for the wave in the coarse-scale sub-system. By this way, no reflection of the wave is expected at the boundary. Secondary, consider the case in which a wave travels from the left (the fine-scale) to the right (the coarse-scale). The $\{u_f\}$ in the fine-scale is transferred to $\{U_f^v\}$ following Eqn. (1). Then the wave of $\{U_f^v\}$ travels toward $\{U_c\}$ in Ω_c . While the wave of $\{u_c^v\}$ in the fine-scale sub-system propagates in the virtual particles. A part of $\{u_c^v\}$ described as $\sum_f N_{if}^+ U_{c,i}$ in Eqn. (2), which uses the coarse-scale information, keeps travelling in the virtual particles and offers the non-reflecting boundary condition for such a long-wavelength wave-component of $\{u_f\}$, while the remaining part $u_{c,i}^v + \sum_l N_{il}^+ (-\sum_j f_{lj} u_{c,j}^v)$ in Eqn. (2) relating to a short-wavelength wave-component is damped with α as shown in Eqn. (3).

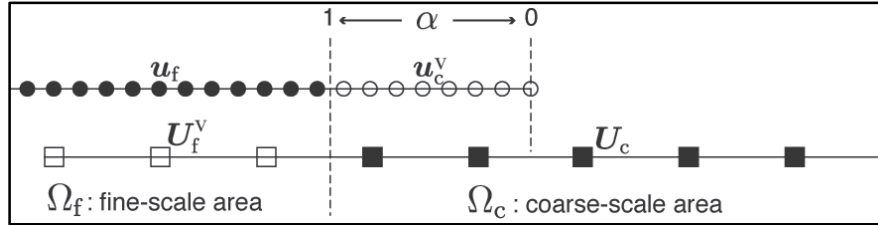


Figure 1. Schematic illustration of the scale-coupling virtual-layers method. Black circles and squares indicate real particles; while, open circles and squares, virtual particles.

3. Example of Wave Propagation

We apply the SCVLM to a simple one-dimensional spring-beads model. Here we set the spring constant, mass, and inter-particle distance of the fine-scale sub-system to 1. The coarse particles are prepared so that a coarse particle represents four fine particles. The properties of the coarse particles such as the spring constants and masses are obtained by the CGP procedure using the weighting matrix, f [1,2].

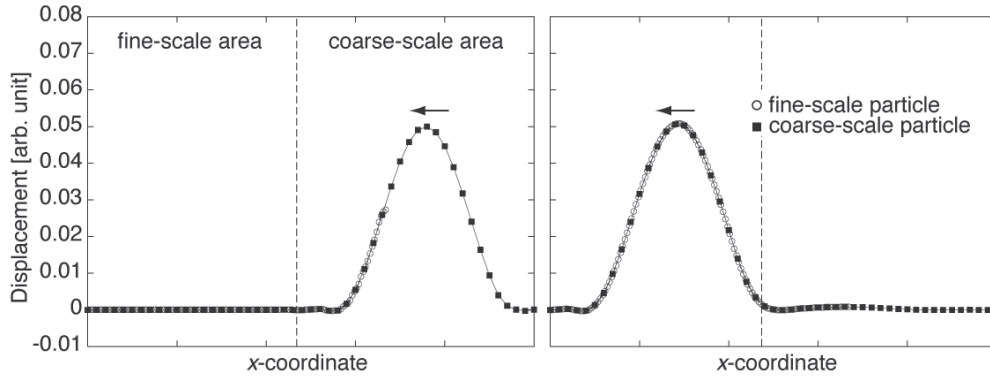


Figure 2. A wave-packet passes through the boundary from the coarse-scale area to the fine-scale area. (Left) at the initial, (right) at the final.

Firstly consider the case in which a wave-packet passes through the boundary from the coarse-scale area to the fine-scale area. Figure 2 shows the simulation result. The wave-packet passes through the boundary with little reflection. The SCVLM works quite well.

Second we consider the case in which a wave-packet passes through the boundary from the fine-scale area to the coarse-scale area. As an initial condition, we set a wave-packet by combining short and long wavelength waves, in the fine-scale area. The short wavelength wave-component cannot propagate in the coarse-scale area since the wavelength is too short. Figure 3 shows the simulation result. The long wavelength wave-component passes through the boundary, as expected. On the other hand, a slight reflection of the short wavelength is observed. Considering that the present method does not use the time history to evolve the wavelength wave, the wave propagation behavior is satisfactory.

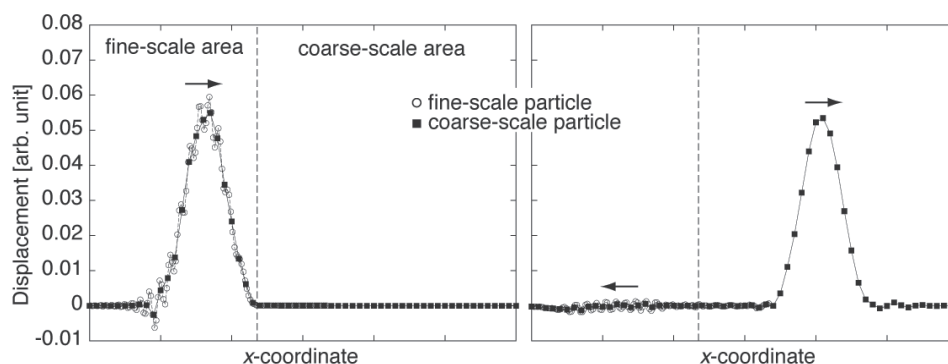


Figure 3. A wave-packet propagates through the boundary from the fine-scale area to the coarse-scale area. (Left) at the initial, (right) at the final.

The SCVLM has advantages as compared with the former methods: The computation uses instantaneous and local data only. Its implementation is simple with little computation cost. Extension to 2D and 3D systems, such as oscillating nanorods, are straightforward, which will be demonstrated in the conference.

References

- [1] R. E. Rudd and J. Q. Broughton, "Coarse-grained molecular dynamics and the atomic limit of finite elements", *Physical Review B* **58**, R5893 (1998).
- [2] R. Kobayashi, T. Nakamura, and S. Ogata, "Development and Implementation of Recursive Coarse-Grained Particle Method for Meso-scale Simulation", *Material Transaction*, vol.49 (2008), in press.
- [3] G. Wagner and W. K. Liu, "Coupling of atomistic and continuum simulations using a bridging scale decomposition", *Journal of Computational Physics*, vol.190, 249 (2003).
- [4] S. Xiao and T. Belytschko, "A bridging domain method for coupling continua with molecular dynamics", *Computer Methods in Applied Mechanics and Engineering*, vol.193, 1645 (2004).

Atomistic/continuum models for multiscale heat conduction

Kenny Jolley, Simon P.A. Gill

Department of Engineering, University Road,
University of Leicester, Leicester, UK, LE1 7RH

ABSTRACT

A method for controlling the thermal boundary conditions of non-equilibrium molecular dynamics (NEMD) simulations by concurrent coupling with a continuum far field region is presented. The method is simple to implement into a conventional molecular dynamics (MD) code and independent of the atomistic model employed. It regulates the temperature in a thermostatted boundary region by feedback control to achieve the desired temperature at the edge of an inner region where the true atomistic dynamics are retained. This is necessary to avoid intrinsic boundary effects in NEMD simulations. A stadium damping thermostat is employed to avoid the adverse reflection of phonons that occurs at an MD interface. The effectiveness of the algorithm is demonstrated for the example of transient heat flow down a three-dimensional atomistic composite rod.

1. Steady state nonequilibrium molecular dynamics

Concurrent multiscale simulation methods have been proposed for extending the length and time scale of atomistic simulations by replacing unnecessary degrees-of-freedom by a continuum representation. Such methods have mainly been developed at zero temperature [1], although there are some notable achievements in extending this to finite temperature (e.g. [2]). These have predominantly focused on isothermal models. Here a method is proposed for extending this type of approach to inhomogeneous thermal problems. In order to do so, it is firstly necessary to obtain accurate control of the thermal boundary conditions of an MD simulation. Here we restrict our interest to ballistic heat transport in insulators via phonon interaction (i.e. conduction by electrons is neglected) in the classical regime (i.e. above the Debye temperature). The temporal evolution of a thermostatted particle of mass m_i at a position \mathbf{x}_i is described by the usual equations of motion

$$m_i \ddot{\mathbf{x}}_i = -\frac{\partial V}{\partial \mathbf{x}_i} - \gamma m_i \dot{\mathbf{x}}_i + R\mathbf{f} \quad (1.1)$$

where γ is a damping coefficient, $-1 \leq R \leq 1$ is a uniformly distributed random variable and $f_n = \sqrt{\frac{6\gamma m_i T_c}{\Delta t}}$ is the magnitude of each component ($n=x, y$ or z) of the stochastic force \mathbf{f} for a

target temperature T_c and a time step Δt . The stochastic Langevin thermostat is active in regions where γ is non-zero. In regions where γ is zero the true (unthermostatted) dynamics are retained. The local Langevin thermostat is advantageous for NEMD simulations as it allows for the (average) temperature of each atom to be specified at the boundaries. Local thermostats are beneficial for rapidly changing transient boundary conditions as they respond quickly to local changes in temperature. The results of imposing a temperature gradient along the length of an MD simulation are shown in Fig. 1a. The temperature gradient is much less than expected. This is due to phonon scattering at the boundaries. Heat is transported in crystals by the correlated motion of atoms. Thermostats disrupt the motion and reduce the thermal conductivity in their vicinity. Such Kapitza effects occur at all interfaces, although it is undesirable here as the interface is artificial.

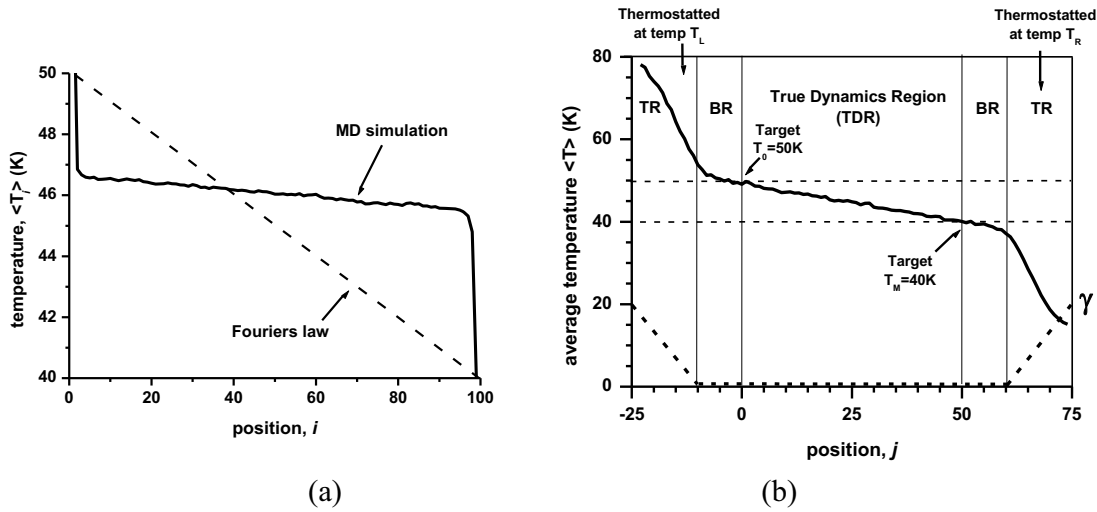


Figure 1. (a) Steady state temperature profile along a 1D 100 atom Lennard-Jones chain (parameters for argon) with fixed ends. The two end atoms are thermostatted at 50K and 40K respectively using a stochastic Langevin thermostat. The large deviation from Fourier's law (dashed line) arises from the discontinuity in the temperature profile at each end due to phonon scattering. (b) Precise imposition of a steady state temperature gradient along a three-dimensional 8x8x100 atom rod by feedback control of the thermal boundary conditions using stadium damping thermostats. The target temperatures in the left and right thermostatted regions (TRs) are regulated at T_L and T_R by (1.2) such that the prescribed temperatures at the edges of the true dynamics region (TDR) (at $j=0$ and $j=50$) are maintained at $T_0=50K$ and $T_M=40K$. A buffer region (BR) of 10 atomic slices is introduced between the TRs and the central TDR to avoid Kapitza effects at the TR/BR interfaces.

A simple pragmatic approach to the artificial Kapitza effect has been proposed by Jolley and Gill [3]. This does not aim to avoid the Kapitza effect, but uses standard thermostats to impose the precise temperature gradient that is desired upon a thermostatted region of the system through a simple control loop. Typical time-averaged temperature profiles for a stadium damping Langevin thermostat [2] are shown for an 8x8x100 Lennard-Jones solid in Fig. 1b. The aim is to maintain different prescribed temperatures at the boundaries of an (unthermostatted) true dynamics region (TDR) in the centre of the sample. These are defined as $T_0=50K$ and $T_M=40K$ on the left and

righthand ends respectively, where $M=50$ is the number of atomic planes in the TDR. The target temperatures of the thermostatted regions (TR) at the left and righthand ends, T_L and T_R are not known. They are determined during the simulation via a very simple feedback control algorithm

$$Q_T \dot{T}_L = (T_0 - \langle T_0 \rangle) \quad Q_T \dot{T}_R = (T_M - \langle T_M \rangle) \quad (1.2)$$

where $\langle T_0 \rangle$ and $\langle T_M \rangle$ are the actual measured temperatures at the TDR boundaries and the constant Q_T determines the responsiveness of the thermostat. There is a buffer region (BR) between the TRs and the TDR to allow for the nonlinear Kapitza effect.

2. A coupled atomistic/continuum model for transient heat flow

The TDR is now coupled to a continuum region. Previously the thermostatted regions (TRs) were used to regulate the temperature at the boundary of the true dynamics region (TDR). The TDR is the only region of interest for the numerical experimentalist. It is simple to couple the TDR to a quasi-static finite difference region evolving under Fourier's law. Now the temperatures at the boundaries of the TDR are not known. They are determined naturally during the simulation from the energy coupling between the atomistic and continuum regions. The temperatures of the TRs are now regulated to ensure conservation of thermal energy such that

$$Q_q \dot{T}_L = \int_0^t (q_L - \langle q \rangle_L) dt \quad Q_q \dot{T}_R = \int_0^t (q_R - \langle q \rangle_R) dt \quad (2.1)$$

where T_L and T_R are the thermostat target temperatures (as in (1.2)), Q_q is a constant which determines the responsiveness of the thermostats, and $q - \langle q \rangle$ is the difference between the heat fluxes in the continuum and the (spatially-averaged) atomistic system along a shared boundary at the centre of the BR. The integrals ensure that heat is conserved exactly over time. As the thermostats are slightly removed from the TDR boundary there is a small delay in the response of the system to changes in the TDR boundary conditions. However, by ensuring the conservation of thermal energy at the mid-point between the TR and the TDR boundary, this delay can be minimized and rendered unnoticeable, even under extremely rapid thermal changes. An example of a fully transient coupled simulation is shown in Fig. 2. The temperature in the atomistic TRs and BRs is not shown as these exist purely for the purposes of controlling the boundary conditions of the TDR. The righthand (continuum) temperature of the system is fixed at 20K and the lefthand (continuum) temperature is cycled sinusoidally between 20K and 40K at a frequency of 0.9GHz. The coupling between the atomistic and continuum models is excellent with no observable jump in the temperature profile at the interface between them. 12ns of time was simulated in total, of which the first 4ns is shown in Fig. 2a.

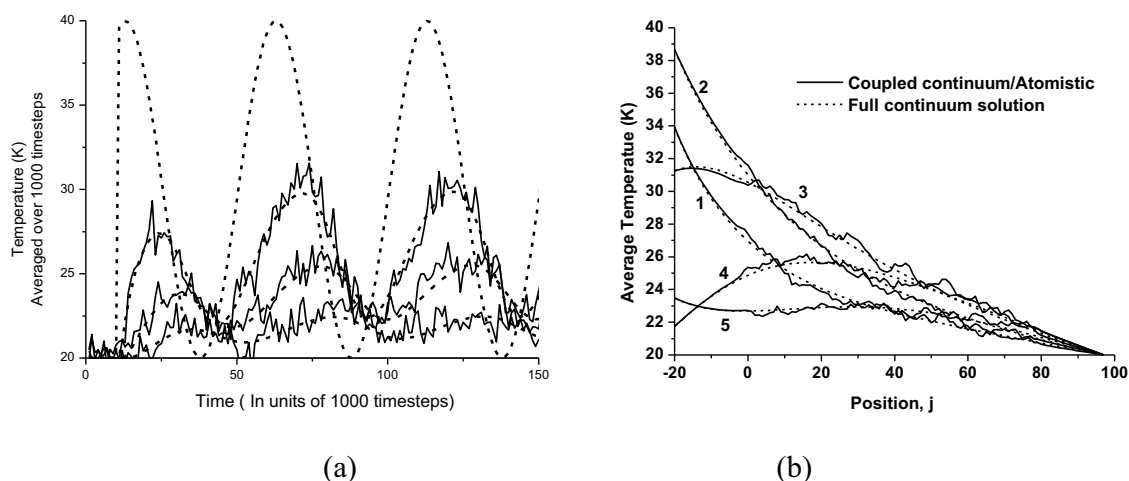


Figure 2. (a) The variation in temperature at three equally spaced points within the TDR region with time for a coupled atomistic/continuum model (solid lines). The full continuum solution and the imposed lefthand (continuum) temperature are also shown (dashed lines). (b) The temperature profile of the atomistic/continuum model (solid lines) and full FD continuum solution (dashed) are plotted at five consecutive times. Each graph is an average of 10000 timesteps (~ 0.2 ns) to reduce thermal noise. The atomistic and continuum models are in excellent agreement during the whole simulation.

Acknowledgements

S Gill and K Jolley gratefully acknowledge the support of a Royal Academy of Engineering-Leverhulme Senior Research Fellowship and EPSRC grant no. EP/P501547/1 respectively.

References

- [1] W.A. Curtin, R.E. Miller, "Atomistic/continuum coupling in computational materials science", *Modelling Simul. Mater. Sci. Eng.* **11** R33-R68 (2003).
- [2] S. Qu, V. Shastry, W.A. Curtin, R.E. Miller, "A finite temperature dynamic coupled atomistic/discrete dislocation method", *Modelling Simul. Mater. Sci.* **13** 1101 (2005).
- [3] K. Jolley, S.P.A. Gill, "Modelling transient heat conduction in solids at multiple length and time scales: A coupled non-equilibrium molecular dynamics/continuum approach", *J Comp Phys* (to appear).

Hot Quasicontinuum calculations of nanovoids evolution under volumetric expansion

C. Arévalo¹, Y. Kulkarni², M.P. Ariza¹, M. Ortiz³, J. Knap⁴, J. Marian⁴

¹ Escuela Superior de Ingenieros /University of Seville, Camino de los descubrimientos s/n, 41092, Seville, Spain (carevalo@us.es, mpariza@us.es);

² University of California, San Diego, La Jolla, CA 92093, USA.

(ykulkarni@ucsd.edu)

³ Division of Engineering and Applied Science, California Institute of Technology, Pasadena, CA 91125, USA (ortiz@aero.caltech.edu)

⁴ Lawrence Livermore National Laboratory, Livermore, CA 94551, USA.

ABSTRACT

Breaking tensile test of ductile materials starts with the formation, in the test material central area, of a choking followed by the nucleation of several cavities at nanoscopic scale. Nanovoids growth and coalescence give rise to a crack which propagates towards the surface in the perpendicular direction to the applied charge. This work is focused on the study of the evolution of these nanovoids for face centered cubic (fcc) crystals. The Quasicontinuum (QC) method [1] has been performed to carry out such an analysis. This method is framed inside the multiscale modelling techniques and it is based on a mixed approximation of the system, continuum and atomistic. QC is a method for systematically coarse-graining lattice models at finite temperature [2]. In the atomistic area, different potentials have been considered for the interaction between atoms. Simulations with our model are presented for uniform dilatation loading mode.

[1] J. Knap, M. Ortiz, “An analysis of the Quasicontinuum method”, *Journal of the Mechanics and Physics of Solids*, **49**, 1899 (2001).

[2] Y. Kulkarni, J. Knap, M. Ortiz, “A variational approach to coarse graining of equilibrium and non-equilibrium atomistic description at finite temperature”, *Journal of the Mechanics and Physics of Solids*, **56**, 1417 (2008).

We gratefully acknowledge the support of the Department of Energy through Caltech’s ASCI ASAP Center for the Simulation of the Dynamic Response of Materials, the support received from the National Science Foundation through an ITR grant on Multiscale Modeling and Simulation and Caltech’s Center for Integrative Multiscale Modeling and Simulation, the support of the Army Research Laboratory through the CHSSI II Project on Scalable Quasi-Continuum Software for Advanced Mixed Atomistic-Continuum Simulation of Material Behavior at the Nanoscale, and the support of the Ministerio de Educación y Ciencia of Spain (DPI2006-05045) and the Consejería de Innovación of Junta de Andalucía (P06-TEP1514).

Coupling Atomistic and Continuum Descriptions: Continuity of Energy Flux and Correlation

Don Nicholson¹, S. Namila¹, P. K.V.V. Nukala¹, Y.N.Osteskiy¹, C.Y.Gao², D.J. Keffer²

¹Oak Ridge National Laboratory, Oak Ridge, TN, USA

**²University of Tennessee, Knoxville, TN, USA
(nicholsondm@ornl.gov)**

ABSTRACT

As an example of closely coupled multiscale modeling we have explored the coupling of a region treated atomistically with molecular dynamics (MD) and a surrounding region treated as finite element (FE). Comparison will be made between conventional handshaking schemes and our proposed absorbing boundary conditions. Further formal development of a correlation function based multiscale coupling will be presented. The relationship between this correlation based approach and the atomic density functional and phase field crystal approaches will be discussed. Acknowledgments: This research was sponsored by the Laboratory Directed Research and Development Program of Oak Ridge National Laboratory and by the Division of Materials Sciences and Engineering, Office of Basic Energy Science, U. S. Department of Energy under Contract No. DE-AC05-00OR22725 managed by UT-Battelle LLC for the Department of Energy and by the University of Tennessee Computational Sciences Initiative.

Reformulation of Continuum Mechanics to Include Multiple Length/Time Scales

Youping Chen¹ and Liming Xiong²

**Department of Mechanical and Aerospace Engineering
University of Florida**

¹ypchen2@ufl.edu, ²lmxiong@ufl.edu

ABSTRACT

A key challenge in nearly all of the dynamically-coupled multiscale modeling methods is to interface the atomistic model with continuum theory. This work aims to find the field representation of fundamental physical quantities and their time evolution laws at atomic length/time scales, and to demonstrate the existence of a field representation of classical atomic-level N-body dynamics for general crystalline materials. This will then lead to the formulation of a new continuum theory of mechanics that is equivalent to a fully atomistic model at the atomic scale and can be reduced to classical continuum mechanics at the macroscopic scale. It will enable concurrent atomic and continuum simulation of materials within a single theoretical framework, thus completely eliminating the numerical interface between atomistic and continuum descriptions in multiscale modeling. Application of the formulated field theory in modeling and simulation of dislocation, phase transformation, fracture and failure of single and polycrystalline materials will be presented.

A Comparative Study of Multiscale Modeling of Generalized Finite Elements and Molecular Dynamics

Peter W. Chung¹ and Michael F. Macri²

¹**Army Research Laboratory, AMSRD-ARL-CI-HC, Aberdeen Proving Ground, MD;**

²**Benet Laboratories, Troy, NY
(pchung@arl.army.mil)**

ABSTRACT

We investigate the performance of new multiscale methods involving generalized finite element techniques that are coupled with a region of fully resolved molecular dynamics. Using the zero-temperature-dynamics assumption (atoms in a frozen configuration until disturbed by an impulse), the error propagation through the atomistic-continuum interface is studied using varying qualities of interpolation in the continuum region in the sense of meshfree methods. We specifically examine the differences among Bubnov-Galerkin, partition of unity, and moving least squares finite element methods in the continuum part of the domain. Through numerical experiments and theoretical simplifications for a one-dimensional chain of atoms, we demonstrate that the assumptions of the generalized continuum region directly influence the quality of the multiscale interface. With these findings, we propose a new stability criterion for bounded error of phonons that travel through the interface.

Reduced Models Obtained by Nonlocal Quasi-continuum-like Approaches

Mihai Anitescu¹, Anter El-Azab², Peter Zapol¹ and Dan Negrut⁴

¹Argonne National Laboratory, Argonne, IL 60439, USA
(anitescu@mcs.anl.gov, zapol@anl.gov)

²Florida State University, Tallahassee, FL 32301, USA (anter@scs.fsu.edu)

³University of Wisconsin, Madison, WI 53706-1572, USA (negrut@eng.wisc.edu)

ABSTRACT

This presentation investigates model reduction techniques that are based on a nonlocal quasi-continuum-like approach. These techniques reduce a large optimization problem to either a system of nonlinear equations or another optimization problem that are expressed in a smaller number of degrees of freedom. The reduction is based on the observation that many of the components of the solution of the original optimization problem are well approximated by certain interpolation operators with respect to a restricted set of representative components. Under certain assumptions, the “optimize and interpolate” and the “interpolate and optimize” approaches result in a regular nonlinear equation and an optimization problem whose solutions are close to the solution of the original problem, respectively. The validity of these assumptions is investigated by using examples from potential-based and electronic structure-based calculations in Materials Science models. A methodology is presented for using quasi-continuum-like model reduction for real-space DFT computations in the absence of periodic boundary conditions. The methodology is illustrated using a basic Thomas–Fermi–Dirac case study.

Mapping Mesoscale Heterogeneity in the Deformation of Single Crystal Copper

John Morris¹, Karen Magid², Nobumichi Tamura³, Jeff Florando⁴, David Lassila⁴, Mary leBlanc⁴

¹University of California, Berkeley, CA, USA (jwmorris@berkeley.edu)

²ETH ETH Hönggerberg, Zurich, Switzerland (karen.magid@mat.ethz.ch)

³Advanced Light Source, Berkeley, CA (ntamura@lbl.gov)

⁴Lawrence Livermore National Laboratory, 94551-0808 Livermore, CA (florando1@llnl.gov, lassila1@llnl.gov, leblanc2@llnl.gov)

ABSTRACT

The work reported here is part of a ‘multiscale characterization’ study of heterogeneous deformation patterns in metals. A copper single crystal was oriented for single slip in the (111)[101] slip system and tested to ~10% strain in roughly uniaxial compression. The macroscopic strain field was monitored during the test by optical ‘image correlation’. The macroscopic strain developed in an inhomogeneous pattern of broad, crossed shear bands. One, the primary band, lay parallel to (111). The second, the ‘conjugate’ band, was oriented perpendicular to (111) with an overall habit that contains no common slip plane of the fcc crystal. The mesoscopic deformation pattern was explored with selected area diffraction, using a focused synchrotron radiation. The mesoscopic defect structure was concentrated in broad, somewhat irregular primary bands that lay nominally parallel to (111) in an almost periodic distribution with a period of about 30 μm . These primary bands were dominant even in the region of conjugate strain. There were also broad conjugate defect bands, almost precisely perpendicular to the primary bands, that tended to bridge primary bands and terminate at them. The residual shear stresses were large (ranging to well above 500 MPa) and strongly correlated with the primary shear bands; interband stresses were small. The maximum resolved shear stresses within the primary bands were oriented out of the plane of the bands, and, hence, could not recover the dislocation structure in the bands. The results are compared to the mesoscopic defect patterns found in Cu in etch pit studies done some decades ago, which also revealed a mesoscopic dislocation structure made up of orthogonal bands.

Continuum Modeling of Plastic Deformation in Polycrystalline Thin Films

Saurabh Puri, Amit Acharya

**119 Porter Hall, 5000 Forbes Avenue,
Department of Civil and Environmental Engineering, Carnegie Mellon University
Pittsburgh, Pennsylvania- 15213
(acharyaamit@cmu.edu)**

ABSTRACT

Phenomenological Mesoscopic Field Dislocation Mechanics (PMFDM) is a recently developed continuum model for studying plasticity at the mesoscale. It is a combination of (a) Field Dislocation Mechanics— as a model for the plastic flow of polar, mobile dislocation density and long-range internal stress, and (b) gradient polycrystal plasticity which is used as a model for plastic flow of statistical dislocation distributions and strength arising from short-range interactions. The mesoscopic model is derived from Field Dislocation Mechanics through an elementary space-time averaging of its equations. It has been shown to be successful in predicting benchmark problems of micron scale plasticity, such as size effects in work hardening and initial yield, Bauschinger effect, modeling of a Frank Read source and spatial inhomogeneity in a homogeneous material under boundary conditions corresponding to a homogeneous deformation. This talk will demonstrate the effect of surface passivation and film thickness on the mechanical response of polycrystalline thin films under plane strain tension. Stronger stress-strain response with decreasing film thickness, increase in Bauschinger effect with subsequent cycles of loading and unloading, and stiffening of mechanical response due to a passivation layer at fixed size are demonstrated. These results are in qualitative agreement with experimental observations. The unloading behavior of thin films of varying thickness is also investigated at different strain levels. Time-permitting, the implementation and some preliminary results from the finite deformation counterpart of the theory will also be demonstrated.

Role of Intra-granular Plastic Slip Heterogeneities on Lattice Rotations: comparisons between experimental measurements and a new micromechanical modeling

**Camille Perrin^{1,2}, Thiebaud Richeton¹, Stéphane Berbenni¹,
Marcel Berveiller¹, Horst Vehoff²**

¹LPMM UMR 7554, ENSAM, Technopôle, 4 rue Augustin Fresnel, 57078 Metz (France)

²WWM, Universität des Saarlandes, Geb. 43B, D-66123 Saarbrücken, (Germany)

Camille.Perrin@metz.ensam.fr

ABSTRACT

In the present study, a new micromechanical approach is developed to derive the mechanical fields (stress, distortion, lattice curvature, elastic energy) arising from the presence of an inelastic strain field representing a typical internal "microstructure". This "microstructure" is due to the formation of discrete (spatial-temporal) intra-granular plastic slip heterogeneities characterized by at least two internal lengths: the first one is the individual grain size, and, the second one is the spatial distance between active slip lines associated with inhomogeneous plastic slip in the interior of grains. Intra-granular plastic slip heterogeneities are modeled using periodic distributions of circular glide dislocation loops for a grain embedded in an infinite elastic matrix. In contrast with the mean field approach based on the Eshelby formalism, this model is able to capture different behaviors between near grain boundary regions and grain interiors. These results are confirmed by EBSD measurements carried out with orientation imaging mapping (OIM) on deformed polycrystals.

1. Introduction

During the last decades, models based on scale transition techniques gain a growing attention in the objective to predict the mechanical behavior of metals and alloys. These models are traditionally based on a mean-field approximation which makes use for grain description of the classic Eshelby's formalism of the homogeneous ellipsoidal inclusion. Therefore, the intra-granular plastic slip heterogeneities are not considered in such approaches. However, recent studies (like discrete dislocation dynamics simulations [1,2]) showed that it appears fundamental to account for the self-organization of dislocations within grains in order to predict grain-size effects on the mechanical behavior of polycrystals. In this work, we consider an inclusion/matrix problem where plastic strain is no more assumed homogeneous as in the classic Eshelby's framework but is given as a discrete distribution of parallel glide dislocation loops constrained at the grain boundary. Such configuration is a first approximation in order to describe plastic slip heterogeneities and the formation of slip line patterns during the early stages of plastic deformation [3]. In a recent contribution [4], it was demonstrated that such approach captured other contributions near grain boundaries on the internal stresses as well as a natural grain size effect on the internal elastic energy than the ones provided by the conventional methods based on the Eshelby's solution. Here, we compute in addition the elastic rotation fields in order to

perform direct comparisons with experimental measurements of local lattice rotation fields obtained by orientation imaging mapping (OIM) on Ni polycrystals during tensile tests.

2. Inclusion problem with inhomogeneous plastic strain

A spherical grain of radius R embedded in an infinite elastic matrix V is considered (Fig. 1). Field equations are given by the stress equilibrium condition for the symmetric Cauchy stress tensor $\boldsymbol{\sigma}$ and the compatibility relation for total distortion $\boldsymbol{\beta}$ (or total strain $\boldsymbol{\varepsilon}$ which is the symmetric part of $\boldsymbol{\beta}$). In the small perturbation hypothesis, $\boldsymbol{\beta}$ is the sum of elastic $\boldsymbol{\beta}^e$ and plastic $\boldsymbol{\beta}^*$ distortions. Field equations lead to solve the so-called Navier type partial differential equation:

$$C_{ijkl}u_{k,jl}(\mathbf{x}) - C_{ijkl}\beta_{lk,j}^*(\mathbf{x}) = 0 \quad (1)$$

where \mathbf{u} is the displacement field and \mathbf{C} is the elastic moduli tensor.

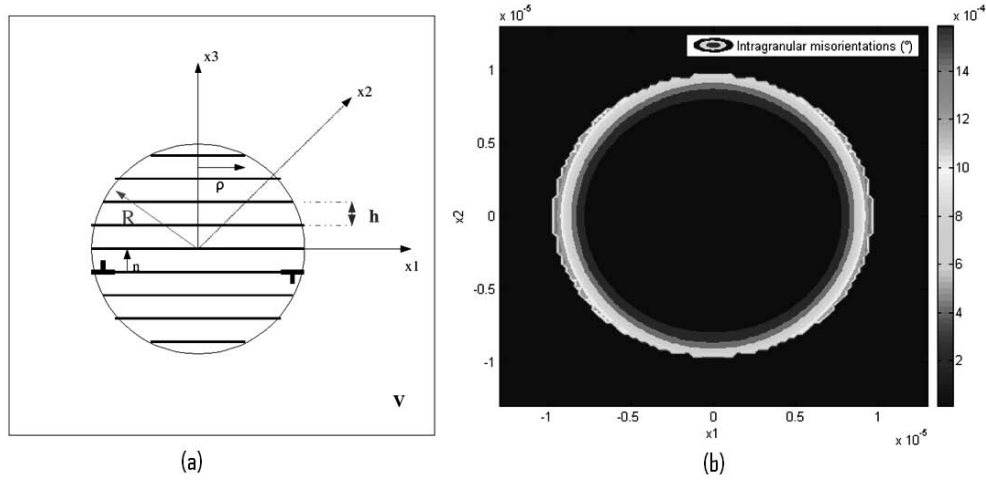


Fig. 1. (a) Spherical grain with radius R and periodic dislocation loops. (b) Intragranular misorientation mapping obtained by the model. ($R = 10\mu\text{m}$ and $h = 2.86\mu\text{m}$) The misorientations are defined with respect to a reference point located in the grain center.

The present study focuses on the peculiar case of a periodic distribution of circular glide dislocation loops lying in successive parallel planes along the grain (Fig. 1). Successive loops are spaced by a periodic distance h . All loops have same Burgers vector \mathbf{b} and same unit normal \mathbf{n} . The loops are constrained by the spherical grain boundary. An odd number $(2N+1)$ of circular loops is considered so that the only non-zero component of $\boldsymbol{\beta}^*$ is:

$$\beta_{31}^*(x) = b \sum_{n=-N}^{+N} H\left(1 - \frac{\rho}{a^{(n)}}\right) \delta(z - nh) \quad (2)$$

where $a^{(n)} = (R^2 - (nh)^2)^{0.5}$ is the radius of the loop at altitude $z = nh$.

In order to determine the whole mechanical fields and elastic energy, a Fourier Transforms method is adopted. Assuming isotropic elasticity, and, keeping in mind that the plastic field due to dislocations is incompressible (Eqn. (2)), the transformation of Eqn. (1) in the Fourier space gives the displacement field solution:

$$u_k(\mathbf{x}) = \frac{-i}{4\pi^3} \int_{V_\xi} \left(\frac{\delta_{ik} \xi_j}{\xi^2} - \frac{1}{2(1-\nu)} \frac{\xi_i \xi_j \xi_k}{\xi^4} \right) \tilde{\varepsilon}_{ij}^*(\xi) e^{+i\xi \cdot \mathbf{x}} dV_\xi. \quad (3)$$

In Eqn. (3), ξ is the Fourier vector and the superscript \sim denotes the Fourier Transform. $\beta(\mathbf{x})$, $\varepsilon(\mathbf{x})$ as well as the rotation field $\omega(\mathbf{x})$ (skew-symmetric part of β) can then be computed either from the displacement in the real space or in the Fourier space. Then, the Euler angles evolution arising from the presence of dislocation loops can be calculated for each point of the space. As seen in Fig. 1b, lattice rotations due to a distribution of periodic loops are almost uniform in a region surrounding the centre of the grain and highly inhomogeneous in the region close to the grain boundary. The obtained results are quite interesting because direct comparison with OIM measurements is possible.

3. Experimental measurements and comparisons with the theoretical model

From experimental studies of deformed polycrystals, plastic strain within grains is known to be strongly heterogeneous and intermittent. As a consequence of the collective motion of dislocations, sample surfaces (which can be observed by optical microscopy or atomic force microscope) are indeed characterized by the presence of slip lines and slip bands (as slip traces) ([3,5]). These slip lines can be observed by light microscopy (with a Nomarski contrast [3]) or atomic force microscopy [6]. They correspond to the emergence of many dislocation loops on a slip plane. Several slip lines can then clustered to form a slip band as described by Neuhäuser [3]. For the present study, a particular grain deforming in single slip in a polycrystalline pure nickel sample (with 1-3% strain) is considered (Fig. 2a). Statistical studies on slip bands spacing are performed.

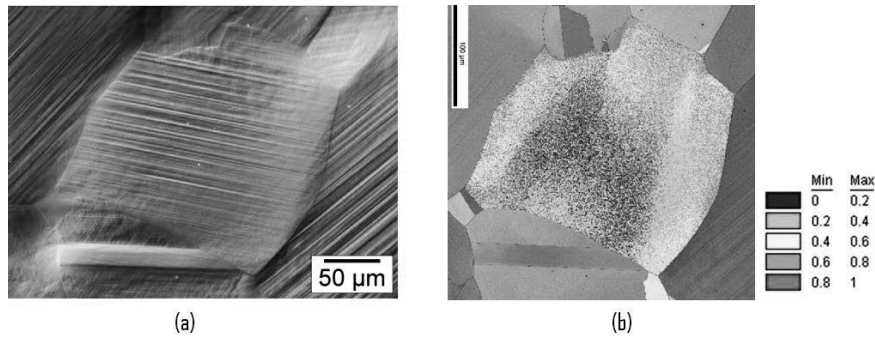


Fig. 2: (a) Optical micrograph (Normarski contrast) : Deformation microstructure of a polycrystalline pure nickel sample with 1% strain. (b) OIM measurement: Intragranular misorientation in relation to a reference point in the grain center after 1% strain.

Intragranular misorientations are measured by orientation imaging mapping (OIM). Fig. 2(b) shows the misorientations with respect to a reference point taken in the grain center. A layer in the region closed to the grain boundary is observed with a strong gradient of lattice misorientation compared to the centre of the grain.

In order to compare both approaches, the two internal lengths (grain size and average slip band spacing) used in the model are directly measured by optical microscopy and atomic force microscopy. Dislocations pile-ups are modelled by “super-dislocations” having an apparent

Burgers vector magnitude B of many b . B was adjusted, in order to maintain a mean plastic deformation in the grain equal to the macroscopic plastic deformation. The calculated values (Fig. 3b) fit the experimental results (Fig. 3a) quite well. The order of magnitude for the maximal misorientation (1°) is notably retrieved. However, in the vicinity of the grain boundary, the misorientation gradient is much stronger than in the experiment. This difference may be due to the fact that “super-dislocations” were considered instead of discrete pile-up mechanisms. The discrete plastic behaviour of surrounding grains which was not taken into consideration in the model may also have an influence, especially close to the grain boundary.

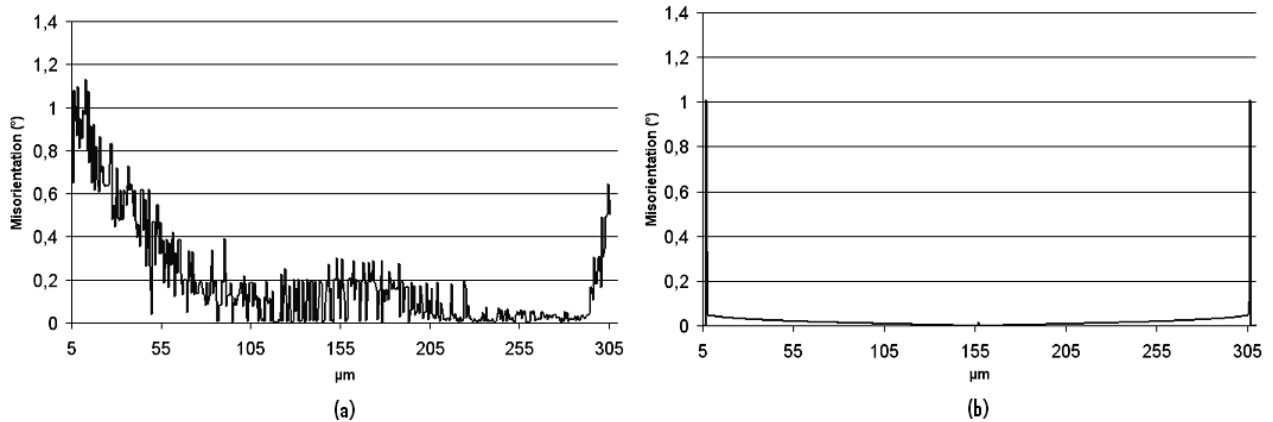


Fig. 3: Intragranular misorientation ($^\circ$) in relation to a reference point in the grain center along a line parallel to the slip lines after 1% strain: (a) OIM measurement, (b) theoretical values.

4. Conclusions and perspectives

Intra-granular plastic slip heterogeneities have been modeled by periodic distributions of circular glide dislocation loops for a grain embedded in an infinite elastic matrix. Lattice rotation fields are quasi uniform in the grain except in a grain boundary layer where strong gradients occur. This new micromechanical approach makes it possible to capture intra-granular phenomena which were confirmed by OIM measurements. In a future work, we will investigate the effects of dislocation loop pile-ups and the influence of discrete plastic deformation in surrounding grains.

Acknowledgements

The authors thank the “Agence Nationale de la Recherche” (ANR) and the French-German University (UFA-DFH) for financial support.

References

- [1] S. Lefebvre, B. Devincere, T. Hoc, “Yield stress strengthening in ultra-fined grained metals: A simulation of dislocation dynamics” *J. Mech. Phys. Solids*, 55, 788-802. (2007)
- [2] G. Saada, “From single to the nanocrystal”, *Philos. Mag.* 85, 3003-3018. (2005)
- [3] H. Neuhäuser, “Slip-line formation and collective dislocation motion”, in *Dislocation in Solids* edited by F. R.N. Nabarro, (Elsevier Science, Amsterdam, 1983) Vol. 6, 319-440
- [4] S. Berbenni, M. Berveiller, T. Richeton, “On plastic slip heterogeneities within grains: discrete vs. mean field approaches”, *Int. J. Solid and Structures*, 24, 1549-1580 (2008).

- [5] B. Jaoul, “Etude de la plasticité et application aux métaux“, Dunod, (1965).
- [6] S. Fréchar, F. Martin, C. Clément, J. Cousty, “AFM and EBSD combined studies of plastic deformation in a duplex stainless steel”, Mater. Sci. Eng A 418, 312–319. (2006)

Higher Order Conditions at Grain Boundaries: Finite Element Simulations of Polycrystal Behavior

Nicolas Cordero, Esteban Busso, Samuel Forest

**Centre des Materiaux, Ecole des Mines de Paris, Paris, France
(nicolas.cordero@ensmp.fr, esteban.busso@ensmp.fr, samuel.forest@ensmp.fr)**

ABSTRACT

Classical plasticity theories are not designed to predict the size-effect on the material response and become irrelevant to investigate microstructure whose size is of the order of magnitude of 1-10 microns or below. Indeed experimental evidence shows that inhomogeneous plastic flow is naturally size-dependent. Generalized-continuum and non-local plasticity models incorporating intrinsic length scales account for such size effects. The aim of this study is to compare directly finite element size-dependent solutions obtained with two different models: Cosserat crystal plasticity and the non-local crystal plasticity theory of Gurtin. These models introduce higher order interface conditions at grain boundaries, involving the continuity of either lattice rotation or plastic strain. Although comparison of such enhanced models has been performed in the past in the case of single and double slip, large scale finite element simulations of polycrystalline aggregates have not been considered yet. For that purpose, 2D and 3D simulations of inhomogeneous deformation close to grain boundaries will be performed. The extent and grain size dependence of the boundary layer at interfaces will be determined for both classes of models.

Microstructural Aspects of Ductile Rupture in Solids

T.W. Wright^{1,2}, K.T. Ramesh²

¹U.S. Army Research Laboratory, 4600 Deer Creek Loop, Aberdeen Proving Ground, MD 21005, USA, tw@arl.army.mil;

²Johns Hopkins University, Mechanical Engineering, 34th & Charles St., Baltimore, MD 21218, USA, ramesh@jhu.edu

ABSTRACT

Ductile rupture in solids can be thought of as a local process that initiates on a micro scale, but is driven by stresses on a macroscale. Thus it is truly a coupled micro-macro phenomenon. We can conceive of the process roughly as follows. Voids nucleate when the external stresses exceed a local cavitation threshold, which in a continuum description may be thought of as a volumetric bifurcation under multiaxial tension [1]. In actuality a void initiates with atomic separation, followed by a cascade of dislocations emanating essentially from a point in a crystalline lattice. Microstructural complexity in ordinary polycrystalline alloys virtually precludes further atomic analysis, but it is actually an advantage in a continuum analysis because it ensures that there will be a distribution of critical cavitation stresses throughout the material. Thus there will be competing, but independent, processes at work. The rate of void nucleation depends on the rate at which growing external stress exceeds higher and higher critical stresses within a neighborhood of the material [2]. However, void growth, and hence porosity, is controlled by the integrated dynamics of material surrounding each void. The macroscopic regime of external stresses is fully coupled to the microscopic, local regime surrounding a void so that eventually the growth rate of porosity forces the external tensile stress to pass a maximum [3]. In this paper we present a theoretical interpretation of these competing processes and show how it leads to a prediction of a rate dependent spall strength where microinertia around a growing void generates most of the rate dependence at the highest rates of expansion.

- [1] Y. Huang, J.W. Hutchinson, and V. Tvergaard, “Cavitation Instabilities in Elastic-Plastic Solids”, *Journal of the Mechanics and Physics of Solids*, **39**, 223 (1991).
- [2] A. Molinari and T.W.Wright, “A Physical Model for Nucleation and Early Growth of Voids in Ductile Material under Dynamic Loading”, *Journal of the Mechanics and Physics of Solids*, **53**, 1476 (2005).
- [3] T.W. Wright and K.T. Ramesh, “Dynamic Void Nucleation and Growth in Solids: A Self-Consistent Statistical Theory, *Journal of the Mechanics and Physics of Solids*, **56**, 336 (2008).

Determination of Burgers Vectors from Atomistic Data

Jun Hua¹, Alexander Hartmaier¹, Mark Duchaineau²

¹**Interdisciplinary Centre for Advanced Materials Simulation (ICAMS), Ruhr-Universität Bochum, Stiepeler Straße 129, 44780 Bochum, Germany**

²**Lawrence Livermore National Laboratory, Livermore, CA 94551-0808, USA
(E-mail: jun.hua@ruhr-uni-bochum.de)**

ABSTRACT

Large-scale molecular dynamics simulations have been widely used to investigate the mechanical behavior of materials. But complex datasets, involving the positions of many million atoms, generated during the simulations make quantitative data analysis quite a challenge. This paper presents a novel method to determine not only dislocations in the crystal, but also to quantify their Burgers vectors. This is achieved by combining geometrical methods to determine the atoms lying in the dislocations cores, like for example the common neighbor analysis [1] or the bond angle analysis [2], with the slip vector analysis [3]. The first methods are used to filter out the atoms lying in undisturbed regions of the crystal; the latter method yields the relative slip of the remaining atoms and thus indicates the Burgers vector of those atoms lying in the dislocation cores. The validity of the method is first demonstrated on single edge dislocations in relatively small samples. Examples on large-scale atomistic simulations of nanoindentation reveal the full potential of the Burgers vector analysis. Furthermore a way will be sketched how this analysis can be used to determine densities of statistically stored and geometrically necessary dislocations, respectively. Hence, this method can be expected to provide valuable input for strain gradient plasticity models.

- [1] J.D. Honeycutt, H.C. Andersen, Molecular-dynamics study of melting and freezing of small Lennard-Jones clusters, *J. Phys. Chem.* 91 (1987) 4950–4963.
- [2] P.J. Steinhardt, D.R. Nelson and M. Ronchetti, Bond orientational order in liquids and glasses, *Phys. Rev. B.* 28 (1983) 784-805.
- [3] J.A. Zimmerman, C.L. Kelchner, P.A. Klein, J.C. Hamilton and S. M. Foiles, Surface step effects on nanoindentation, *Phys. Rev. Lett.* 87 (2001) 165507.

Modelling the Growth of Hydrogen-Induced Platelets in Silicon with the “Learn On The Fly” Multiscale Molecular Dynamics Technique

Gianpietro Moras¹, Lucio Colombi Ciacchi², Christian Elsässer³ and Alessandro De Vita¹

¹Department of Physics, King’s College London, Strand, WC2R 2LS London, UK,
(gianpietro.moras@kcl.ac.uk, alessandro.de_vita@kcl.ac.uk)

²Institut Für Zuverlässigkeit von Bauteilen und Systemen, University of Karlsruhe,
Kaiserstrasse 12, 76131 Karlsruhe, Germany (lucio@izbs.uni-karlsruhe.de)

³Fraunhofer Institut für Werkstoffmechanik, Wöhlerstrasse 11, 79108 Freiburg, Germany
(el@iwf.fhg.de)

ABSTRACT

Hydrogen-induced platelets (HIPs) are believed to play an important role in the “Smart Cut” process, where a thin layer of oxidized silicon is transferred from a hydrogen-implanted wafer onto a substrate after wafer bonding and heat treatment [1]. Despite the vast interest devoted to this technology over the last decade, neither the structure of these hydrogen-related extended defects nor the mechanisms involved in their growth have been completely understood. Experimental investigations suggest that hydrogen contributes in two ways to the thermal evolution of the platelets into microcracks, eventually leading to the splitting of the silicon wafer. Firstly, hydrogen could act “chemically” by facilitating Si-Si bond-breaking or by passivating existing Si dangling bonds, leading to the formation of flat internal surfaces. Secondly, hydrogen molecules confined inside the platelets could have a more “physical” role acting as a source of internal pressure.

Atomistic modelling of the thermally activated platelet growth requires a combination of quantum-mechanical accuracy and large system sizes in order to couple the chemical reactions occurring at the platelet edges with the stress field in the silicon crystal.

In this talk, I will present the results of multiscale hybrid molecular dynamics simulations of (100) HIPs in silicon, performed using the “Learn On The Fly” scheme [2,3]. Simulations of a full ~10 nm HIP system, performed in the experimental 600K-900K temperature range, suggest a possible platelet growth mechanism where H₂ molecules form by desorption from the hydrogen-passivated platelet surfaces. The molecules diffuse filling the platelet volume and eventually reach the highly stressed silicon bonds located at the platelet lateral boundaries, where they are observed to dissociate yielding irreversible Si-Si bond breaking and platelet growth.

- [1] M. Bruel, “Silicon on insulator material technology”, *Electronic Letters*, **31**, 1201 (1995).
- [2] G. Csanyi, T. Albaret, M. C. Payne, and A. De Vita, ““Learn on the Fly”: A Hybrid Classical and Quantum-Mechanical Molecular Dynamics Simulation”, *Physical Review Letters*, **93**, 175503 (2004).
- [3] G. Moras, L. Colombi Ciacchi, G. Csanyi, and A. De Vita, “Modelling (100) hydrogen-induced platelets in silicon with a multi-scale molecular dynamics approach”, *Physica B*, **401-402**, 16 (2007).

Heterogeneous Dislocation Nucleation in Defective Metal Surfaces during Nanoindentation

Oscar Rodríguez de la Fuente

**Departamento de Física de Materiales, Universidad Complutense, Madrid, SPAIN
(E-mail: oscar.rodriguez@fis.ucm.es)**

ABSTRACT

To exploit mechanical properties of materials in a controlled way, a profound knowledge of the defects generated during deformation is required. But atomic deformation mechanisms (specially at the very initial stages) have proven to be complex and many issues are not well known yet. Nanoindentation experiments, with both very high spatial and load resolution, allow to determine the defects emerging at the surface, and their relation to the discontinuities in the load vs penetration curve. But sub-surface defect morphology generally remains hidden, and quite often only indirect conclusions can be inferred. Simulations offer then a very valuable tool to unveil defect configurations and their generation mechanisms. Here we present atomistic nanoindentation simulations (using molecular dynamics and static minimization approaches with up to several million atoms) performed in gold, both on flat and defective surfaces. The reliability of these simulations is proven by direct comparison with experiments from our own group [1], shedding light on them and showing a close match. We analyze the defect configurations during the local deformation of the surface, while monitoring their evolution. Generally speaking, the very first plastic events consist in the formation of dislocation half-loops that either glide or split into more complex dispositions. The gliding and further switch of these loops to other slip planes (cross-slip) give rise to step traces on the surface, which we propose as a generalized mechanism for the usual debris piling-up observed around nanoindentation traces. To provide a closer insight into real surfaces, we have performed simulations on defective surfaces, which show a qualitatively distinct plastic behavior with respect to flat (ideal) ones. The role of pre-existing surface steps is studied, which is often ignored when analyzing surface mechanical properties. Controversial issues, such as plastic activity preceding pop-ins in the force vs penetration curves, is addressed in the present work. We show how surface defects determine the nucleation site and geometry of the generated dislocations, as well as the very incipient surface plastic properties (the strength is lower with respect to flat surfaces). Moreover, the local critical shear stress prior to dislocation formation is reduced when the indentation is performed at a surface step. The present simulations provide a clear example of how heterogeneous defect nucleation during the deformation of a surface can influence the final plastic properties of the material at the nanoscale. We also show that these atypical deformation events do not result in pop-ins and exhibit a large degree of reversibility. All these issues may have profound implications in plasticity models, as well as in contact mechanics and friction between rough solids.

[1] O. Rodríguez de la Fuente et al., Phys. Rev. Lett. 88, 036101 (2002); E. Carrasco et al., Phys. Rev. B 68, 180102 (2003); E. Carrasco et al., Surf. Sci. 572, 467 (2004); V. Navarro et al., accepted in Phys. Rev. Lett. (2008).

New Computational Technique for Evaluating Deformation of Nanocrystalline Metal using Phase Field Crystal Method

Tomoyuki Hirouchi¹, Tomohiro Takaki², Yoshihiro Tomita¹

¹Graduate School of Engineering, Kobe University,
1-1, Rokkodai, Nada, Kobe, 657-8501, Japan, hirouchi@solid.mech.kobe-u.ac.jp;

²Graduate School of Science and Technology, Kyoto Institute of Technology,
Matsugasaki, Sakyo, Kyoto, 606-8585, Japan

ABSTRACT

The phase field crystal (PFC) method is anticipated as a new multiscale method, because this method can reproduce physical phenomena depending on atomic structures in metallic materials on the diffusion time scale. Although the PFC method has been applied to some phenomena, there are few studies related to evaluations of mechanical behaviors of materials by appropriate PFC simulation. In a previous work using the PFC method, tensile deformation simulations have been performed under conditions where the volume change was unavoidable during plastic deformation. In this study, to reproduce deformation under isovolumetric conditions, we proposed a novel numerical technique for PFC deformation simulation. Moreover, to evaluate the contribution of the driving force α (temperature) on deformation behaviors, we performed the tensile deformation simulations of nanopolycrystalline structures with different temperatures. The results confirmed that the resistance to dislocation motions increased by lowering temperature. As a results, grain rotation and grain boundary migration were restrained.

1. Introduction

It is of great importance to predict macroscopic properties of industrial metallic materials depending on defects in microstructures to improve material properties and/or create novel functions of such materials. Therefore, the development of a multiscale model bridging a molecular description and a continuum field theory is an urgent need. Recently, the phase field crystal (PFC) method [1] has been developed as a new multiscale numerical method that operates for atomic length scale with diffusive time scale. The PFC model introduces a periodic order parameter, which represents a local-time-averaged atomic density field to express regular arrangements of atoms in a solid phase. Therefore, this model inherently includes features of crystal systems, elasticity, plasticity and multiple orientations. Although, the PFC method has been applied to some phenomena, there are few studies on appropriate deformation simulation using this method. In previous PFC simulations of tensile deformation [1, 2], the volume of polycrystalline structure increases during plastic deformation simulation due to the difficulty in setting the boundary conditions appropriately. In this study, we propose a novel numerical technique for deformation simulation by the PFC method. By employing this technique, the deformation behaviours of nanopolycrystalline structures are studied at different temperatures.

2. Phase Field Crystal Method

The free energy functional in the PFC method is minimized by a periodic order parameter or the phase field ϕ , which is defined as the local-time-averaged atomic density and is a conserved value [1]. Therefore, this model can reproduce the dynamics based on individual atoms on the diffusion time scale that is much larger than the atomic vibrational time scale. In the steady solid phase of metallic materials, atomic locations are independent of time and become regular arrangements. Therefore, to express these periodic states, the phase field ϕ must have periodic profiles. Here, the local maxima of the phase field ϕ correspond to atomic positions. On the other hand, since atomic positions in the liquid phase become random depending on time, the phase field ϕ is averaged and becomes a constant value ϕ_0 . From the phase field ϕ defined above, the dimensionless free energy functional F is given by [1]

$$F = \int \left[\frac{\alpha}{2} \phi^2 + \frac{\phi^4}{4} + \frac{\phi}{2} (1 + \nabla^2)^2 \phi \right] dV, \quad (1)$$

where α is the driving force, which is proportional to a distance in temperature from a melting point, $T - T_m$. Here, T is a temperature and T_m is a melting point. Since ϕ is the time-averaged density and a conserved value, the Chan-Hilliard equation provides the evolution of ϕ as

$$\frac{\partial \phi}{\partial t} = \nabla^2 \frac{\delta F}{\delta \phi} = \nabla^2 \left[\alpha \phi + \phi^3 + (1 + \nabla^2)^2 \phi \right]. \quad (2)$$

Fig. 1(a) schematically shows the proposed numerical scheme for PFC deformation simulation in two dimensions. To reproduce tensile deformation under isovolumetric condition, the grid size in x-direction increases by the displacement increment $d = \dot{\epsilon} \Delta x \Delta t$ at every time step, and the grid size in y-direction decreases so as to maintain $\Delta x \Delta y = \Delta x' \Delta y'$. Here, Δx and Δy are initial grid sizes, and $\Delta x'$ and $\Delta y'$ are grid sizes changed during deformation, and Δt and $\dot{\epsilon}$ are the time increment and dimensionless strain rate, respectively. In this methodology, since a constant strain rate is applied to all atoms, the deformation state becomes the affine deformation state, and periodic conditions can be used as boundary conditions.

3. Deformation Simulation

The deformation behaviors of a nanopolycrystalline structure are simulated by the PFC method with our technique. Before deformation simulation, a regular hexagonal grain structure with predetermined orientations is prepared by solidification simulation.

3.1 Computational model and conditions

Fig. 1(b) is a schematic illustration of the desired nanopolycrystalline structure with regular hexagonal grains of which a distance between two sides is approximately 14 atoms. The predefined crystal orientations of each grain are shown at the center of each grain. The computa-

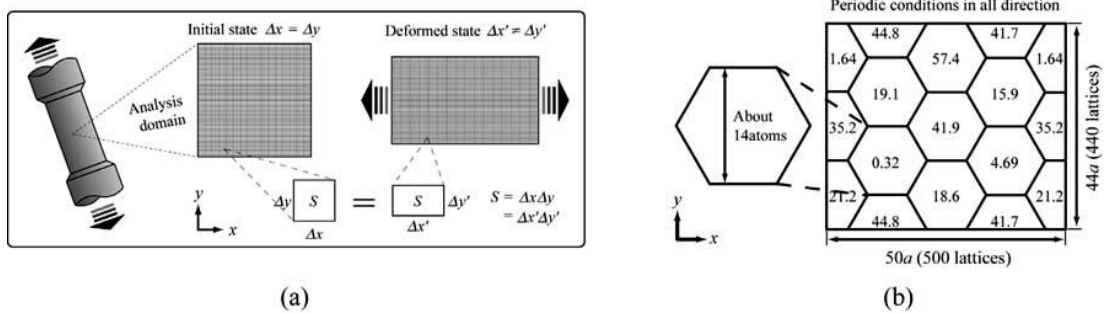


Figure 1. (a) Numerical scheme of tensile deformation simulation in two dimensions and (b) desired nanopolycrystalline structure with regular hexagonal grains and crystal orientations.

tional domain size is set to be $50a \times 44a$ (500×440 lattices) and $\phi_0 = -0.285$ is selected. Here, a is a distance between nearest atoms. To perform the deformation simulations under two different temperatures, $\alpha = -0.25$ and -0.50 are employed. The temperature corresponding to $\alpha = -0.25$ is higher than that of $\alpha = -0.50$. The initial structure is formed by solidification simulation that starts from nuclei with predefined crystal orientations. As a result of solidification simulation with $\alpha = -0.25$, the initial structure shown in Fig. 2(a) is obtained. To prepare same atomic structure for $\alpha = -0.50$, after obtaining the structure shown in Fig. 2(a), further relaxation simulation is performed by changing to $\alpha = -0.50$. The computed structure is shown in Fig. 3(a). Tensile deformation simulations are performed under a constant dimensionless strain rate $\dot{\epsilon}$ of 1.84×10^{-6} , which corresponds to realistic strain rates of approximately 10^0 s^{-1} to 10^1 s^{-1} , and use the dimensionless time step $\Delta t = 3.0 \times 10^{-3}$. Periodic conditions are used in all directions.

3.2 Numerical results and discussion

Fig. 2 indicates the deformation states of the nanocrystalline structure for the case of $\alpha = -0.25$. As the strain increases, grain rotations occur and cause the motions of dislocation at grain boundaries, such as the dislocation shown in the circle of Fig. 2(a). It is also observed that grain rotation occurs between two neighboring grains with a relatively small misorientation (arrows in Figs. 2(a)(b)). As a result of coalescence due to grain rotation, the grain boundary between integrated grains disappears and the grain boundary migration driven by curvature is accelerated, such as the grain boundary in the circle of Fig. 2(c). With further deformation, grain rotations and grain boundary migrations occur continuously in other grains (Figs. 2(d)(e)).

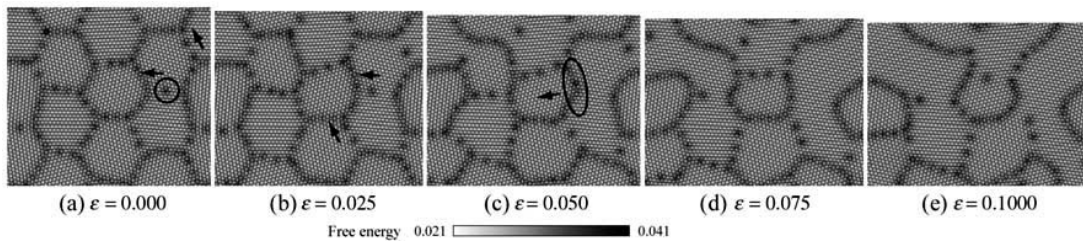


Figure 2. Deformation process of nanocrystalline structures in the case of $\alpha = -0.25$.

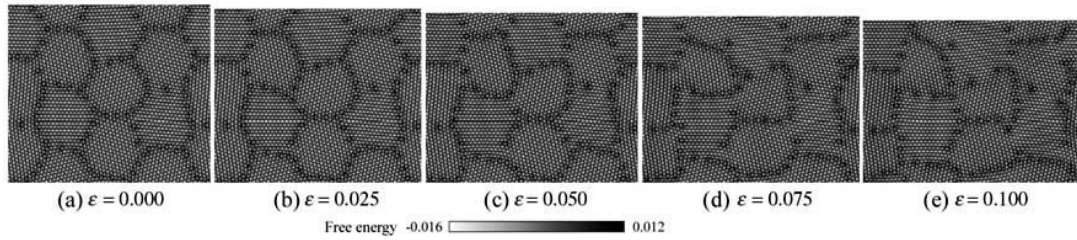


Figure 3. Deformation process of nanocrystalline structures in the case of $\alpha = -0.50$.

Fig.3 shows the deformation states in the case of $\alpha = -0.50$ that is a lower-temperature state than the former. The comparison between Figs. 2(a)-(c) and Figs. 3(a)-(c) suggests that the dislocation motion at grain boundary becomes slower than those at higher temperature. Moreover, grain rotation is harder to occur. As a result, grain coalescence observed in the former can't be confirmed. With further deformation as shown in Figs. 3(d)(e), unlike the former, it can be confirmed that grain boundary migration is restrained. These results clarify that the PFC deformation simulation with our technique can reproduce the increase of the resistance to dislocation motion by lowering temperature.

4. Conclusion

To express deformation under isovolumetric condition, we proposed the novel numerical scheme for PFC deformation simulation. Moreover, to evaluate the influence of the driving force α on deformation behaviours, we performed the tensile deformation simulation of nanopolycrystalline models at two different temperatures. At higher temperature ($\alpha = -0.25$), the intergranular deformation such as grain rotation, grain boundary migration and grain growth became the dominant deformation mechanism. On the other hand, at lower temperature ($\alpha = -0.50$), unlike the former, the resistance to dislocation motions at grain boundary increased by lowering temperature. As a result, grain rotation and grain boundary migration were restrained.

Acknowledgements

Financial support from the Ministry of Education, Culture, Sports, Science and Technology of Japan through a Grant-in-Aid for Scientific Research is highly appreciated

References

- [1] K. R. Elder and M. Grant, "Modeling elastic and plastic deformations in nonequilibrium processing using phase field crystals", *Physical Review E*, **70**, 051605 (2004).
- [2] T. Hirouchi, T. Takaki and Y. Tomita, "Phase Field Crystal Simulation during Plastic Deformation of Nanopolycrystal Metal", *Proceedings of Third Asian-Pacific Congress on Computational Mechanics (CD-ROM)*, MS31-6-3, 1-8 (2007).

Modeling the interphase layer between CNT and matrix in nanocomposites using nonlinear large deformation hierarchical multiscale

Jaafar Ghanbari¹, Reza Naghdabadi²

¹**Mechanical Engineering Department, Sharif University of Technology, Azadi Ave.,
Tehran, Iran (ghanbari@mech.sharif.edu);**

²**Institute for Nano Science and Technology, Sharif University of Technology
(naghdabd@sharif.edu)**

ABSTRACT

We have used a hierarchical multiscale modeling scheme for the analysis of carbon nanotube reinforced nanocomposites. This scheme consists of definition of two boundary value problems, one for macroscale (the scale in which the material exists homogeneously and we are interested in modeling the material behavior on that scale), and another for microscale (the scale in which the material becomes heterogeneous and microstructural constituents emerge). The coupling between these scales is done by using homogenization techniques. Using the presented scheme, we have studied carbon nanotube (CNT) reinforced composites behavior and the effects of an interphase layer between CNT and matrix material. Several nanocomposites with different CNT volume fractions are analyzed and the effects of CNT volume fraction on the global behavior of nanocomposites are studied. For interphase layer, two parameters, namely the thickness and elastic modulus, are optimized so that the effective elastic properties of the nanocomposite match the results obtained using more detailed molecular dynamics studies.

1. Introduction

Carbon nanotubes are believed to have elastic moduli of the order of 1 TPa with strengths in the range of 30 GPa in addition to exceptionally high electrical and thermal conductivity. These properties combined with recent advances in scaling-up production techniques for carbon nanotubes have generated considerable interest in utilizing carbon nanotubes as nanoscale reinforcement in composites [1].

For better understanding the behavior of nanostructured materials, several modeling techniques including Molecular Dynamics, Micromechanical methods, Continuum based methods and multiscale methods have been developed. Although the continuum based methods have been applied to study the effective mechanical properties of nanocomposites, these methods are usually limited to simple microstructures. So, other approaches have been developed which are known as homogenization techniques. While homogenization techniques are known to be excellent tools to predict the effective linearly elastic properties of heterogeneous materials, most of the existing homogenization methods are not suitable to deal with large deformations and complex loading paths and cannot account for an evolving microstructure [2]. To overcome these

problems a computational homogenization approach has been developed, which is essentially based on the solution of two boundary value problems, one for the macroscopic and one for the microscopic scale [3,4]. In the macroscale level, there is no assumption on the material constitutive equation and the constitutive model is obtained numerically in every point. At the microscale level, there is no limitation on the material model of the constituents and any arbitrary material model may be used for each constituents.

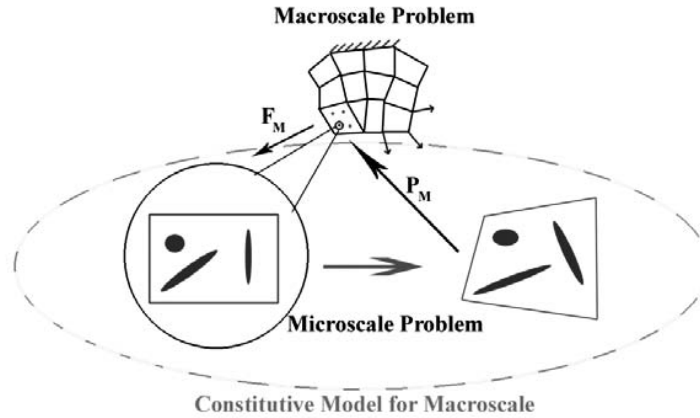


Figure 1. Hierarchical multiscale modeling scheme

2. Hierarchical multiscale modeling scheme

Hierarchical multiscale modelling scheme is essentially based on the derivation of the local macroscopic constitutive response from the underlying microstructure through the adequate construction and solution of a microstructural boundary value problem.

The macroscale problem is discretized using finite element method without any assumption on the material constitutive response. In every material point, where the constitutive response is needed, a microscale boundary value problem is defined and solved, and then the overall constitutive response is determined and returned back to the macroscale problem. Using full numerical integration rule in the elements, we need four microscale problems in every macroscopic element (i.e. in quadrature points). This is shown in Fig. (1).

For every material point in the macroscale problem, the macroscopic deformation gradient tensor, \mathbf{F}_M , is calculated and next used to formulate the boundary value problem in the microscale level. Then the microscale problem is solved to find the microscopic stress distribution in the entire microscale domain. Using the computational homogenization method, the macroscopic stress tensor, \mathbf{P}_M , is calculated from the stress distribution in the microscale problem and transferred back to the macroscale. As a result, the macroscopic stress tensor is calculated in every material point and every equilibrium iteration by solving the corresponding representative volume element (RVE) problem.

The macro-to-micro transition is done by imposing the macroscale deformation gradient tensor \mathbf{F}_M as the boundary conditions on the RVE problem and solving the consequent boundary value problem. To this end, we consider the undeformed position vector of a point in the boundary of the RVE which deforms according to

$$\vec{x} = \mathbf{F}_M \vec{X}, \quad \vec{X} \text{ on } \Gamma_0 \quad (1)$$

where Γ_0 is the undeformed boundary of the RVE. Applying the above boundary condition on the all points located on the boundary of the RVE, we can solve the RVE problem and hence the stress distribution and boundary reaction forces will be available.

The transition from microscale to the macroscale is done using the averaging theorems. We use the volume averaging rule for the case of the first Piola-Kirchhoff stress tensor to get the macroscopic measure from the microstructure results as follows:

$$\mathbf{P}_M = \frac{1}{V_0} \int_{V_0} \mathbf{P}_m dV_0 \quad (2)$$

3. Numerical examples

We have modelled carbon nanotube reinforced polymer nanocomposites with different volume fractions of nanotube content. The nanotubes in these models are assumed to be similar in diameter and length, with the diameter of 1.4 nm and length of 50 nm. For the matrix material, the NASA LaRC-SI polymer is used, with a Young’s modulus of 3.8 GPa and Poisson’s ratio of 0.4. These values are chosen so that the results can be compared with the similar studies published in the literature [5,6].

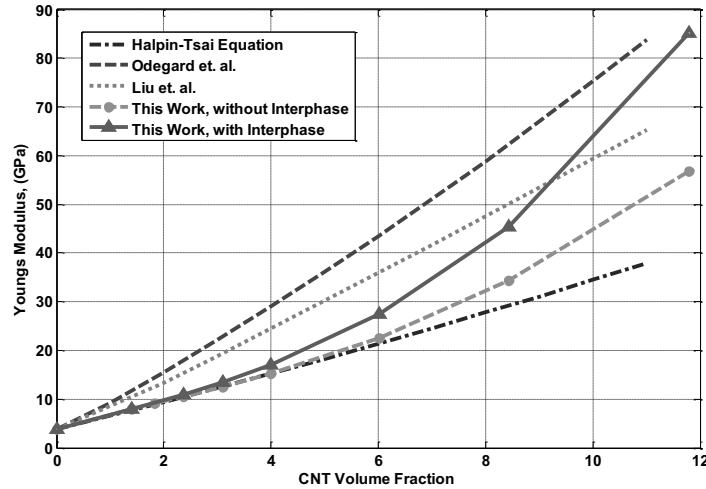


Figure 2. Young’s modulus of CNT/Polymer nanocomposite with respect to CNT volume fraction

Using the presented multiscale scheme, the Young's modulus of CNT reinforced polymer nanocomposites with various CNT volume fractions is determined. CNTs are modelled both with and without an interphase layer to study the effects of considering an interphase layer on the effective properties of nanocomposites. The thickness of the interphase layer is assumed to be equal to the mean diameter of the CNT and its elastic modulus is considered to be 10 times that of the matrix polymer [7]. There is a nonlinear relation between effective Young's modulus and reinforcement volume fraction contrary to the simple rule of mixtures commonly used in determining effective elastic properties of classical composites. In Fig. (2) the results obtained

here are compared with those obtained using different methods published in the literature. Odegard *et al.* [6] have presented a constitutive model for nanotube reinforced polymer composites using a multiscale MD/equivalent continuum approach. Liu *et al.* [5] have studied elastic properties of nanocomposites using a boundary element method based on rigid fiber model. The results obtained in these references are compared with our results in Fig. (2). In addition, the results obtained using the micromechanical Halpin-Tsai equation from Ref. [5] are compared with these results. The Young's modulus of models including the interphase layer approaches to the results obtained with more detailed MD results of Ref. [6], with very smaller computational costs.

4. Conclusions

We have used a hierarchical multiscale modeling scheme for the analysis of elastic properties of CNT/Polymer nanocomposites. This scheme consists of definition of two boundary value problems for coarse and fine scales. Using the computational homogenization method, the coarse scale stress measures are calculated and used in the coarse scale problem. Nanocomposites with arbitrary RVE and constituents materials can be analyzed using the presented scheme.

We have studied nanocomposites with and without an interphase layer between CNT and polymer. The effective elastic properties of nanocomposites with respect to CNT volume fraction are determined and compared with the similar studies. It is observed that Young's modulus of the models with the interphase layer approaches to that of the detailed full atomistic MD simulations.

References

- [1] E.T. Thostenson and T.W. Chou, "On the elastic properties of carbon nanotube-based composites: modelling and characterization", *J. Phys. D: Appl. Phys.* **36**, 573 (2003).
- [2] V.G. Kouznetsova, M.G.D. Geers, and W.A.M. Brekelmans, "Multi-scale second-order computational homogenization of multi-phase materials: a nested finite element solution strategy", *Comput. Methods Appl. Mech. Engrg.* **193**, 5525(2004).
- [3] F. Feyel and J.L. Chaboche, "FE2 multiscale approach for modelling the elastoviscoplastic behaviour of long fiber SiC/Ti composite materials", *Comput. Methods Appl. Mech. Engrg.* **183** 309, (2000).
- [4] K. Terada and N. Kikuchi, "A class of general algorithms for multi-scale analysis of heterogeneous media", *Comput. Methods Appl. Mech. Engrg.* **190**, 5427, (2001) .
- [5] Y.J. Liu, N. Nishimura, and Y. Otani, "Large-scale modeling of carbon-nanotube composites by a fast multipole boundary element method", *Computational Materials Science*, **34**, 173, (2005).
- [6] G.M. Odegard, T.S. Gates, K.E. Wise, C. Park, and E.J. Siochi, "Constitutive modeling of nanotube-reinforced polymer composites", *Compos. Sci. Technol.* **63**, 1671, (2003) .
- [7] H. Wan, F. Delale, and L. Shen, "Effect of CNT length and CNT-matrix interphase in carbon nanotube (CNT) reinforced composites", *Mechanics Research Communications*, **32**, 481 (2005).

Grain Size Effects in the Wedge Indentation of Polycrystals: a Discrete Dislocation Analysis

Andreas Widjaja¹, Alan Needleman², Erik Van der Giessen¹

¹University of Groningen, Groningen, Netherlands
(a.widjaja@gmail.com, E.van.der.Giessen@rug.nl)

²Brown University, Providence, Rhode Island
(needle@unt.edu)

ABSTRACT

Indentation of a model polycrystal is studied using two-dimensional discrete dislocation plasticity. The polycrystal consists of square grains having the same orientation. Grain boundaries are modelled as being impenetrable to dislocations. Every grain has three slip systems, with a random distribution of initial sources and obstacles, and edge dislocations that glide in a drag-controlled manner. The indenter is wedge shaped, so that the indentation depth is the only geometrical length scale. The microstructural length scale on which we focus attention is the grain size, which is varied from $0.625\mu\text{m}$ to $5\mu\text{m}$. While the predicted uniaxial yield strength of the polycrystals follows the Hall-Petch relation, this grain size dependence couples to the dependence on indentation depth. Polycrystals with a sufficiently large grain size exhibit the same "smaller is harder" dependence on indentation depth as single crystals, but an inverse indentation depth dependence occurs for fine-grained materials. For sufficiently deep indentation, the predicted nominal hardness is found to scale with grain size d according to $(H_N) = H_N^\infty (1 + d^*)^{1/2}$, with H_N^∞ the single crystal nominal hardness and d^* a material length scale.

Multi-scale plasticity modeling: from atoms to continuum crystal plasticity

William Curtin

**Brown University, Providence, Rhode Island
curtin@engin.brown.edu**

ABSTRACT

It has long been a goal in mechanics to develop multiscale models that concurrently handle important mechanical phenomena spanning from the atomistic scale to the continuum scale. This goal is particularly important in metal fracture, where the separation of material at the crack tip is inherently atomistic but is influenced by dislocation plasticity occurring scales up to 100s of microns. Dislocation plasticity itself shows size-dependent features at the micron scale, necessitating treatments such as discrete-dislocation modeling or gradient plasticity models that go beyond standard continuum plasticity. The coupling of atomistic models to discrete dislocation models has been achieved by the author and coworkers in recent years [1]. The final piece of the hierarchical model – connecting discrete dislocation plasticity to continuum crystal plasticity – has now been accomplished and is the subject of this presentation. Specifically, we present a hierarchical multiscale model that couples a region of material described by discrete dislocation plasticity to a surrounding region described by conventional crystal plasticity [2]. The coupled model captures size-dependent plasticity phenomena, such as dislocation structuring and formation of geometrically necessary dislocations, that can occur at the micron scale while also capturing the plastic flow, and associated energy dissipation, at much larger scales where size-dependent effects are minimal. The key to the model is the treatment of the interface between the discrete and continuum regions, where continuity of tractions and displacements is maintained in an average sense and the flow of burgers vector via “passing” of discrete dislocations is managed. The model is validated through uniaxial plane-strain tension tests which show that the coupled model deforms similarly to both single-scale models. The multiscale model is then applied to study crack growth, where both near-tip dislocation structures and far-field plastic dissipation are crucial to the overall toughening. The integration of the present method with atomistic/discrete-dislocation models¹ will be briefly discussed, and points toward achievement of a true atom-to-continuum multiscale model for metallic materials.

[1] Shilkrot L, Miller R, Curtin W, Multiscale plasticity modelling: coupled atomistics and discrete dislocation mechanics, *J. Mech. Phys. Solids* 52, 755-787 (2004).

[2] M. Wallin, W. A. Curtin, M. Ristinmaa, and A. Needleman, “Multiscale plasticity modeling: coupled discrete dislocation and continuum crystal plasticity”, submitted to *J. Mech. Phys. Solids*.

Applications of Adaptive Sampling in Multi-scale Simulations

Nathan R. Barton¹, Joel V. Bernier¹, Jaroslaw Knap²

¹Lawrence Livermore National Laboratory, Engineering Technologies Division,
PO Box 808, Livermore CA 94551, barton22@llnl.gov;

²U. S. Army Research Laboratory, AMSRD-ARL-CI-HC,
Aberdeen Proving Ground, MD 21005-5067

ABSTRACT

While embedded multi-scale material modeling offers an attractive path for capturing the effects of detailed sub-scale behaviors in a coarse-scale response, direct embedding of expensive sub-scale models typically entails high computational cost. Using an adaptive sampling methodology, this expense is ameliorated and we are able to perform calculations which are otherwise intractable. Our adaptive sampling approach utilizes multivariate-kriging interpolation in conjunction with the metric-tree database, and has been used successfully to simulate deformation of polycrystalline metals of cubic symmetry [1,2,3]. Recent efforts focus on the use of adaptive sampling with a multi-scale model that captures the profound deformation heterogeneity in multi-phase and low symmetry polycrystalline metals. Various modeling and algorithmic developments enabling this new work will be presented. Example applications include large scale simulations using multiple-data multiple-program parallelism.

- [1] N. R. Barton, J. Knap, A. Arsenlis, R. Becker, R. D. Hornung, and D. R. Jefferson, “Embedded polycrystal plasticity and adaptive sampling”, *International Journal of Plasticity*, **24**, 242 (2008).
- [2] J. Knap, N. R. Barton, R. D. Hornung, A. Arsenlis, R. Becker, and D. R. Jefferson, “Adaptive sampling in hierarchical simulation”, *International Journal for Numerical Methods in Engineering*, (2008). doi: 10.1002/nme.2339.
- [3] J. V. Bernier, N. R. Barton, and J. Knap, “Polycrystal plasticity based predictions of strain localization in metal forming”, *Journal of Engineering Materials and Technology*, **130**, 021020 (2008).

This work performed under the auspices of the U.S. Department of Energy by Lawrence Livermore National Laboratory under Contract DE-AC52-07NA27344 (LLNL-ABS-401750). This project 07-ERD-024 is funded by the Laboratory Directed Research and Development Program at LLNL.

Modeling Hydrogen Embrittlement in Metals: Coupling Quantum Mechanical, Empirical Potential and Kinetic Monte Carlo Approaches

Ashwin Ramasubramaniam¹, Mitsuhiro Itakura², Michael Ortiz³ and Emily A. Carter⁴

¹**Program in Applied and Computational Mathematics, Princeton University, Princeton NJ 08544, aramasub@princeton.edu;**

²**Center for Computational Science and E-systems, Japan Atomic Energy Agency, 6-9-3 Higashiueno, Taito-ku, Tokyo 110-0015, Japan, itakura.mitsuhiro@jaea.go.jp;**

³**Graduate Aeronautical Laboratories, California Institute of Technology, Pasadena CA 91125, ortiz@aero.caltech.edu;**

⁴**Department of Mechanical and Aerospace Engineering and Program in Applied and Computational Mathematics, Princeton University, Princeton NJ 08544, eac@princeton.edu.**

ABSTRACT

The problem of hydrogen diffusion in metals and its implications for stress corrosion cracking are studied from an atomistic perspective. Long-range diffusion of hydrogen within the crystal is modeled using on-the-fly kinetic Monte Carlo (KMC) calculations. Diffusion barriers and rates are ascertained from the local environments of H atoms using embedded atom (EAM) potentials. To improve computational efficiency, on-the-fly calculations are supplemented with precomputed strain-dependent energy barriers in defect-free parts of the crystal. These precomputed barriers, obtained with high-accuracy density functional theory (DFT) calculations, are used to ascertain the veracity of the EAM barriers and correct them when necessary. Examples of bulk diffusion over extended time scales in defective crystals are presented and shown to be in good agreement with theory. Computational studies of the interaction of hydrogen with Mode-I cracks and the ensuing embrittlement of the host metal are also presented. Our model provides an avenue for simulating the interaction of hydrogen with cracks, dislocations, grain boundaries, and other lattice defects, over extended time scales.

[1] A. Ramasubramaniam, M. Itakura, M. Ortiz, and E. A. Carter, “The Effect of Atomic Scale Plasticity on Hydrogen Diffusion in Iron: Quantum Mechanically Informed and On-the-fly Kinetic Monte Carlo Simulations”, *Journal of Materials Research*, in press (2008)

This work was supported by a grant from the Office of Naval Research. Computational resources were provided by the Arctic Region Supercomputing Center and the Maui High Performance Computing center.

Stress analysis during the interaction between dislocations and a main crack: Case of a bi-material

M. Chabaat¹ and H. Hamli Ben Zahar²

¹Professor, ²Doctorate student, Built & Envir. Res. Lab., Civil Engineering Faculty,
University of Sciences and Technology Houari Boumediene, B.P. 32 El Alia, Bab
Ezzouar, Algiers 16111, Algeria
(E-mails: mchabaat2002@yahoo.com, hzahar2004@yahoo.fr)

ABSTRACT

In this study, stress and displacement fields for an edge dislocation near a semi-infinite interfacial crack are obtained using the complex potential of Muskhelishvili's elasticity treatment of plane strain problems. It is shown herein that if the dislocation is originated elsewhere and moves to the vicinity of a finite interfacial crack then, the image forces exerted on the dislocation have an oscillatory character (with respect to the dislocation position). It is also proven that there is no such oscillation of image forces if the edge dislocation is emitted from the finite interfacial crack. Thus, the Stress Intensity Factor (SIF) produced by the edge dislocation also has an oscillatory character for both semi-infinite and finite interfacial cracks. This latest depends on whether the dislocation is emitted from the crack or comes from elsewhere.

1) Introduction

In the last decade, studies on the elastic behaviour of interfacial cracks have been intensively documented [1-4]. It has been proven that the interfacial fracture strength of multiphase solids may depend on the properties of cracks embedded in the interfaces. On the other hand, there is an oscillatory character in the stress and displacement field near the tip of interfacial cracks. Recently, several researchers [4-6] have focused their work toward the study of the stress field generated during the interaction of singularities with interfacial cracks. It is obvious that interactions between dislocations and cracks play an important role in fracture. These interactions produce image forces on the dislocation and generate stresses around the crack tip. This latest can either shield or amplify the stress field in the vicinity of the crack tips. In this study, the stress field is derived in the case where the dislocation is originated from elsewhere and moves to the vicinity of the crack.

2) Interactions interface cracks

Considering a two dimensional, linear elastic solid with a planar interface along plane $x_2 = 0$. The solid is made of two materials A and B as shown in Figure 1 and the boundary conditions on the border of the interface are such as: $u_i^A(x_1, x_2 = 0^+) = u_i^B(x_1, x_2 = 0^-)$,

$\sigma_{i2}^A(x_1, x_2 = 0^+) = \sigma_{i2}^B(x_1, x_2 = 0^-)$ where u_i represents the displacement in the direction x_i and σ_{i2} the component of stress $i = 1, 2$

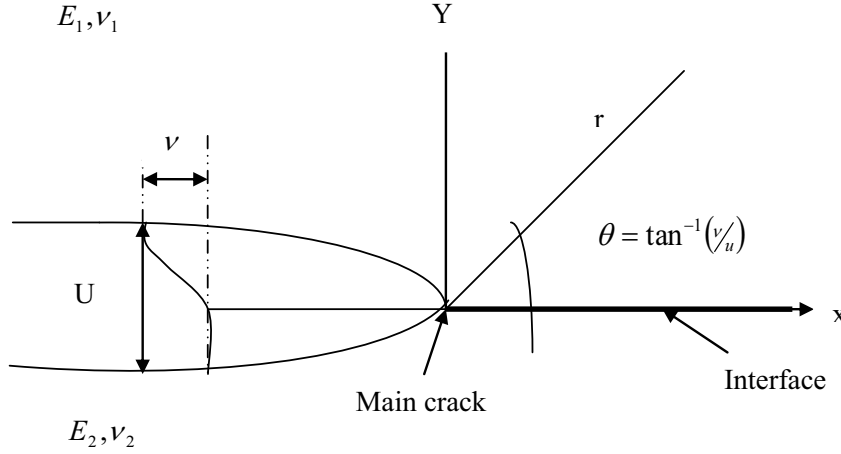


Figure 1: A slit with the material interface in two dimensions.

In this work, analysis of the influence of this zone of dislocations on the principal crack. This study is based on the investigation of the elastic interaction of a crack with neighbouring dislocations directed in an arbitrary way. In this case, the principal crack is presented like a semi-infinite crack. This latest is subjected to a stress field which is characterized by a stress intensity factor (K_I). Thus, the interaction of dislocation with the principal crack is evaluated in term of amplified (or reduced) stress intensity factor acting at the tip of the main crack This theory regards the process of propagation of the crack as being a development and a subsequent coalescence of micro defects in the vicinity of the point of the principal crack.

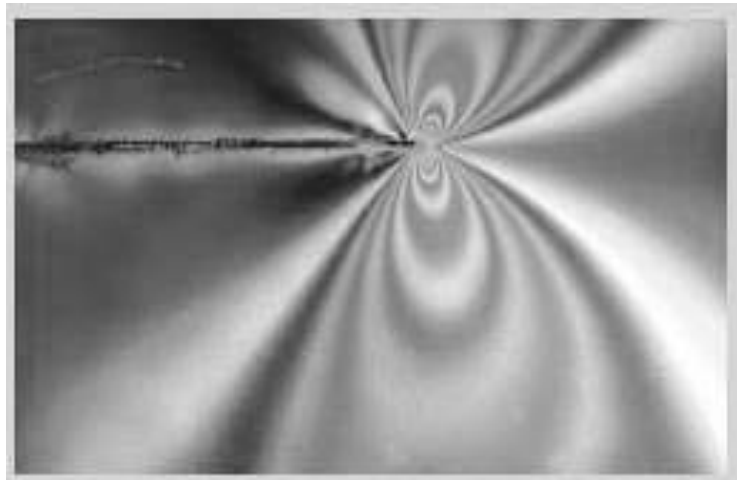


Figure 2: Isochromatic cuttings of fringe observed in a slit under mode I.

The problem is formulated in terms of the complex potentials given by ϕ and ψ [1].

For the plane stress, the displacement and the stress field can be expressed by two complex analytical potentials as;

$$u(z) = u_1 + iu_2 = \left(\frac{1}{\mu}\right) \left[k\phi(z) - z\overline{\phi'(z)} - \overline{\psi(z)} \right] \quad (1)$$

$$\sigma_{11} + \sigma_{22} = 2 \left[\phi'(z) + \overline{\phi'(z)} \right] \quad \text{and} \quad \sigma_{22} - \sigma_{11} + 2i\sigma_{12} = 2 \left[z\overline{\phi''(z)} + \overline{\psi'(z)} \right] \quad (2)$$

If the dislocation is located in the medium A, then, the complex potentials can be written as;

$$\phi_{fente}^A = \frac{1}{1-\beta^2} \left[(1-\beta^2)\gamma^A \ln(z-z_d) + (\alpha+\beta^2)\gamma^A \ln(z-\overline{z_d}) - (1+\alpha)\beta\gamma^A \ln(z-\overline{z_d}) \right] \\ - \frac{1}{1-\beta^2} \left[(\alpha-\beta)(1-\beta)\overline{\gamma^A} \frac{z_d-\overline{z_d}}{z-\overline{z_d}} \right] \quad (3)$$

$$\psi_{fente}^A = \frac{1}{1-\beta^2} \left[(1-\beta^2) \left(\overline{\gamma^A} \ln(z-z_d) - \gamma^A \frac{\overline{z_d}}{z-\overline{z_d}} \right) + (\alpha+\beta^2) \left(\overline{\gamma^A} \ln(z-\overline{z_d}) - \gamma^A \frac{z_d}{z-\overline{z_d}} \right) \right] \\ - \frac{1}{1-\beta^2} \left[(\alpha-\beta)(1-\beta) \left(\overline{\gamma^A} - \gamma^A \right) \frac{z_d-\overline{z_d}}{z-\overline{z_d}} + \overline{\gamma^A} \frac{(z_d-\overline{z_d})\overline{z_d}}{(z-\overline{z_d})^2} \right] \\ + \frac{1}{1-\beta^2} \left[(1+\alpha)\beta \left(\overline{\gamma^A} \ln(z-\overline{z_d}) + \gamma^A \frac{z_d}{z-\overline{z_d}} \right) \right] \quad (4)$$

If the dislocation of edge is located in the medium B, the two complex potentials are obtained by exchanging the superscripts A and B to obtain,

$$\phi^B = \frac{1+\alpha}{1-\beta^2} \left[\gamma^A \ln(z-z_d) + \beta\gamma^A \ln(z-\overline{z_d}) \right] \quad (5)$$

$$\psi^B = \frac{1+\alpha}{1-\beta^2} \left[\left(\overline{\gamma^A} \ln(z-z_d) - \gamma^A \frac{\overline{z_d}}{z-\overline{z_d}} \right) - \beta \left(\overline{\gamma^A} \ln(z-\overline{z_d}) + \gamma^A \frac{z_d}{z-\overline{z_d}} \right) \right] \quad (6)$$

According to Dundurs, the stress field is expressed in term of functions of Airy using two parameters, α and β :

$$\alpha = \frac{\Gamma(k^A+1) - (k^B+1)}{\Gamma(k^A+1) + k^B+1} \quad \text{and} \quad \beta = \frac{\Gamma(k^A-1) - (k^B-1)}{\Gamma(k^A+1) + k^B+1} \quad (7)$$

where $\Gamma = \frac{\mu^A}{\mu^B}$ in which μ^A and μ^B refer to the rigidity of materials A and B, respectively.

3) Complex analytical functions of dislocation:

The presence of dislocation in the vicinity of the main crack is expressed by two complex analytical functions as follows;

$$\phi_{mico}^A = \frac{\mu^A \mu^B b_e}{i \pi (\mu^A + \mu^B k^A)} \ln(z - z_{1d}) \quad (8)$$

$$\psi_{mic}^A = \frac{\mu^A \mu^B \bar{b}_e}{-i \pi (\mu^B + \mu^A k^B)} \ln(z - z_{1d}) - \frac{\mu^A \mu^B b_e z_{1d}}{i \pi (\mu^A + \mu^B k^A) (z - z_{1d})} \quad (9)$$

where b_e is the vector of Burger and Z_{1d} is the dislocation's position. In the presence of a dislocation (see Figure 3), the solution is given using the principle of superposition on the basis of the following potentials functions;

$$\phi_{tot}(z) = \phi_{int}(z) + \phi_{fente}(z) \quad (10)$$

$$\psi_{tot}(z) = \psi_{int}(z) + \psi_{fente}(z) \quad (11)$$

In the case of homogeneous materials, all parameters are equal ($\mu^A = \mu^B$ and $K^A = K^B$). Then, the parameters Δ, ∇, η are all zero i.e. $\alpha = \beta = 0$ and the total potential complex becomes;

$$\phi_{tot} = [\gamma \ln(z - z_d)] + \frac{\mu b_e}{i \pi (1+k)} \ln(z - z_{1d}) \quad (12)$$

$$\psi_{tot} = \left[\left(\bar{\gamma}^A \ln(z - z_d) - \gamma^A \frac{\bar{z}_d}{z - z_d} \right) \right] + \frac{\mu \bar{b}_e}{-i \pi (1+k)} \ln(z - z_{1d}) - \frac{\mu b_e z_{1d}}{i \pi (1+k) (z - z_{1d})} \quad (13)$$

Substitution of Eqn. (12) and (13) into Eqn. (2), the stress field becomes;

$$\begin{cases} \sigma_{11} \\ \sigma_{22} \\ \sigma_{12} \end{cases} = \frac{2\mu r}{\pi(1+k)\rho} \begin{cases} 4 \sin(\theta - \beta) - \sin(\beta + \theta) - \sin(\beta) \cos(\theta - 2\beta) \\ \sin(\beta + \theta) + \sin(\beta) \cos(\theta - 2\beta) \\ \cos(\theta + \beta) + \sin(\beta) \sin(\theta - 2\beta) - 2 \sin(\theta - \beta) \end{cases} \quad (14)$$

where ρ is the distance between the main crack and a neighbouring dislocation, β is the orientation of dislocation with respect to the crack, r is the length of the dislocation and θ is the angle of orientation of r (see Figure. 3).

4) Stress intensity factor:

The stress field is of interest if it is characterized by an important parameter such the stress intensity factor. This latest is essential for the study of the breaking strength of materials since it is considered as being the root of a breaking process. Assuming that the dimensions of

dislocation are small compared to those of the main crack, the mode I SIF can be written as follows;

$$K_1 - i K_2 = \lim_{z \rightarrow 0} \sqrt{2\pi z} (\sigma_{yy} - i \sigma_{xy}) \quad (15)$$

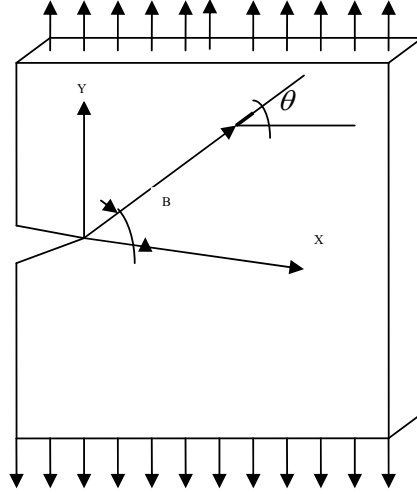


Figure 3 : Schematic representation of a crack interacting with a dislocation.

Substitution of Eqn. (15) into Eqn. (16) and using identity properties, the following expressions for the SIF;

$$K_1 = k_1 = \frac{2\sqrt{2}\mu r}{\sqrt{\pi\rho}(1+k)} \left\{ \sin\left(\frac{3\beta}{2} + \theta\right) + \sin(\beta) \cos\left(\theta - \frac{5\beta}{2}\right) - 2\sin\left(\frac{\beta}{2}\right) \sin(\theta - \beta) \right\} \quad (16)$$

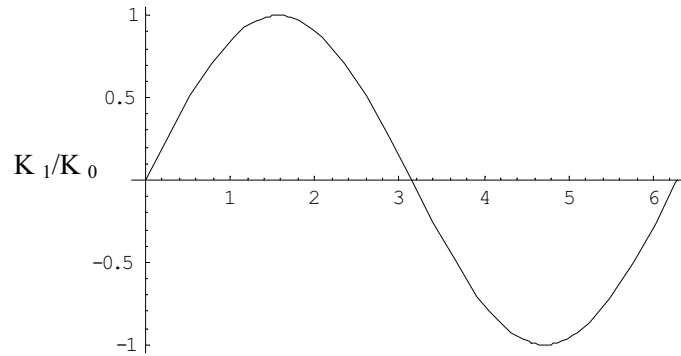


Figure 4: Stress intensity factor for the case ($\theta = 0$).

The mode I SIF in the absence of dislocation can be written as follows;

$$k_1^{ip} = \frac{2\sqrt{2}\mu b}{\sqrt{\pi(1+k)}\sqrt{\rho}} \left\{ \sin(\theta) \cos\left(\frac{3\beta}{2}\right) - \frac{1}{2} \cos\left(\frac{\beta}{2}\right) \sin\left(\theta - \frac{7\beta}{2}\right) - \frac{1}{2} \sin\left(\frac{\beta}{2} - \theta\right) \right\} \quad (17)$$

but in presence of n successive dislocations, the mode SIF is a superposition of all effects as;

$$k_1^\infty = k_1^{ip} + k_1^D = k_1^{ip} + 2 \times \left\{ \frac{3\mu b}{4\sqrt{\pi}(1-\nu)} \sum_{i=1}^n \frac{1}{\sqrt{\rho_i}} \right\} \quad (18)$$

where $k_1^{ip} = K_1$ is the SIF at the main crack tip.

Substitution of Eqn. (17) into Eqn. (18), the global SIF becomes;

$$k_1^1 = \frac{2\sqrt{2}\mu b}{\sqrt{\pi(1+k)}\sqrt{\rho}} \left\{ \sin(\theta) \cos\left(\frac{3\beta}{2}\right) - \frac{1}{2} \cos\left(\frac{\beta}{2}\right) \sin\left(\theta - \frac{7\beta}{2}\right) - \frac{1}{2} \sin\left(\frac{\beta}{2} - \theta\right) + \frac{3}{\sqrt{2}} \right\} \quad (19)$$

5) Conclusion:

If the slip plane of the edge dislocation passes through the tip of a semi-infinite interfacial crack, the slip part of the image force is independent of the angular position of the dislocation and is inversely proportional to the distance from the crack tip. The stress intensity factors change continuously when the edge dislocation moves from one medium through the interface to the other medium. For a finite interfacial crack, an edge dislocation emitted from one of the crack tips usually shields that crack tip but antishields the other tip. On the other hand, an edge dislocation originated elsewhere and moves to the vicinity of a finite interfacial crack will shield or antishield both crack tips.

References:

- [1] N. Muskhelishvili, Some basic problems of mathematical theory of elasticity, Noordhoff, Holland, (1953).
- [2] Tong-Yi Zhang and J. C. M. Li., Interaction of an edge dislocation with an interfacial crack, Materials Science Engineering A, 35 (1992).
- [3] J. Dundurs, in Mathematical Theory of Dislocations, edited by T. Mura, ASME New York (1969).
- [4] Naman Recho, Rupture par fissuration des structures, éditions Hermès (1995).
- [5] G. C. Sih, Handbook of stress intensity factors for researchers and engineers, Institute of Fracture and Solid Mechanics, Lehigh Univ., Bethlehem, Pa., USA (1973).

Damage Evolution in Foams

Katerina E. Aifantis^{1,2}, Avraam A. Konstantinidis², Michael Zaiser³

¹Lab of Mechanics and Materials (Box 468), Aristotle University of Thessaloniki, GR54124, Greece (kaifanti@seas.harvard.edu, akonsta@mom.gen.auth.gr)

²School of Engineering and Applied Sciences, Harvard University, MA 02138, USA

³Centre for Materials Science and Engineering, The University of Edinburgh, Edinburgh EH93JL, UK (M.Zaiser@ed.ac.uk)

ABSTRACT

Due to their unique properties metallic foams are promising material components for various industrial applications, such as in the automotive industry, as well as in power sources (Ni battery electrodes). Experimental evidence has documented that during compression of metal foams, deformation is governed by the development of horizontal localization bands; cell failure (brittle fracture or plastic buckling) occurs within the bands leading to the collapse of the material. In the present study cellular automaton numerical simulations are performed to model the damage evolution during compression and to predict the stress-strain response. The simulation predicted stress-strain curve is found to be in very good agreement with experimental stress-strain data obtained for Al foams.

1. Introduction

Some of the unique properties of metal foams are good stiffness and strength to weight ratios, high impact energy absorption (relevant for applications in the automotive industry), good sound damping, electromagnetic wave absorption, thermal insulation and non combustibility [1].

From a mechanical point of view one of the main processes of interest is the formation and evolution of damage during deformation. The present study will focus on compressive loadings. Experimental evidence has documented that damage evolution under compressive stresses is governed by the formation of multiple localization bands, which lead to localized collapse of the material [2]. Over the past decade various modeling approaches such as gradient plasticity [3] and the micromorphic continuum [2] have been used for analytical and numerical modeling in order to capture the stress-strain response and localization band thickness in foams. Here the 1D method presented in [4] is extended in two dimensions and implemented using cellular automaton simulations, which give the stress-strain response under compressive loads. It should be noted that this method allows for randomness in strength to be taken into account, which is a generic feature associated with the irregular microstructure of metal foams (as opposed to regular honeycombs).

2. Theoretical Formulation

Experiments [1,2,5] have shown that foams as porous materials undergo three stages during compression: initially the beams or cell walls bend elastically, then plasticity takes place through the formation of strain localization bands, and eventually the material collapses due to fracture or plastic buckling that occurs within the bands. To capture this behaviour in a phenomenological manner, the stress-strain response is defined as

$$\sigma = \begin{cases} M\varepsilon & \text{for } \varepsilon < \varepsilon_c = \sigma_c/M \\ M\varepsilon_c \left[e^{\frac{\varepsilon_{\text{comp}}(\varepsilon - \varepsilon_c)}{\varepsilon_{\text{comp}} - \varepsilon}} - \varepsilon_0(\varepsilon - \varepsilon_c) \right] & \text{for } \varepsilon > \varepsilon_c \end{cases}, \quad (1)$$

where M is the elastic modulus, σ_c the crushing threshold, and ε_0 the parameter determining the extension of the softening regime given as

$$\varepsilon_0 = \frac{1}{\varepsilon_{\text{crush}}} \left[e^{\frac{\varepsilon_{\text{comp}}\varepsilon_{\text{crush}}}{\varepsilon_{\text{comp}} - \varepsilon_{\text{crush}} - \varepsilon_c}} - 1 \right]. \quad (2)$$

These parameters are defined in Figure 1.

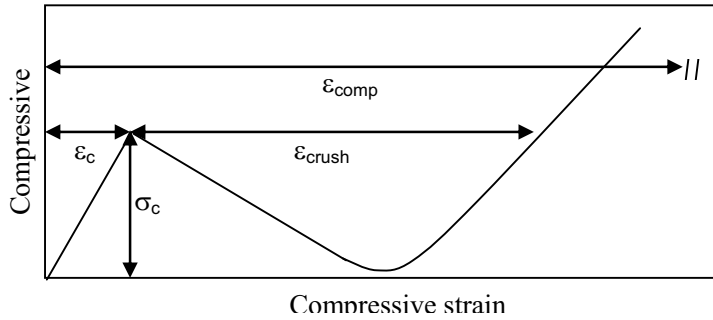


Figure 1: Qualitative representation of stress-strain response.

As individual cells collapse, their neighbours are affected. We describe this local interaction in terms of an interaction stress between adjacent cells i and j , as

$$\sigma_{ij} = D_{ij}(\varepsilon_i - \varepsilon_j), \quad (3)$$

where $D_{ij} = \beta_{ij}(\sigma_c/\varepsilon_{\text{crush}})$ and β_{ij} is the non-dimensional coupling constants depending on the orientation with respect to the compression direction.

The quasi-static stress balance, which is the equilibrium equation for our system is written as [4]

$$\sigma_{\text{ext}} - \sigma(\varepsilon_i) - \sum_j D_{ij}(\varepsilon_i - \varepsilon_j) = 0. \quad (4)$$

Coarse graining now the above equation, over a large volume that is comparable to the cell size d , and following the same procedure as in [4], for the two-dimensional case the strain-gradient type equilibrium condition has the form:

$$\sigma_{\text{ext}} - \sigma(\varepsilon(\mathbf{r})) + \nabla[D\nabla\varepsilon(\mathbf{r})] = 0; \quad D = d^2 \frac{\sigma_c}{\varepsilon_c} \begin{bmatrix} \beta_p & 0 \\ 0 & \beta_n \end{bmatrix}, \quad (5)$$

where β_p, β_n are coupling constants at the parallel and normal to loading direction, respectively.

3. Simulation results

Numerical simulations of the constitutive Eqn. (4) have been performed using a cellular automaton. The local heterogeneities in the properties of real cellular materials are taken into account in the simulations by assigning random variations of the crushing thresholds to the cells, i.e. the thresholds σ_c are considered independent random variables obeying a Weibull distribution with scale and shape parameters m and h respectively, leading to specific values for the mean $\langle \sigma_c \rangle$ and variance $\delta\sigma_c$. The system is loaded by increasing the external stress σ_{ext} from zero in small steps $\Delta\sigma_{\text{ext}}$. In each of the cells where the local (external plus internal) stress exceeds the local crushing threshold, the local strain is increased by a small constant amount $\delta\varepsilon$. Then, new internal stresses are computed for all sites and it is checked again whether the sum of the external and internal stresses exceeds the local crushing threshold. The local strain at the now “damaged” sites is again increased, etc. This is repeated until the system has reached a new stable configuration. Figure 2 shows an instance of the damage evolution in the foam predicted by the cellular automaton simulations.

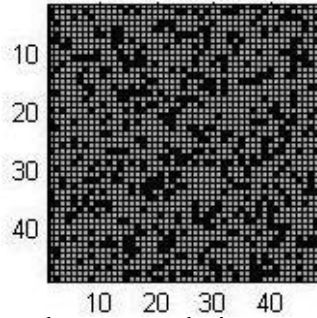


Figure 2: Simulation results during damage evolution at $\varepsilon = 0.5$; green denotes “damaged” cells.

In Figure 3 plots of the effective stress vs. effective strain computed this way, in the case of a relatively high-disordered (Fig. 3a) and a low-disordered (Fig. 3b) material are shown. In the former case the values of the various parameters used are: $\beta_p = 0.1$, $\beta_n = 0.1$, $\varepsilon_{\text{crush}} = 0.65$, $\varepsilon_{\text{comp}} = 1$, $\varepsilon_c = 0.001$, $M = 70$ GPa, while $\langle \sigma_c \rangle = 0.13$ MPa and $\delta\sigma_c = 0.002$ MPa, while in the latter all parameters are the same except $\delta\sigma_c = 3 \cdot 10^{-6}$ MPa. Experimental data from compression of aluminum foams [5] are also included, showing good agreement between the simulation predictions and real measurements.

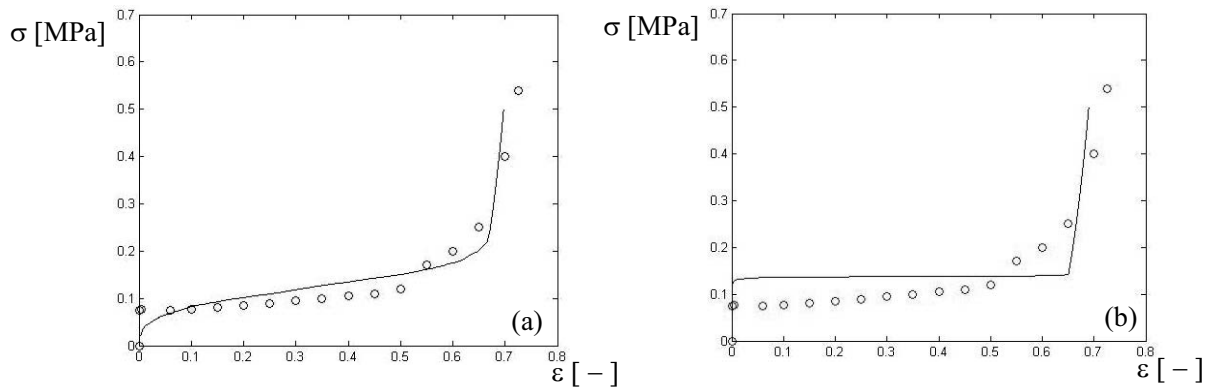


Figure 3: Effective stress-strain response; circles: experimental data [5], line: numerical prediction. (a) Relatively high-disordered foam; (b) Low-disordered foam.

3. Discussion

It is important to note that by including strong disorder into the formulation described in the previous sections, one can describe a global stress strain graph that is monotonically ascending (see Fig. 3) in accordance with experimental measurements, in spite of a local stress strain relationship that has softening (see Fig. 1); one would expect a deterministic law for the same parameters to produce a horizontal strain jump at constant stress (and at a much higher stress level). It is also noted that the above formulation is an initial attempt to describe the compression behavior of metallic foams. This formulation can further be enhanced, e.g. by modifying the assumption for the local stress-strain response given by Eqn. (1). A complete comparison between the simulation results of the method presented in this paper with the results of finite element implementation, as well as further comparison with available experimental data is under preparation [6].

Acknowledgement

The European Research Council is grateful acknowledged for its support through the ERC-Starting Grant No. 211166.

References

- [1] L.J. Gibson and M.F. Ashby, “Cellular Solids”, Cambridge University Press (1998).
- [2] S. Forest, J.S. Blazy, Y. Chastel and F. Moussy, “Continuum modelling of strain localization phenomena in metallic foams”, *Journal of Materials Science*, **40**, 5903 (2005).
- [3] E.C. Aifantis, “On the microstructural origin of certain inelastic models”, *Trans. ASME, J. Engineering Materials and Technology*, **106**, 326 (1984).
- [4] M. Zaiser and E.C. Aifantis, “Modeling the crushing of a cellular material”, in: *Proc. 6th Nat. Cong. of Mechanics*, Eds. E.C. Aifantis and A.N. Kounadis, vol. 3, p.102, Giahoudi-Giapouli Publ., Thessaloniki (2001).
- [5] A.H. Brothers and D.C. Dunand, “Mechanical properties of a density-graded replicated aluminum foam”, *Materials Science and Engineering A*, **489**, 439 (2008).
- [6] K.E Aifantis, A.A. Konstantinidis and S. Forest, “Modelling strain localization bands in metallic foams”, *Journal of Computational and Theoretical Nanoscience*, to appear (2008).

Adaptive Embedding of the Electronic-Density-Functional-Theory in the Classical Molecular Dynamics: Application to Nano-Indentation

Shuji Ogata,^{1,2} Yuya Abe,^{1,2} and Ryo Kobayashi^{1,2}

¹**Department of Scientific and Engineering Simulation, Graduate School of Engineering, Nagoya Institute of Technology, Gokiso-cho, Showa-ku, Nagoya, Aichi 466-8555, Japan; (ogata@nitech.ac.jp)**

²**CREST, Japan Science and Technology Agency, 4-1-8 Honcho, Kawaguchi, Saitama 332-0012, Japan**

ABSTRACT

We have been developing a hybrid simulation scheme by concurrently combining the electronic-density-functional-theory (DFT) and the atomistic molecular dynamics (MD) method. In the hybridization scheme, multiple DFT regions, each of which is composed of a relatively small number of atoms, are embedded in a system of classical MD atoms. For robust coupling of the DFT and MD regions with reasonable mechanical accuracy, the buffered cluster method [1] has been proposed, which requires no link-atoms and is applicable to a wide range of materials (Si, C, alumina, Al, etc.) and settings. In this paper, we add a new feature to the hybrid DFT-MD simulation scheme: the sizes of the DFT regions can change adaptively using instantaneous inter-atomic distances and three-body angles to trace the chemical reactions with reduced computation cost as compared to the full DFT calculation.

Both indentation- and friction-induced local oxidation of a Si surface in water environment have been reported [2,3]. Understanding such atomic-scale chemical processes in realistic setting is a key to advance MEMS-related technologies such as the high fabrication precision, high resistance to wear, and low friction. Motivated by these, in this paper, we apply the hybrid DFT-MD simulation scheme to nano-indentation and friction of H-terminated diamond-tip to H-terminated Si(100) surface with a water molecule in-between. We thereby find that the water molecule either decomposes to oxidize the Si surface or escapes from the contact region depending on the combination of simulation settings (the sharpness of the tip, the direction and position of the tip with respect to the Si surface, etc.).

- [1] S. Ogata, “Buffered-Cluster Method for Hybridization of Density-Functional Theory and Classical Molecular Dynamics: Application to Stress-Dependent Reaction of H₂O on Nanostructured Si”, *Physical Review B*, **72** 45348 (2005).
- [2] I. Zarudi, L.C. Zhang, and M.V. Swain, “Effect of Water on the Mechanical Response of Mono-Crystalline Silicon to Repeated Micro-Indentation”, *Key Engineering Materials*, **233-236**, 609 (2003).
- [3] L. Zhang and I. Zarudi, “An Understanding of the Chemical Effect on the Nano-Wear Deformation in Mono-crystalline Silicon Components”, *Wear*, **225-229**, 669 (2003).

Python Based Combined Continuum-atomic Modeling for Single Crystal Nickel

Ismail Tirtom, Tetsuo Shoji

Fracture and Reliability Research Institute, Graduate School of Engineering, Tohoku University

COE Experiment Bldg., 6-6-1, Aoba, Aramaki, Aoba-ku, 980-8579, Sendai, Japan

Tel: +81-22-795-7520, Fax: +81-22-795-7543, E-mail: itirtom@rift.mech.tohoku.ac.jp

ABSTRACT

A flexible, extendable and easy to use FEM/MD combination code has been developed. The flexibility and modularity is achieved by using Python language. Python has gained considerable involvement in scientific computing because of its complementary characteristics. The Fortran subroutines of MD and FEM methods are the main calculators. Although Fortran still has the majority in scientific computing because of its construction purpose as pure numerical calculations, it takes numbers and gives results as again numbers, preparation of input data for complex situations and handling huge numbers of results is quite inconvenient processes in Fortran. Therefore, recently developed scripting languages may help to close these inconveniencies. The combination of MD and FEM methods using a handshake region method, implemented by Python, has been produced. The main calculations carried on with Fortran subroutines however management of the subroutines and some parts of pre-post processing stages governed by Python. The purposes of this study are to reduce the modeling/analyzing time for the focusing on problem more than the computing details and initiate an extendable computation frame via its modular structure.

1. Introduction

Several computational models, which link different length and time scales, are developed to predict the behaviour of materials. Favourable progresses have been made especially in combining of atomic and continuum methods. However, significant challenges in theory and numerical algorithm developments are still remaining to be overcome. On the other hand, it is easily seen that, whatever the combination technique, one of the main limitation for multiscale modeling is preparation of the model, handling the huge amount of data and visualize the results for analyzing. Therefore, in this study, Python which offers strong support for integration with other languages and tools and comes with extensive standard libraries, has been selected as development platform for combine different methods and support them by its versatile properties at the pre-post processing stages. Python applications are increasing in scientific computing for various fields, such as computational materials, chemistry and biology. Python is an object-

oriented, flexible and extensible scientific programming platform that offered various computational tools for data generation, management, analysis and visualization.

A combined continuum-atomic method implemented by python language is applied to the fracture problem of single crystal Nickel metal. Linear elastic FEM and molecular mechanics with Morse potential Fortran routines are interconnected with each other using the Python scripting language. At the processing stage, loadings and constraints are governed by FEM and discrete fracture process is governed by atomic simulation. Continuum and atomic combination is made by force equilibrium of coincided atoms and nodes in the model geometry. Progress of the simulation process can be investigated during iterations by graphical result window developed with matplotlib, python plot library. Because of modular structure, developed python framework can easily be expanded by adding new functions of material modeling methods and different materials.

2. Combination Method & Model

Because of the interatomic distances are Angstroms unit in length, the size of a discrete atomic model is very small. However, a continuum domain can be simulated in any size if the used parameters are selected in appropriate units. Even it is possible to model in very small scales, continuum models cannot handle the discrete nature processes of material behaviors such as fracture. Therefore, advantages of discrete nature of atomic modeling and computational benefits of continuum modeling can be used together by combination of them.

For simplicity, it is considered in this study 2D coupling between the two models (Figure 1). A crack inserted molecular dynamics region of FCC Ni crystal surrounded by 200×200 Å square continuum region which divided into finite element mesh has been modeled. All the calculations governed by a main program written in python. The main calculation tasks are carried out by Fortran subroutines. The connection of the main program and these subroutines are made by using F2PY, Fortran to Python interface generator tool that converts Fortran source code into python binary modules [1].

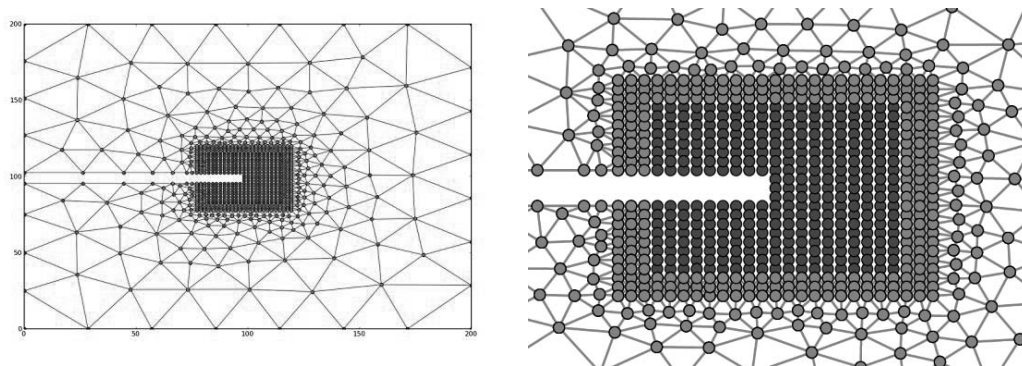


Figure 1. An example model of the FEM/MD coupling module. A crack inserted molecular dynamics region of FCC Ni crystal surrounded by continuum region which divided into finite element mesh.

2.1 Finite Element Region

There are different approximation techniques to analyze continuous systems. One of the mostly common techniques is the finite element method. The FEM is a technique for solving partial differential equations by discretising these equations in their space dimensions. The discretisation is carried out locally over small regions of simple but arbitrary shape, the finite elements [2].

The linear static finite element procedure has been used with triangle elements. During the fem solution, the assembly of the global stiffness matrix which requires huge amount of storage and limit the element numbers of the system is avoided and instead a better solution procedure, a “mesh-free” approach by the preconditioned conjugate gradient (pcg) technique has been used. FEM implementation carried out by using the subroutines explained in reference 2. The single crystal Nickel material properties have been applied to consistency of two methods [3].

2.2 Molecular Dynamics Region

MD calculation carried out by using Morse interatomic potential. Morse function is one of the oldest potential energies for metals. The parameters has been used in the model can be seen in the next table. A notification is necessary due to the 2D nature of the model. It has been adopted the similar approach of quasi-continuum method here [4]. In this example, the MD cell dimension along the out-of-plane direction, $dz = 3.52 \text{ \AA}$, is the same for the lattice constant of Ni crystal. Periodic boundary condition has been applied along the out-of-plane direction in this MD region. Therefore, it will correctly treat atoms with different values of dz .

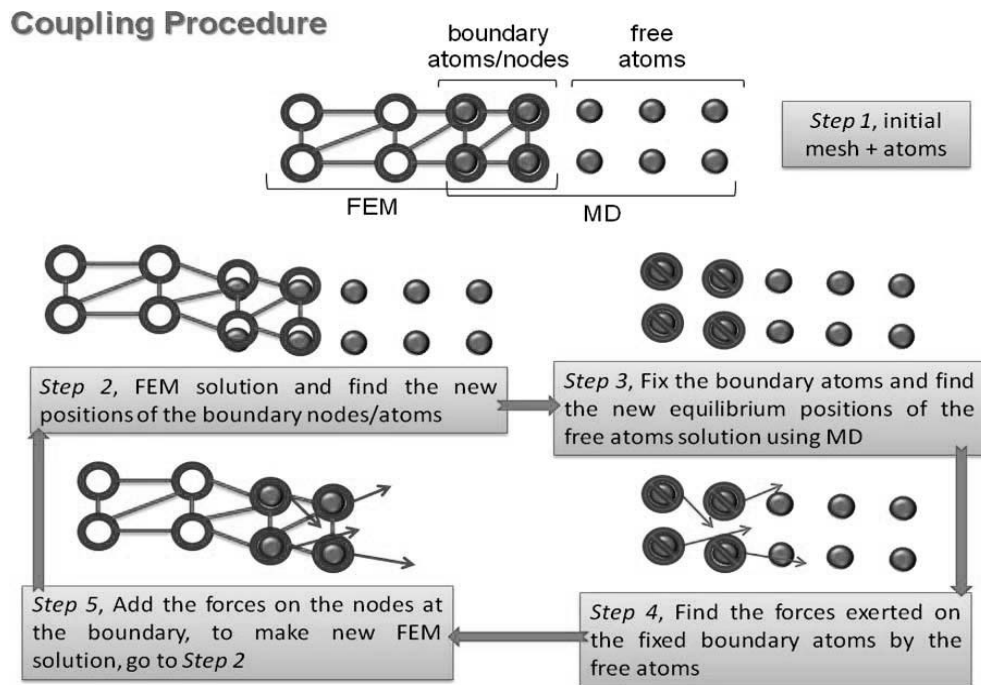


Figure 2. Details of the coupling procedure of FEM and MD

2.3 Handshake Region

The interface region in Figure 1 has both discrete atoms and finite elements overlapped each other as the atom and node coordinates exactly coincide. The points in the interface region are called boundary atoms/nodes. The coupling procedure of atomic and continuum which is introduced by Kwon [5] has been implemented in this handshake region. The details of the procedure can be seen in the Figure 2.

4. Results & Discussion

The crack opening was modeled in atomic resolution by displacement of atoms which covered by the finite element region where the loading and boundary conditions applied on it. The nodes at the right side of the fem model were fully fixed to move. The tensile load is applied in the vertical direction at the top and bottom boundary. The equilibrium positions of atoms are shown in the following figure during the incremental loading. Using the plotting libraries of python, the result of each step can be observed during the simulation. It can easily seen that the difference of the combined model from the only MD model. Combined model gives more realistic results because flexible boundary conditions provided by FEM. The ability of integration of other languages and object-oriented property of python make it possible to enhance this model with tight binding molecular dynamics that the chemical bonding/debonding of crack tip atoms can be simulate by it.

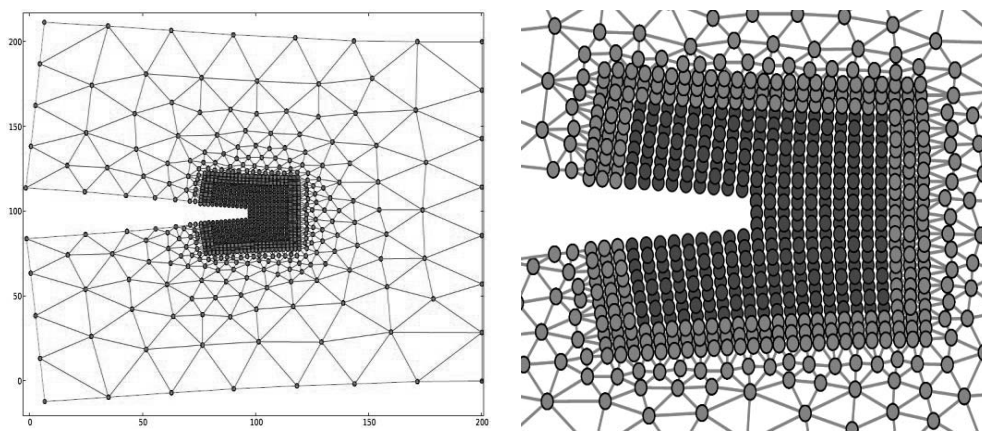


Figure 3. Simulation result of the model under the loading.

References

- [1] <http://www.scipy.org/F2py>
- [2] I.M. Smith and D.V. Griffiths, "Programming the Finite Element Method", Wiley Ltd., 2006
- [3] Z.C. Lin, J.C. Huang, Y.R. Jeng, "3D nano-scale cutting model for nickel material", J. of Mater. Proc. Tech., 192-193, 27-36 (2007).
- [4] R. E. Miller, E. B. Tadmor, "QC Tutorial Guide, ver. 1.3", www.qcmethod.com, May 2007
- [5] Y.W. Kwon, "Multi-scale modeling of mechanical behavior of polycrystalline materials", J. of Comp.-aided Mater. Design, 11:43-57 (2004).

Investigating the Time Dependency of the Viscoelastic Bulk Modulus using Gnomix PVT Apparatus

Manoj K Saraswat

**Technical University of Delft, The Netherlands
m.k.saraswat@3me.tudelft.nl**

ABSTRACT

Accurate reliability calculations require a complete characterization of the bulk modulus. Bulk modulus specifically assumes importance in the case of constrained geometries (for example lead frame and die), where the deformation cannot be assumed to be one-dimensional, in which case shear modulus is more important than bulk modulus. Most polymers exhibit much more compliant shear response compared to the bulk response. The shear response of most polymeric systems is independent of the hydrostatic loading which makes it simpler to measure the shear response of the materials besides the fact that long time scales and very small order of output signals associated with the time based bulk modulus measurements, makes it very difficult to investigate time dependency of viscoelastic bulk modulus. Moreover most effort to study the bulk response of the material has been limited to temperature range close to glass transition as otherwise the rapid volume changes are difficult to record.

In this paper, effect of time on viscoelastic bulk modulus of the Low Profile Additive (LPA) based Polyesters was investigated using PVT (Pressure Volume Temperature) apparatus. Viscoelastic Bulk creep measurements were made by pressure step experiments at different temperatures. Besides variation in temperature levels, magnitude of pressure steps applied was varied to observe the resulting influence on viscoelastic creep modulus. A significant effort was made to illustrate that the apparent time dependency of the bulk modulus as reported by several authors using pressure loading creep measurements is not correct owing to major calibration issue when conducting time based measurements. It was observed that the bulk modulus shows negligible time dependence. Bulk modulus is therefore not a viscoelastic parameter whereas the temperature and pressure dependence of the bulk modulus is appreciable. Finally a material model is developed for time, temperature and pressure dependency of the Bulk Modulus. Moreover a very detailed methodology for conducting creep measurements for investigating the time dependency using a PVT dilatometer is presented. The calibration issues associated with the PVT apparatus, leading to erroneous results implying an apparent time dependency of the bulk modulus as reported by other authors, are resolved.

Size Effect of Finite Deformable Nanopillar by Focused-ion-beam Chemical Vapor Deposition

Hiro Tanaka¹ and Yoji Shibutani^{1,2}

¹Department of Mechanical Engineering, Osaka University, Osaka 565-0871, Japan,
tanaka@comec.mech.eng.osaka-u.ac.jp

²Center for Atomic and Molecular Technologies, Osaka University, Osaka 565-0871, Japan,
sibutani@mech.eng.osaka-u.ac.jp

ABSTRACT

Nanopillars (called pillar) with nanosized diameter and microsized length can be constructed by chemical vapor deposition using a focused-ion-beam. For the pillar consisting of an outer amorphous carbon (*a*-C) ring and an inner gallium (Ga) core, we performed the bending test under the lateral load driven by the other pillar jointed together in the scanning electron microscope (SEM). The obtained load-deflection curves suggest that the deposited pillar has the size dependence to the mechanical response. The pillar with the diameter over 190 nm shows a wide low-hardening region after a linear response and then becomes extremely hardened at the finite displacement. Thus, the pillar intrinsically possesses much more flexible deformability for bending than expected, in contrast to tensile deformation. This size effect may be caused by the atomistically bonding anisotropy of bond-stretching, bond-bending, and bond-dihedral angular bending observed in covalent *a*-C.

1. Introduction

Focused-ion-beam (FIB) induced chemical vapor deposition (FIB-CVD) has distinctive advantages, such as much higher deposition rate, in the fabrication of complicated structures. Some delicate microstructures have been actually designed with this micro-beam technology [1]. They are composed of the deposited beam members made from amorphous carbon (*a*-C) and thus the overall structural characteristics are, in principle, determined by the mechanical behavior of the member. The mechanical response of the whole *a*-C pillar is closely related to the fundamental physical properties as density and Young's modulus, and it has already been investigated by the dynamic resonance vibration and the quasi-static small bending with the piezoactuator [2-4]. It has also been reported that the *a*-C pillars have the cross section with a Ga core in nanosized diameter [5]. We here propose the simple deflection test with a rigid connection of two identical pillars using a focused electron beam (EB) in scanning electron microscope (SEM), and develop the evaluation technique for not the infinitesimal deformation but the large deflection of *a*-C pillars, which intrinsically equip the remarkable large deformability [6].

2. Experimental Techniques

2.1 Fabrication of microstructure with a pair of *a*-C pillars

The pillar was grown by a commercial FIB-CVD system (SMI9200, Seiko Instruments, Inc.) with the Ga^+ ion beam. In the course of the fabrication, phenanthrene vapor ($\text{C}_{14}\text{H}_{10}$) was used as the supplied precursor gas. In this study, micro-framed structures for a bending experiment were assembled by connecting these two pillars with equal diameters and longitudinal lengths, as shown in Fig. 1. We call it double cantilever model (DC-model). The *a*-C pillars were joined at the intersection of two pillars by the irradiation using a focused EB in SEM (JEOL JSM5310, background pressure: $\sim 10^{-4}$ Pa). The silicon nitride (SiN) cantilever coated with Au (BL-RC150VB, Olympus Corporation, Inc.) is used in all bending tests, the spring constant of which is $k = 0.006$ N/m. The specification longitudinal length (L), width (b) and thickness (t) of the commercially manufactured cantilever are $100 (\pm 10)$ μm , $30 (\pm 2)$ μm and $0.18 (\pm 0.04)$ μm , respectively. The flexural and tensile rigidities are herein assumed $E_2 I_2 = kL^3/3 = 2.0 \times 10^{-15}$ Nm^2 and $E_2 A_2 = 1.15$ N using Young's moduli of SiN and Au (234 GPa and 78 GPa).

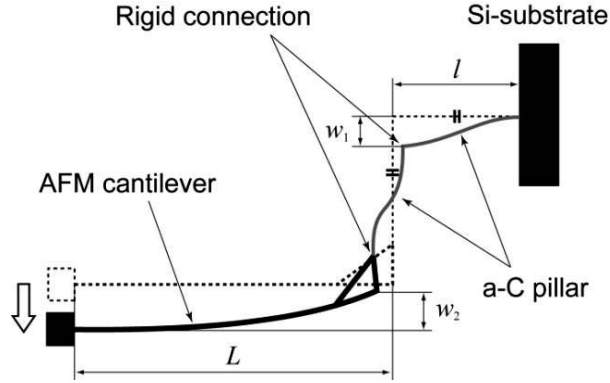


Figure 1. A schematic illustration of deformed shape of DC-model.

2.2 Large deflection test

We demonstrate large deflection tests by applying load to the above DC-model which encompasses the AFM cantilever specified to provide the measurable deflection. This structure seems to be framed rigidly because the connection is exposed to the EB for sufficiently long time. The large deflection tests were carried out to displace the AFM cantilever in a vertical direction. The displacement w_1 of the horizontal pillar and displacement w_2 of the cantilever were then measured by in-situ observation using SEM. Figures 2 show SEM images of the testing including the initial configuration in Fig. 2(a). The microstructure was deformed largely beyond a small bending by manipulating the cantilever as shown in Fig. 2(b). Subsequently, it has achieved the tension-dominated shape, in which two members have been linearly oriented (see Fig. 2(c)). It is noted that the joint connected by two pillars keeps a right angle through the deformation process even under large deflection.

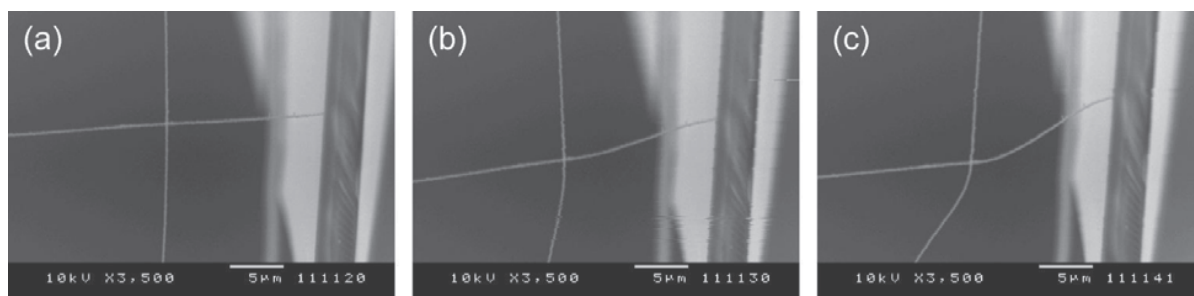


Figure 2. SEM images show the sequence of deformed configurations for a pillar with a diameter 210 nm. Figures (a)–(c) are the magnified views of a joint and the deflection w_1 of the horizontal a -C pillar can be measured.

3. Results and Discussion

Figures 3 show three large deflection curves among four types of pillars ($d = 160, 190, 210$ and 280 nm and $l = 15 \mu\text{m}$), which are plotted as the relationship between the normalized deflection of w_1/l and the normalized one of w_2/L . The experiments were conducted by two ways of bending to evaluate the elasticity of a -C pillars, one of which is only loading (open symbols) and the other is loading and then unloading (solid symbols). In the case of 160 nm of Fig. 3(a), the curve first increases linearly and then shows the hardening, which may usually be understood due to the nonlinear large deflection term in the structural mechanics. The large deflection curves indicate the weakening of stiffness in the medium deformation region after linear response, which is remarkably observed for the diameter over 190 nm (see Figs. 3(b) and (c)). Thus, the pillar has the size dependence that the bending rigidity tends to decrease after linear response as increasing the diameter. We have already suggested that the loss of rigidity is caused by change of deformation mode of the a -C in ref. [6] where the pillar with diameter of 234 nm was employed. That is, the weakest torsional rotation and bending of the covalent molecular system may be prior operative after the revertible linear response. The present results give a new fact of the size dependence to the loss of rigidity. Meanwhile, the increasing diameter introduces decrease of density of the whole pillar [6]. Thus, this size dependence is linked to the amorphous covalent molecule system of carbon and also the density.

4. Conclusions

We have proposed the experimental technique called double cantilever model to measure large deflection of the pillar manufactured by FIB-CVD. Two identical pillars with the same diameter and the same length are rigidly jointed at the interconnected point by the focused electron beam. Results from the proposed testing verified the size dependence of the deposited pillar to the mechanical response. The pillar with diameter over 190 nm exhibits loss of stiffness in the medium deformation region after linear response. Some considerable factors of the stiffness weakening are the properly atomistic deformation manner with covalent interaction based on sp^2 - sp^3 bonding and also the density of the pillar.

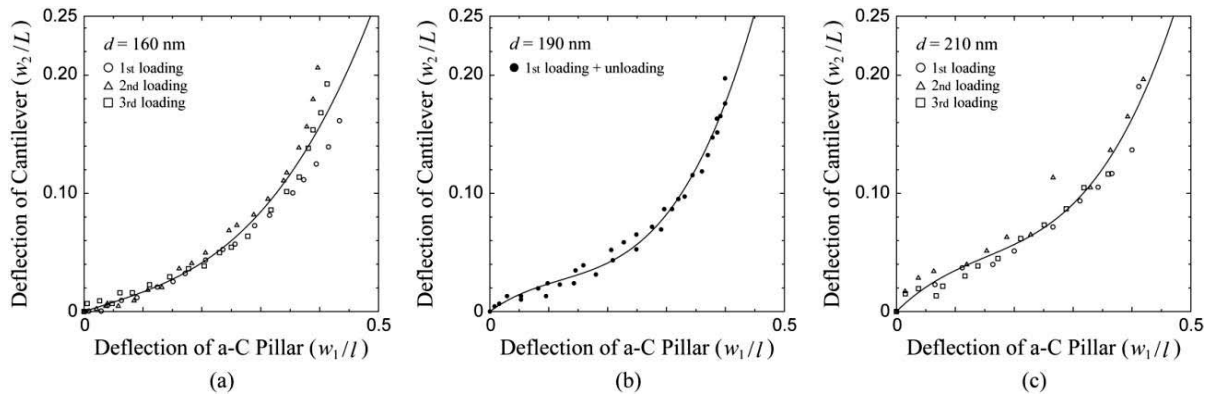


Figure 3. Relationship between normalized deflections of the cantilever and one of the pillar for some diameters (160, 190 and 210 nm). The open symbol represents an experimental value for only loading and the solid one represents the value of a loading and unloading test. The solid curve here is the cubic polynomial through the origin, fitted by all experimental data.

Acknowledgements

The author (YS) gratefully acknowledges support from the Grants-in-Aid from Japan Society for the Promotion of Science (Exploratory Research, 20656020).

References

- [1] S. Matsui, “Focused-ion-beam Deposition for 3-D Nanostructure Fabrication”, *Nuclear Instruments and Methods in Physics Resercher B*, **257**, 758 (2007).
- [2] J. Fujita et al., “Observation and Characteristics of Mechanical Vibration in Three-dimensional Nanostructures and Pillars Grown by Focused-ion-beam Chemical Vapor Deposition”, *Journal of Vacuum Science & Technology B*, **19**, 2834 (2001).
- [3] M. Ishida et al., “Density Estimation for Amorphous Carbon Nanopillars Grown by Focused-ion-beam Assisted Chemical Vapor Deposition”, *Journal of Vacuum Science & Technology B*, **20**, 2784 (2002).
- [4] J. Fujita et al., “Growth of Three-dimensional Nano-structures using FIB-CVD and its Mechanical Properties”, *Nuclear Instruments and Methods in Physics Resercher B*, **206**, 472 (2003).
- [5] T. Morita et al., “Free-space-wiring Fabrication in Nano-space by Focused-ion-beam Chemical Vapor Deposition”, *Journal of Vacuum Science & Technology B*, **21**, 2737 (2003).
- [6] Y. Shibututani and T. Yoshioka, “Inelastic Deformability of Nanopillar by Focused-ion-beam Chemical Vapor Deposition”, *Journal of Vacuum Science & Technology B*, **26**, 201 (2008).

Reaction Pathway Analysis of Dislocation-Interface Interactions in Cu-Ni Multilayered Systems

S. Hara, T. Take, S. Izumi and S. Sakai

Department of Mechanical Engineering, The University of Tokyo, 7-3-1 Hongo,
Bunkyo-ku, Tokyo, 113-8656 JAPAN
(E-mail: hara.shotaro@fml.t.u-tokyo.ac.jp)

ABSTRACT

Strength of the nanoscale multilayered composites is strongly controlled by the interface mediated slip transfer reaction. In this paper, by using the nudged elastic band (NEB) method, we investigate the 3D reaction pathway where the screw dislocation inserted in the Cu layer penetrates into the Ni layer across the (001) interface. The quantitative values of the activation parameters (the activation energy and activation volume) that involve the transmission for the leading partial dislocation are determined using atomistic approach. When the activation energy is 0.68 eV, the corresponding activation volume is about $150b^3$. The dependence of the activation parameters on the film thickness is also considered. Due to the Koehler force effect, the activation energy decreases as the film thickness decreases.

1. Introduction

Epitaxial interfaces act as the source of the slip resistance. In particular, recent experiments suggested that the strength of Cu/Ni nanolayered composites is strongly related to the stress that a single dislocation needs to transmit the interface [1]. Much effort has been devoted to understand the details of the slip transfer events, revealing that the interface barrier for slip is attributed to the several factors, such as elastic modulus mismatch, lattice mismatch and core structure changes at the interface [2,3].

Although a molecular dynamics (MD) is an effective tool to probe an atomic scale event, to predict the lower-bound threshold stress required for the slip transfer reaction is a crucial task. Since a slip transfer event may be the stress-mediated thermally activated process, a MD generally suffers from the limitation to directly access the event which takes place at the time scale of seconds or hours.

Recently, Zhu et.al [4] demonstrated that a reaction pathway analysis is critical for the quantification of thermally activated processes and the atomistically calculated activation parameters for the slip transfer in the nano-twined Cu can be directly connected with the experimental measurements. In this study, we apply the reaction pathway analysis to the slip transfer event at the Cu/Ni coherent interface and evaluate the activation energy for this event.

2. Molecular Dynamics Modeling

Fig. 1 shows the atomic configuration of dislocation-interface interaction model. Only defect atoms are visualized by computing the central symmetry parameter. A fcc Ni crystal is placed above a fcc Cu crystal. The x , y and z axes of the simulation cells are $[110]$, $[\bar{1}10]$ and $[001]$ direction for the Cu and Ni lattice. The system contains 480000 atoms and the cell sizes are $30.3 \text{ nm} \times 12.6 \text{ nm} \times 14.3 \text{ nm}$. A Ni film thickness h is 7.1 nm . Due to the 2.7% lattice misfit between Cu and Ni, both lattices are pre-strained to create a coherent interface. The coherency stresses acting in the Cu and Ni lattice are -2.2 GPa and 2.2 GPa , respectively. Then, a screw dislocation with the burgers vector $\mathbf{b} = a/2[110]$ is introduced in the Cu crystal by displacing the atoms according to the elastic dislocation displacement fields. Periodic boundary conditions are applied along the dislocation line, while the atoms within the outermost four layers from the y and z faces are fixed. The structural relaxation using the generalized EAM potentials [5] leads to the dissociation of the screw dislocation \mathbf{b} into two Shockley partial dislocations of $\mathbf{b}_1 = a/6[121]$ (leading partial) and $\mathbf{b}_2 = a/6[211]$ (trailing partial), as shown in Fig.1.

Toward the reaction pathway analysis, we determine the athermal stress τ_{ath} , which is a critical value when a dislocation spontaneously transmits across the interface without thermal fluctuation. Our MD computations show that the 2D leading and trailing partial dislocations completely overcome the Cu/Ni interface at the resolved shear stress of 1.06 GPa .

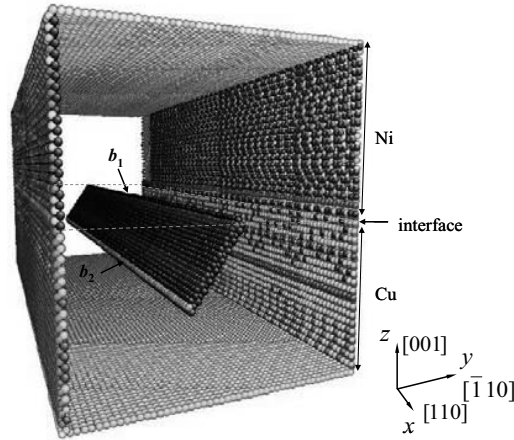


Figure 1. Atomistic model of the dislocation-interface interaction in coherent Cu-Ni system.

3. Reaction Pathway Analysis

At the various load below τ_{ath} , the free-end nudged elastic band (FE-NEB) method [4] is used to evaluate the minimum energy path (MEP) and activation energy for the slip transfer reaction. In FE-NEB computation, the initial state is chosen where the leading partial \mathbf{b}_1 is blocked at the interface, while the trailing partial \mathbf{b}_2 is still located in the bulk Cu. On the other hand, the final state is chosen where the two partials are completely located in the bulk Ni.

At the load below $0.9\tau_{ath}$, we observed two energy barriers along the MEP, which correspond to the reaction path involving the transmission for the leading partial \mathbf{b}_1 and trailing partial \mathbf{b}_2 , respectively. We found that the activation energy associated with the leading partial \mathbf{b}_1 is higher than that with the trailing partial \mathbf{b}_2 . In the range of $0.9\tau_{ath} < \tau < \tau_{ath}$, the energy barrier for the \mathbf{b}_1 transmission was observed and the energy barrier for \mathbf{b}_2 was vanished. Thus, the present study put an emphasis on the investigation about the transmission of the leading partial \mathbf{b}_1 only.

Fig. 2(a) shows the MEP for the transmission of the leading partial \mathbf{b}_1 at the applied resolved shear stress of 0.81 GPa. In Fig. 2(b), the atomic view of the saddle configuration is shown. The part of the straight leading partial extends into the Ni side in the forward and lateral direction. At the saddle point, the magnitude of the extensions in the forward and lateral direction is about 1 nm and 22 nm, respectively. The corresponding activation energy ΔE at this shear stress is 0.68 eV.

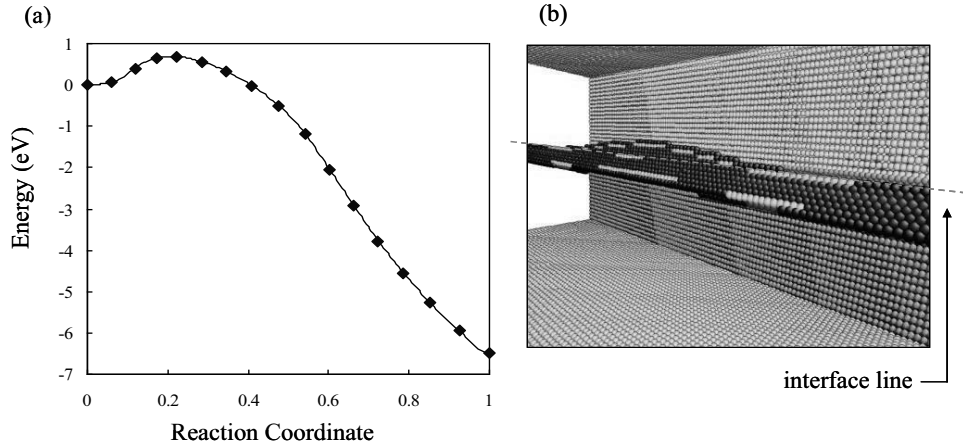


Figure 2. (a) The minimum energy path for the slip transfer of the leading Shockley partial dislocation \mathbf{b}_1 at the applied resolved shear stress of 0.81 GPa. (b) The corresponding saddle configurations.

In Fig. 3, we present the dependence of the activation energy on the resolved shear stress. According to transition state theory, the frequency of the transmission event can be given by $\nu = Q \exp(-\Delta E_{act}/k_B T)$, where Q is the constant and $k_B T$ is the thermal energy. Assuming that the activation energy ΔE which gives the value of $\nu = 1 \text{ s}^{-1}$ at room temperature is about 0.7 eV [4,6], we find that the stress above 85% of the athermal limit should be given in order to achieve the transmission event.

The $\Delta E - \tau$ relation in Fig.3 can be generalized by using the following equation $\Delta E = A(1 - \tau/\tau_{ath})^n$ [6]. Here, the parameters $A=4187.5 \text{ eV}$, $n=5.24$ and $\tau_{ath}=1.19 \text{ GPa}$ are obtained. In addition, the activation volume, which is the derivative of activation energy with respect to stress, is computed. It is found that when the activation energy is 0.68 eV, the corresponding activation volume is about $150b^3$.

The influence of the film thickness on the activation energy is also considered. To this end, the NEB calculations for the multilayered Cu/Ni systems with an individual thickness $h = 1.8 \text{ nm}$

and $h = 3.6$ nm are separately carried out. The results are shown in Fig. 3. Due to the increase of the Koehler effect, the activation energy decreases as the film thickness decreases. Thus, the threshold resolved stress required for the slip transfer also decreases as the film thickness decreases. As Misra et. al suggested [1], if the yield stress of Cu/Ni nanolayered composites is characterized by the stress that a single dislocation needs to transmit the interface, our NEB results predict that the yield stress also decreases as the film thickness decreases. This tendency is in good agreement with the experimental results [1].

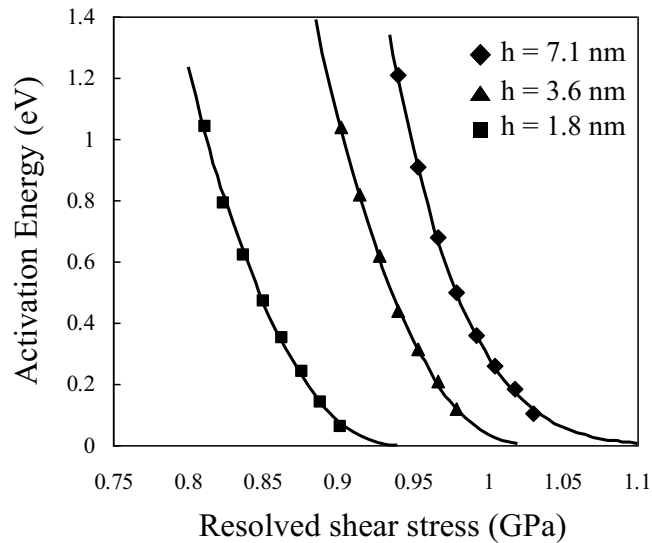


Figure 3. Dependence of the activation energy on resolved shear stress for the transmission of the leading Shockley partial dislocation b_1 .

Acknowledgements

This research was partially supported by the Ministry of Education, Science, Sports and Culture, Grant-in-Aid for Young Scientists (B), 19760058, 2008.

References

- [1] A. Misra, J. P. Hirth, R. G. Hoagland, *Acta Mater* 53, 4817 (2005).
- [2] S. I. Rao, P. M. Hazzledine, *Philo Mag A* 80, 2011 (2000).
- [3] R. G. Hoagland, R. J. Kurtz, C. H. Henager Jr., *Scripta Mater* 50, 775 (2004).
- [4] T. Zhu, J. Li, A. Samanta, H. G. Kim, S. Suresh, *PNAS*, 104, 9, 3031 (2007)
- [5] X. W. Zhou, H. N. G. Wadley, R. A. Johnson, D. J. Larson, N. Tabat, A. Cerezo, A. K. Petford-Long, G. D. W. Smith, P. H. Clifton, R. L. Martens, T. F. Kelly, *Acta Mater.* 49, 4005 (2001)
- [6] T. Zhu, J. Li, A. Samanta, A. Leach, K. Gall, *Phys Rev Lett*, 100, 025502, (2008)

Elasto-Viscoplastic Micromechanical Modelling of the Transient Creep of Ice

O. Castelnaud¹, P. Duval², M. Montagnat², R. Brenner¹

¹LPMTM-CNRS, Institut Galilée, Université Paris 13, av. J.B. Clément, 93430 Villetaneuse, France (oc@lpmtm.univ-paris13.fr, rb@lpmtm.univ-paris13.fr);

²LGGE-CNRS, Université Joseph Fourier, rue Molière, B.P. 96, 38402 Saint-Martin d'Hères, France (duval@lgge.obs.ujf-grenoble.fr, maurine@lgge.obs.ujf-grenoble.fr)

ABSTRACT

A salient feature of the rheology of isotropic polycrystalline ices is the decrease of the strain-rate by more than two orders of magnitude during transient creep tests, to reach a secondary creep regime at a strain which is systematically of 1%. We use a recent (so-called "affine") version of the self-consistent mean-field theory to model the elasto-viscoplastic behavior of ice. The model aims at bridging scales between the rheology of single grain and the one of polycrystals, by evaluating the intergranular interactions. It takes into account the long-term memory effects, which manifests itself by the fact that local stress and strain-rate in grains depend on the whole mechanical history of the polycrystal. It is shown that the strong *hardening amplitude* during the transient creep is entirely explained by the stress redistribution within the specimen, from an almost uniform stress distribution upon instantaneous loading (purely elastic response) to strong inter- and intra-phase heterogeneities in the stationary regime (purely viscoplastic response). The experimental *hardening kinetic* is much too slow to be explained by the same process; it is attributed to the hardening of hard glide slip systems (prismatic slip) in the transient regime. Moreover, the model very well reproduces the permanent creep-rate of several highly anisotropic specimens of the GRIP ice core (pronounced crystallographic textures), when accounting for a single grain rheology that well matches the experimental one. Our results are consistent with recent findings concerning dislocation dynamics in ice.

Synthesis for Ceramic Oxides

Xinghua Xie¹, Huisheng Zhou², Jing Zhu¹, Jin Guo¹ and Shilong Yan¹

¹School of Chemical Engineering, Anhui University of Science and Technology, Huainan 232001, China; E-mails: xxh1963@163.com, jingzhu@aust.edu.cn, jinguo@aust.edu.cn, slyan@aust.edu.cn

² School of Medicines, Anhui University of Science and Technology, Huainan 232001, China; E-mail: xiejunzhs@163.com

ABSTRACT

This investigation promotes the design of emulsion explosives and the development of detonation theory on a microscale. As the total composition of oxidizing and reducing elements of the reactants leave related to the thermochemistry of the system, the computational details of predicting the temperatures of detonation were introduced. It was found that a significant improvement was achieved in the emulsion explosives with an aquiferous system. An improvement in the detonation synthesis of nano-lithium and zinc oxides is due to the formation of an activated matrix of the metal nitrates' oxidizer with the corresponding fuel. Temperatures of detonation of emulsion explosives and explosive formulations are predicted using thermochemistry information. XRD analysis shows that nanoparticles of lithium and zinc oxides can be produced from detonation of emulsion explosives due to fast quenching as well as appropriate detonation velocity and temperature.

Keywords: Lithium and zinc oxides, emulsion explosive, XRD, temperature of detonation

1. Introduction

Water-contained explosives developed in the late 1950s became quite widespread in their use from the mid 1960s [1]. Mohammad Hossein Keshavarz [2] introduced a simple procedure by which detonation pressure of CaHbNcOd explosives can be predicted from a, b, c, d and calculated gas phase heat of formation of explosives at any loading density without using any assumed detonation products and experimental data. This class of explosive has now mainly replaced traditional nitroglycerine based dynamites and gelignites for commercial blasting. Emulsion explosives offer many advantages over dynamites including being more economical, safer to handle and relatively insensitive to mechanical initiation and having a good shelf life. They are composed of aqueous solutions of inorganic oxidizing salts, generally ammonium nitrate, held in a gelatinous matrix, using gelling agents such as highly branched polysaccharides, e.g. guar gum and starch. Density, and hence sensitivity, is controlled using a variety of materials including hollow glass microspheres, and surfactants such as laurylamine acetate to entrap air into the explosive matrix. Further oxidants including lithium nitrate and zinc nitrate are suspended in the matrix, along with combustible materials such as oil and paraffine.

2. Computational Details

If we consider the water of detonation products in liquid state,

$$N = (5.42 + 7.04 + 0.18)/1000 = 12.64/1000 = 0.01264 \text{ (mol/g)}$$

$$M = (5.42 \times 44 + 7.04 \times 28 + 0.18 \times 32)/12.64 = (238.48 + 197.12 + 5.76)/12.64 = 34.92 \text{ (g/mol)}$$

$$Q = Q_{v \text{ [H}_2\text{O (l)]}}/4.18 = 3825.46/4.18 = 915.18 \text{ (cal/g)}$$

$$\phi = 0.01264 \times 34.92^{1/2} \times 915.18^{1/2} = 0.01264 \times 5.91 \times 30.25 = 2.259$$

When $\rho = 845 \text{ kg.m}^{-3}$, theoretically

$$D = 1.01 \times 2.259^{1/2} (1 + 1.3 \times 0.845) = 1.01 \times 1.503 \times 2.099 = 3.186 \text{ (Km/s)}$$

$$P_{CJ} = 1.56 \times 0.845^2 \times 2.259 = 2.52 \text{ (GPa)}$$

Subscript e and pr mean the experimental and predicting values of detonation parameters respectively.

$$D_e = 1743 \text{ m/s,}$$

If we consider the water of detonation products in liquid state,

$$Q_e = D_e^2 \times Q/D^2 = 1743^2 \times 3825.46/3186^2 = 1144.95 \text{ KJ}$$

$$t_{pr} = \frac{-2218.02 + \sqrt{2218.02^2 + 4 \times 26.69 \times 10^{-3} \times 1144.95 \times 10^3}}{2 \times 26.69 \times 10^{-3}} + 298.15$$

$$= 811.19 \text{ K}$$

If we consider the water of detonation products in vapor state,

$$N = (5.42 + 7.04 + 0.18 + 23.33)/1000 = 35.97/1000 = 0.03597 \text{ (mol/g)}$$

$$M = (5.42 \times 44 + 7.04 \times 28 + 0.18 \times 32 + 23.33 \times 18)/35.97 = 23.94 \text{ (g/mol)}$$

$$Q = Q_{v \text{ [H}_2\text{O (l)]}}/4.18 = 2861.44/4.18 = 684.56 \text{ (cal/g)}$$

$$\phi = 0.03597 \times 23.94^{1/2} \times 684.56^{1/2} = 0.03597 \times 4.89 \times 26.16 = 4.604$$

$$D = 1.01 \times 4.604^{1/2} (1 + 1.3 \times 0.845) = 1.01 \times 2.146 \times 2.099 = 4.548 \text{ (Km/s)}$$

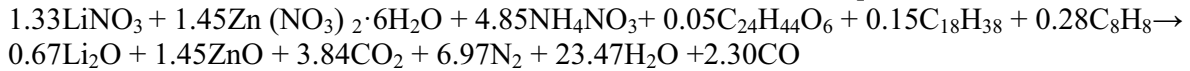
$$P_{CJ} = 1.56 \times 0.845^2 \times 4.604 = 5.13 \text{ (GPa)}$$

$$Q_e = D_e^2 \times Q/D^2 = 1743^2 \times 2861.44/4548^2 = 420.28 \text{ KJ}$$

$$t_{pr} = \frac{-862.550 + \sqrt{862.55^2 + 4 \times 236.43 \times 10^{-3} \times 420.28 \times 10^3}}{2 \times 236.43 \times 10^{-3}} + 298.15$$

$$= 503.17 \text{ K}$$

When the mass fraction of EPS is 3%, the detonation reaction equation is as follows.



$$Q_{v \text{ [H}_2\text{O (l)]}} = 3611.39 \text{ kJ} + (3.84 + 6.97 + 2.30) \times 8.314 \times 10^{-3} \times 298.15 \text{ kJ} = 3643.89 \text{ kJ}$$

$$t = \frac{-2209.28 + \sqrt{2209.28^2 + 4 \times 26.72 \times 10^{-3} \times 3643.89 \times 10^3}}{2 \times 26.72 \times 10^{-3}} + 298.15$$

$$= 1617.71 \text{ K}$$

If we consider the water of detonation products in vapor state,

$$Q_{v \text{ [H}_2\text{O (g)]}} = 2583.40 \text{ kJ} + (3.84 + 6.97 + 23.47 + 2.30) \times 8.314 \times 10^{-3} \times 298.15 \text{ kJ}$$

$$\begin{aligned}
 &= 2674.08 \text{ kJ} \\
 t &= \frac{-845.68 + \sqrt{845.68^2 + 4 \times 237.72 \times 10^{-3} \times 2674.08 \times 10^3}}{2 \times 237.72 \times 10^{-3}} + 298.15 \\
 &= 2315.87 \text{ K} \\
 N &= (3.84 + 6.97 + 2.30)/1000 = 13.11/1000 = 0.01311 \text{ (mol/g)} \\
 M &= (3.84 \times 44 + 6.97 \times 28 + 2.30 \times 28)/13.11 = 32.69 \text{ (g/mol)} \\
 Q &= Q_{v \text{ [H}_2\text{O (l)]}}/4.18 = 3643.89 / 4.18 = 871.74 \text{ (cal/g)} \\
 \phi &= 0.01311 \times 32.69^{1/2} \times 871.74^{1/2} = 0.01311 \times 5.72 \times 29.53 = 2.214 \\
 \text{When } \rho &= 686 \text{ kg.m}^{-3}, \text{ theoretically} \\
 D &= 1.01 \times 2.214^{1/2} (1 + 1.3 \times 0.686) = 1.01 \times 1.488 \times 1.892 = 2.843 \text{ (Km/s)} \\
 P_{CJ} &= 1.56 \times 0.686^2 \times 2.214 = 1.63 \text{ (GPa)} \\
 \text{Yet, } D_e &\text{ (subscript e means the experimental value of detonation parameters)} = 1806 \text{ m/s,} \\
 \text{If we consider the water of detonation products in liquid state,} \\
 Q_e &= D_e^2 \times Q/D^2 = 1806^2 \times 3643.89/28432 = 1470.44 \text{ KJ} \\
 t_{pr} &= \frac{-2209.28 + \sqrt{2209.28^2 + 4 \times 26.72 \times 10^{-3} \times 1470.44 \times 10^3}}{2 \times 26.72 \times 10^{-3}} + 298.15 \\
 &= 958.45 \text{ K} \\
 \text{If we consider the water of detonation products in vapor state,} \\
 N &= (3.84 + 6.97 + 23.47 + 2.30)/1000 = 36.58/1000 = 0.03658 \text{ (mol/g)} \\
 M &= (3.84 \times 44 + 6.97 \times 28 + 23.47 \times 18 + 2.30 \times 28)/36.58 = 23.26 \text{ (g/mol)} \\
 Q &= Q_{v \text{ [H}_2\text{O (l)]}}/4.18 = 2674.08 / 4.18 = 639.73 \text{ (cal/g)} \\
 \phi &= 0.03658 \times 23.26^{1/2} \times 639.73^{1/2} = 0.03658 \times 4.82 \times 25.29 = 4.459 \\
 D &= 1.01 \times 4.459^{1/2} (1 + 1.3 \times 0.686) = 1.01 \times 2.112 \times 1.892 = 4.035 \text{ (Km/s)} \\
 P_{CJ} &= 1.56 \times 0.686^2 \times 4.459 = 3.27 \text{ (GPa)} \\
 Q_e &= D_e^2 \times Q/D^2 = 1806^2 \times 2674.08/4035^2 = 535.70 \text{ KJ} \\
 t_{pr} &= \frac{-845.68 + \sqrt{845.68^2 + 4 \times 237.72 \times 10^{-3} \times 535.70 \times 10^3}}{2 \times 237.72 \times 10^{-3}} + 298.15 \\
 &= 846.95 \text{ K}
 \end{aligned}$$

3. Conclusions

A computational methodology has been developed to predict the heats of detonation for emulsion explosive formulations. The methodology is based on a simple scheme to calculate detonation properties. The method assumes that the heat of detonation of an explosive compound of composition $C_aH_bN_cO_dLi_eZn_f$ can be approximated as the difference between the heats of formation of the detonation products and that of the explosive formulation, divided by the formula weight of the explosive. The detonation products are assumed to correspond to the H_2O – CO_2 – C – Li_2O – ZnO arbitrary. For emulsion explosives, this methodology presented here has the advantage that neither heats of formation nor densities need to be measured or estimated to

calculate the heat of detonation of an explosive. The calculations presented herein show that this methodology to predict heats of detonation of emulsion explosives and explosive formulations is a reasonable computational tool to be used in the rapid assessment and screening of notional energetic materials. The detonation products were identified from X-ray powder diffraction (XRD) patterns and scanning electron microscopy (SEM) measurements. XRD analysis shows that nanoparticles of lithium and zinc oxides can be produced from detonation of emulsion explosives due to fast quenching as well as appropriate detonation velocity and temperature.

Acknowledgements

This work was supported by the Anhui Provincial Program for the Tackling Key Problem (07010302189), the Program for the Provincial Innovation Research and Development Team of Anhui Provincial Universities (TD200705) and the 2007 Municipal Natural Science Foundation of Huainan and the Doctoral Fund of Anhui University of Science and Technology.

References

- [1] D. T. Burns, R. J. Lewis, J. Bridges, *Analytica Chimica Acta*, 375 (1998) 255-260.
- [2] M. H. Keshavarz, *Journal of Hazardous Materials A119* (2005) 25–29.
- [3] B.M. Rice, J. Hare, *Thermochimica Acta*, 384 (2002) 377–391.
- [4] D.L. Ye, J.H. Hu, *Practical handbook of energetic data for inorganic compounds*, 2nd Edition, Metallurgical Industry Press, Beijing, China, 2002, p. 533-594.
- [5] J. Akhavan, *The Chemistry of Explosives*. The Royal Society of Chemistry, Cambridge, U.K., 1998, p. 103.
- [6] S.M. Xu, *Journal of Shenyang Institute of Technology*, 13 (3) (1994) 55-61.
- [7] X.S. Xu, W.X. Zhang, *Theoretical Guide of Banausic State Equation*. Science Press, Beijing, China, 1986. p. 270.
- [8] J.A. Zukas, W.P. Walters, *Explosive Effects and Applications*. Springer-Verlag New York, Inc., New York, U.S.A., 1998, p. 124.
- [9] P.W. Chen, F.L. Huang, S.R. Yun, *Materials Research Bulletin* 39 (2004) 1589–1597.
- [10] J.B. Donnet, E. Fousson, T.K. Wang, M. Samirant, C. Baras, M. Pontier Johnson. *Diamond and Related Materials* 9 (2000) 887–892.
- [11] S. Zeman, *Thermochimica Acta*, 384 (2002) 137–154.
- [12] X.M. Lin, L.P. Li, G.S. Li, W.H. Su, *Materials Chemistry and Physics* 69 (2001) 236–240.
- [13] X.J. Li, X.H. Xie, R.Y. Li, *Explosion and Shock Waves* 25 (3) (2005) 271-275.
- [14] X.H. Xie, X.J. Li, R.Y. Li, H.H. Yan, Y.D. Qu & T. Chen, in: Y.J. Wang, P. Huang, S.C. Li (Eds.), *Theory and Practice of Energetic Materials Vol.VI*. Science Press, Beijing, China, 2005, p. 169-174.
- [15] X.J. Li, X.H. Xie, R.Y. Li, Y.D. Qu & T. Chen, in: Y.J. Wang, P. Huang, S.C. Li (Eds.), *Theory and Practice of Energetic Materials Vol.VI*. Science Press, Beijing, China, 2005, p. 153-158.

Evaluation of influence of size of inclusion on the Effective Material Property of Particle reinforced Composites

Amol Agrawal¹ and Rohit Saha²

**Senior Undergraduate, Department of Mechanical Engineering,
Institute of Technology, Banaras Hindu University, Varanasi , India
¹amolecy@gmail.com, ²saha.rohit@gmail.com**

ABSTRACT

The micro-macro mechanical approaches offer new insights of the material behavior of particle and fibre reinforced composite and may result in new procedures to develop realistic material models for design and optimization purposes. The conventional numerical homogenization technique is employed to evaluate the effective material properties and influence of interphase of complex microstructured three phase composites like transversely randomly distributed fiber and randomly distributed spherical particle composites. The consideration of randomly distributed inclusions opens new possibilities to investigate more realistic composites which incorporates automatically such effects like the influence of different distances between the particles. under the assumption of small strains and elastic material behavior. In order to validate our developed numerical homogenization tools, comparisons are made between our numerical results and results reported in literature for uni-directional regular arrangement of fiber composites. The fibre/ inclusion material is taken as SiC and the matrix is the Al alloy. It is seen from the finite element studies, that the representative volume element (RVE) containing multiple inclusion of spherical and cylindrical shape with ordered arrangement, the effective property increases with decrease in size of inclusion at the particular volume fraction with an exception of RVE containing only 2 inclusions. However, the obtained results are verified with the results those obtained by analytical and available in literature.

Generalized self consistent polycrystalline model applied to heterogeneous materials exhibiting log normal grain size distribution

Quang H. Bui¹, Salah Ramtani², Guy F. Dirras³

Laboratoire des Propriétés Mécaniques et Thermodynamiques des Matériaux,
LPMTM – CNRS UPR 9001, Université Paris 13
99 avenue J. B. Clément 93430 Villetaneuse, France

¹bui@lpmtm.univ-paris13.fr, ²salah.ramtani@lpmtm.univ-paris13.fr,
³dirras@lpmtm.univ-paris13.fr

ABSTRACT

A generalized self consistent approach, recently proposed by Jiang and Weng [1] for investigating the properties mechanical of nanocrystalline (NC) materials, is revisited and reformulated following an incremental scheme. The NC material is modeled as composed of spherical randomly distributed grains with a lognormal grain size distribution. Each oriented grain and its immediate grain boundary form a pair, which in turn is embedded an infinite effective medium with a property representing the average orientation of all these pairs. The plastic deformation of the grain phase takes into account the dislocation glide mechanism whereas the boundary phase is modeled as an amorphous material.

1. Introduction

NC and ultrafine-crystalline materials (UFG) are research topic subjects that bridge several fields, from materials science to mechanical engineering since more than a decade [2]. This type of materials processes superior mechanical strength over their microcrystalline counterparts but limited plastic deformation. Both experimental and theoretical investigations show deformation mechanisms being dominated by the grain boundary phase activity. More generally, when the grain size decreases down to about tenth of nanometers, the yield strength increases linearly with the inverse square root of the grain size as described by the Hall-Petch law: $\sigma_y = \sigma_0 + kD^{-1/2}$, where σ_0 is the frictional stress, k the Hall-Petch slope and D the mean grain size. Nevertheless, it should be noticed that the mechanical properties of a given material depend on the as-processed microstructure characteristics (such as the grain size distribution, the crystallographic texture, the grain boundary structure, the grain shape etc...) and not only on the mean grain size. Most of these microstructures characteristics are often out of reach experimentally. In the same time, numerical simulations are good means for predicting, optimizing, and controlling the processing of material. Jiang and Weng developed a generalized self consistent polycrystal model [1], based on Christensen and Lo's solution [3] and Lou and Weng's solution [4] to predict the influence of the as processed microstructure on the subsequent mechanical behavior.

In doing so, they considered solely the average grain size as structural parameter. However, experimental investigations do demonstrate that the grain size is dispersed in an interval within the lognormal distribution. Taking into account the lognormal distribution and the dispersion around the mean grain size allows to better simulating, with more accuracy, the behavior of the bulk NC or UFG materials and constitutes the goal of this study presented here.

2. The generalized self-consistent approach

In this paper, the generalized self-consistent model, recently proposed by Jiang and Weng [1], is rewritten following an incremental small strain scheme. The representative volume element (RVE) of this micromechanical model is an oriented grain identified by Eulerian angles (ϕ_1, θ, ϕ_2) and its immediate boundary forming a pair embedded in a homogeneous equivalent medium. Under the macroscopic Cauchy stress rate $\dot{\Sigma}_{ij}$, the plastic deformation of the grain is governed by its crystallographic slips systems. However the stress and strain of the surrounding grain boundary, modelled as an amorphous material, are closely related to the plastic strain of its enclosed grain. The nonlinear problem can be resolved by superposition of two linear auxiliary problems as schemes in Fig 1.

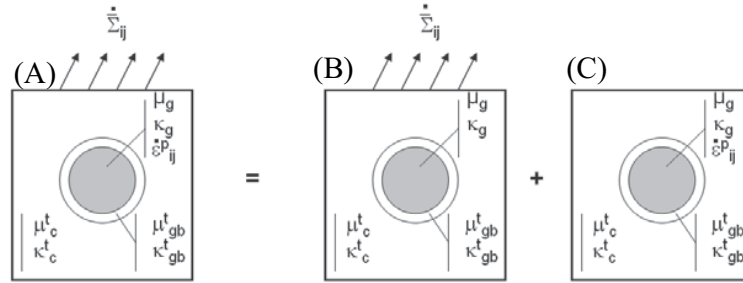


Figure 1. The decomposition scheme of the initial non-linear (A) problem into two linear auxiliary problems according to Christensen and Lo (B) and Lou and Weng (C).

The stress-strain relation of each oriented grain is given by

$$\dot{\sigma}_{ij}^{(g)} = C_{ijkl}^{(g)} \left(\dot{\varepsilon}_{kl}^{(g)} - \sum_s \nu_{kl}^{(s)} \dot{\gamma}^{(s)} \right) \quad (1)$$

where $C_{ijkl}^{(g)}$ is the crystal elasticity tensor, $\dot{\gamma}^{(s)}$ is the shear rate, $\nu_{kl}^{(s)}$ is the Schmid factor tensor of the slip system s , defined as the tensor product of the unit slip direction tensor and the slip plane normal tensor of the considered slip system.

The plasticity of the grain-boundary phase is isotropic and incompressible ($p=0$). The yield function described by [5]: $\sigma_e^{(gb)} = \sigma_y^{(gb)} + h_{gb} (\varepsilon_e^{p(gb)})^{n_{gb}}$ where $\sigma_e^{(gb)}$, $\varepsilon_e^{p(gb)}$ and $\sigma_y^{(gb)}$ are the Mises' effective stress, effective plastic strain and the yield strength initial of grain boundary respectively. The parameters h_{gb} and n_{gb} are the material constant related to the grain boundary. The grain boundary thickness was given a value of $\delta=1$ nm [1].

3. Results and discussions

The application of the present model for the copper processed by inert gas condensation method [6] was presented in this section. Fig. 2a compares the true stress-true strain curve obtained from experimental tensile test at room temperature at the strain rate of 10^{-4}s^{-1} and the one of the current model prediction. Three types of material, corresponding to three different mean grain sizes of 49 nm, 110 nm and 20 μm , were studied. It is clear that the flow stress depends on the grain size and the simulation compares fairly well with the experimental results.

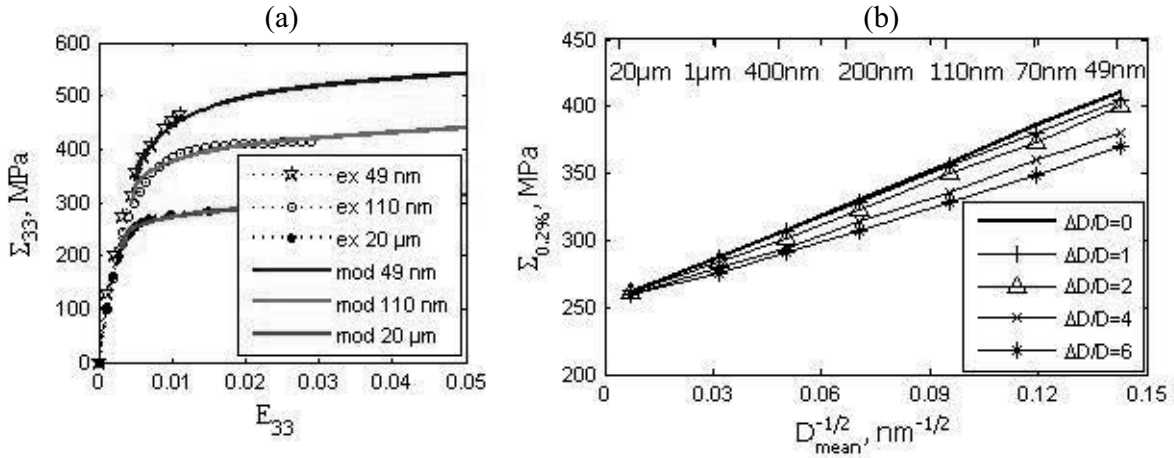


Figure 2. (a) Calculated (mod) and experimental (ex) stress-strain relations of copper with different grain sizes. (b) Predicted flow stress at 0.2% plastic strain as a function of mean grain size for different relative dispersion $\Delta D/D$.

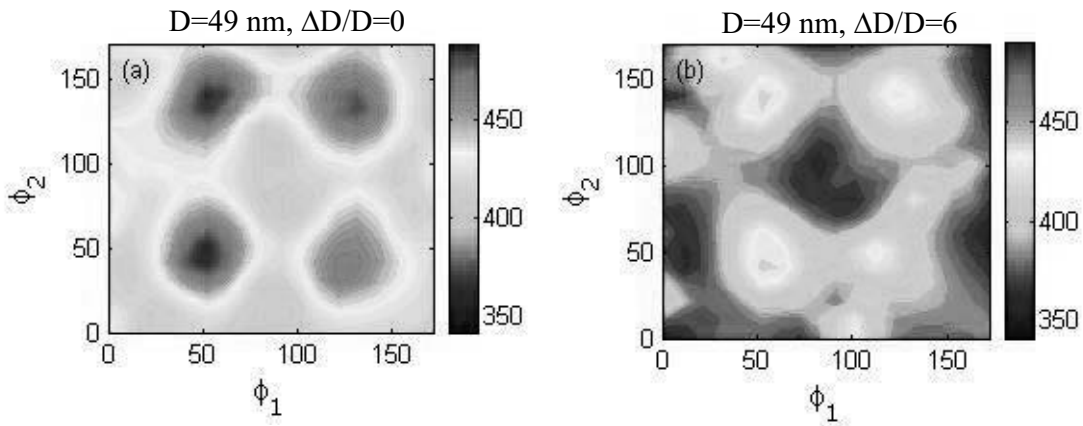


Figure 3. Map for the effective stress of the grain phase (at the overall axial plastic strain level $E^p=1\%$) in terms of the orientation of the grain (random orientations) at mean grain size $D_{\text{mean}}=49\text{ nm}$ and different relative dispersion.

A procedure is used to generate different discrete lognormal distribution with given means and dispersions [7]. The flow stresses at 0.2% plastic strain are plotted in Fig. 2b as a function

of $D_{mean}^{-1/2}$. The relative dispersion $\Delta D/D$ takes the values 0, 1, 2, 4, 6 and all the curves appear to be quite linear. Our results, like those presented by Berbenni et al [7], display a unique effect of the grain size dispersion which becomes more significant at the NC regime (49 nm).

Fig. 3 illustrates the evolution of effective stress of the grain phase (which is defined as $\sigma_e^{(g)} = \left(\frac{3}{2} \sigma_{ij}^{(g)} \sigma_{ij}^{(g)} \right)^{1/2}$) at the overall axial plastic strain level $E^p=1\%$ taking into account the initial grain orientation, different mean grain sizes and associated relative dispersions. It can be seen that in the all cases, the effective stress of the grain phase is heterogeneous and the high effective stresses are located at $(\phi_1, \phi_2) = (50^\circ, 50^\circ), (50^\circ, 125^\circ), (125^\circ, 50^\circ)$ and $(125^\circ, 125^\circ)$. In the case of ($D_{mean}=49\text{nm}, \Delta D/D=6$), the effective stress exhibits more heterogeneity than the other cases with the presence of additional high effective stress located at $(\phi_1, \phi_2) = (0^\circ, 110^\circ), (40^\circ, 160^\circ), (100^\circ, 0^\circ)$, and $(130^\circ, 80^\circ)$ (see Fig. 3b). Comparing the effective stress in the case of the coarsest mean grain size $D_{mean}=20\mu\text{m}$ with no dispersion ($\Delta D/D=0$) to the case of a broader dispersions like $\Delta D/D=6$, the resulting stress fields are very close (in position and levels) (not show here). As for the NC sample ($D_{mean}=49\text{nm}$), a loss of the effective stress fields is found when the two extreme dispersions $\Delta D/D=0$ and $\Delta D/D=6$ (Fig. 3a and 3b) are compared. These results confirm that the effect of the grain size dispersion on the effective stress fields at $E^p=1\%$ becomes more significant at finest mean grain sizes.

As in previous work [7], we have numerically investigated the hypothesis that broad dispersions tend to reduce the grain size dependence whereas the individual grain behaviour is grain size dependent.

References

- [1] B. Jiang, G.J Weng, "A generalized self consistent polycrystal model for the yield strength of nanocrystalline materials", *J. Mech. Phys. Solids.*, **52**, 1125-1149 (2004).
- [2] M.A. Meyers, A. Mishra, D.J. Benson, "Mechanical properties of nanocrystalline materials", *Progress in Materials Science*, **51**, Issue 4, Pages 427-556 (2006).
- [3] R.M Christensen, K.H. Lo, "Solution for the effective shear properties in three phase sphere and cylinder models", *J. Mech. Phys. Solids.*, **27**, 315-330 (1979).
- [4] H.A. Luo, G.J. Weng, "On Eshelby's inclusion problem in a three phase spherically concentric solid, and a modification of Mori-Tanaka's method", *Mechanics of Materials*. **6**, 347-361 (1987).
- [5] D.C Drucker, "Some implication of work hardening and ideal plasticity". *Q. Appl. Math.* **7**, 411-418 (1950).
- [6] P.G. Sanders, J.A. Eastman, J.R. Weertman, "Elastic and tensile behaviour of nanocrystalline copper and palladium". *Acta mater.* **45**, 4019-4025 (1997).
- [7] S. Berbenni, V. Favier and M. Berveiller, "Impact of the grain size distribution on the yield stress of heterogeneous materials". *International Journal of Plasticity* **23**, 114-142 (2007).

Two Step Homogenization of Thermal Conductivities for Macroscopically Orthotropic C/C Composites

Jan Vorel¹, Michal Sejnoha¹

¹Czech Technical University in Prague, Faculty of Civil Engineering,
Department of Mechanics, Thákurova 7, 16629, Prague 6, Czech Republic.
(Email: sejnom@fsv.cvut.cz)

ABSTRACT

Evaluation of effective thermal conductivities of carbon-carbon (C/C) composites using the Mori-Tanaka (MT) averaging scheme is presented. Two step homogenization approach is adopted both at the level of fiber tow and the level of plain weave textile ply.

1. Introduction

Carbon-Carbon plain weave fabric composites belong to an important class of high-temperature material systems. An exceptional thermal stability together with high resistance to thermal shocks or fracture due to rapid and strong changes in temperature have made these materials almost indispensable in a variety of engineering spheres including aeronautics, space and automobile industry. While their appealing thermal properties such as low coefficients of thermal expansion and high thermal conductivities are known, their prediction from the properties supplied by the manufacturer for individual constituents is far from being trivial since these systems are generally highly complicated. In the last decade, effective media theories, widely used in classical continuum micromechanics, have been recognized as an attractive alternative to time-consuming finite element based methods.

2. Theoretical formulation

Assuming steady state conditions the estimates of effective thermal conductivities follow from the solution of a heat conduction problem which can be described by the Laplace equation. The solution of this equation is combined here with the Mori-Tanaka method to provide for the homogenized material properties of C/C textile composites. In view of this approach the local gradient (\mathbf{H}) is split into the average gradient in matrix (\mathbf{H}_0) and the fluctuation part (\mathbf{H}_f)

$$\mathbf{H} = \mathbf{H}_0 + \mathbf{H}_f = \mathbf{H}_0 + \mathbf{S}\mathbf{H}^* \quad (1)$$

Note that the second order tensor \mathbf{S} and the vector \mathbf{H}^* are analogous to the Eshelby tensor and transformation strain, respectively, for the elasticity problem. Explicit solution of the \mathbf{S} is expressed in [1]. The Mori-Tanaka estimates are then provided by

$$\mathbf{K} = \mathbf{K}_0 + \left[\sum_{i=0}^N c_i (\mathbf{K}_i - \mathbf{K}_0) \mathbf{A}_i \right] \left(c_0 \mathbf{I} + \sum_{i=0}^N c_i \mathbf{A}_i \right)^{-1} \quad (2)$$

where indexes $0, 1, \dots, i, \dots, N$ refer to individual constituents with 0 related to matrix phase and c_i are the volume fractions. The concentration factor \mathbf{A}_i can be determined as

$$\mathbf{A}_i = [\mathbf{I} + \mathbf{S} \mathbf{K}_0^{-1} (\mathbf{K}_i - \mathbf{K}_0)]^{-1} \quad (3)$$

The expression above provides two possible approaches for the determination of the effective material parameters, one-step or multi-step method. The first treats all inhomogeneities simultaneously. The second one adopts the procedure where each inclusion is embedded into a new homogenized matrix in a certain hierarchical manner. The latter approach is employed henceforth.

3. Effective properties

As already mentioned, C/C plain weave composites are used as a reference material. The properties and dimensions of each constituent are taken from [2, 3].

Table 1. Phase thermal conductivities [$\text{Wm}^{-1}\text{K}^{-1}$]

<i>Material</i>	<i>Thermal conductivity</i>
Carbon fibers	(0.35; 0.35; 35)
Carbon matrix	6.3
Voids filled with air	0.02

1.1 Micro scale

The basic structural element is the fiber tow with significant amount of transverse cracks and voids resulting in porosity up to 15% (Fig. 1a). Tab. 2 summarizes effective thermal conductivities derived with the help of the Mori-Tanaka method. As expected, a reasonably good agreement with finite element simulations presented in [3] was achieved.

Table 2. Phase thermal conductivities [$\text{Wm}^{-1}\text{K}^{-1}$]

<i>Analysis</i>	<i>Material</i>		<i>Conductivity</i>
	<i>Fiber</i>	<i>Inhomogeneity</i>	
Multi-step MT	1; 1; ∞	1.6; 10; ∞	1.12; 1.85; 19.44

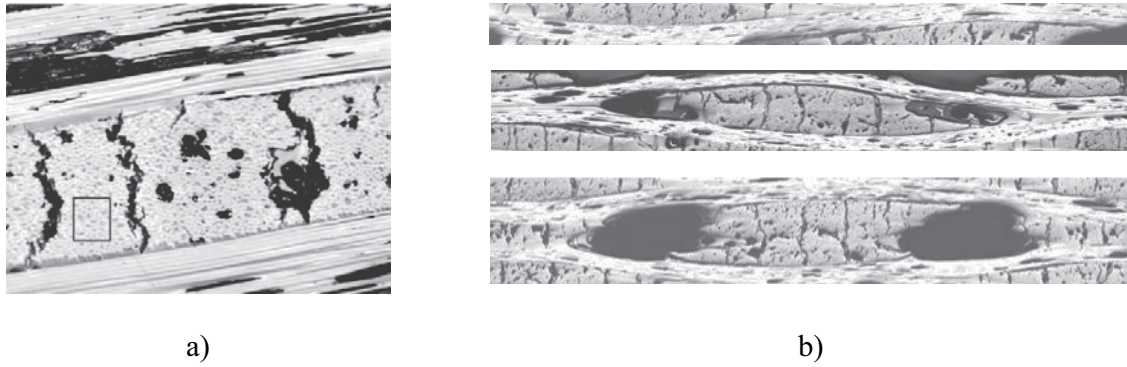


Figure 1.: (a) Micro scale, (b) meso scale

1.2 Meso scale (fiber tow)

The material properties determined on micro-scale are subsequently used on meso-scale as a basic step for a multi-step procedure. First, the wavy, generally nonuniform, fiber tow path is taken into account by employing the orientational averaging introduced in [3]. In this method it is possible to employ either a uniform distribution (Tab. 3) or real histograms of inclination angle [3]. To further grasp an imperfect nature of C/C composites three different types of PUCs are considered (Fig. 1b), see also [2, 3] providing real dimensions of the fiber tow for MT predictions. In addition, an optimal shape of an equivalent ellipsoidal inclusion addressed in [3] is adopted.

Table 3. Effective thermal conductivities [$Wm^{-1}K^{-1}$] (meso scale)

Analysis	Type	Tow		Air voids		Conductivity	
		Mutual ratio	Vol.	Mutual ratio	Vol.	Longitudinal	Transversal
1 st step	Opti - mized	1; 0.486; 0.092	0.648	-		8.25	2.70
			0.800			8.70	2.29
2 nd step	PUC 1		0.800	-	-	9.29	2.21
	PUC 2		4x(150; 30; 30)	0.097	8.19	1.77	
	PUC 3		8x(150; 30; 30)	0.141	7.70	1.60	
	PUC 1		-	-	8.73	2.56	
PUC 2	4x(150; 30; 30)	0.097	7.71	2.02			
	8x(150; 30; 30)	0.141	7.26	1.82			

Note, that on the micro-scale the application of the Mori-Tanaka method is particularly simple since in both homogenization steps, when limiting our attention to transverse cross-section only, the underlying matrix is isotropic. This, however, is no longer true if performing the same analysis on the meso-scale, where the second homogenization step calls for the solution of an isotropic (air) inclusion in an orthotropic matrix [4]. The corresponding homogenized properties are summarized in Tab. 3. In order to have comparable results of material properties two values of tow volume are considered. The volume 0.648 belongs to a real 3D meso-structure and value 0.800 represents the tow in 2D analysis used in [2].

1.3 Textile ply

The final, clearly the most simple, step requires a construction of the homogeneous laminated plate. The stacking sequence of individual periodic unit cells complies with that observed for the actual composite sample [2]. Clear evidence is available in Tab. 4 comparing the numerical and experimental results.

Table 4. Effective thermal conductivities [$\text{Wm}^{-1}\text{K}^{-1}$] (textile ply)

<i>Method</i>	<i>Vol. frac. of fiber tow</i>	<i>Conductivity</i>	
		<i>Longitudinal</i>	<i>Transversal</i>
MT	0.800	8.36	1.85
	0.687	7.87	2.12
Measured	-	10.00	1.60

5. Conclusions

Two levels of hierarchy are introduced in this contribution to derive the effective thermal conductivities of plain weave textile composites. In this paper, the multi-step formulation as an efficient method based on the generalization of the Mori-Tanaka method is discussed. The results presented for all levels demonstrate a good agreement with FE simulations as well as with experimental data [2]. Variations between the data obtained for these approaches are mostly caused by the simplifications in [2] where the 2D samples are considered.

Acknowledgements

The financial support provided by the research project CEZ MSM 684077003 and partially also by the GAČR Grant No. 106/07/1244 is gratefully acknowledged.

References

- [1] H. Hatta and M. Taya, "Equivalent inclusion method for steady state heat conduction in composites", *International Journal of Engineering Science*, **24**:1159-1172, (1986).
- [2] B. Tomková, M. Šejnoha, J. Novák, and J. Zeman, "Evaluation of Effective Thermal Conductivity of Porous Textile Composites", Accepted for publication in *International Journal for Multiscale Computational Engineering*.
- [3] J. Skoček, J. Zeman, and M. Šejnoha, "Effective Properties of Carbon-Carbon Textile Composites: Application of the Mori-Tanaka Method", Submitted to *Modelling and Simulation in Materials Science and Engineering*, <http://arxiv.org/abs/0803.4166>.
- [4] T. Chen, and S.-H. Yang, "The problem of thermal conduction for two ellipsoidal inhomogeneities in an anisotropic medium and its relevance to composites materials", *Acta Mechanica* 111, 41-58, (1995).

Failure of Granular Materials under Impact – Multiscale Simulations and High-Speed Experiments

Martin O. Steinhauser

**Fraunhofer Ernst-Mach Institute for High-Speed Dynamics (EMI), Eckerstrasse 4, D-79104 Freiburg, Germany
Martin.Steinhauser@emi.fraunhofer.de**

ABSTRACT

A mesoscopic discrete particle model for simulating fracture and failure of brittle materials is presented. The model has only a few adjustable parameters, but is able of reproducing many salient features of macroscopic ceramics under tensile, compressive and shock impact load [1,2]. Under shear load, the model exhibits the formation of macroscopic shear bands in the material. The particle model is discussed in detail and the results of non-equilibrium strain and shear load simulations are discussed in comparison to corresponding high-speed experiments. In particular, the explicit macroscopic experimental set-up of the edge-on-impact experiment is modeled and it is shown that the experimentally observed crack patterns can in principle be explained by the distribution of mesoscopic local differences in strength in the material.

- [1] M.O. Steinhauser, “Computational Multiscale Modeling of Fluids and Solids – Theory and Applications”, Springer, Berlin, Heidelberg, New York (2008).
- [2] M. O. Steinhauser, K. Grass, K. Thoma, and A. Blumen “Impact Dynamics and Failure of Brittle Solid States by means of Nonequilibrium Molecular Dynamics Simulations”, Europhysics Letters, **73**, 62 (2006).

Multiscale Model of Nanoindentation Test in Cu and Ni

Miroslav Černý, Jaroslav Pokluda, Jana Horníková, Pavel Šandera

Faculty of Mechanical Engineering, Brno University of Technology, Technická 2896/2,
Brno 616 69, Czech Republic.
cerny.m@fme.vutbr.cz

ABSTRACT

The nanoindentation test in the dislocation free volume of the grain in a metallic polycrystal was simulated by utilizing a multiscale analysis. The onset of microplasticity, associated with the pop-in effect identified in experimental nanoindentation tests (generation of first dislocation loops [1,2]), is assumed to be related to the moment of reaching the value of the ideal shear strength for that crystal. In particular, the influence of the compressive normal load (acting on the shear plane) on the ideal shear strength value [3], the three dimensionality of the nanoindentation test, the nonlinearity of the stress-strain relation, the orientation of relevant crystallographic planes and the anisotropy of elastic response of the crystal were considered in the model. The mechanical characteristics of the perfect metallic crystal (grain) were calculated by using the ab initio approach [4]. The three-dimensional isotropic FEM analysis, was used to simulate the development of the stress-strain field in the substrate. The computed displacement value was compared with experimentally measured pop-in effect in the nickel and copper crystals and a good agreement was obtained. The results reveal that the nanoindentation test can serve as a sufficiently precise tool for experimental determination of the ideal shear strength.

- [1] J. Horníková, V. Buršíková, P. Šandera, M. Černý and J. Pokluda, “Multiscale Modelling of Nanoindentation Test in Nickel Crystal” *Acta Metallurgica Slovaca*, **13**, 65 (2007).
- [2] M. Göken and M. Kempf, and W.D. Nix, “Pop-ins in nanoindentations – the initial yield point” *Zeitschrift für Metallkunde*, **92**, 1061 (2001).
- [3] M. Černý and J. Pokluda, “Tensile Strength of Perfect Cubic Crystals under Superimposed Transverse Plain Stress”, *Materials Science Forum*, **567-568**, 73 (2008).
- [4] G. Kresse and J. Furthmuller, “Efficient iterative schemes for ab initio total-energy calculations using a plane-wave basis set”, *Physical Review B* **54**, 11169 (1996).

The research was supported by European agency COST (Action P19) and the Ministry of Education and Youth of the Czech Republic under the grant No. OC 148.

Hardening by completely and partially absorbed $\frac{1}{2}\langle 111 \rangle$ and $\langle 100 \rangle$ dislocation loops reacting with dislocations in α -Fe.

D. Terentyev¹, D.J. Bacon², P. Grammatikopoulos² and Yu.N. Osetsky³.

¹SCK-CEN, Nuclear Material Science Institute, Boeretang 200, B-2400, Mol, Belgium
(E-mail: dterenty@sckcen.be)

²Materials Science and Engineering, Department of Engineering, The University of Liverpool, Brownlow Hill, Liverpool L69 3GH.

³Computer Sciences and Mathematics, ORNL, Oak Ridge, TN 37831, USA

ABSTRACT

Molecular dynamics simulations were used to investigate reactions between an $\frac{1}{2}\langle 111 \rangle\{110\}$ edge dislocation with interstitial dislocation loops with Burgers vector equal to either $\frac{1}{2}\langle 111 \rangle$ or $\langle 100 \rangle$. The loop size was varied from 0.5 nm up to 8.6 nm, and simulations of both static and dynamic conditions were performed. The results obtained show that small loops (with size up to ~ 1 nm) are easily absorbed by reaction with edge dislocations, independently of their Burgers vector. Large loops are strong obstacles and, depending on the difference in orientation of the dislocation and loop Burgers vectors, are either completely or partially absorbed. The mechanism that provides complete absorption of relatively large loops involves propagation of the reaction segment, formed in favourable dislocation reaction, over the loop surface. This motion is controlled by cross-slip of the screw dislocations formed in a dipole and can involve complicated dislocation reactions. Thus, thermally-activated glide and/or decomposition of the pinning segment formed in the favourable reaction determines both the absorption and critical stress, and therefore depends on temperature, strain rate and loop size.

1. Introduction

The microstructure of neutron-irradiated ferritic alloys, which are important structural materials for nuclear reactors, typically consists of dislocation loops, nano-voids and second-phase particles. At sufficiently high doses (a few dpa), defects detectable by transmission electron microscopy (TEM) in bcc Fe and Fe-based alloys are mainly self-interstitial atom (SIA) dislocation loops (henceforth DLs) with Burgers vector, \mathbf{b}_L , equal to either $\frac{1}{2}\langle 111 \rangle$ or $\langle 100 \rangle$ (see [1,2] and references cited therein). DLs present in the matrix pin dislocations by either contact or elastic interaction and obstruct their motion, which leads to an increase of the yield stress and reduction in ductility. Furthermore, experiments suggest that the ability of dislocations to absorb DLs assists in the formation of defect-free channels, which may cause plastic instability and loss of work hardening [3]. Rationalization of these phenomena requires detailed understanding of the interaction mechanisms between dislocations and radiation-induced defects, including dislocation loops. This can be provided by atomic-scale computer simulations

using molecular dynamics (MD) techniques. In such simulations, shear strain, γ , is applied at a constant rate, $\dot{\gamma}$, to a model crystal containing a dislocation line and loop, and the corresponding shear stress, τ , is calculated from the reaction force exerted on the sheared boundaries by the crystal [4].

A series of MD studies has been focused on the interaction of a $\frac{1}{2}\langle 111 \rangle \{110\}$ edge dislocation with a periodic row of DLs in iron with \mathbf{b}_L equal to either $\frac{1}{2}\langle 111 \rangle$ or $\langle 100 \rangle$ [5-9]. For the $\frac{1}{2}\langle 111 \rangle$ loops it has been revealed that those with \mathbf{b}_L parallel to the dislocation glide plane (DGP) do not offer significant resistance to the glide of an edge dislocation and can be easily absorbed or dragged by it: we do not consider them further here. DLs with \mathbf{b}_L inclined to the DGP are attracted by an edge dislocation and react with it [7]. Small DLs (e.g. containing up to 37 SIAs) are easily absorbed as superjogs on the dislocation line [7]. Larger ones (>100 SIAs) react with the dislocation to form a segment with \mathbf{b} of $\langle 100 \rangle$ type, which is sessile in the DGP and thus pins the dislocation [5,7,8]. The reaction mechanism and the critical stress, τ_C , required to unpin the dislocation was found to depend on temperature and loop size [5-8]. The results obtained so far suggest that even relatively large $\frac{1}{2}\langle 111 \rangle$ loops (331 SIAs) can be completely absorbed at sufficiently high temperature ($\geq 300\text{K}$). Favourable reactions with $\langle 100 \rangle$ loops form $\frac{1}{2}\langle 111 \rangle$ segments and, in contrast with $\frac{1}{2}\langle 111 \rangle$ DLs, have a wider variety of outcomes, ranging from no to total loop absorption by the edge dislocation [9]. Furthermore, $\langle 100 \rangle$ DLs with \mathbf{b}_L laying in the dislocation slip plane are strong barriers to dislocation glide, others are weak.

The main goal of the present work is to review details of absorption of $\langle 100 \rangle$ and $\frac{1}{2}\langle 111 \rangle$ loops by reaction with an edge dislocation and the factors controlling it. We therefore used MD simulations to study reactions of the edge dislocation with DLs with size varied from 0.5nm (invisible in a TEM) up to 8.6nm (easily resolvable), in both static ($T = 0\text{K}$) and dynamic ($T = 1 - 600\text{K}$) conditions. Headings (e.g. Introduction, Procedure, Numerical Methods, Results, Discussion, etc.) should be in 12 pt, bold and title case. Please number headings (1., 2., 3., etc.). Provide one space between heading and text and double spaces between text and following heading.

2. Simulation technique

The $\frac{1}{2}[111](\bar{1}\bar{1}0)$ edge dislocation was constructed using the model of a periodic array of dislocations developed in [4]. Dislocation glide occurred by applying a $[111](1\bar{1}0)$ shear strain at a constant rate, $\dot{\gamma}$, in the range from 10^6 to $5 \times 10^7 \text{ s}^{-1}$. The corresponding stress-strain relationships ($\tau - \gamma$) for the dislocations reacting with loops were obtained, by estimating the stress acting on the fixed parts of the MD crystallite subject to displacement [4].

A straight edge dislocation was formed in the MD cell and the atoms relaxed to minimize potential energy before the DL was created, after which relaxation was performed again. The model was then equilibrated at the chosen temperature, T , prior to application of shear strain. Circular $\frac{1}{2}\langle 111 \rangle$ SIA loops were placed below the dislocation slip plane, while square $\langle 100 \rangle$ loops (with sides oriented along $\langle 110 \rangle$ directions) were placed so that the dislocation could intersect them. The number of defects in the DLs was varied from 37 up to 1225 interstitials. Simulation of reactions with the largest loops was performed in crystals containing up to 6M of atoms, whereas reactions involving smaller loops were modelled in crystals containing $\sim 1\text{M}$ of atoms. The length of the dislocation line (L) was varied from 20.5nm up to 61.5nm and the

crystal size along [111] direction was varied from $100b$ up to $200b$ depending on the DL size and simulation temperature, to avoid the self interaction of the dislocation via periodic boundary (along [111] direction). The size of the crystal along $[1\bar{1}0]$ direction was kept constant equal to 20nm. Thus, the dislocation density was varied in the range $1-2 \times 10^{15} \text{ m}^{-2}$, resulting in the equilibrium dislocation velocity (in the range of above-specified strain rates) ranging from 2 to 200 m/s.

All simulations were performed within NVE ensemble without additional temperature control. MD integration time step was 5fs for simulations at 1K and 2fs at higher T . All simulations used the many-body interatomic potential for Fe from [10]. Identification of the dislocation line and dislocation loops was realized via atomic disregistry and/or coordination number and/or potential energy deviation analyses [4]. For understanding of the dislocation reactions introduced later, the direction of the Burgers vector and line sense is as defined by the RH/FS convention, e.g. [11].

3. Results and discussion

3.1. Absorption of $\frac{1}{2}\langle 111 \rangle$ loops

Two reaction mechanisms resulting in complete absorption by the edge dislocation of DLs (with \mathbf{b}_L equal to either $\frac{1}{2}[1\bar{1}1]$ or $\frac{1}{2}[\bar{1}11]$ inclined to the $(1\bar{1}0)$ glide plane) have been reported [5,7,8]. In one ($\mathbf{b}_L = \frac{1}{2}[1\bar{1}1]$ [7,9]), the reaction forms a $\langle 100 \rangle$ segment which pins the dislocation and causes a screw dipole to form on the dislocation as it bows forward under increasing τ . Eventually, the reaction segment glides across the loop surface and converts \mathbf{b}_L to $\frac{1}{2}[111]$. In the other ($\mathbf{b}_L = \frac{1}{2}[\bar{1}11]$) [5,9]), the $\langle 100 \rangle$ reaction segment splits into two screw segments, which also glide across the loop surface and convert it into a set of superjogs. Here, we have observed both mechanisms, but complete or even partial loop absorption did not occur in all reactions. As demonstrated already in [7], small $\frac{1}{2}\langle 111 \rangle$ loops (up to 37 SIAs) change \mathbf{b}_L spontaneously to that of the dislocation and the absorption process does not require an additional stress. With the interatomic potential used here, the smallest loop to undergo spontaneous absorption at 300K contained 37 SIAs (diameter $D \sim 1.5$ nm), while additional stress was required for a loop containing 61 SIAs ($D \sim 1.9$ nm). Furthermore, the stress needed for the absorption reaction to proceed increases approximately linearly with D for simulations at the same T and $\dot{\gamma}$, as seen in Fig. 1(a) for 300K and 10^7 s^{-1} . Thus, the absorption of relatively large SIA loops (1.5-4.5 nm) occurs at high stress. The largest loop ($D = 8.6$ nm containing 1225 SIAs) was not absorbed in the same simulation conditions, however, for the two screw arms forming the pinned dipole were seen to glide towards each other in the DGP and annihilate at τ_C .

Loop size is not the only factor controlling absorption. As noted above, absorption of relatively large DLs requires motion of the $\langle 100 \rangle$ reaction segment across the loop surface, and this occurs under the action of cross-slip of the two screw side arms of the dislocation as it bows out [7,8]. The stress (say $\tau_{\langle 100 \rangle}$) required for glide of the $\langle 100 \rangle$ segment and/or cross-slip of a screw dipole appears to depend on T , since a significant decrease of τ_C in reactions with $\frac{1}{2}[1\bar{1}1]$ loops was observed in [8] for simulations above 300K and was found here as well (see Fig. 1(b)). In low- T simulations, when $\tau_{\langle 100 \rangle}$ is relatively high and the reaction segment less mobile, the screw dipole simply extends under the applied stress. On reaching sufficient length, the screw arms glide (in the DGP) under their mutual attraction, annihilate and release the dislocation from the loop.

Thus, the probability of absorption decreases with decreasing T at fixed D and $\dot{\gamma}$. Furthermore, it is observed that the probability decreases with increasing $\dot{\gamma}$. This is due to a combination of the low mobility of the $\langle 100 \rangle$ reaction segment and rapid elongation of the screw dipole, which allows the two screw dislocations to reach a length when they annihilate by glide in the DGP rather than cross-slip.

Below we present a few illustrative examples. Reactions with a $\frac{1}{2}[1\bar{1}1]$ loop of 169 SIAs ($D=3.2\text{nm}$) at $\dot{\gamma}=10^7\text{s}^{-1}$ result in complete absorption for $T > 100\text{K}$. In low- T or simulations, the dipole annihilates via glide of the screw dislocations, with the result that no absorption occurs. The configuration of the dislocation and loop at τ_C for $T=0\text{K}$ (static simulations) is shown in Fig. 2(a). Note the large difference in τ_C for the reactions at 0 and 300K in the plot of Fig.1(b). For large loops, $\tau_{\langle 100 \rangle}$ is sufficiently high for the screw dipole to grow and reach the critical length for annihilation even at relatively high temperature (e.g. 300K). The situation where glide of the $\langle 100 \rangle$ reaction segment and closure of the screw dipole by glide of screw arms are competing processes occurs for a 4.6nm $\frac{1}{2}[1\bar{1}1]$ DL (containing 360 SIAs) at 300K. The dislocation configurations at τ_C and the stress-strain curves obtained at different $\dot{\gamma}$ are presented in Fig.3. It is clear that the dipole is much shorter at τ_C for lower strain rate (Fig.3(a)), where complete absorption occurs. Reactions at higher $\dot{\gamma}$ lead to partial absorption only. Again, there is a significant difference in τ_C for low and high $\dot{\gamma}$.

3.2. Absorption of [001] loops by the edge dislocation

Let us first describe the observed absorption mechanism and then discuss factors controlling it. Visualization snapshots extracted from MD simulations showing the dislocation-DL configurations with increasing time for reactions involving [001] loops containing 169 SIAs are presented in Fig. 4. The square loops have $[110]$ and $[1\bar{1}0]$ sides. The uppermost loop segment has direction $[110]$ and lies in the dislocation slip plane in Fig.4(a1) and the centre of the loop is located in the dislocation slip plane in Fig.4(b1). The interaction process in these reactions is as follows.

a) The dislocation is initially attracted towards the loop and undergoes a reaction (energetically-favourable according to Frank's rule) with the upper side of the loop to form a $\frac{1}{2}[11\bar{1}]$ segment (Fig.4(a2)). This reaction segment propagates across the loop surface (Fig.4(a3)), converting b_L to $\frac{1}{2}[111]$, so that the loop is incorporated in the dislocation line as a set of superjogs (Fig.4(a4)). The superjogs rearrange into a U -shape with segments aligned along $\langle 112 \rangle$ directions and the dislocation continues to glide.

b) The dislocation is initially attracted towards the loop to form a short $\frac{1}{2}[1\bar{1}\bar{1}]$ reaction segment (Fig.4(b2)) with one of the $[1\bar{1}0]$ loop sides direction perpendicular to the DGP. b_L of the larger part of the loop then converts into $\frac{1}{2}[1\bar{1}1]$ orientation, resulting in the configuration shown in Fig.4(b3). The latter consists of a set of edge and screw segments (labeled $\frac{1}{2}[\dots]$ s in Fig.4(b3)) connecting two arms of the edge dislocation. The newly-created screw segments, formed by splitting of the $[010]$ segment, glide across the loop surface removing the $[001]$ segment and

forming the configuration shown in Fig.4(b4). The latter is incorporated on the edge dislocation as a set of glissile $\frac{1}{2}[111]$ superjogs (see Fig.4(b5)).

The critical stress, τ_c , and the fraction of interstitials absorbed in the reactions above depend on loop size and T (and presumably on $\dot{\gamma}$, but this has not been studied as yet). The size-dependence of τ_c for the reaction in Fig.4(a) for $T=300\text{K}$ and $\dot{\gamma}=10^7\text{s}^{-1}$ is shown in Fig.1(a). τ_c increases linearly with the D to reach 470MPa for the largest size considered (7nm), which is close to the value for the $\frac{1}{2}[1\bar{1}1]$ DL of 8.5nm size. (Both of these loops contain approximately the same number ~ 1225 of SIAs.) However, despite the same critical stress, the $[001]$ loop was completely absorbed in the simulations whereas the $\frac{1}{2}[1\bar{1}1]$ loop was not.

The T -dependence of τ_c for the reaction at $\dot{\gamma}=10^7\text{s}^{-1}$ with the $[001]$ loop of 3nm size shown in Fig.4(a) is presented in Fig.1(b), where τ_c is seen to reduce from 560MPa at $T=0\text{K}$ (static simulations) to 70MPa at 300K. Further increase of T to 600K does not change τ_c . Complete absorption of the loop was observed in reactions modelled above 100K. Below 100K, the formation and glide of relatively long screw segments occurs, as in the cases above for loops having $\mathbf{b}_L = \frac{1}{2}[1\bar{1}1]$ or $\frac{1}{2}[11\bar{1}]$. The dislocation-DL configurations just before glide of the screw arms at τ_c are compared in Fig.2 for the $\frac{1}{2}[1\bar{1}1]$ and $[001]$ loops (each containing 169-SIAs, simulated at 0K). Thus, in low- T simulations, release of the dislocation is controlled by glide of the screw dipole segments, which occurs prior to motion of the $\frac{1}{2}\langle 111 \rangle$ reaction segment, which also controls absorption. Hence, the mechanisms of absorption are similar for the $\frac{1}{2}\langle 111 \rangle$ and $\langle 100 \rangle$ dislocation loops. We note, however, that the stress at which a $\frac{1}{2}\langle 111 \rangle$ reaction segment glides over $\langle 100 \rangle$ DL surface may be significantly different from that at which a $\langle 100 \rangle$ segment glides over a $\frac{1}{2}\langle 111 \rangle$ loop.

4. Concluding remarks

The simulation of reactions between edge dislocations and dislocation loops with $\mathbf{b}_L=1/2\langle 111 \rangle$ or $\langle 100 \rangle$ has shown the following.

- (i) Small loops (with size up to $\sim 1\text{nm}$) are easily absorbed by reaction with edge dislocations, independently of their Burgers vector.
- (ii) Large loops are strong obstacles and, depending on the difference in orientation of the dislocation and loop Burgers vectors, are either completely or partially absorbed. The critical stress and reaction product depend on T and are controlled by the mobility of either the dislocation segment formed by a favourable DL-dislocation reaction or screw dislocations in a dipole drawn out on the pinned dislocation.
- (iii) In general, the mechanism that provides complete absorption of relatively large loops involves propagation of the reaction segment over the loop surface. This motion is controlled by cross-slip of the screw dislocations formed in a dipole and can involve complicated dislocation reactions. (Examples of different reactions can be found in [9].)
- (iv) Thus, thermally-activated glide and/or decomposition of the pinning segment formed in the favourable reaction determines both the absorption and critical stress, and therefore depends on temperature, strain rate and loop size.

(v) Irrespective of whether loop absorption on the dislocation is complete or not, the absorbed interstitials form a set of glissile $\frac{1}{2}\langle 111 \rangle$ superjogs, so that after unpinning the edge dislocation moves under approximately the same stress as a perfect straight dislocation.

Acknowledgements

This work was performed in the framework of the 7th Framework Programme collaborative project GETMAT, partially supported by the European Commission, grant agreement number 212175.

References:

- [1] S.J. Zinkle and B.N. Singh, *J. Nucl. Mater.* **351** (2006) 269.
- [2] A.C. Nicol, M.L. Jenkins and M.A. Kirk, *MRS Symp. Proc.* **650** (2001) R.1.3.1.
- [3] M. Victoria, N. Baluc, C. Bailat, et al. *J. Nucl. Mater.* **276** (2000) 114.
- [4] Yu.N. Osetsky and D.J. Bacon, *Model. Simul. Mater. Sci. Eng.* **11** (2003) 427.
- [5] A. Nomoto, N. Soneda, A. Takahashi and S. Ishino, *Materials Transactions* **46** (2005) 463.
- [6] Z. Rong, Yu.N. Osetsky and D.J. Bacon, *Phil. Mag.* **85** (2005) 1473.
- [7] D.J. Bacon, Yu.N. Osetsky and Z. Rong, *Phil. Mag.* **86** (2006) 3921.
- [8] D. Terentyev, L. Malerba, D.J. Bacon and Yu.N. Osetsky, *J. Phys.: Condens Matter* **19** (2007) 13.
- [9] D.A. Terentyev, P. Grammatikopoulos, D.J. Bacon and Yu.N. Osetsky, *Acta Mat.* (2008) submitted.
- [10] G.J. Ackland, M.I. Mendeleev, D.J. Srolovitz, D. Han and A.V. Barashev, *J. Phys: Condens. Matter* **16** (2004) 1.
- [11] D. Hull and D.J. Bacon, *Introduction to Dislocations*, 4th edition, Oxford: Butterworth-Heinemann (2001).

α - α' phase separation in Fe-Cr alloys and its impact on mechanical properties: An atomistic study

Giovanni Bonny¹, Dmitry Terentyev¹, Lorenzo Malerba¹

¹SCK-CEN, Nuclear Materials Science Institute, Boeretang 200, B-2400 Mol, Belgium
(E-mails: Gbonny@sckcen.be; Dterenty@sckcen.be; Lmalerba@sckcen.be)

ABSTRACT

In this work atomistic kinetic Monte Carlo is applied to simulate thermal ageing of binary Fe-Cr alloys, where a description of the atomic interactions is provided by semi-empirical interatomic potentials, fitted to density functional theory data. We performed our studies varying the Cr content in the range of 12-21 at.% Cr in the temperature range 600-900K. The evolution of the phase separation process is characterised in terms of density and mean size of the formed precipitates, allowing for the estimation of the critical size for stable precipitates. The obtained results are compared with experimental works.

1. Introduction

Fe-Cr alloys are the base for ferritic and ferritic/martensitic (F&FM) steels, which have a wide range of applications as structural materials in aggressive high temperature environments, such as gas turbines in conventional power plants, or key components in future nuclear reactors. Binary Fe-Cr alloys and F&FM steels undergo α - α' phase separation if the Cr content, x_{Cr} , exceeds ~ 9 at.%, in the region of temperatures potentially important for technological applications (>700 K) [1-3]. The formation of finely-dispersed, nanometric-size, coherent Cr-rich precipitates in the bulk and at dislocations is long since known to be the cause of hardening and embrittlement of F&FM steels with $x_{Cr} > 9$ at.% after thermal ageing and under irradiation. Therefore, a quantitative understanding of the kinetics of α - α' decomposition and its impact on mechanical property changes in Fe-Cr alloys is an important issue to be addressed.

In the present work atomistic kinetic Monte Carlo (AKMC) methods are used to simulate bulk thermal ageing in Fe-Cr crystals, where the cohesive model is provided by a density functional theory (DFT) based interatomic potential. The kinetic evolution of the α - α' phase separation is characterised in terms of precipitate size and density, allowing for the estimation of the critical size for stable precipitates.

2. Methodology

The thermal ageing was modelled using a rigid lattice AKMC technique [4]. The evolution of the system was driven by single vacancy diffusion, performing migration jumps at a rate

$G = n_0 \exp(-E_m/k_B T)$, where n_0 is an attempt frequency (taken as $6 \times 10^{12} \text{ s}^{-1}$), E_m is the local atomic environment (LAE) dependent migration energy, k_B is the Boltzmann constant and T is the absolute temperature. The dependence of E_m on LAE is introduced as $E_m = E_0 + \Delta E_{f-i}/2$, where ΔE_{f-i} is the total energy change due to the vacancy jump and E_0 is the excess migration energy. E_0 is taken as the migration barrier for an Fe (Cr) atom exchanging position with the vacancy, calculated by DFT (in the limit of dilute solution [5]) to be 0.65 and 0.55 eV for Fe and Cr species, respectively. The atomic interactions defining the total energy are described by an interatomic potential developed by Olsson et al. [6].

The Cr-concentration x_{Cr} and temperature T were chosen to be within the miscibility gap where α - α' phase separation is expected to occur, and also to be relevant for technological nuclear applications: 12-18% Cr and 600-900 K. Initially, Cr atoms were randomly distributed in a bcc Fe matrix with size $40 \times 40 \times 40$ cubic cells, containing 128,000 atoms in total. The atomic configurations resulting from the vacancy diffusion process were analysed using a technique developed by the authors [7], so that the average precipitate size and density could be extracted.

3. Results

Applying the above methodology, the precipitates were identified during thermal annealing and their average diameter d_p and density N_p were determined as a function of Monte Carlo time t_{MC} . Both are presented in Figs. 1a and 1b. From these figures, the three regimes of the precipitation process, namely nucleation, growth and coarsening, can be identified. The initial step increase of N_p and slow growth of d_p denote a dominant nucleation regime. The presence of the plateau around the peak density N_p^{max} and the simultaneous fast growth of d_p is to be attributed to the onset of the growth stage. Finally, the decrease of N_p and simultaneous increase of d_p indicates the coarsening stage, at which larger precipitates grow at the cost of the dissolution of smaller ones.

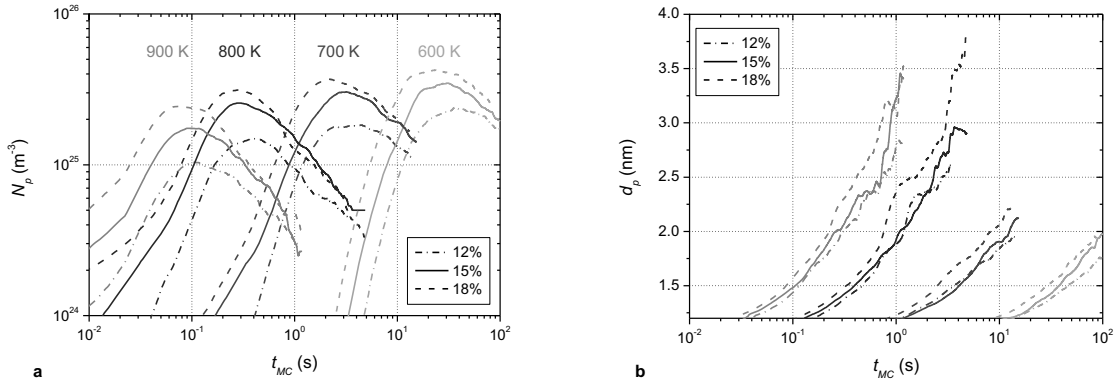


Figure 1. (a) The precipitate density and (b) average diameter as a function of t_{MC} .

It was found that N_p^{max} increases linearly with x_{Cr} and decreases with T , and that the corresponding d_p stays constant at 1.4 ± 0.1 nm, for all x_{Cr} and T here studied. This means that at 'peak time' (the moment corresponding to the higher precipitate density in the system) only the density of the precipitates varies with x_{Cr} and T and not d_p .

The clear identification of the three stages of the precipitation process and the agreement with theoretical considerations allows us to go further and use the obtained simulation results to assess the critical free energy barrier and cluster size for a precipitate to become stable. In the theory of homogeneous nucleation [8] the nucleation rate, \dot{N}_p , scales as

$$\dot{N}_p \propto \exp(-\Delta G_c / k_B T), \quad (1)$$

where ΔG_c is the critical free energy barrier for nucleation, i.e. for the precipitate to become stable. Applying Eqn. (1) to \dot{N}_p obtained from the N_p -curves in Fig. 1a, ΔG_c is estimated around 0.76 eV. Assuming spherical precipitates, within the same theory [8] the expression for the critical radius, R_c , reads

$$R_c = \sqrt{\frac{3\Delta G_c}{4ps}}, \quad (2)$$

where σ denotes the α - α' interface energy. Estimating σ around 5-10 meV/Å² (depending on the surface orientation), R_c is found to be about 0.6-0.4 nm.

4. Discussion

A direct comparison of the results obtained using the AKMC simulations with thermal ageing experiments is difficult due to the absence of a safe criterion connecting t_{MC} with real time t_{real} . Here, we use experimental data to establish the synchronization of t_{real} and t_{MC} , based on the correspondence between d_p seen in simulations and experiment. After intensive literature survey, the most suitable experimental works found were [2, 3] where relatively pure Fe-20at.%Cr alloys were thermally aged at 793 K. The small angle neutron scattering (SANS) technique was used to trace the precipitation evolution. The shortest studied ageing time was 12 h and 20 h, respectively and from then on only the coarsening stage was observed. Additional AKMC simulations for Fe-20at.%Cr aged at 793 K were therefore performed to obtain the synchronization coefficient, C , as $t_{real} = C t_{MC}$. The latter was estimated to be 4.15×10^5 and 6.92×10^4 using data regarding d_p from [2] and [3], respectively. The results for N_p and d_p are presented and compared with the experimental data [2, 3] in Figs. 1a and 1b, respectively.

It is clear that for both estimates of the synchronisation factor C the agreement with experiment is reasonable. Note that the discrepancy between the two experiments is probably due to slightly different interpretations of the SANS data.

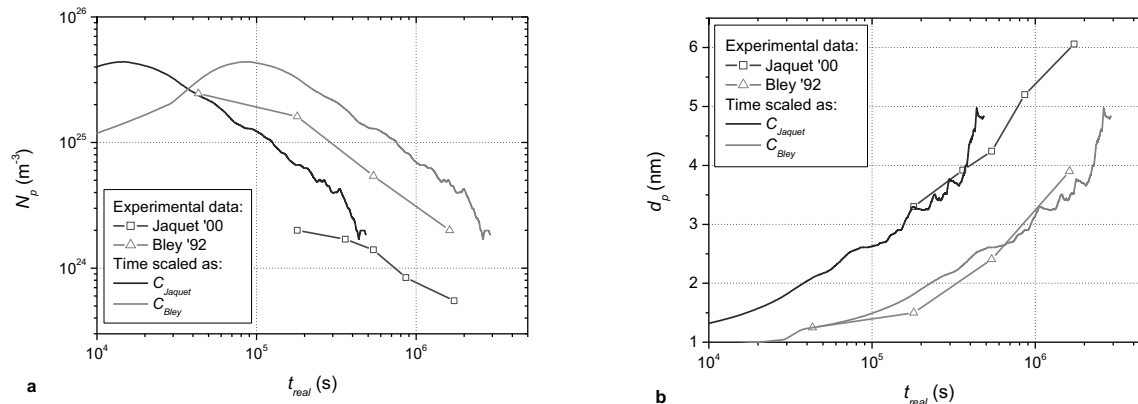


Figure 2. (a) Comparison of the precipitate density and (b) average diameter with experimental observations.

5. Conclusions

An atomistic kinetic Monte Carlo approach has been applied to study the precipitation process in Fe-Cr alloys varying Cr content and temperature. The precipitation process has been characterized in terms of precipitate size and density. The obtained results have shown that the precipitation process in the studied alloys occurs in three stages, namely: nucleation, growth and coarsening.

The critical size for stable precipitates was determined to be less than 1.2 nm, which is at the limit of the resolution of experimental techniques. The maximum density was found to vary with temperature and Cr content, but the average precipitate size (at the moment when the maximum density is reached) remains the same ($d_p=1.4$ nm) within the error of the calculations.

Comparison of the precipitate size and density showed adequate agreement with experiment. We therefore believe that the presented results can serve to describe the evolution of precipitation process in its early stages, which is beyond the current experimental observation techniques.

6. References

- [1] R.M. Fisher, E.J. Dulis, and K.G. Carroll, *Trans. AIME*, **197**, 690 (1953).
- [2] F. Bley, *Acta Metall. Mater.*, **40**, 1505 (1992).
- [3] V. Jaquet, PhD. Thesis, Ecole Polytechnique, Palaiseau, France (6 March 2000).
- [4] C. Domain, C.S. Becquart, and J.C. Van Duysen, *Mater. Res. Soc. Symp. Proc.*, **650**, R3.25.1 (2001).
- [5] P. Olsson, C. Domain, J. Wallenius, *Phys. Rev. B*, **75**, 014110 (2007).
- [6] P. Olsson, J. Wallenius, C. Domain, K. Nordlund, and L. Malerba, *Phys. Rev. B*, **72**, 214119 (2005).
- [7] G. Bonny, D. Terentyev, and L. Malerba, *Comput. Mater. Sci.*, **42**, 107 (2008).
- [8] J.W. Gibbs, *Trans. Conn. Acad.*, **3**, 102 (1878).

Dislocation Core Fields and Elasticity Theory: The Screw Dislocation in Iron

Emmanuel Clouet^{1,2,3}, Lisa Ventelon¹, and François Willaime¹

¹Service de Recherches de Métallurgie Physique, CEA-Saclay, 91191 Gif-sur-Yvette, France; ²Laboratoire de Métallurgie Physique et Génie des Matériaux, UMR CNRS 8517, Université de Lille 1, 59655 Villeneuve d'Ascq, France
E-mail : ³emmanuel.clouet@cea.fr.

ABSTRACT

Recent ab initio calculations in bcc iron [1] show that the displacement created by a screw dislocation cannot be described only by the Volterra solution. A short-range elastic field is created too by a dilatation of the dislocation core. We model this supplementary elastic field in anisotropic elasticity theory using force dipoles located in the core along the dislocation line. This dilatation field is responsible for the dislocation formation volume measured in ab initio calculations ($\delta V = 2.5 \pm 0.5 \text{ \AA}^2$ for the screw dislocation). Taking into account this core dilatation in the elastic modeling allows reproducing the ab initio displacement maps obtained for different configurations of the dislocation dipole. Moreover, because of the interaction between the Volterra elastic field and the one created by the core dilatation, it is necessary to consider both contributions when calculating the elastic energy associated to a dipole. Neglecting the core field in the calculation will lead to dislocation core energy with a strong dependence on the dipole geometry and on the size of the simulation unit cell.

[1] L. Ventelon and F. Willaime, “Core Structure and Peierls Potential of Screw Dislocations in α -Fe from First Principles: Cluster versus Dipole Approaches”, *J. Computer-Aided Mater. Des.* **14**, 85 (2007).

This work was supported by the European Fusion Materials Modeling program and by the SIMDIM project under contract ANR-06-BLAN-250.

On micromechanical models of nonlocal media

Xi Yuan

**Advanced Simulation Technology of Mechanics (ASTOM) R & D
yuanxi@astom.co.jp**

ABSTRACT

Despite the recent noticeable development in nonlocal mechanics, the micromechanical analysis on nonlocal effects arising from heterogeneous media is still rife with conflicting views. The author has recently developed a new micromechanics based homogenization method (Mechanics research communications, 35 (2008), 126-133) trying to resolve this problem. In this work, the method is applied to derive cosserat moduli of some media with simple microstructure.

Analysis of Transformation Plasticity Using a Finite Element Model Coupled with a Phase Field Method

Yi-Gil Cho¹, Jin-You Kim², Pil-Ryung Cha², Jae Kon Lee³, Heung Nam Han¹

¹**Department of Materials Science and Engineering, Seoul National University, Sillim 9-dong, Gwanak-gu, Seoul, 151-744, Republic of Korea;**

²**School of Advanced Materials Engineering, Kookmin University, Seoul, 136-702, Republic of Korea;**

³**Sheet Product and Process Research Group, Technical Research Laboratories, POSCO, Pohang, 790-785, Republic of Korea;**

ABSTRACT

Transformation plasticity is that when a phase transformation of ferrous or non-ferrous alloys progresses even under an extremely small applied stress compared with a yield stress of the material, a permanent deformation occurs [1-6]. One of widely accepted description for the transformation plasticity was proposed by Greenwood and Johnson [1]. Their description is based on an assumption that a weaker phase of an ideal plastic material could deform plastically to accommodate the externally applied stress and the internal stress caused by the volumetric change accompanying the phase transformation.

In this study, an implicit finite element model was developed to simulate the deformation behavior of a low-carbon steel during phase transformation. The finite element model was coupled with a phase field method, which could simulate the kinetics for ferrite-to-austenite transformation of the steel. The latent heat generation by the phase transformation was implemented in both simulations. The thermo-elasto-plastic constitutive equation for each phase was adopted to confirm the weaker phase yielding, which was proposed by Greenwood and Johnson [1]. From the simulation, the origin of the transformation plasticity was quantitatively discussed comparing with the other descriptions [2-6] of it.

- [1] G.W. Greenwood and R.H. Johnson, Proc. R. Soc. London A, **283**, 403 (1965).
- [2] P. Zwigl and D.C. Dunand, Acta Mater., **45**, 5285 (1997).
- [3] E. Gautier, A. Simon and G. Beck, Acta metall. **35** 1367 (1987).
- [4] J.B. Leblond, J. Devaux and J.C. Devaux, Int. J. Plasticity **5** 551 (1989).
- [5] H.N. Han and D.-W. Suh, Acta mater. **51** 4907 (2003).
- [6] H.N. Han, J.K. Lee, D.-W. Suh and S.-J. Kim, Philos. Mag. **87** 159 (2007).

The authors would like to thank for support by the Korea Science and Engineering Foundation (KOSEF) grant funded by the Korea government (MOST) (R0A-2007-000-10014-0).

Al atomistic dislocation simulations using a tight-binding method

Chee Gan¹, Siu-Sin Quek²

Materials Theory and Simulation, IHPC, Singapore
¹ganck@ihpc.a-star.edu.sg, ²quekss@ihpc.a-star.edu.sg

ABSTRACT

We present a novel multiscale modeling approach that can simulate millions (or even billions) of electrons effectively with density functional theory (DFT). The method is based on a full formulation of quasicontinuum (QC) approach, including both local and nonlocal contributions. The only energetic formulation is the present method is Orbital-Free DFT (OFDFT). The local QC contribution is handled by Cauchy-Born rule with OFDFT calculations. The quantum mechanical problem of the nonlocal electrons is solved in the presence of the local electrons and nuclei. The coupling between the local/nonlocal atoms is calculated quantum mechanically via OFDFT. The method is demonstrated with a nano-indentation study of Al thin film (the entire system contains more than 60 millions atoms). The results are compared with those determined from EAM-based QC simulations.

Numerical Analysis of Ceramics under Impulsive Loads at Grain Scale

Sascha Knell, Martin Sauer, Klaus Thoma

**Fraunhofer Institute for High-Speed Dynamics, Ernst-Mach-Institut
Eckerstrasse 4, 79104 Freiburg, Germany
sascha.knell@emi.fhg.de**

ABSTRACT

The response of a ceramic material to impulsive loads depends on its composition and structure at grain scale. The analysis of this dependency is still an open issue. Knowledge of the key characteristics at that scale would allow the purposive design of ceramic materials optimized for a desired macroscopic response. The grain structure of a ceramic is characterized by morphology, distribution of orientation and size of the crystalline grains and the material properties of grains and grain boundaries. Typically, the grain diameters of the regarded ceramics range between a few up to one hundred micrometers. The considered scale suggests treating single grains as continua and grain boundaries as planes. Transient FEM accounting for interfacial failure is applied as numerical method. The numerical analysis is conducted on the basis of three-dimensional virtual samples consisting of a representative number of grains. These representative volumes (RVs) are generated via power diagrams whose statistical moments are optimized to be in accordance with those of the considered ceramic [1]. Preceding numerical analyses of the pure elastic response of a RV under dynamic loading suggest that the crystal lattice based anisotropy of the single grains has to be accounted for [2].

In this study the inelastic response, specifically grain boundary failure, of dynamically loaded, generic ceramic RVs is analyzed. Interfacial failure is represented by dynamically inserted interface elements whose response is governed by a cohesive law. The cohesive law is scaled in accordance with the ratio of the typical lengths of the process zone and the discretization. In particular, it is investigated if grain anisotropy influences the threshold and pattern of failure.

- [1] M. Kühn, “Optimierung von Power-Diagrammen zur Modellierung keramischer Mikrostrukturen”, Diplomarbeit, EMI-Bericht **15/05**, Fraunhofer Institut für Kurzzeitdynamik & FU Hagen (2005).
- [2] S. Knell, M. Sauer and K. Thoma, “Mesomechanical Simulation of Elastic Wave Propagation in Al_2O_3 Ceramics”, MMM 2006 Conference proceedings, 469 (2006).

Virtual Processing of Dual Phase Steels – A Microstructure Based Simulation Approach

Alexander Butz¹, Tobias Rist¹, Bianca Springub², Franz Roters³, Stefan Schultz³,

¹Fraunhofer Institute for Mechanics of Materials IWM,
Wöhlerstraße 11, 79108 Freiburg, Germany (alexander.butz@iw.fraunhofer.de)

²Salzgitter Mannesmann Forschung GmbH,
Eisenhüttenstraße 99, 38239 Salzgitter, Germany (b.springub@sz.szmf.de)

³Max-Planck-Institute for Iron Research MPIE,
Max-Planck-Straße 1, 40237 Düsseldorf, Germany (f.roters@mpie.de)

ABSTRACT

The simulation of manufacturing processes is of increasing interest since it enables the virtual optimization of material properties and process parameters. Consequently, this approach implies a high potential to reduce time and cost during development and fabrication. This contribution discusses the simulation of a dual phase steel manufacturing process which is based on a micromechanical approach. The properties of the final steel sheet do strongly depend on the microstructure evolution during processing. For this reason, different modelling strategies are brought together, among them crystal plasticity, cellular automata and continuum mechanics. Special considerations are necessary to ensure an appropriate exchange and transfer of the required data which depend on the modelling strategy of the particular process step. Starting from the hot rolled sheet, a unit cell model is generated to represent the initial ferritic-perlitic microstructure. The essential data to define the initial microstructure are obtained from experiments. The first process step simulated is cold rolling. Here, a single crystal plasticity model is applied to consider texture development, hardening and evolution of anisotropic material properties. The following thermal treatment of the steel sheet takes into account the microstructural changes caused by phase transformation, recrystallization and recovery. A transformation of the initial microstructure into a dual phase microstructure consisting of ferrite and martensite is expected. The final dual phase microstructure is assessed in the “virtual lab” for a numerical homogenization of the mechanical properties. These data will be used to fit appropriate phenomenological plasticity models and to facilitate subsequent process simulation steps.

1. Introduction

The successful introduction of new dual phase steels in the automotive industry strongly depends on the availability of suitable simulation tools. The microstructure of this material changes significantly during processing and affects also the mechanical properties on the macroscopic level such as yield stress, formability, toughness and fatigue resistance. The objective of this research project is to develop an integral simulation concept for the process chain simulation which covers consecutive stages of production beginning with the hot rolled steel sheet and ending with a crash simulation of the particular component. This contribution is focused on the

micro-mechanical aspects which have to be considered within the process chain simulation. Therefore, cold rolling, annealing and the numerical homogenization procedure is discussed in detail.

2. Experimental Simulation and Characterization

The experimental characterization of the hot rolled steel sheet provides the input data for the numerical model. Additional experimental characterizations after each process step are performed to validate the particular results obtained from the numerical simulation. The hot rolled material consists of ferrite and lamellar shaped pearlite. The microstructure and texture of the hot rolled strip are determined by EBSD measurements and will be considered in the subsequent cold rolling simulation, see Fig. 1. Thus, this approach allows to include microstructural data like grain shape and phase distribution and consequently implies material inhomogeneities within the model. Since both phases are modeled separately in the cold rolling simulation, it is also necessary to characterize the mechanical behavior (flow curves) of the ferrite and the pearlite. Therefore, annealing tests were accomplished at a laboratory annealing system. The variation of thermal treatment enables the realization of different well-defined phase compositions with the hot rolled material. Flow curves of the annealing samples are derived from tensile tests and were used to determine the flow curves for each single phase.

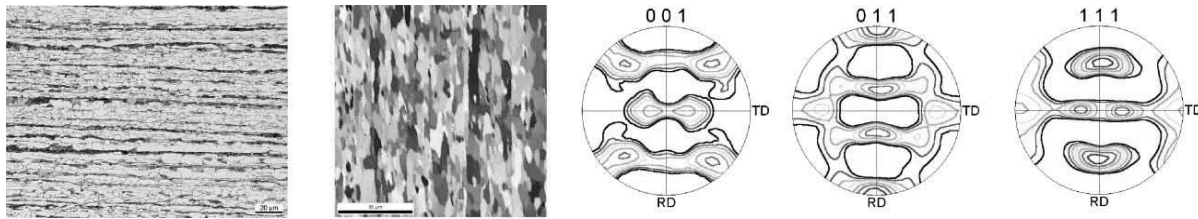


Figure 1. Experimental measurements to determine the of input data for cold rolling simulation. Left: Micrograph of the hot rolled sheet. Center: Orientation map. Right: Pole figures.

3. Cold Rolling Simulation

To take into account the microstructure morphology of the hot rolled sheet within the simulation, the concept of representative volume elements (RVE) is used. A unit cell with 400 ferrite grains and two band-shaped perlitic regions with a volume fraction of 22 % is generated, see Fig. 2. The mechanical behavior of the ferrite grains is modelled within the framework of crystal plasticity; see e.g. [1]. This physically based theory describes plastic flow as a result of the movement of dislocations in a continuum way. This means, that plastic deformation is the result of continuous shearing (slip) along well-defined planes of the crystal lattice. For the numerical simulation a crystal plasticity model, based on [2], and implemented as ABAQUS user material subroutine, is used. A Voce hardening law was also implemented [3]. This modelling strategy allows to predict the texture development, intergranular stresses and morphology evolution as illustrated in Fig. 2. To model the cold rolling process, appropriate periodic boundary conditions have to be defined. Therefore, a prescribed deformation in 3-direction is applied. The deformation in transverse direction is suppressed, since it is assumed that the width of the sheet remains constant. A

mechanical stress in rolling direction can be applied to account for the tensile forces during rolling. The relevant simulation results are transferred to the subsequent annealing simulation using cellular automata.



Figure 2: Left: Periodic unit cell model of the generated microstructure. The band-shaped red region represents the pearlite phase. Center: Deformed unit cell model after cold rolling simulation. Right: Von Mises equivalent stress distribution within the unit cell.

4. Annealing Simulation

The heat treatment of the cold rolled sheet is simulated with a cellular automaton (CA) which is a versatile computational principle [4]. For this purpose, the volume considered is divided into a number of cells. These cells are discrete and assumed to be homogenous. The actual state of each cell is defined by a number of internal variables which independently evolve according to their local neighbourhood by the CA switching rules ζ . For the simulation of the annealing process, the function ζ is based on two internal quantities: the texture information and a driving force in form of e.g. a dislocation density. To define the initial state, the necessary data of one integration point from the previous finite element unit cell calculation are projected to one cell of the cellular automaton. While the current texture is obtained directly from the cold rolling simulation, the dislocation density is not available. Thus, this quantity is correlated with the accumulated plastic slip that follows from the crystal plasticity model [5].

5. Virtual Laboratory

Besides the simulation of microstructure evolution, the unit cell model is utilized to obtain information about the macroscopic material behavior. Therefore, a numerical homogenization procedure [6] is employed. This procedure allows the calculation of macroscopic flow curves under consideration of varying loading directions. This is equivalent to tensile tests with different specimen orientations, and may be denoted as a “Virtual Material Testing” procedure. In principle, this virtual testing can be performed after each simulation step and can predict mechanical properties during the process chain simulation. Further, it allows also to analyze load cases which can not be realized with experiments. The prediction of flow curves after heat treatment is of special interest, since these data are used to calibrate phenomenological plasticity models (e.g. Barlat89) for the subsequent deep drawing simulation step. First results confirm the potential of this approach. In Fig. 3 (left) a dual phase unit cell model with nine ferrite grains and

a spherical martensite portion is depicted after two different steps of deformation. The virtual testing of the deformed unit cell with varying loads is illustrated in the middle of Fig. 3. The resulting yield locus diagram is calculated for three different degrees of deformation and illustrates the influence on the hardening behavior. Further validation and improvements will be performed in near future.

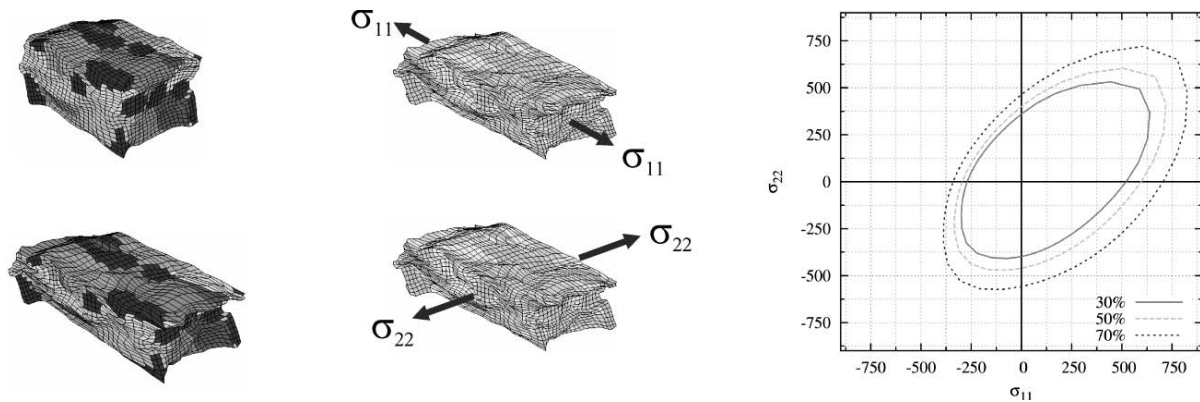


Figure 3: Virtual material testing procedure and resulting yield locus diagram for different degrees of deformation of a dual phase unit cell.

Acknowledgements

The Authors are grateful to Mr. Aruna Prakash for the implementation of the Voce hardening law into the crystal plasticity material subroutine and Dr. Ingo Schmidt for providing the routines to carry out the numerical homogenization procedure. The authors are grateful to the German Ministry for Education and Research for financial support under grant-no. 03X0501E.

References

- [1] R. J. Asaro, "Micromechanics of Crystals and Polycrystals", *Advances in Applied Mechanics*, **23**, (1983).
- [2] Y. G. Huang, "A User-Material Subroutine Incorporating Single Crystal Plasticity in the ABAQUS Finite Element Program", Harvard Univ., Rep. MECH-178 (1991).
- [3] A. Prakash, S. M. Weygand, H. Riedel, "Modeling the Evolution of Texture and Grain Shape in Mg Alloy AZ31 Using the Crystal Plasticity Finite Element Method", *Computational Material Science*, doi:10.1016/j.commatsci.2008.06.015 (2008).
- [4] D. Raabe, "Cellular Automata in Materials Science with Particular Reference to Recrystallization Simulation", *Annual Review of Materials Research*, **32**, (2002).
- [5] D. Raabe, R. C. Becker, "Coupling of a Crystal Plasticity Finite-Element Model with a Probabilistic Cellular Automaton for Simulating Primary Static Recrystallization in Aluminium, *Modelling and Simulation in Materials Science and Engineering*, **8** (2000).
- [6] I. Schmidt, "Deformation Induced Elasto-plastic Anisotropy in Metal Foams – Modeling and Simulation". *International Journal of Solids and Structures*", **41** (2004).

On a Finite Strain Micromorphic Plasticity Model for Bound Particulate Materials

Richard Regueiro

University of Colorado at Boulder, Colorado, USA
regueiro@colorado.edu

ABSTRACT

There is great interest currently in accounting for underlying microstructural response at the grain/particle/fiber scale on the overall continuum mechanical behavior of heterogeneous materials---such as particulate ceramics, concrete, masonry, geomaterials (soils and rocks), asphalt, bone, etc---in terms of *predicting* their damage, initiation of fracture, and localized deformation. Much research has been done on traditional macro-continuum inelastic constitutive modeling such that a wide range of books are available to reference. Likewise, research has been done and is ongoing on simulating directly the inelastic microstructural mechanical response---at the grain/particle/fiber scale---and reported in the literature. One of the current research challenges, however, is how to bridge these length scales, from grain/particle/fiber scale (sometimes called the 'meso'-scale) to the macro-continuum scale of the engineering application, without losing salient kinematic structure and micro-stresses. The finite strain micromorphic plasticity model framework presented in this talk is meant to bridge the mechanics between the grain/particle/fiber and macro-scales: to do so not only in a hierarchical information-passing (homogenization) multi-scale fashion, but also for concurrent multiscale modeling retaining the grain/particle/fiber scale resolution in spatial regions of interest---for instance where damage/micro-cracking initiate---while transitioning to a 'far'-field macro-scale continuum representation via a micromorphic continuum region. The additional degrees of freedom and constitutive richness of the micromorphic continuum mechanics and plasticity equations provide a more plausible transition than standard macro-continuum mechanics. This talk will discuss a phenomenological bridging-scale constitutive modeling framework in the context of finite strain micromorphic plasticity based on a multiplicative decomposition of the deformation gradient F and microdeformation tensor \mathcal{X} . In addition to the 3 translational displacement vector \mathbf{u} degrees of freedom (dofs), there are 9 dofs associated with the unsymmetric microdeformation tensor \mathcal{X} (micro-rotation, micro-stretch, and micro-shear). The Clausius-Duhem inequality formulated in the intermediate configuration yields the mathematical form of three plastic evolutions equations in either 1) Mandel-stress form, or 2) Metric form. The particulars are spelled out for a pressure-sensitive cap plasticity model for bound particulate materials.

Microyield Behaviour of Metallic Multilayers

Marc Verdier

**SIMaP-Center National de la Recherche Scientifique, France
mverdier@ltpcm.inpg.fr**

ABSTRACT

By extracting the variation of the plastic strain rate from measurements of the stress-strain curves of free standing multilayers of varying thickness, the large extent of the microdeformation stage was determined. The stress varies dramatically with strain during this stage [1]. In this work, Dislocation Dynamic simulations [2] are used to investigate the microyield evolution with layer thickness of idealized periodic multilayers configurations : parallel interfaces are introduced in a cubic volume with varying layer thickness, from a few micron period to 300 nm. Crystalline orientations and elastic constants between the layers are kept equal, the 'interfaces' being only defined by a critical normal stress threshold for the crossing of dislocations. Impenetrable boundary conditions are imposed on the cube side. Tensile tests are carried out until macroscopic plasticity is reached, i.e. the cube is sheared through its whole volume. A scaling of the microyield regime is observed with the layer thickness. Moreover, cooperative mechanisms between different slip systems are observed on both side of an interface which bypasses the pile up mechanism imposed by the threshold stress at the interfaces. The results are discussed and compared to experimental conditions.

[1] Saada, G.; Verdier, M. & Dirras, G. F., *Phil Mag*, 2007, 87, 4875-4892 [2] Verdier, M.; Fivel, M. & Groma, I. *Modell. Sim. Mat. Sci. Eng.*, 1998, 6, 755-770

Numerical investigations of compact tension fracture specimens

Pablo Mueller and Philippe Spätig

**EPFL-CRPP, Center de Recherches en Physique des Plasmas, Association Euratom-Confédération Suisse, CH 5332, Villigen PSI, Switzerland
(pablo.mueller@psi.ch, philippe.spatig@psi.ch)**

ABSTRACT

Finite element modeling (FEM) is widely used to predict the response of complex structures to external conditions like applied loads and displacements or temperature changes. FEM is also an important research tool in fracture mechanics where few engineering problems have analytical solutions. Numerical investigations have largely contributed to improve the understanding of the specimen size and geometry effects on cleavage fracture of tempered martensitic, bainitic and ferritic steels in the transition region between the ductile and brittle regime. In order to do so, the so-called local approach of cleavage has been extensively used in the past to account for the size and geometry effect on fracture toughness. In this approach, it is assumed that cleavage occurs when a critical condition, characterized by the attainment of the critical stress state, is reached under increasing load. The material investigated in this study is a high-chromium tempered martensitic steel called Eurofer97 developed within the European fusion reactor material development program. We present a series of 2D plane strain and 3D finite element simulations of loaded pre-cracked compact tension specimens. The simulations were done for constitutive behaviors determined at temperatures in the transition region. The calculated load-displacement curves obtained from the 2D and 3D simulation results are compared with the experimental ones. It is shown that the overall experimental load-deflection curve cannot be properly reconstructed with the 2D simulations, which yield a significantly larger macro-yielding point and a larger elastic slope than the experiments. The limits of the applicability of the 2D simulations to calibrate the critical stress state of the local approach are then discussed. Using a large set of data of the Eurofer97 steel, including two different compact tension specimen sizes, the predictions of the specimen size effect on fracture are analyzed on the basis of the critical stress condition to trigger cleavage.

An Energy Approach to Determine the Martensite Morphology in Nano-Structured NiTi Alloys

T. Antretter¹, W. Pranger¹, T. Waitz², F.D. Fischer¹

¹**Institute of Mechanics, Montanuniversität Leoben, Franz-Josef Strasse 18, A-8700 Leoben, Austria, mechanik@unileoben.ac.at;**

²**Physics of Nanostructured Materials, University of Vienna, Strudlhofgasse 4, 1090 Vienna, Austria, thomas.waitz@univie.ac.at**

ABSTRACT

Nano-structured NiTi alloys are produced by high pressure torsion up to complete amorphization and subsequent recrystallization. Its morphology is essentially influenced by the energies introduced into the material when an austenitic grain instantaneously transforms into martensite. For grain sizes in the order of 50nm one frequently observes typical martensite laminates composed of an alternating sequence of twin-related Bain correspondence variants [1]. For larger grains in the order of 100nm it becomes more likely to observe two such martensite laminates whose arrangement relative to each other, as it appears in a micrograph, gives the impression of a “herring-bone pattern”. Such a configuration prevails if it minimizes the energy that needs to be overcome in order to be able to create the new phase [2]. In partially transformed grains one frequently finds wedge-shaped martensite sections with a certain energy optimizing wedge-angle. Consequently, this paper focuses on the evaluation of the energies involved in the phenomenon of martensitic transformation. As one of the predominant contributions the strain energy is computed by both the finite element method and, where available, analytical means. The total energy is then obtained by additionally taking into account the chemical interface energies at the twin- as well as the grain-boundaries. An extensive parameter study allows to find the configuration minimizing the total energy barrier, which enables to predict what eventually appears in a grain of a given diameter. The resulting morphology is in good agreement with the experimental evidence obtained by means of high-resolution transmission electron microscopy.

- [1] T. Waitz, T. Antretter, F.D. Fischer, and H.P. Karnthaler, “Size Effects on the Martensitic Martensitic Phase Transformation of NiTi Nanograins”, *Journal of the Mechanics and Physics of Solids*, **55**, 419 (2007).
- [2] T. Waitz, W. Pranger, T. Antretter, F.D. Fischer, and H.P. Karnthaler, “Competing Accommodation Mechanisms of the Martensite in Nanocrystalline NiTi Shape Memory Alloys”, *Materials Science and Engineering A*, **481-482**, 479 (2008).

Towards identification of microstructure-property correlations in a titanium alloy using image-based modeling

M. A. Siddiq Qidwai¹, Alexis C. Lewis² and Andrew B. Geltmacher²

¹SAIC, c/o Code 6350, Naval Research Laboratory, 4555 Overlook Ave. SW, Washington, DC 20375; ²Naval Research Laboratory, Code 6350, Multifunctional Materials Branch, 4555 Overlook Ave. SW, Washington, DC 20375.

ABSTRACT

Image-based modeling is used to investigate the mechanical response of a beta titanium alloy (β 21S) at micro and meso scales with a goal to identify microstructural features that cause initial plastic flow. Actual three-dimensional (3D) morphological and crystallographic description of metallic grains is embedded into finite element models to analyze local spatial heterogeneity of state variables, such as stress and crystallographic slip, under simple loading conditions applied at mesoscale. Analysis of the data demonstrates the complex nature of the interactions between crystallography, morphology, and mechanical response in this alloy, and additionally highlights the importance of considering the nearest-neighbor interactions when investigating the microstructure-property correlation. The methodology presented here should be widely applicable to other alloys and materials for the identification and development of microstructure-property correlations and trends.

1. Introduction and Methodology

Image-based modeling is currently being employed to simulate local deformation and damage mechanisms, to predict the effective properties of heterogeneous metallic materials, and to examine the mechanical response of microscale components at the mesoscale, for example see Refs. [1, 2]. Advanced material characterization techniques such as serial sectioning, X-ray tomography and X-ray diffraction have made it possible to characterize and quantify 3D microstructural data. Finite element (FE) modeling using complete 3D morphological and crystallographic information can be employed to identify critical microstructural features where plasticity is likely to initiate and affect mechanical performance at higher scales, as well as other phenomena. The foundations of this paper are set in the co-authors' work on the creation of high-fidelity 3D microstructural reconstructions and their incorporation into large-scale FE models [2]; however, the previous work was limited to linear elastic and/or isotropic continuum plasticity regimes. Current work extends the material behavior into crystal plasticity and applied to the bcc titanium alloy β 21S.

For this work, a large 3D morphological and crystallographic reconstruction of the bcc beta-titanium was generated by serial sectioning and optical microscopy with periodic electron

backscatter diffraction (EBSD), followed by computerized reconstruction, see Ref. [3] for complete details. In order to reduce computational time and memory requirements of the simulations, a smaller and low-resolution subset, which consists of $136 \times 128 \times 137 \mu\text{m}^3$ (92 total grains with 16 interior grains), is arbitrarily selected from the larger reconstructed volume. A regular mesh is superposed on the microstructure by using 1-to-1 correspondence between image data points and centroids of 8-node brick elements. Individual grains are created as element sets and assigned the average crystallographic orientation calculated using EBSD for the corresponding grain. The microstructural subset with superimposed FE mesh is shown in Fig 1. Commercial FE software (ABAQUS[®]) is used to simulate the mechanical response of the RVE. Three sets of displacement-based loading conditions are considered: 1) uniaxial tension in three global directions; 2) pure shear in three orthogonal planes, XY, XZ and YZ; and 3) biaxial tension in the same planes. Single crystal material behavior is simulated based on hypoelasticity and Schmid's resolved shear stress assumption along with one-stage hardening behavior. For numerical implementation, a user-material subroutine created by Huang [4] is employed. Representative material parameters available in literature are used and given in Tab 1.

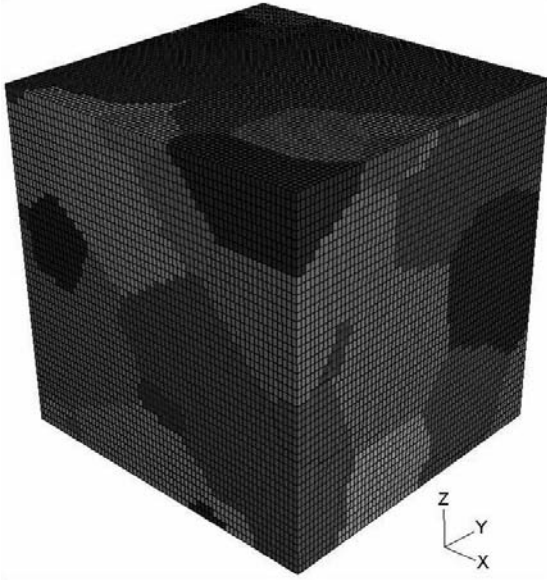


Figure 1. Reduced grain dataset (RVE) and the superimposed FE mesh. The colors are randomly generated.

Table 1. Representative Ti β 21s material parameters for the single crystal model.

Material Parameter	Value
Family of slip systems	$\mathbf{s}_1 = \langle 111 \rangle$, $\mathbf{n}_1 = \{110\}$ $\mathbf{s}_2 = \langle 111 \rangle$, $\mathbf{n}_2 = \{112\}$ $\mathbf{s}_3 = \langle 111 \rangle$, $\mathbf{n}_3 = \{123\}$
Elastic moduli	$C_{11} = 97.7 \text{ GPa}$, $C_{12} = 82.7 \text{ GPa}$, $C_{44} = 37.5 \text{ GPa}$
Shearing rate parameters	$m = 50$, $\gamma_o = 0.0023 \text{ s}^{-1}$
Hardening moduli parameters (Taylor hardening is assumed)	$h_{o1} = 1.5 \text{ GPa}$, $h_{o2} = 1.98 \text{ GPa}$, $h_{o3} = 1.64 \text{ GPa}$ $\tau_{o1} = \tau_{o2} = \tau_{o3} = 200 \text{ MPa}$, $\tau_{s1} = \tau_{s2} = \tau_{s3} = 500 \text{ MPa}$ $q_1 = q_2 = q_3 = 1$

2. Results and Discussion

The effective stress-strain behavior of the 92-grain RVE under multiple loading conditions is shown in Fig 2. The mechanical responses under tensile Y and Z, pure shear XY and XZ, and biaxial XY and XZ loadings, respectively, are alike; therefore only one from each pair is shown here. The response in X-direction has a higher effective modulus and flow stress than those of Y-

and Z- directions. This indicates that the size of the RVE is not enough to account for the macroscopic behavior of the titanium alloy, which is isotropic. The pure shear responses of the material in XY and XZ planes are stiffer and stronger than the pure shear response in the YZ plane. This is due to the tensile response in X-direction being stiffer and stronger than those in the Y- and Z-directions. Under biaxial tensile loading, the effective responses in the XY and XZ planes are more compliant and weaker than the YZ plane response. Due to Poisson’s effect and the isochoric nature of plastic slip, the biaxial tension cases should be equivalent to uniaxial compression in the third direction for isotropic materials (i.e. biaxial tension in the YZ (or XZ) plane is equivalent to compression in the x- (or y-) direction). This is found from the simulations as shown in Fig 2 in which effective stress-effective strain behavior of the RVE under tension in the X-direction (the constitutive relationship used in the simulations does not differentiate between tension and compression) matches closely with the behavior under biaxial tension in the YZ plane. Since the tensile response in the X-direction is stiffer and stronger than those in the Y- and Z- directions, it explains why the order of performance in terms of higher stiffness and strength reverses from pure shear loading to biaxial tensile loading of the RVE.

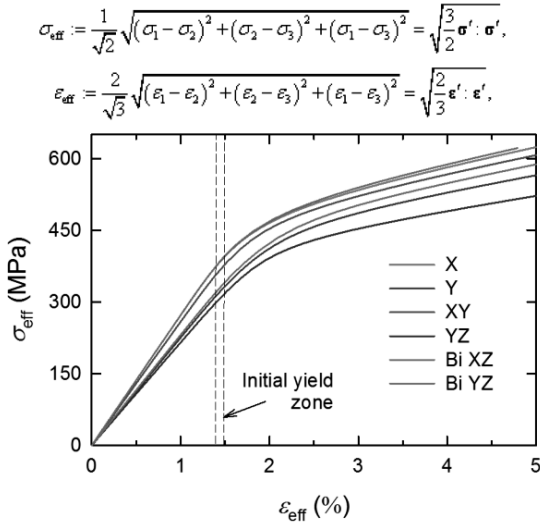


Figure 2. Comparison of effective RVE behavior under representative applied loads.

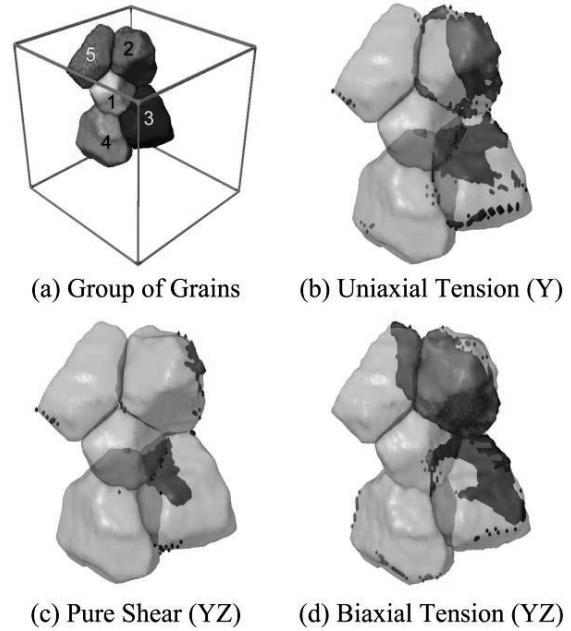


Figure 3. Plastic slip activity in selected grains for three representative loading cases.

Although the RVE selected for this analysis does not offer a large enough sampling size to simulate global trends in the material, the results from the image-based FE simulations can be analyzed in conjunction with the reconstructed microstructure to investigate the correlations between local microstructural features and mechanical response, while acknowledging the difficulty in ascertaining their general applicability. In the current RVE, a group of five gains provides an interesting example of the effects of morphology and crystallography on the local material response. The grains are shown labeled from numbers 1 to 5 in Fig 3a with the bounding box defining the confines of the RVE. Figs 3b-3d show the plastic slip activity as described by the cumulative shear strain at the onset of global yield (ε_{eff} approximately equal to 1.5 %) for three representative loading cases, as shown in Figure 2. In Figure 3, the yielded material points

are marked with the same shade of color as that of the grain in Fig 3a, and the semi-transparent view through the grains allow the yielded points on the back faces to be seen in dull tones in contrast with the brighter ones in the front. A material point is defined to have yielded when its cumulative shear strain ≥ 0.01 %. Of note in this group of grains is that the center grain (no. 1) does not show any yielded points for all loading cases even though all other grains surrounding it yield. This is observed for all simulated loading cases including those that are not shown here. Additionally, the adjacent grains (nos. 2 and 3) show the highest level of plastic flow activity among all grains in the RVE. In the case of uniaxial tension in the X-direction, the central grain (no. 1) has its [001] orientation closely aligned with the loading axis, while grains 2 and 3 have a [111] and [112] axis, respectively, closely aligned with the loading axis. Recall that for cubic materials the stiffest and the least stiff orientations are typically $\langle 111 \rangle$ and $\langle 100 \rangle$, respectively. This implies that grains 2 and 3 have higher effective moduli in the loading direction and thus carry most of the tensile load, and therefore, undergo large plastic slip; whereas grain 1 remains at relatively low tensile stress. These results indicate that the microstructure-property correlations in this material are not necessarily straightforward, and must include effects of the crystallography and morphology of the nearest neighbor grains. These effects may also extend into next-nearest neighbors as well, the extent of which could be studied only with a larger 3D dataset.

This work presents an initial case for the usefulness of the integrated techniques of high-fidelity microstructural reconstruction and FE modeling in developing robust microstructure-property correlations for initial plastic slip or yielding in metals. The mechanical analysis of the 92-grain titanium $\beta 21s$ alloy RVE resulted in the peculiar case of the five grains which highlights the utility of the image-based modeling framework in identifying critical microstructural features. In general, the investigation of an appropriately large number of grains (representative volume element) is paramount to achieving definite correlations and a high degree of confidence in them.

Acknowledgements

This research was supported by the Office of Naval Research and Defense Advanced Research Projects Agency under grant #N0001407WX20381. FE Simulations were performed through the DoD High Performance Computing Modernization Program.

References

- [1] G. Cailletaud, S. Forest, D. Jeulin, F. Feyel, I. Galliet, V. Mounoury, and S. Quilici, "Some Elements of Microstructural Mechanics", *Computational Materials Science*, **27**, 351 (2003).
- [2] A.C. Lewis, and A.B. Geltmacher, "Image-Based Modeling of the Response of Experimental 3D Microstructures to Mechanical Loading", *Scripta Materialia*, **55**, 81 (2006).
- [3] D.J. Rowenhorst, A. Gupta, C.R. Feng, and G. Spanos, "3D Crystallographic and Morphological Analysis of Coarse Martensite: Combining EBSD and Serial Sectioning", *Scripta Materialia*, **55**, 11 (2006).
- [4] Y. Huang, "A User-Material Subroutine Incorporating Single Crystal Plasticity in the ABAQUS Finite Element Program", Division of Applied Sciences, Harvard University, Cambridge, MA (1991).

Numerical and analytical homogenisation approach for modelling mechanical behaviour of heterogeneous geomaterials

Duc Phi Do¹, Naïma Belayachi², Dashnor Hoxha², Albert Giraud¹

¹ **LaEGO ENSG, Nancy Universités, rue du Doyen Marcel Roubault, B.P. 40,
54501 Vandoeuvre lès Nancy, FRANCE
(E-mails: Duc-Phi.Do@ensg.inpl-nancy.fr, Albert.Giraud@ensg.inpl-nancy.fr)**

² **Institut PRISME, (EA4229) Polytech'Orléans, rue Léonard de Vinci,
45072 Orléans Cedex 2, France
(E-mails: Naima.Belayachi@univ-orleans.fr, Dashnor.Hoxha@univ-orleans.fr)**

ABSTRACT

This paper deals with micromechanical analysis of nonlinear behaviour of a rock material. To model the deformation response realistically both microstructures as well as the non linear behaviour of the heterogeneities are taken into account through a micro-macro procedure. The natural material is assumed like two phase composite with argillaceous matrix and spherical quartz or calcite inclusion for problem simplification. A nonlinear Von Mises model combined with Perzyna's viscopla inclusions were considered as being linear elastic materials. Two alternative approaches have been used: an analytical and a numerical, finite element based. For the analytical approach a Mori-Tanaka schema has been used and for each increment the viscoplastic material is replaced by a conveniently chosen linear comparison material. In numerical approach the axisymmetric unit cell concept with periodic boundary conditions and an elastoviscoplastic material have been used. Good agreement is obtained between experimental and simulated results.

1. Introduction

The material studied in this paper is a mudstone from the East of France known as argillite of Meuse-Haute-Marne (M/H-M) and extensively studied these ten last years in rapport with the possibilities of nuclear waste disposal construction. While a number of macroscopical models for this rock have already been developed([1], [5]), the work is going on to justify the hypothesis of these models from micromechanical mechanisms or/and to develop micromechanical models for long term predictions, up to several thousands of years.

In this study, two classes of homogenisation modelling approaches have been proposed to evaluate the effective mechanical responses of argillite composites. The first class treats the problem analytically in the frame work of Eshelby and Hill polarization approach and by adapting a convenient linear comparison material. The advantage of these methods is that the macroscopic constitutive model follows readily from the analytical treatment. The second class uses micro-macro numerical procedures based on the classical concept of local spatial periodic representative volume element [4] combined with finite element method.

2. General considerations on material and principal hypotheses

At mesoscopic level (some millimetres to some centimetres) the M/H-M argillite appears as a composite material with a clay matrix and random inclusions of quartz and calcite that occupy up to 40% of the volume of the rock (figure 1). Some macropores could be observed around the inclusions, but the microscopic observations reveal that the most part of pores is found

inside of the clay matrix which is composed by palettes of clay minerals (illite, chlorite, smectite) and micro- and nano-pores (up to 18% of the total volume of the rock).

In this paper the rock is considered to be a three phase composite composed by a clayey matrix and spherical inclusions of quartz and calcite, in such a way that the volume fractions of these phases satisfies the unity partition, i.e :

$$f_m + f_{qu} + f_{ca} = 1 \tag{1}$$

where subscripts m , qu and ca stand for clayey matrix, quartz and calcite inclusion respectively. A further simplification, used later in numerical homogenisation procedure, could be made by supposing that mechanical properties of quartz and calcite are the same (which is true approximately) that leads to a bi-phase composite. Elastic properties of pure minerals that composed the inclusions are known from the literature ([2]) while those of clay matrix could be obtained by an inverse problem using known macroscopical data for this rock (see for example[2]). In this paper this same inverse procedure identification has been used to obtain the parameters for the nonlinear behaviour of the clay matrix. For the range of stresses susceptible to be applied on the rock, the behaviour of quartz and calcite inclusions could be considered to be linear elastic, so the only nonlinear phase is the clay matrix which is supposed to follow a viscoplastic behaviour. Considering the structure of clay platelets one could reasonably assumes that instantaneous nonlinear behaviour of the matrix would be governed by the sliding of clay platelets and uses a Von-Mises model to describe this non-linearity, with the yield function written as :

$$F = \sigma_e - \sigma_0^{in} - H(\epsilon_e^p) \tag{2}$$

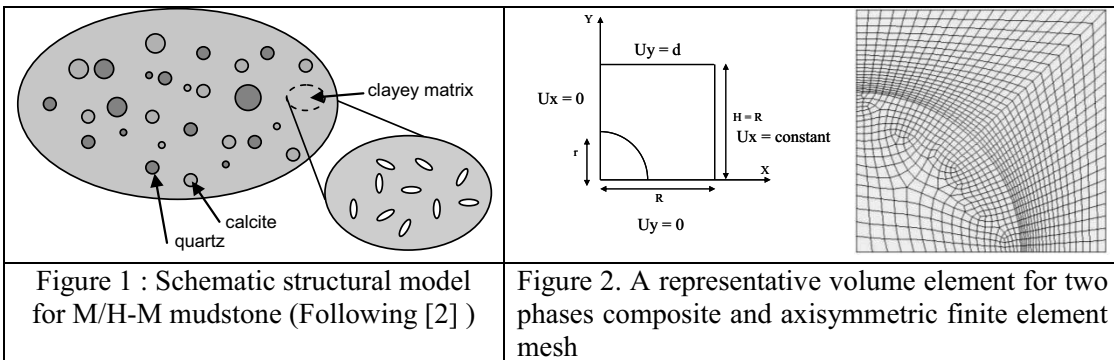
where σ_e is the equivalent stress, σ_0^{in} is the initial onset of plasticity, $H(\epsilon_e^p)$ is a hardening function of the equivalent plastic strain ϵ_e^p . In this work a hardening function of Voce type is used:

$$H(\epsilon_e^p) = R_0 \epsilon_e^p + R_{inf} (1 - e^{-b \cdot \epsilon_e^p}) \tag{3}$$

The time dependent behaviour of the rock is derived from a Perzyna's approach, i.e. by supposing that the strain rate could be written as :

$$\dot{\epsilon}^{vp} = \gamma \left(\frac{\sigma}{\sigma_0} - 1 \right)^{\frac{1}{m}} \tag{4}$$

Here m, γ define respectively the strain hardening and the viscosity parameters (i.e. the sensitivity strain rate parameters). and σ_0 is the static yield stress of the material.



3. Micromechanical modelling of nonlinear elastoplastic behaviour of M/H-M mudstone

3.1 Analytical approach

The modified secant method as described in [3] has been used in this approach in order to construct the linear comparison material that replaces the nonlinear clayey matrix for each increment. It is known that such method coincides with the variational approach proposed by Ponte-Castaneda ([3]). Once the equivalent secant elastic tensor C_m^{sec} is obtained for a given increment for the clayey matrix, then the homogenised behaviour of the rock for this increment is written as :

$$\Sigma = C_{\text{hom}}^{\text{sec}} : E \quad (5)$$

where the homogenised secant elastic tensor is obtained through a classical Mori-Tanaka procedure using the elastic properties of inclusions and C_m^{sec} for the clayey matrix, i.e:

$$C_{\text{hom}}^{\text{sec}} = C_m^{\text{sec}} + \sum_i f_i (C_i - C_m^{\text{sec}}) : A_i^{\text{MT}} \quad i=ca,qu \quad (6)$$

In this last expression A_i^{MT} represents the fourth order concentration tensor of the i^{th} inclusion phase. The details of modified secant method are not presented here but could be found in [3]. The figure 2.a shows a comparison of model with experimental data on this rock. Even though a good general agreement is obtained, the volumetric strains, as expected could not be correctly described by the model since no plastic volumetric strains has been considered. The dilatancy observed for high level stress could be taken into account by introducing some kind of damage, neglected here for the sake of simplicity.

3.2 Numerical approach

The object of numerical modelling was in one hand to obtained the elastoplastic behaviour of the rock based on its structure and in the other hand to extended such modelling in the case of time dependent behaviour which was not treated by analytical method.

For convenience of studies, the constituents are assumed to be isotropic. Perfect bonding is assumed at the interfaces between quartz (calcite) inclusion and matrix. Spherical inclusions are assumed to be packed as a hexagonal periodic array as discussed above. Symmetry arguments are then used to limit the RVE to $\frac{1}{4}$ of the axisymmetric cell (Fig. 1.b). R , is the initial radius of the unit cell, H , the initial height of the cell and r the initial radius of the particle.

The analysis was performed using the commercial code ANSYS. Referring to Fig. 1, symmetry boundary conditions are used for sides ($x = 0$, and $y = 0$), while side ($x = R$) has a uniform displacement in the x direction for periodic boundary conditions. At side ($y = H$) a uniform displacement in the y direction is considered as uniaxial loading.

The macroscopic stress-strain components are computed as the volume average of microscopic components ($\sigma_{ij}; \varepsilon_{ij}$) according to the following equations:

$$\bar{\sigma}_{ij} = \frac{1}{V} \int_V \sigma_{ij} dV \quad ; \quad \bar{\varepsilon}_{ij} = \frac{1}{V} \int_V \varepsilon_{ij} dV \quad (7)$$

Where $\bar{\sigma}_{ij}$ and $\bar{\varepsilon}_{ij}$ are the macroscopic average component of stresses and strains over the microscopic volume V of the periodic representative volume element.

An inverse procedure has been used based on this modelling in order to adjust the parameters of viscoplastic model for the clayey matrix. For this purpose triaxial tests with different strain rate could be used. For each test a set of FE analysis is performed by varying parameters.

Local fields of stresses, total and viscoplastic strains were determined. Then using equation (7), values of macroscopic stress strain tensor were calculated. The method adopted here for identifying the clayey matrix parameters consists on minimizing the sum of the differences between the experimental and predicted results. In respect with the model described in §2, the following set of parameters has been obtained calculation $E_a = 7600 \text{ MPa}$; $\nu_a = 0.1$; $\sigma_0 = 1.2185 \text{ MPa}$; $R_0 = 572.47 \text{ MPa}$; $R_{\text{inf}} = 14.3151 \text{ MPa}$; $b = 252.059$ and ($m = 0.8$; $\gamma = 0.01$). As an example in the figure 2.b is shown a comparison of the macroscopic experimental data and numerical response of argillite under triaxial loading at strain rate of 10^{-5} s^{-1} .

Globally the simulated and experimental results are in good agreement for the identified parameters, except at the strain about 0.01.

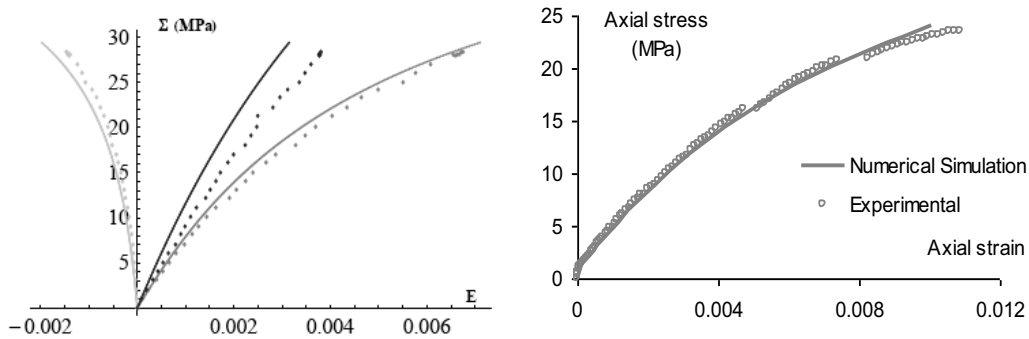


Figure 2 : Comparison of model responses with laboratory data

- a) Elastoplastic behaviour, modified secant method (continuous lines) b) Elastoviscoplastic behaviour, numerical homogenisation (continuous line).

4. Conclusions

An analytical and a numerical approach were used to describe the effective behaviour of a rock considered as a three phase composite. The prediction of analytical model was restraint in the elastoplastic behaviour modelling where a good overall accordance was found with laboratory data. The numerical modelling was successfully used in identification of viscoplastic parameters of clayey matrix and in prediction of effective response of the rock.

5. References

- [1] A. S. Chiarelli, J-F Shao, N. Hoteit, "Modelling of elastoplastic damage behaviour of a claystone", *Int. J. Plasticity*, **19**, 23 (2003).
- [2] A. Giraud, Q. V. Huynh, D. Hoxha, D. Kondo, "Effective poroelastic properties of transversely isotropic rock-like composites with arbitrarily oriented ellipsoidal inclusions" *Mech. Mat.*, **39**, 1006 (2007).
- [3] P. Ponte Castaneda, P. Suquet, "Nonlinear composites", *Adv. Appl. Mech.* **34**, 171 (1998).
- [4] Hill R. "Elastic properties of reinforced solids: some theoretical principles", *J. Mech. Phys. Solids*, **11**, 357 (1963).
- [5] Hoxha D., Homand F., Giraud A., Auvray C "Saturated and unsaturated behaviour modelling of Meuse-Haute-Marne argillite", *Int. J. Plasticity*, **23**, pp. 733-766, (2007) -
- [6] E. Voce, "A practical strain hardening", *Metallurgica*, **51**, 219 (1955).
- [7] P. Perzyna, "Fundamental problems in viscoplasticity", *Advances in applied mechanics*. Academic press, new york **9**, 243 (1966).

An Adaptive Coarse-Graining Scheme for the Simulation of Elastomer Networks

Misty Davies and Adrian Lew

**Stanford University, Stanford, CA – 94305,USA
(misty.davies@stanford.edu, lewa@stanford.edu)**

ABSTRACT

We describe a mixed continuum and discrete computational approach for the simulation of elastomers at the rubbery plateau. Salient features of the method include: a) a systematic and automatic coarse-graining of the degrees of freedom of a network in large regions of an elastomeric solid, b) a very fast way to accurately compute the free energy of the coarse-grained network, and c) a resolution to the level of crosslinks in those regions of the solid that merit a finer description. The coarse-grained model automatically adapts as the body is deformed. Some applications for this method include the simulation of nanoindentation, with possible extensions to double-network hydrogels and cracks with crazing.

Dislocation Quasi-Statics: Implicit Time Integration for Dislocation Dynamics Simulations

Tom Arsenlis¹, Vasily Bulatov², Gregg Hommes³, Moono Rhee⁴ and Meijie Tang⁵

Lawrence Livermore National Laboratory, Livermore, CA, USA

¹arsenlis1@llnl.gov, ²bulatov1@llnl.gov, ³hommes1@llnl.gov,

⁴rhee1@llnl.gov, ⁵tang7@llnl.gov

ABSTRACT

Dislocation dynamics simulations are currently limited in their ability to simulate plastic deformation in crystals at strain rates below 1 s^{-1} . There is a strong drive to be able to perform simulations at much lower strain rates that are easily accessible with common experimental equipment, and to be able to relax dislocation structures from loaded to completely unloaded states so that microstructures could be directly compared with TEM observations. This practical strain rate limit in dislocation dynamics manifests itself through a combination of the intrinsic mobility of dislocations, the gradients in forces acting on dislocations as they approach other dislocations, the frequency of discontinuous topological events, and the time integration procedures used to evolve the system. As a result, the distribution of dislocations velocities for a dislocation network becomes sharper as the strain rate decreases, and the high velocity tail of the distribution remains. Much of these difficulties are intrinsic to the crystal. However, the sharp gradients in the force may be modified by the spreading dislocation cores, and robust implicit time integration procedures may be developed to push the lower strain rate limit of dislocation dynamics simulations. Analysis of different algorithmic for dislocation quasi-statics will be compared for in their ability to decrease the practical limit of accessible strain rates and in their relative computational cost.

Orientation Dependence of Friction in PTFE

Peter R. Barry¹, Patrick Y. Chiu¹, Scott S. Perry¹, W. Gregory Sawyer,^{1,2} Simon R. Phillpot¹ and Susan B. Sinnott¹

¹Department of Materials Science & Engineering, University of Florida, Gainesville, Florida 32611-6400

²Department of Mechanical & Aerospace Engineering, University of Florida, Gainesville, Florida 32611-6250

ABSTRACT

Atomic-scale simulations provide valuable insights into the mechanisms responsible for experimentally observed friction at the atomic or molecular scale. We use classical molecular dynamics simulations in conjunction with experimental data to determine the influence of material type, surface structure, and temperature on observed friction coefficients. While friction in solids is generally considered to be athermal, under certain conditions thermally activated behavior has been observed experimentally. Interestingly, both thermally activated and athermal friction have been experimentally observed in tribological studies of polytetrafluoroethylene (PTFE) sliding surfaces. Here we explore the origins of these effects. We find that, by changing the relationship between the sliding direction and the polymer chain direction, the friction can be switched from a wear-free to a highly wearing friction mode. The simulations explore the relationship of these regimes to the thermally activated behavior.

This was supported by an AFOSR-MURI grant FA9550-04-1-0367. The University of Florida High-Performance Computing Center is also acknowledged for providing computational resources and support.

Multiscale Analysis of Cell-Gold Adhesion

Jinghong Fan¹ and Mauro Chinappi²

¹ Alfred University, Alfred, NY, USA (fanjing@alfred.edu)

² Sapienza University of Rome, Italy (mauro.Chinappi@uniroma1.it)

ABSTRACT

This work is to conduct multiscale computational simulations combined with experimental verification to evaluate the adhesive strength and thus biocompatibility at the interface between implant of different materials and bio-cells. Computational simulations includes Molecular Dynamics (MD) at the atom-nano scale, Finite Element Analysis (FEA) at the microscopic-cellular scale, and FEA at the macroscopic scale. Experimental approaches to verify simulation results include synthesizing biomaterials (biocomposite), cell culture, atomic force measurement, and microscopic fluid shear force measurement and high resolution electronic and nanoprobeing techniques. - At the atom-nano scale The interface chemical composition of several kinds of synthesized biocomposites of implant is designed. Molecular dynamics (MD) calculations are conducted. This low-scale analysis will allow pre-selection of the chemical compositions with high interfacial adhesions through comparing the shearing strength and normal strength of different implant materials. In addition, physical parameters such as interfacial kinetic frictional coefficient and viscosity are assessed to consider the effect of chemical composition and the body fluid effect on these parameters. - At the microscopic (micron, single cell) scale Based on the measured basic surface geometric parameters and the MD-obtained physical parameters (e.g. kinetic frictional coefficient and viscosity), the FEA at the microscopic (micronmeter) scale are conducted to obtain the corresponding maximum shear stresses. Comparing the calculated maximum shear stress with the measured shear strength by a rotating rheometer, the modified physical coefficient of the synthesized material and shear strength criterion are obtained, and thereafter, the coupled surface geometry-cell residency effects on the physical coefficient and strength criterion can be accounted for. - At the macroscopic scale (> mm, multiple cells) The research work is still in the above two scales. After it is successful, the result will be used to design the interface morphology for the implant which include waviness, roughness, and porosity based on the measured basic surface geometry of the material coupon at the microscopic scale. FEA simulation, based on the confirmed physical coefficients, will be conducted to investigate the stress distribution with multiple cells in the model, and conduct a parametric study of asperities, waviness and porosities of the designed interface morphology on shear strength to optimize and enhance the interfacial adhesion.

Stress relaxation and dynamic strain aging of Zr-Sn-Nb alloy

Jun Tan¹, Cong Li², Chao Sun¹, Shihao Ying¹

¹National Key Laboratory for Nuclear Fuel and Materials, Nuclear Power Institute of China, P.O. Box 436, Chengdu, Sichuan, 610041, PR China
(E-mail: juntan_china@yahoo.com)

²China Nuclear Power Technology Research Institute, 1788 Xi Huan Road, Suzhou, 215004, PR China (E-mail: licongcd@yahoo.com.cn)

ABSTRACT

Stress relaxation (SR) experiments were performed on a Zr-Sn-Nb alloy over a broad temperature range from room temperature to 600, and at each temperatures SR were carried out at three different strain levels (0.02, 0.05, 0.08), in order to reveal the elementary dislocation process responsible for the plastic deformation, and investigate the dynamic strain aging (DSA) of zirconium alloys. The stress reduction ratio at the end of the relaxation increases with temperature, except that at 300 there exhibits a local minimum in the temperature dependence of the ratio, which is attributed to DSA. The plastic deformation rate as a function of time during relaxation was determined by the analysis of the experimental data. It is interesting to note that the plastic deformation rate at 300 is always lower than those at other temperatures at the same relaxation time. It indicates that DSA could reduce the plastic deformation rate during SR, and thus restrains the relaxation of stress of the alloy, as demonstrated by the minimum in the temperature dependence of the stress reduction ratio. The activation volume associated with the deformation process was found from the relationship between stress and relaxation time. A noticeable maximum value appears at 300 when the activation volume plotted against the temperature, which is indicative of DSA [1], and this value decreases as the strain level increases. However, outside the temperature region of DSA, the activation volume remains almost constant for each strain levels. Based on the analysis of the strain dependence of the activation volume, the rate controlling deformation mechanism is identified as the overcoming of solute atoms by dislocations, and the dislocation density is found to have an effect on DSA.

[1] S. I. Hong, W. S. Ryu, and C. S. Rim, "Thermally Activated Deformation of Zircaloy-4", *Journal of Nuclear Materials*, 120, 1(1984).

Financial support from the National Nature Science Foundation of China (Grant No. 50601024) is gratefully acknowledged.

Development of Statistically Equivalent Representative Volume Elements for Multi-scale Modeling of Composite Materials

Ted Vaughan, Conor McCarthy¹

Composites Research Centre, Materials & Surface Science Institute, Dept. of Mechanical and Aeronautical Engineering, University of Limerick, Ireland.

¹ Corresponding Author: conor.mccarthy@ul.ie

ABSTRACT

The non-uniform spatial arrangement of fibers in composite materials leads to an irregular stress distribution in the microstructure allowing localized microscopic damage mechanisms to occur more easily. In order to accurately predict such damage mechanisms, statistically equivalent representative volume elements (SERVE) are often used. A hard-core random model, where fibers are randomly placed, is generally used to create these SERVE's but such models do not reproduce the microstructure well for high volume fraction composites, such as those used for high strength applications in the aerospace industry. In this paper, a novel method is developed to generate SERVE's for high volume fraction composites. This method uses experimentally measured nearest neighbor distribution functions to define inter-fiber distances. The resulting SERVE is found to show very similar geometric distribution functions (i.e. radial distribution and nearest neighbor distribution) to the actual microstructure. The proposed algorithm is currently being used to generate micromechanical finite element models for multi-scale damage prediction of composite structures.

1. Introduction

Due to their high specific strength and stiffness fiber reinforced composite materials are widely used in the aerospace industry. These materials allow for lighter structures leading to lower fuel consumption or increased payload. In order to predict material damage and failure in composite structures, computational methods are now being used extensively to reduce some of the experimental testing needed for certification of aircraft. However, finite element (FE) modeling of fiber reinforced composites presents a challenge due to the fact that they are heterogeneous, brittle and can display non-linear constitutive behavior. Failure in composite materials is a result of microscopic damage accumulation in the fiber and/or the matrix leading to a multitude of macroscopic failure modes. In order to more accurately predict microscopic damage accumulation and its effect on the macroscopic structure, multi-scale modeling approaches have begun to emerge [1]. These methods couple macro-mechanical models with micro-mechanical models, which represent the fiber and matrix phases discretely, in the form of a representative volume element (RVE).

The microstructure of a composite material exhibits a non-uniform spatial arrangement of fibers, with apparently random fiber rich and fiber denuded regions. The presence of these leads to an irregular stress distribution across the microstructure, thus allowing microscopic damage mechanisms to occur more easily [2]. For accurate damage prediction at the microscopic level, a statistically equivalent representative volume element (SERVE) is commonly used. In an SERVE, the distribution functions of parameters reflecting local morphology should be statistically equivalent to the overall microstructure [3]. In generating an SERVE, the hard-core random model has been extensively used whereby the fibers are considered as non-overlapping disks, whose centers have been distributed randomly and uniformly in a square region of finite size. However, this model has been shown to have an upper volume fraction limit in the region of 50% and is therefore unsuitable in representing microstructures of high-volume fraction composites [4]. An alternative method [4] has been developed to achieve a high volume fraction SERVE based on a variation of the hard-core random model. The resulting fiber arrangement from this theoretical approach is characterized by a random distribution.

This paper presents a novel method of generating high volume fraction SERVE's using statistical microstructural data found from experimental analysis. The material under study is HTA/6376, a high strength carbon fiber reinforced plastic (CFRP) used extensively in the aerospace industry. The SERVE's are currently being used to generate three-dimensional FE models to predict microscopic damage mechanisms in CFRP using a multi-scale approach and this will be reported on in a later publication.

2. Digital Image Analysis

Buehler® Omnimet® imaging software was used to analyze 35 images captured from the CFRP microstructure, such as that shown in Figure 1(a), each measuring $320\ \mu\text{m} \times 240\ \mu\text{m}$. The software automatically detects a color 'threshold' level within each image and this allows it to identify the fibers, as shown in Figure 1(b). Data such as volume fraction, fiber diameter and fiber centre (i.e. x, y) coordinate is extracted. From this, statistical data characterizing the spatial arrangement of the fibers was generated, specifically the nearest neighbor distribution function [5] which is found by calculating the distance for each fiber to its closest neighbor and expressing the results as a probability density function. Similarly, in this work the 2nd nearest neighbor distribution function is found using a similar approach.

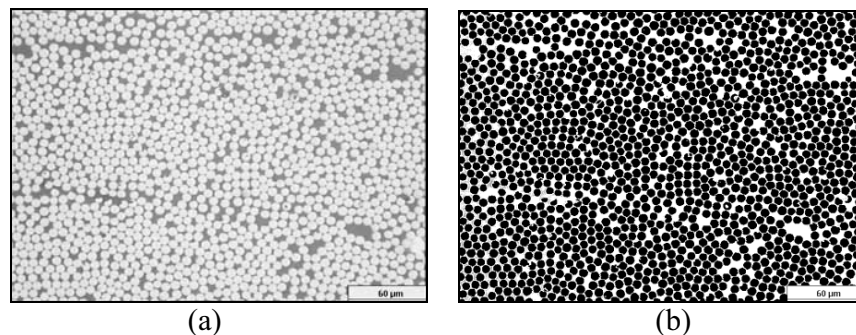


Figure 1: Sample area chosen for image analysis ($320\ \mu\text{m} \times 240\ \mu\text{m}$), (a) actual micrograph, (b) computed microstructure based on a color threshold algorithm

3. Program Development

The program was written in Matlab and its purpose is to generate high volume fraction SERVE's of a CFRP using the following procedure,

1. A random point is created having coordinates (x_1, y_1) , lying in a sample square area, A ; the size of A being defined by the user. The diameter, d_1 , of the surrounding fiber is drawn from a lognormal distribution fitting the experimentally measured diameter distribution.
2. Two additional points, (x_2, y_2) and (x_3, y_3) are created, which form the centers of the first and second nearest neighbors of the first fiber. The distance from (x_1, y_1) to (x_2, y_2) and from (x_1, y_1) to (x_3, y_3) are assigned from the first and second nearest neighbor distribution functions, respectively. Both points are oriented at angles chosen randomly between 0-360°. Fiber diameters are assigned from the same lognormal distribution as before.
3. The program then moves on to the second fiber and assigns its first and second nearest neighbors, (x_4, y_4) and (x_5, y_5) , for which the near neighbor distances are drawn from their respective distributions and fiber diameters are assigned as before.
4. The program then moves on to the third fiber and the same procedure is carried out. This process is repeated for each fiber thereafter until the sample area, A , is full.
5. The program performs numerous checks at each iteration to ensure that none of the fibers overlap with one another. If overlaps occur, orientation angles or inter-fiber distances are reassigned until a suitable configuration is found.

4. Generated SERVE Candidates

Shown in Fig. 2 are two possible SERVE candidates generated by the Matlab program measuring $100\mu\text{m} \times 100\mu\text{m}$ and $170\mu\text{m} \times 170\mu\text{m}$. The generated SERVE's show evidence of fiber clustering and matrix rich regions similar to those found in the actual microstructure (shown in Fig. 1a). The volume fraction of the larger SERVE is 60.4% which compares well with the actual experimentally determined volume fraction of 59%. The nearest neighbor distribution function computed from the larger SERVE in Fig. 3 shows a similar trend to the experimental distribution with slight deviations evident where peak distributions occur. Radial distribution functions [5] for both the generated SERVE's and the CFRP microstructure have also been compared (not shown) and give good correlation. The program is therefore capable of generating statistically equivalent representations of the CFRP microstructure under investigation. This new approach can easily be applied to other types of composite materials once the relevant distribution functions had been found using the image analysis procedure as above.

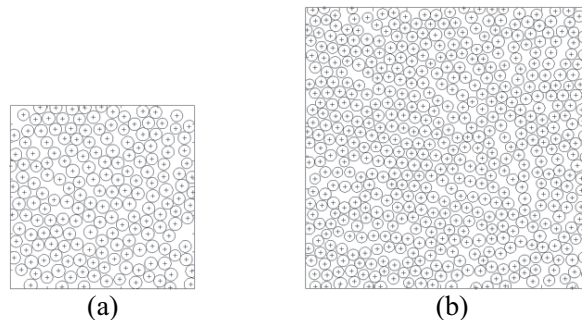


Figure 2: Generated SERVE candidates, (a) $100\mu\text{m} \times 100\mu\text{m}$ (b) $170\mu\text{m} \times 170\mu\text{m}$

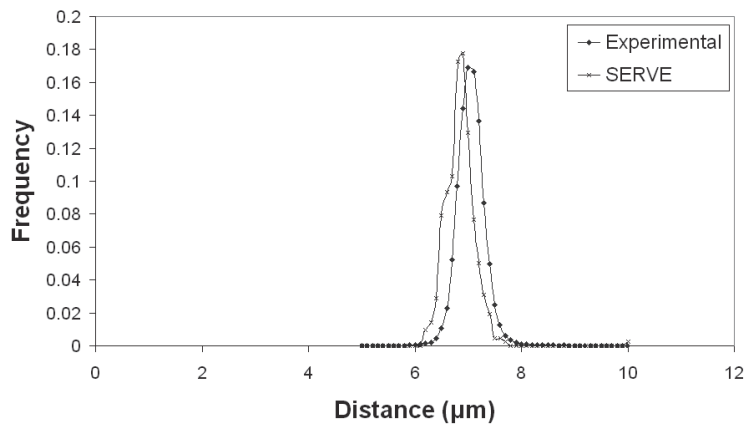


Figure 3: Nearest neighbor distribution functions

5. Conclusions and Future Work

A novel method has been developed in order to generate accurate representations of a composite material microstructure with a high volume fraction. The microstructure of a CFRP composite was experimentally characterized in terms of fiber volume fraction, fiber diameter and nearest neighbor distributions. Using this data a program was developed which can generate SERVE's with high volume fractions with and the same geometric features as the experimental samples, as determined using statistical analysis. The program is currently being updated to ensure that the generated SERVE's are geometrically periodic for subsequent micromechanical damage modeling using finite element analysis.

Acknowledgements

This authors wish to acknowledge the funding provided by the Irish Research Council for Science, Engineering and Technology (IRCSET) and Science Foundation Ireland (SFI).

References

- [1] C. González and J. Llorca, "Multiscale Modeling of Fracture in Fiber-Reinforced Composites", *Acta Materialia*, **54**, 4171 (2006).
- [2] D. Trias, J. Costa, J.A. Mayugo, and J.E. Hurtado, "Random Models Versus Periodic Models for Fibre Reinforced Composites", *Computational Materials Science*, **38**, 316 (2006).
- [3] S. Swaminathan, S. Ghosh, and N.J. Pagano, "Statistically Equivalent Representative Volume Elements for Unidirectional Composite Microstructures: Part I - without Damage", *Journal of Composite Materials*, **40**, 583 (2006).
- [4] A.R. Melro, P.P. Camanho, and S.T. Pinho, "Generation of Random Distribution of Fibres in Long-Fibre Reinforced Composites", *Composites Science and Technology*, **68**, 2092 (2008).
- [5] S. Yang, A. Tewari, and A.M. Gokhale, "Modeling of Non-Uniform Spatial Arrangement of Fibers in a Ceramic Matrix Composite", *Acta Materialia*, **45**, 3059 (1997).

Micromechanical modeling of the anisotropy of elastic biological composites - Theory and fundamental concepts

J.Rahmoun¹, J. Halgrin¹, F. Chaari¹, E. Markiewicz¹, P. Drazetic¹

¹Laboratory of Industrial and Human Automatic, Mechanic and Informatics, UMR CNRS 8530, University of Valenciennes, Le Mont Houy, 59313 Valenciennes, France

ABSTRACT

The present work is devoted to the micromechanical modeling of elastic properties of trabecular bone by using the Eshelby and Hill polarization tensors of an isolated ellipsoidal inhomogeneity embedded in an infinite matrix. The problem is entirely geometrized and is treated in terms of averages of Walpole's components of the fourth-order tensors describing the problem [2]. The Ponte Castañeda scheme is given to investigate the effect spatial distribution of the ellipsoidal inclusions on the effective behavior [3]. Architecture of trabecular bone can be quantified with increasing accuracy using quantitative computer tomography, which opens the perspective of estimating the associated mechanical properties from 3D image reconstructions. For this purpose, the most promising variables are volume fraction and fabric [4].

1. Introduction

The overall properties of multi-phasic materials first depend on the relative concentrations of their constitutive phases, they also crucially vary with the spatial arrangement of these phases. Continuous theoretical and experimental progress in the fields of microstructural characterizations have gone along with improvements in modelling as well as in measuring materials (physical, mechanical, etc.) properties. This has resulted in continuous gain for optimizing composite structures devoted to specific applications. In particular, morphological analyses can now be directly obtained from 3D informations issued from high resolution X-rays tomography [4].

In the present work, we aim at formulating a micromechanical model, based on the Eshelby equivalent inclusion [1], to evaluate the effective elastic properties of multi-phasic materials [3,5], and in which the morphology anisotropy of constituent phases is investigated by means X-ray micro-tomography.

2. Formulation of a micromechanical model of anisotropic multi-phasic materials

2.1. *Basic principles of the modelling*

Consider a representative volume element (R.E.V.) Ω of a composite consisting of N families of ellipsoidal inclusions made up of phases r ($r = 1, \dots, N$) with elastic stiffness tensors $\mathbb{C}^{(r)}$, which are distributed randomly in a continuous matrix with elastic stiffness tensor $\mathbb{C}^{(m)}$. The inclusions of phase r are all taken to be identical in shape and orientation. Under a uniform macroscopic strain field E be prescribed on the boundary of the R.E.V., Ponte Castañeda and Willis [3] proposed a rather novel approach to separate the spatial distribution of inclusions from the inclusion shape by means of two Hill-type tensors ($\mathbb{P}_w^{(s)}$ associated with the shape and \mathbb{P}_d corresponding to the spatial distribution). The strain concentration tensor takes then the following form:

$$\mathbb{A}_w^{(r)} = \mathbb{A}_w^{(r)} : \left[f^{(m)} \mathbb{I} + \sum_{s=1}^N f^{(s)} \left[\mathbb{I} + (\mathbb{P}_w^{(s)} - \mathbb{P}_d) : (\mathbb{C}^{(s)} - \mathbb{C}^{(m)}) \right] : \mathbb{A}_w^{(s)} \right]^{-1} \quad (1)$$

where $f^{(m)}$ and $f^{(r)}$ are, respectively, the matrix and inclusions volume fraction and where:

$$\mathbb{A}_w^{(r)} = \left[\mathbb{I} + \mathbb{P}_w^{(r)} : (\mathbb{C}^{(r)} - \mathbb{C}^{(m)}) \right]^{-1} \quad \text{and} \quad \mathbb{A}_w^{(s)} = \left[\mathbb{I} + \mathbb{P}_w^{(s)} : (\mathbb{C}^{(s)} - \mathbb{C}^{(m)}) \right]^{-1} \quad (2)$$

In this development, the inclusions are taken to be ellipsoidal, and their spacial distribution is also will be assumed to exhibit ellipsoidal symmetry (i.e $\mathbb{P}_w^{(s)} = \mathbb{P}_d$), the expression (1) reduces to:

$$\mathbb{A}^{(r)} = \mathbb{A}_w^{(r)} : \left(f^{(m)} \mathbb{I} + \sum_{s=1}^N f^{(s)} \mathbb{A}_w^{(s)} \right)^{-1} \quad (3)$$

and the effective stiffness tensor writes:

$$\mathbb{C}^{hom} = \mathbb{C}^{(m)} + \sum_{r=1}^N f^{(r)} (\mathbb{C}^{(r)} - \mathbb{C}^{(m)}) : \mathbb{A}_w^{(r)} : \left(f^{(m)} \mathbb{I} + \sum_{s=1}^N f^{(s)} \mathbb{A}_w^{(s)} \right)^{-1} \quad (4)$$

2.2. Hill tensor for an arbitrarily oriented ellipsoidal inclusion

The starting point for the calculation of the Hill tensor is the following definition (see [5,3]):

$$\mathbb{P}_w^{(r)} = \frac{\det(\underline{\underline{Z}}^{(r)})}{4\pi} \int_{|\underline{\xi}|=1} \mathbb{H}^{(m)}(\underline{\xi}) | \underline{\underline{Z}}^{(r)} \underline{\xi} |^{-3} dS(\underline{\xi}) \quad (5)$$

for which the integration is on the unit sphere centered at the origin of space (ξ_1, ξ_2, ξ_3) , defined by $|\underline{\xi}| = 1$. $\underline{\underline{Z}}^{(r)}$ is the shape tensor characteristic of the equivalent inclusion of the r phase and $H^{(m)}(\underline{\xi})$ is defined by:

$$H_{ijpq}^{(m)}(\underline{\xi}) = \xi_i [K^{(m)}(\underline{\xi})]_{jp}^{-1} \xi_q \Big|_{(ij)(pq)} \quad \text{and} \quad K_{ip}^{(m)}(\underline{\xi}) = C_{ijpq}^{(m)} \xi_j \xi_q \quad (6)$$

called the acoustic tensor and which depends on the tensor of elasticity $\mathbb{C}^{(m)}$ of the matrix. The notation $\Big|_{(ij)(pq)}$ indicates the symmetrization with respect to the couples (i, j) and (p, q) . We are interested here in the case of an isotropic linear elastic solid matrix weakened by N families of isotropic ellipsoidal inclusions aligned in a given direction \underline{n} (by convention we choose $\underline{n} = e_3$). The shape of inclusions correspond to a spheroid characterized by its normal \underline{n} , radius a and the average half-opening c . Then, the composite material exhibits transversely isotropic symmetry. Then, by using (6), the expression (5) of the Hill tensor becomes:

$$P_{ijpq}^{(m)} = \frac{wa^3}{4\pi} \int_{|\underline{\xi}|=1} \frac{\xi_i [K^{(m)}(\underline{\xi})]_{jp}^{-1} \xi_q \Big|_{(ij)(pq)}}{[\sqrt{a^2(\xi_1^2 + \xi_2^2 + w^2\xi_3^2)}]^3} dS(\underline{\xi}) \quad (7)$$

where $w = \frac{c}{a}$ is the aspect ratio of inclusions. In general, we set [5]:

$$P_{ijpq}^{(r)} = \frac{1}{4} (M_{ijpq}^{(m)}(\underline{\xi}) + M_{jipq}^{(m)}(\underline{\xi}) + M_{ijqp}^{(m)}(\underline{\xi}) + M_{jiqp}^{(m)}(\underline{\xi})) \quad (8)$$

with:

$$M_{ijpq}^{(m)}(\underline{\xi}) = \frac{w}{4\pi} \int_{|\underline{\xi}|=1} \frac{\xi_i [K^{(m)}(\underline{\xi})]_{jp}^{-1} \xi_q}{[\sqrt{\xi_1^2 + \xi_2^2 + w^2\xi_3^2}]^3} dS(\underline{\xi}) \quad (9)$$

According to the isotropy of the solid matrix, the stiffness tensor, $\mathbb{C}^{(m)}$, reads $\mathbb{C}^{(m)} = 3\kappa^{(m)} \mathbb{J} + 2\mu^{(m)} \mathbb{K}$, where $\kappa^{(m)}$ and $\mu^{(m)}$ represent the bulk and shear moduli of the matrix, respectively. Then, we have:

$$M_{ijpq}^{(m)}(\underline{\xi}) = \frac{w}{4\pi} \int_{|\underline{\xi}|=1} \left(\frac{\xi_i \delta_{jp} \xi_q}{\mu^{(m)} [\sqrt{\xi_1^2 + \xi_2^2 + w^2\xi_3^2}]^3} - \frac{3\kappa^{(m)} + \mu^{(m)}}{\mu^{(m)} (3\kappa^{(m)} + 4\mu^{(m)})} \frac{\xi_i \xi_j \xi_p \xi_q}{[\sqrt{\xi_1^2 + \xi_2^2 + w^2\xi_3^2}]^3} \right) dS(\underline{\xi}) \quad (10)$$

For materials which are transversely isotropic, it is interesting for standard notations and the associated tensorial representations to introduce the Walpole's base which is constituted of a set of direction-related fourth-order tensors \mathbb{E}^i , $i = 1, \dots, 6$ [2]. By using this algebra, any transversely isotropic fourth-order tensor can be expressed as a linear combination of these six elementary tensors. Therefore, for inclusions r oriented with respect to the e_3 axis, Walpole's components of $\mathbb{P}^{(r)}$ are given by [5,2]:

$$\mathbb{P}_w^{(r)} = \left(M_{1111}^{(m)} + M_{1122}^{(m)}, M_{3333}^{(m)}, M_{1111}^{(m)} - M_{1122}^{(m)}, \frac{1}{2} (M_{2332}^{(m)} + M_{3223}^{(m)} + 2M_{2323}^{(m)}), M_{1133}^{(m)}, M_{1133}^{(m)} \right) \quad (11)$$

These components may be integrated analytically [3] and its are given in Appendix A.

3. Homogenized effective properties of porous materials

3.1. Mean Intercept Length method for the measurement of inclusion volume fractions

In this section, we aim at generalizing the formalism described in the previous sections to incorporate microstructural characteristics of inclusions phases by means of the Mean Intercept Length (MIL) method. The computation of the MIL consists of the sampling of intersections between a sampling grid and the pores/matrix interface as a function of the grid's orientation \underline{n} by the following expression:

$$MIL_{pores}(\underline{n}) = \frac{\sum L(\underline{n})}{N(\underline{n})} \quad (12)$$

where $\sum L(\underline{n})$ is the total length of the sampling grid and $N(\underline{n})$ is the number of intercepts sampled at orientation \underline{n} . Moreover, Harrigan [4] showed that the mean intercept lengths in all directions in a three-dimensional porous material would be represented by an ellipsoid and would therefore be related to a positive definite second rank tensor $\underline{\underline{H}}$ in the direction $\underline{n} = (\theta, \phi)$ by the following equation:

$$MIL_{pores}(\underline{n}) = \bar{l}(\underline{n}) = \frac{1}{\sqrt{\underline{n} \otimes \underline{n} : \underline{\underline{H}}}} \quad (13)$$

For a family of ellipsoidal inclusions r characterized by its normal \underline{n} and radius a , we can compute its aspect ratio as $w = \frac{\bar{l}(\underline{n})}{2a}$. Then, the volume fraction of the r th inclusions family is approximately expressed as:

$$f^{(r)} = \frac{4\pi}{3V} \frac{\bar{l}^3(\underline{n})}{8w^2} \quad (14)$$

Thus, for a fixed aspect ratio and by using the equation (13), the total volume fraction of all inclusions is given by:

$$f_p = \frac{1}{4\pi} \int_0^{2\pi} \int_0^\pi \frac{4\pi}{3V} \frac{\bar{l}^3(\underline{n})}{8w^2} \sin \theta d\theta d\phi = \frac{\pi}{3w^2V} \frac{1}{\sqrt{\lambda_3\lambda_1}} \quad (15)$$

where λ_i are the eigenvalues of the fabric tensor $\underline{\underline{H}}$ and V the porous material volume.

3.2. Homogenized effective properties of porous materials

Then, the Walpole's components of the effective stiffness tensor \mathbb{C}^{hom} of the elastic porous materials are given by:

$$\mathbb{C}^{hom} = (2\kappa_p^{hom}, n^{hom}, 2\mu_p^{hom}, 2\mu_n^{hom}, l^{hom}, l^{hom}) \quad (16)$$

where the expression of these components is computed by means of (4), (15) and (A.1). and where we consider that $\kappa^r \rightsquigarrow 0$ and $\mu^r \rightsquigarrow 0$ for porous materials.

The conventional longitudinal Young's modulus is given by:

$$E_n = n^{hom} - \frac{(l^{hom})^2}{\kappa_p^{hom}} \quad (17)$$

Figure 1 illustrates the variation of the effective longitudinal Young's modulus E_n of the trabecular bone (normalized by the matrix Young's modulus) with respect to the inclusion volume fraction f_p and the inclusion aspect ratio w . According to this figure, we can find that the shape and orientation of inclusions has the significant effect on the longitudinal Young's modulus. This classical result provides a first validation of the developed approach. Obviously, it will be interesting to proceed to a more complete validation, for instance by performing experimental data of elastic moduli.

4. Conclusion

A micromechanical method coupled to experimental morphological analyses obtained from high resolution X-ray tomography, has been proposed to predict the effective properties of porous biological materials. The model incorporates the micro-structural parameters like inclusions shape, orientation, distribution and volume fraction. The computed results show that the influence of inclusions volume fraction on the macroscopic properties depends closely on the microstructures of the composite.

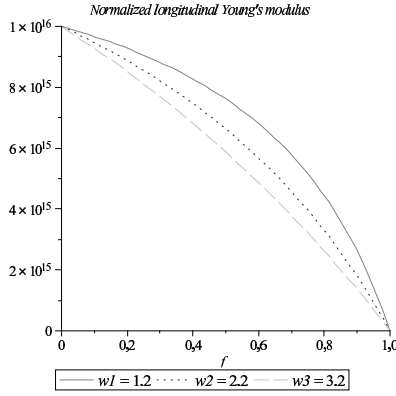


Figure 1. The variation of the normalized longitudinal Young's modulus with the volume fraction of ellipsoidal inclusion for various values of the aspect ratio.

Appendix A. Hill tensor for spheroidal inclusion

The Hill tensor for spheroidal inclusions with aspect ratio w embedded in an isotropic matrix, can be written, by using (10), in the form [3]:

$$\left\{ \begin{array}{l} M_{1111}^{(m)} + M_{1122}^{(m)} = \frac{[7J(w) - 2w^2 - 4w^2J(w)]\mu^{(m)} + 3[J(w) - 2w^2 + 2w^2J(w)]\kappa^{(m)}}{4(1-w^2)\mu^{(m)}(4\mu^{(m)} + 3\kappa^{(m)})} \\ M_{3333}^{(m)} = \frac{[6 - 5J(w) - 8w^2 + 8w^2J(w)]\mu^{(m)} + 3[J(w) - 2w^2 + 2w^2J(w)]\kappa^{(m)}}{2(1-w^2)\mu^{(m)}(4\mu^{(m)} + 3\kappa^{(m)})} \\ M_{1111}^{(m)} - M_{1122}^{(m)} = \frac{[15J(w) - 2w^2 - 12w^2J(w)]\mu^{(m)} + 3[3J(w) - 2w^2]\kappa^{(m)}}{4(1-w^2)\mu^{(m)}(4\mu^{(m)} + 3\kappa^{(m)})} \\ \frac{1}{2}(M_{2332}^{(m)} + M_{3223}^{(m)} + 2M_{2323}^{(m)}) = \frac{2[4 - 3J(w) - 2w^2]\mu^{(m)} + 3[2 - 3J(w) + 2w^2 - 3w^2J(w)]\kappa^{(m)}}{4(1-w^2)\mu^{(m)}(4\mu^{(m)} + 3\kappa^{(m)})} \\ M_{1133}^{(m)} = \frac{(\mu^{(m)} + 3\kappa^{(m)})[-J(w) + 2w^2 - 2w^2J(w)]}{4(1-w^2)\mu^{(m)}(4\mu^{(m)} + 3\kappa^{(m)})} \end{array} \right. \quad (\text{A.1})$$

where $J(w)$ takes the following forms:

$$J(w) = \frac{w \left[\arccos(w) - w\sqrt{1-w^2} \right]}{(1-w^2)\sqrt{1-w^2}} \quad \text{for } w < 1 \quad \text{and} \quad J(w) = \frac{w \left[w\sqrt{1-w^2} - \cosh^{-1}(w) \right]}{(w^2-1)\sqrt{1-w^2}} \quad \text{for } w > 1$$

for spheres ($w = 1$) we take $\lim_{w \rightarrow 1} J(w) = \frac{2}{3}$

References

- [1] J.D. Eshelby, "The determination of the elastic field of an ellipsoidal inclusion, and related problems". Proceedings of the Royal Society Series A, **252(A)**, 561 (1959).
- [2] L.J. Walpole, "On the overall elastic moduli of composite materials. Journal of the Mechanics and Physics of Solids", **12**, 235 (1969).
- [3] P. Ponte Castaneda and J.R. Willis, "The effect of spacial distribution on the effective behavior of composite materials and cracked media". Journal of the Mechanics and Physics of Solids, **43 (12)**, 1919 (1995).
- [4] T. P. Harrigan and R. W. Mann, "Characterization of micro structural anisotropy in orthotropic materials using a second rank tensor". Journal of Material Science, **19**, 761 (1984).
- [5] Laws N., McLaughlin R., "The effect of fibre length on the overall moduli of composite materials". Journal of the Mechanics and Physics of Solids, **27,1** (1979).

Dusty Plasma - Multy Scale

Vladimir Fortov¹, Oleg Petrov², Olga Vaulina³

**Joint Institute for High Temperatures of the Russian Academy of Sciences, Russian
¹fortov@ficp.ac.ru, ²petrov@ihed.ras.ru, ³vaul@ihed.ras.ru**

ABSTRACT

The dusty plasma is a good experimental model for studying the properties of non-ideal systems and for proofing existing empirical models and numerical results, because, owing to their size, dust particles may be videofilmed, which significantly simplifies the use of direct diagnostic methods. This plasma is a partly ionized gas with negatively or positively charged (~ 1000 - 100000 e) dust particles of micron size (~ 1 - 10 mcm) that may form quasi-stationary plasma-dust structures similar to a liquid or a solid. In view of this, dusty plasma may be experimentally investigated on a kinetic level with high temporal and spatial resolution in terms of the appropriate plasma frequency (~ 10 Hz) and particle separation (~ 100 - 1000 mcm). Investigations were directed on the study of dusty plasma structures and dynamics on kinetic level under action of different external forces (visible and uv radiation, magnetic and thermal fields, electron beam) in glow rf and dc discharges. Results of experimental study of the dusty plasma kinematic viscosity and the diffusion are presented. The experiments were performed in plasma of a capacitive rf discharge with the particles of different sizes. A uniform flow of a dusty plasma liquid was experimentally realized under laser beam action, and the results of analysis of the obtained data made it possible to estimate the viscosity coefficient of a dusty plasma liquid. Experimental examination of the Einstein-Stokes relation between the viscosity and diffusion constants is carried out. The results of a comparison of the measured diffusion and viscosity constants with the existing data of numerical simulation are considered. The influence of high magnetic field on dusty plasma structures is now of great interest in the field of dusty plasma physics. In the present work the rotation of the dusty clouds and anomalous dust acceleration near the discharge tube wall in strong magnetic field was observed. The dynamical processes in dusty plasma cloud were studied under action of electron beam. The action of electron beam effects on dusty plasma parameters such as interparticle distance, mean dust velocity and coupling parameter. The results are given of an experimental investigation of heat transport processes in fluid dusty structures in rf discharge plasmas under different conditions: for discharge in argon, and for discharge in air under an action of electron beam. The analysis of steady-state and unsteady-state heat transfer is used to obtain the coefficients of thermal conductivity and thermal diffusivity under the assumption that the observed heat transport is associated with a thermal conduction in dusty component of plasmas. The temperature dependence of these coefficients is obtained, which agrees qualitatively with the results of numerical simulation for simple monatomic liquids. Experimental investigations of structures of monodisperse dust particles in dc low-pressure glow discharge at temperatures of liquid (4.2 K) are presented. Super- 77 K and liquid helium \sim nitrogen dense boundary-free dust structure moved in the discharge at 4.2 K was observed. Structural and dynamic characteristics of the cryogenic dust structures were measured.

This work was supported by the Russian Foundation for Basic Research (Grants No.06-02-17532, No. 06-08-01584 and No. 07-02-13600).

Atomistic Simulations of Tribology at Sliding MoS₂ Surfaces

Tao Liang, W. Gregory Sawyer, Scott S. Perry, Simon R. Phillpot, Susan B. Sinnott

**Department of Materials Science and Engineering, University of Florida, Florida, USA
(E-mail : liang75@ufl.edu)**

ABSTRACT

Molybdenum disulphide (MoS₂) is the most commonly used solid lubricant coating in aerospace applications. In this work, we develop new empirical many-body potentials for Mo and S systems and examine nano-scale friction between sliding MoS₂ surfaces using classical molecular dynamics (MD) simulations. In particular, MD simulations of Mo cross-linked MoS₂ interfacial sliding at various loads, temperatures and sliding directions are carried out. The loads and friction forces are extracted to calculate the friction coefficient of the MoS₂ as a function of temperature, and the results are compared to experimental pin-on-disk measurements of MoS₂ coatings and AFM measurements on single crystal MoS₂ surfaces. The results from both the DFT calculations and the MD simulations help us to better understand the origins of lubricity on MoS₂.

This work was supported by AFOSR-MURI grant FA9550-04-1-0367.

Modelling Damage of the Crystalline Phase in Semicrystalline Polyethylene

José A. Alvarado-Contreras¹, Maria Anna Polak², and Alexander Penlidis³

¹Machine Design and Modelling Group, University of the Andes, Mérida, 5101, Venezuela;

²Department of Civil and Environmental Engineering, University of Waterloo, Waterloo,

ON, N2L 3G1, Canada; ³Department of Chemical Engineering, University of Waterloo,
Waterloo, ON, N2L 3G1, Canada.

ABSTRACT

This work deals with the micromechanical modelling of semicrystalline polyethylene at large deformations. Polyethylene is today one of the most versatile, durable, and economical polymeric materials. Its many uses range from plastic bags to automobile and aircraft parts. Polyethylene possesses a complex microstructure in which molecules arrange themselves into two distinct physical structures: the crystalline and amorphous phases. Using Continuum Damage Mechanics theory, the challenge is the prediction of the mechanical behaviour and degradation processes of semicrystalline polyethylene considering a detailed description of the microstructure. To illustrate the formulation, the proposed model is used to predict the mechanical response and damage evolution of a polyethylene material under uniaxial tension loading conditions, and the numerical results are compared with the experimental data reported in the literature.

1. Introduction

Significant progress has been made in both experimental and modelling aspects of the deformation mechanisms of polymeric materials. In the literature, a number of articles deals with experimental observations and testing methodologies to understand the links between the molecular and macroscopic properties. Nevertheless, to the authors' knowledge, no numerical model has focused on the interpretation of the structural degradation processes taking place in the material microstructure. The constitutive equations proposed herein consist essentially of introducing the concepts of Continuum Damage Mechanics to describe the rupture of the intermolecular bonds of the crystalline structures. The approach used assumes damage occurs only in the crystalline phase, i.e., degradation of the amorphous phase is ignored. The material morphology is simplified as a collection of inclusions comprising the crystalline and amorphous phases with their characteristic average volume fractions. The crystalline phase is considered as the assembly of molecules arranged into an orthorhombic lattice structure, kept together by van der Waals forces. In the model, Continuum Damage Mechanics provides a framework for describing fragmentation caused by the crystallographic debonding. On the other hand, the amorphous phase is modelled within a thermodynamic framework. Hardening is considered and associated to different molecular configurations arising

during the deformation process. The inclusion behaviour is found by applying some compatibility and equilibrium restrictions along the interface plane. The behaviour of the material on the large scale is determined by considering uniform stresses and suitable boundary conditions in the aggregate.

2. Crystalline Phase Model

Ignoring elastic behaviour and assuming crystallographic slip as the microscopic process controlling deformations, deformation rate D_{ij}^c is determined as the sum of the contribution from all the slip systems. Conveniently, a pseudo-linear relationship between the microscopic deviatoric stress S_{ij}^c and deformation rate D_{ij}^c is expressed by mean of a compliance tensor M_{ijkl} as $D_{ij}^c = M_{ijkl}S_{lk}^*$, where due to covalent bond stability, the deviatoric stress is partitioned additively into an unconstrained S_{ij}^* and a constrained \tilde{S}_{ij} stress; that is, $S_{ij}^c = S_{ij}^* + \tilde{S}_{ij}$ [1].

Considering the failure of van der Waals bonds along the slip systems, a damage variable is introduced to characterize the material loss of load-carrying capacity. To describe the damage process, it is assumed that once the critical resolved shear strength is exceeded, an irreversible rearrangement of the microstructure occurs and the number of bonds decreases. The degradation process is described mathematically by a scalar variable Ω^α related to the fraction of atomic debonds as

$$\Omega^\alpha = \frac{\text{Current number of atomic debonds}}{\text{Initial number of atomic bonds}} \quad (1)$$

The four-order compliance tensor can be written as (See details in [2])

$$M_{ijkl} = \dot{\gamma}_0 \sum_{\alpha} \frac{1}{(1 - \Omega^\alpha)g^\alpha} \left| \frac{S_{mn}^* R_{nm}^\alpha}{(1 - \Omega^\alpha)g^\alpha} \right|^{n-1} R_{ij}^\alpha R_{kl}^\alpha \quad (2)$$

where α represents the slip system index, $\dot{\gamma}_0$ is a reference shear strain, g^α is the reference shear strength, and n is the rate sensitivity inverse. $R_{ij}^\alpha = \text{sym}(n_i^\alpha s_j^\alpha)$ is the symmetric part of the Schmid orientation tensor, where n_i^α and s_i^α are the slip normal plane and the slip direction.

It is postulated that damage occurs when resolved forces are high enough to overcome the bonds that hold molecules together into a coherent structure. Assuming that slip system degradation varies from one system to another and depends only on the local stress state, the following damage evolution law is introduced

$$\dot{\Omega}^\alpha = \dot{\Omega}_0 \left| \frac{S_{ij}^* R_{ij}^\alpha}{(1 - \Omega^\alpha)g^\alpha} \right|^m \quad (3)$$

where $\dot{\Omega}_0$ and m denote the reference damage rate and damage rate sensitivity, respectively.

3. Amorphous Phase Model

For the amorphous phase, the constitutive equations are based on a previous phenomenological model [3]. The deformation rate D_{ij}^a results from the weak interaction forces between the molecules. The driving stress is defined as the difference between the deviatoric Cauchy stress S_{ij}^a and a back stress H_{ij}^a generated by the entangled molecular network. Using a power law relationship and an associated flow rule, the material law is given by

$$D_{ij}^a = \dot{\gamma}_0 \left(\frac{\tau_a}{\tau_0} \right)^{n-1} \left(\frac{S_{ij}^a - H_{ij}^a}{\tau_0} \right) \quad (4)$$

where $\dot{\gamma}_0$ is the reference strain rate, τ_0 is the amorphous shear strength, and τ_a is the resolved shear stress, given as $\tau_a = \sqrt{\frac{1}{2}(S_{ij}^a - H_{ij}^a)(S_{ij}^a - H_{ij}^a)}$.

The amorphous phase hardening is modelled as a back stress governed by changes in the molecule configurational entropy. Using non-Gaussian chain statistics and the eight-chain model [4], the constitutive equation for the back stress tensor is given as

$$H_{ij}^a = \frac{C_R}{3} \sqrt{\frac{3N}{B_{kk}^2}} \mathcal{L}^{-1} \left(\sqrt{\frac{B_{kk}^2}{3N}} \right) \left(B_{ij} - \frac{1}{3} B_{kk}^2 I_{ij} \right) \quad (5)$$

where C_R is the shear hardening modulus, N is the average number of rigid links, B_{ij} is the left Cauchy-Green strain tensor, and $\mathcal{L}(x) = \cosh(x) - 1/x$ is the Langevin function.

4. Composite Inclusion Model

Let us consider an aggregate of inclusions representing some material point subjected to a macroscopic velocity gradient \bar{L}_{ij} . From the macroscopic deformation tensor $\bar{D}_{ij} = \text{sym}(\bar{L}_{ij})$, appropriate boundary conditions are derived to be imposed on the inclusion aggregate. To determine the aggregate stress response \bar{S}_{ij} , it is necessary to compute the inclusion stress tensors S_{ij}^i by using the weighted average of the crystalline S_{ij}^c and amorphous S_{ij}^a responses. The stress fields within each phase are calculated from the respective constitutive model and from the conditions enforcing compatibility and equilibrium across the phases interface. Global equilibrium within aggregate ensures that the corresponding macroscopic stress \bar{S}_{ij} equals the volume average of the local stresses S_{ij}^i .

5. Numerical Simulations and Conclusions

To demonstrate the capability of the model to describe the stress-strain behaviour and damage evolution of a semicrystalline polyethylene material, a numerical test is carried out under constant velocity gradient $\bar{L}_{22} = 0.001\text{s}^{-1}$. The simulation results are compared with two previous viscoplastic models and experimental data, as illustrated in Fig. 1(a). It is seen that the predictions

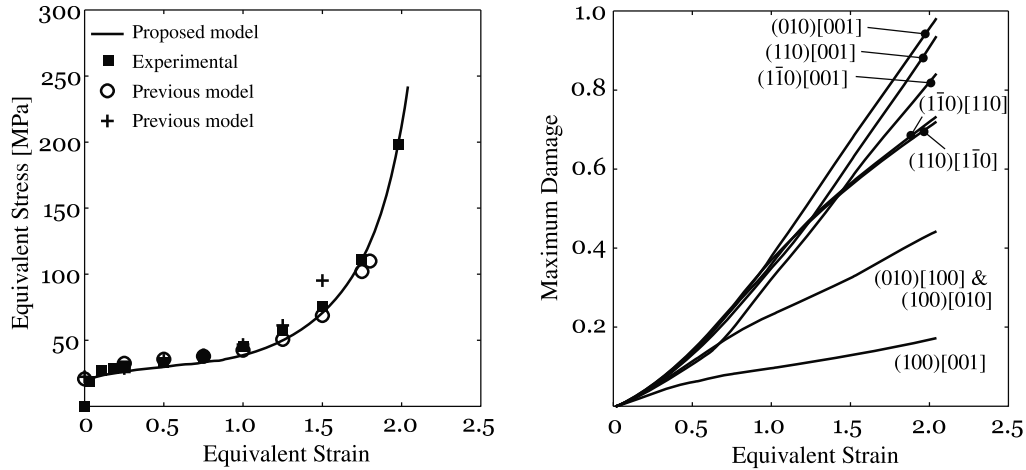


Figure 1: (a) Equivalent stress versus equivalent strain behaviour, (b) Maximum damage versus equivalent strain for the eight slip systems

are in agreement with the experimental data and that the proposed model is able not only to describe larger strains than the previously proposed models, but also to represent the complete range of deformations. The evolution of the damage in the eight slip system is shown in Fig. 1(b). The larger damage values are displayed in the (010)[001], (110)[001], and (1̄10)[001] planes, all of them corresponding to chain slip systems. The lower damage value is observed in the (100)[001] systems.

Acknowledgments

This work was supported by Imperial Oil Canada, the Natural Sciences and Engineering Research Council (NSERC) of Canada, and the Canada Research Chair (CRC) program.

References

- [1] D. M. Parks and S. Ahzi, "Polycrystalline plastic deformation and texture evolution for crystals lacking five independent slip systems", *Journal of the Mechanics and Physics of Solids*, **38**, 7014 (1990).
- [2] J. Alvarado-Contreras, M. A. Polak, and A. Penlidis, "Micromechanical approach to modeling damage in crystalline polyethylene", *Polymer Engineering and Science*, **47**, 410 (2007).
- [3] B. J. Lee, D. M. Parks, and S. Ahzi, "Micromechanical modeling of large plastic deformation and texture evolution in semi-crystalline polymers", *Journal of the Mechanics and Physics of Solids*, **41**, 1651 (1993).
- [4] E. M. Arruda and M. C. Boyce, "A three-dimensional constitutive model for the large stretch behavior of rubber elastic materials", *Journal of the Mechanics and Physics of Solids*, **41**, 389 (1993).

Composite piezoelectric structures used for energy harvesting

Kimberly Cook-Chennault

**Drexel University, Philadelphia, Pennsylvania, USA
(E-mail : kac84@drexel.edu)**

ABSTRACT

Piezoelectric materials generate electrical power when subjected to mechanical loading. Hybrid power generation, i.e. the use of two or more different power supply methods can, if done effectively, improve the lifetime (sustainability) and efficiency of single-source power supply systems such as batteries, fuel cells etc. Regenerative hybrid piezoelectric energy harvesting systems are envisioned for applications requiring lengthy cycle life, such as implantable devices, wherein 20 year life-times are desirable. The ability of piezoelectric devices to capitalize off of inherent device movements and acoustic wave production, offer opportunities to continuously charge secondary sources of power such as batteries, which could potentially increase host device operational lifetime until the active materials of the battery are exhausted or the piezoelectric material crack or break. This work will focus on modeling of composite piezoelectric devices comprised of nano-scaled particles and/or fibers, and comparison of their performance to homogenous and composite devices comprised of micron scaled particles and fibers.

On the micromechanical deformation of particle filled polypropylene compounds

Michael Jerabek¹ and Zoltan Major²

¹Polymer Competence Center Leoben GmbH, Austria

(E-mail: Michael.Jerabek@pccl.at)

²Institute of Materials Science and Testing of Plastics, University of Leoben, Austria

(E-mail: Zoltan.Major@notes.unileoben.ac.at)

ABSTRACT

Particle modified polypropylene (PP) compounds have been widely used in recent years, but still their mechanical behavior is not fully understood. Furthermore, investigations on semi-crystalline polymers below the glass transition temperature have not been carried out. Hence, in this research work the main focus was to characterize the micromechanical deformation during tensile loading of talc and glass bead filled PP at various testing temperatures. Moreover, this investigation was conducted over 5 magnitudes of strain rate to determine the influence of particles on viscoelasticity of the compound. The particles were characterized by SEM pictures to determine their size distribution and in case of talc also their aspect ratio. In order to determine the volumetric response of the compounds and to calculate Poisson's ratio a full filled strain analysis tool was applied. Thus, it was possible to determine the volumetric dilatational behavior up to and beyond the yield point. The results show that rigid particles increase the tensile modulus compared to neat PP at all temperatures investigated. Results calculated by means of micromechanical theories i.e. shear lag theory or the Eshelby theory are in good agreement with the experimental data. Due to the nonlinear viscoelastic and plastic deformation of polymers at the yield point the situation is much more difficult to describe with common models found in literature. Above the glass transition temperature the particles lead to an increase of the yield stress whereas at lower temperatures a decrease of the yield stress could be determined. This effect is attributed to the ductile to brittle transition of the matrix at the glass transition temperature. A detailed description of this effect will be given in the paper. Furthermore, micromechanical models were applied to predict the compound behavior and compared to the experimental values.